PhD-FSTM-2023-131
The Faculty of Science, Technology and Medicine

DISSERTATION

Defence held on 20/12/2023 in Luxembourg

to obtain the degree of

DOCTEUR DE L'UNIVERSITÉ DU LUXEMBOURG

EN PHYSIQUE

by

Marvin JUST
Born on 07 April 1990 in Lahnstein, (Germany)

FLOWABILITY OF HARD METAL GRANULES

Dissertation defence committee

Dr Jörg BALLER, dissertation supervisor
Research scientist, Université du Luxembourg

Dr Christoph BROECKMANN
Professor, RWTH Aachen University

Dr Roland André SANCTUARY, Chairman
Professor, Université du Luxembourg

Dr Raquel DE ORO CALDERON
Professor, TU Wien

Dr Ralph USELDINGER, Vice Chairman
R&D Manager, CERATIZIT Luxembourg S.à r.l.

Affidavit

I hereby confirm that the Ph.D. thesis entitled ”Flowability of Hard Metal Granules” has been written independently and without any other sources than cited.

Trier, 14.10.2023 Marvin JUST

Name

“The behavior of large and complex aggregates
of elementary particles, it turns out, is not to be understood in terms
of a simple extrapolation of the properties of a few particles.
Instead, at each level of complexity entirely new properties appear,
and the understanding of the new behaviors requires research
which I think is as fundamental in its nature as any other.”

P.W. Anderson, 1972 [1]

Abstract

The mass flow rate of granules through an orifice and a flat-bottomed hopper can be estimated with the Beverloo law, considering the properties of the granules, such as the bulk density and granule diameter. The Beverloo Law contains two fitting parameters C and k, which must be determined anew for any granular materials. Understanding the influences on C and k is the key to optimising granules' properties and reaching an ideal granules' flow through an orifice. This study aims to understand the influence of C and k on the flow of hard metal granules. This influence is studied by performing mass flow rate, angle of repose (AOR), and rheological measurements for various materials with changing powder properties. A new technique for AOR measurements has been developed to minimise the influence of avalanching and heap skewness by advanced image processing. The outcome shows that the AOR is no longer sensitive to decentring of the base plate. The findings show that the AOR increases with a decrease in the mean diameter. This increase is attributed to increasing attractive forces, expressed by the granular Bond number, measured with an atomic force microscope (AFM). The attractive forces also influence the mass flow rate through an orifice. Reducing the mean diameter increases the mass flow rate, reaching a maximum. Beyond the maximum, the mass flow rate decreases by the increasing dominance of the attractive forces. Studying the influence on C and k shows that the fitting parameter k is affected by the attractive forces between granules, while the fitting parameter C is linked to the friction coefficient calculated from the AOR. These relationships are considered to propose a modified empirical model to estimate the mass flow rate through orifices for hard metal granules. Rheology measurements showed the applicability of 3D-printed rotor geometries. Plate cup measurements revealed the existence of a linear-viscoelastic regime for hard metal granules in amplitude sweep tests.

Structure

1 Introduction

Hard metals combine high hardness and toughness from a mixture of a hard carbide phase, such as tungsten carbide (WC) and a metallic binder phase, such as cobalt, nickel or iron. Hard metal parts are produced mainly through the powder metallurgy process route. It starts with the mining of ore, which is then chemically treated to acquire ammonium para tungstate (APT). The APT is then calcinated to tungsten oxide (WO_x). These oxides are first reduced to metallic tungsten by hydrogen and then carburized with carbon to tungsten carbide (Figure 1).

In the next step, the tungsten carbide is blended with metallic and organic binders and a milling liquid, e.g., water or organic solvent, in the mixing step. This slurry is then milled in attritors, decreasing the grain size of the tungsten carbide and, at the same time, distributing all components homogeneously. The slurry is then finely dispersed in a spray drying tower, creating small droplets. The tiny droplets are heated by the introduced preheated gas, leading to evaporation of the liquid. The solids, such as tungsten carbide and metallic and organic binders, form spherical hard metal granules known as ready-to-press (RTP) powder.

The granules are used in the direct and indirect shaping process. The latter process uses isostatic presses to compress the granules into axisymmetric parts, such as blocks or rods. The parts are then pre-sintered at temperatures between 500 to 700 °C, leading to the so-called brown parts. The brown parts are then shaped with cutting and turning techniques to the desired shape.

In the direct shaping process, hard metal granules are filled into a cavity via a filling shoe and compressed into green parts with the shape of the cavity.

The pre-sintered shaped parts from the indirect shaping process and the compressed green parts from the direct compression steps are sintered at temperatures between 1300 to 1500 °C. In this step, the parts shrink, leading to hard metal parts with their unique properties. In the post-processing (finishing) step, the sintered hard metal parts can be ground and/or coated.

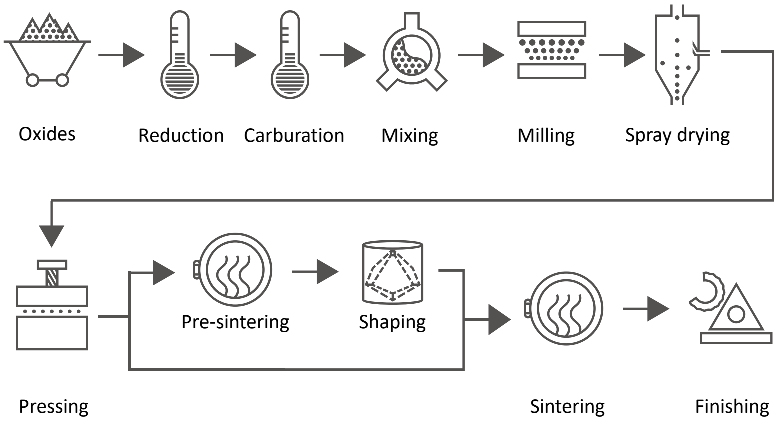

Figure 1: The powder metallurgy process route. The image was adapted based on information provided by CERATIZIT Luxembourg S.à r.l. [2].

It can be seen from Figure 1 that the process steps to reach an optimal hard metal part are challenging, and any inadequate parametrisation in the process route affects all the subsequent steps. A potential influence on the final hard metal part comes from a suboptimal filling of a cavity within the direct shaping process. It is worth summarizing the pressing process (Figure 2). The filling shoe is filled with hard metal granules in the initial position (Figure 2, a). Then, the filling shoe hovers over the cavity opening while the granules fall inside. The filling shoe reaches its final position and covers the cavity's opening Figure 2, b). The cavity is filled with granules. The filling shoe's retraction scrapes the cavity's surface to have an even powder bed surface for the following pressing step. Here, the upper punch moves down and compresses the granules (Figure 2, c). The pressure is released, and the part is ejected (Figure 2, d).

Generally, the filling process aims to fill the die optimally. However, an inadequate interplay between the technical setup and the properties of the granules lead to improper flow into the cavity. The way the granules flow into the cavity is linked to the flowability of granules and is affected by the technical setup, such as the cavity's opening [3] and filling shoe speed [4] and the granular properties, such as the granules' diameter [5].

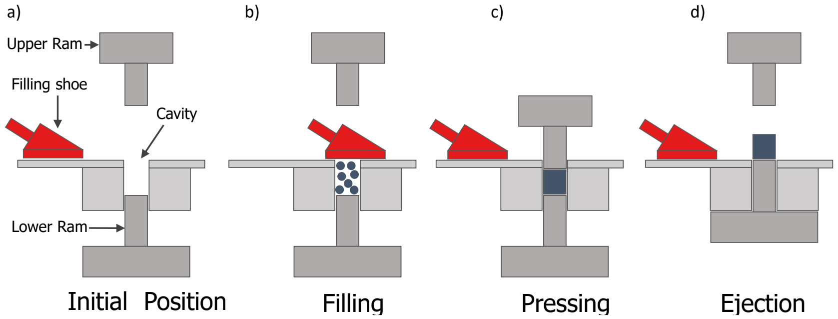

Figure 2: Different steps of a compression cycle. The image is adapted from [6].

The mass flow rate through orifices is one way to describe the flow of granular materials. Beverloo et al. [7] performed in 1960 mass flow rate measurements with different flat-bottomed orifice sizes and granular materials. Based on the outcomes, an empirical model, the so-called Beverloo Law, has been proposed to estimate the mass flow rate for any circular orifice diameter D, considering the bulk density ρ_b, granules diameter d and two fitting parameters C and k. Researchers improved the empirical model by Beverloo et al. [7] to consider other effects contributing to the mass flow rate such as the pressure gradient inside the funnel [8]. However, the Beverloo law has limitations, it fails to estimate the mass flow rate for granule diameters less than 500 µm [8]. Modern modifications of the Beverloo law also consider additional aspects such as attractive forces between granules, to increase the accuracy of the mass flow rate prediction for cohesive powders below 500 µm [9].

The fitting parameters C and k inside the Beverloo law must be determined empirically for every granule system. Any change in the granule's properties also affects granules-related parameters in the Beverloo law, e.g., bulk density. Understanding influences on fitting parameters C and k allows for optimizing hard metal granule properties. An optimisation of the granule's properties provides the opportunity to enhance the mass flow rate, also affecting the quality of the filling process and, thus, the compressed parts. The knowledge to acquire optimal flow properties can help to manufacture even more complex geometries and reduce potential waste in any subsequent powder metallurgy process route. As the diameter of the granules is typically around 200 µm [10], cohesive forces must be considered. Knowing the main influences on both parameters C and k is required to develop an empirical model to estimate the mass flow rate of hard metal granules through orifices. Hence, this study aims to investigate the following questions:

- How does the friction coefficient influence the mass flow rate of hard metal granules through orifices?
- How can the friction coefficient be precisely determined for hard metal granular systems?
- Which properties of the granules affect the friction coefficient?
- How dominant is the role of cohesive forces?
- Are rotor-cup and plate-cup rheological measurements capable of characterising hard metal granules?
- What is the meaning of the fitting parameters C and k in the Beverloo Law for hard metal granules?
- Is there an optimal granule size distribution for the flow of hard metal granules during processing?

This study aims to understand these questions by performing mass flow rate, angle of repose and rheological measurements with samples differing in granule size distributions and compositions.

2 Symbols and Abbreviations

Abbreviation	Description	Abbreviation	Description
ECD	Equivalent circle diameter	AOR	Angle of repose
APT	Ammonium para tungstate	DEM	Discrete element method
SAC	Surface area coverage	FEM	Finite element method
MRI	magnetic resonance imaging	CFD	Computational fluid dynamics
HM	Hard metal	MC	Moisture content
AOR_s	Static angle of repose	AOR_d	Dynamic angle of repose

Symbol	Description	Symbol	Description
α_L / α_R	Left and right angle	$d_{3,2}$	Sauter mean diameter
α	Angle of repose	$d_{4,3}$	De Brouckere mean diameter
D	Outlet diameter, base plate diameter	g	Gravitational acceleration 9.81 m/s^2
d, d_p	Diameter of a particle/granule	γ	Shear deformation, surface tension
m	Mass	C, k	Fitting parameter
v	Velocity	R_{rms}	Surface roughness (root mean square)
A	Area, Hamaker constant	d’	Granules diameter with asperities
F	Force	E	Energy
F_g	Gravitational force	d_{50}	Median diameter
F_{DH}	Downhill force	p,q	Numerical parameter
F_N	Normal force	μ	Friction coefficient
F_R	Friction force	$\mu_{eff,\infty}$	Effective infinite friction coefficient
D_0	Minimal orifice diameter, cut-off distance	μ_w	Wall friction
k	Ratio between two diameters, stiffness constant	ω	Angular velocity
f	Ratio between two slopes	f	Frequency
K	Ratio of horizontal and vertical wall stress	I	Inertial number
n	Quantity / amount	K_1, K_2, K_3 and K_4	Fitting parameter
V	Volume	ρ_b	Bulk density/apparent density
Bo_g	Granular Bond number	β	Fitting parameter
θ	Contact angle, angle of repose	$\dot{m}$	Mass flow rate

τ	Shear stress	d_s	Spherical diameter
σ	Normal stress, surface energy	D_h	Hydraulic orifice diameter
η	Viscosity, packing fraction (density)	K_1	Fitting parameter
L, l	Length	R,r	Radius, distance
W, w	Width	σ_v, σ_h	Vertical and horizontal stresses
H,h	Height	x	Radial position of a granule
a,b,c,e,f,h	Length scale	v_y	Vertical velocity of a granule
g	Gravitational acceleration	z_0	Minimal separation distance
P	Pressure	T_m	Torque
λ	Janssen's length scale	T_s	Torque contributions from side surfaces
ψ	Sphericity	T_e	Torque contributions form rotor end surfaces
Γ	Sensitivity of the LASER, vibration strength	σ^p	Polarsurface energy
Δe	Difference in laser deflection	σ^d	Dispersive surface energy

3 Literature research

3.1 Manufacturing of granular materials

3.1.1 The etymology of the word granule

Oran and Boris [11] describe granular materials as an assembly of particles in a packed system. These particles can be small grains or granules created from the agglomeration of grains through a granulation process [12] (Figure 3). The word *grain* originates from the Proto-Indo-European (PIE) language (ĝrh$_a$nóm) in the years between 9000 to 2500 BC [13]. Cognates exist in various old and current languages such as Old Irish *grán,* Old English *corn*, Lithuanian *žìrnis* (pea), Albanian (16th century onwards) *grurë* (wheat), Old Church Slavonic, Slavic (9th – 13th centuries) *zrĭno* and modern Southeast Iranian *zaṇnai* ~ *zaṛai* (kernel, seed) [13]. Today's word *granules* is linked to the late Latin word *granulum* (grains) and the diminutive word *granum,* which is also used to refer to botanical fruit seeds [14]. *Granosus* (grānōsus) is an adjective related to the Latin word *granum* and means *full of grains*. Today's ending form of the adjective *granular* is connected to the word-formation element "pertaining to, of the nature of" from Latin –arem, -aris meaning "of the kind of, belonging to" [15].

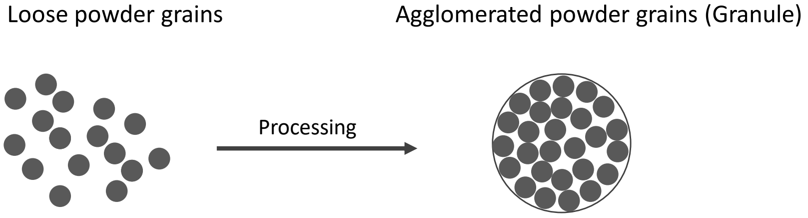

Figure 3: Difference between grain and granule

3.1.2 Granulation process

The powder metallurgy industry uses granular materials to enhance the flowability into a die within the compression step. These granular materials can be manufactured through various granulation processes. The selection of the most suitable granulation process is based on economic aspects such as investment costs, yield, upscaling possibilities, targeted material properties, raw materials and industrial preferences [16].

The manufacturing process of granular materials is not the scope of this work and is a wide-ranging topic. However, a brief description of a few techniques is worth mentioning. The granulation process can be divided into two essential processes: the dry and the wet formulation process. During the dry granulation, small grains are shaped into spheres, tablets or pellets without using liquids or plasticisers. One of the dry granulation processes is the roller compaction process, where small grains are compacted by two rolls [17]. Here, powders are transported towards the rolls through gravity or by the pushing method [17]. The material is compressed under pressure by two counter-turning rolls. Depending on the material, the compressed parts are milled and screened to acquire granules [17].

One of the wet granulation processes is the spray drying process, a common technique in the hard metal industry [10]. Typically, in the first step, a slurry is created from a milling process consisting of powders, liquid and an organic binder. Then, the slurry is dispersed with a nozzle in a drying chamber. The dispersion direction depends on the spray drying technology. A possible spray drying direction is shown in Figure 4 (a), where the suspension (feed) is sprayed in the downward direction, and the heated gas enters from the top (Figure 4, a). Another approach is to spray the suspension upwards while the heated gas enters from the top (Figure 4, b). The created tiny droplets face a vertical (downward or upward) movement depending on the technology. On the way, the heated chamber and gas lead to the evaporation of the organic solvent. During this step, solid particles precipitate at the droplets' surface, creating a solid shell, which increases in thickness in function of the falling distance, leading to a spherical granule at the end of the process [18,19]. Various liquids, such as water or organic solvent, can be used for the spray drying. When an organic solvent is used, nitrogen as a drying gas is commonly used in the hard metal industry [10].

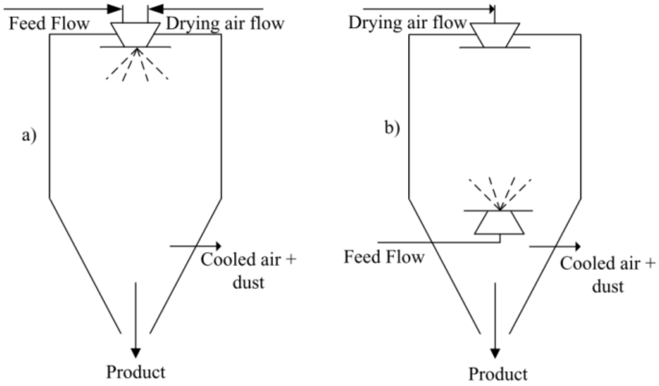

Figure 4: Spray drying process with two different spray variants: co-current (a) and counter-current (b). The image is taken from [20].

<u>*The objective of the granulation process*</u>

The granulation process aims to enlarge fine particles to single and bigger granules which improves handling, reduces fine powders' dustiness, increases resistance against deformation and reduces the risk of segregation [21]. Segregation describes the inhomogeneity of the granules' distribution within a bulk material occurring, for instance, from material flow along an inclined plane [22]. Bhatt and Kumar [23] and Shanmugam [24] describe the ideal characteristics of pharmaceutical granules as uniform, with good flowability and excellent compressibility for the subsequent compression step. Optimal powder characteristics are reached by having ideal spherical shapes, absence of intragranular porosity with a narrow size distribution and adequate moisture of 1 to 2 % [23]. Although this refers to pharmaceutical materials, ideal characteristics to acquire excellent flowability are also needed for other materials in applications such as additive manufacturing [25,26].

3.1.3 Granule size distribution

One way to characterise granular materials is to measure their granule size distribution. The granule size distribution provides information about a granule system's mono- or polydispersity, i.e., the number of granules with discrete diameters in a bulk material.

Many different ways exist to measure the granule size distribution of powders and granular materials. Conventional measurements exist, such as laser diffraction [27] and optical measurements using optical microscopy [28], but also analyses like the Andreasen pipette, which uses sedimentation mechanisms [29]. Sieving with various mesh widths [30] can define the distribution of granules within the bulk material. However, this process may alter the material due to mechanical solicitation during sieving. A comparison of various measurement methods can be found in the literature [31]. This work uses the laser diffraction method for characterizing the granular materials. This method is explained briefly in the following and is adapted from Cyr and Tagnit-Hamou [27]. Typically, granules are dispersed (dry or wet) into a measuring chamber and are exposed to monochromatic light in the form of a collimated laser beam (Figure 5). The granules in the flow cell lead to the diffraction of the laser light. A Fourier lens focuses the light on a detector, which processes the incoming light. The granule size distribution is calculated with a mathematical model applied to the diffracted light pattern. Two known models are the Fraunhofer approximation and Mie theory. The Fraunhofer approximation considers only the diffracted light, assuming the particles are flat and opaque discs. Conversely, the Mie theory needs knowledge about the investigated materials, such as the refractive index, as the light is reflected and refracted.

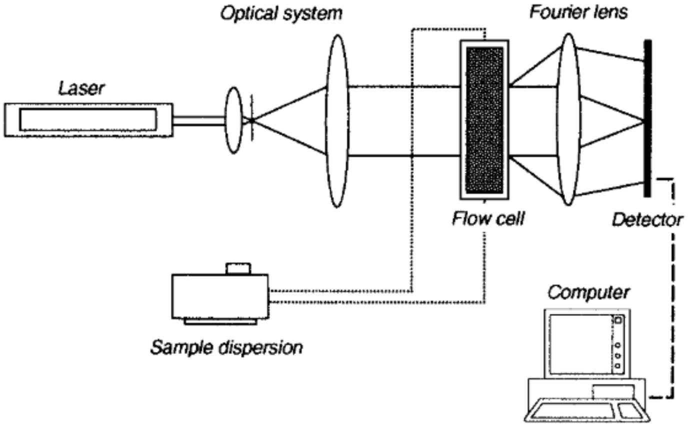

Figure 5: The image shows the measurement setup of a laser diffraction instrument. The image is taken from [27].

3.1.3.1 Diameters d_{10}, d_{50} and d_{90}

The granule size distribution is typically displayed as a volumetric size distribution. Figure 6 shows an exemplary cumulative volumetric distribution. The diameters d_{10}, d_{50} and d_{90} typically describe such a size distribution. The values in the index indicate that 10, 50 and 90 vol.-% of the granules population are smaller than the diameter d [32]. Here, the d_{50} is the median diameter of a size distribution.

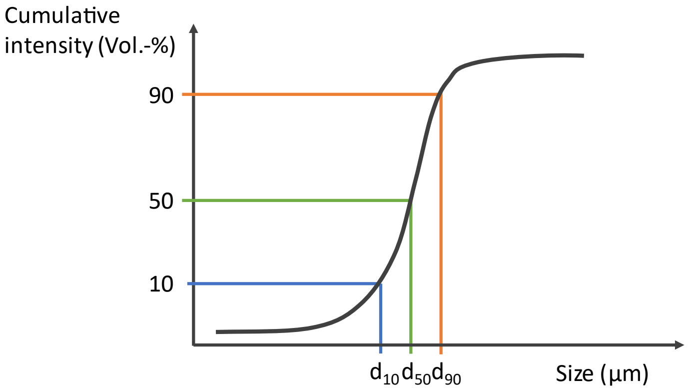

Figure 6: Schematic cumulative volumetric granule size distribution to illustrate the diameters d_{10}, d_{50}, and d_{90}.

3.1.3.2 Sauter mean diameter and de Brouckere diameter

The Sauter mean diameter, or surface-weighted mean diameter, is a representative mean diameter of a polydisperse granule size distribution measured, for instance, with a laser diffraction method. The amount of granules n_i and the diameter d_i of a size class i in a polydisperse granule system can be considered to calculate the Sauter mean diameter [33]. The calculation of the Sauter mean diameter is explained by Kowalczuk and Drzymala [33], transforming the polydisperse system hypothetically into a monodisperse granule system [33]. The transformation is achieved by assuming that the polydisperse system's volume and surface equals a monodisperse system with identical granular sizes (Figure 7) [33]. This chapter is adapted from Kowalczuk and Drzymala [33].

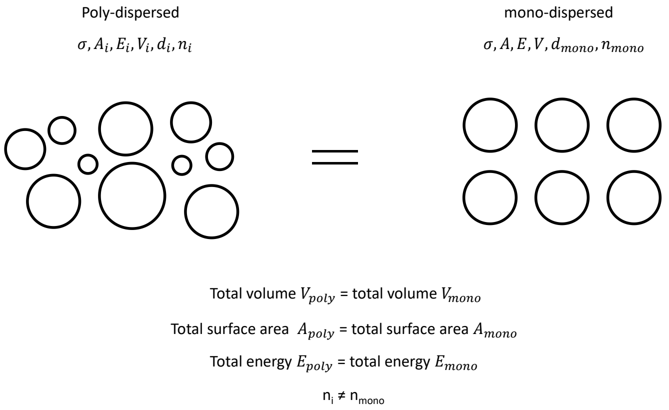

Figure 7: Transforming a polydispersed granular material into a monodispersed granule system with equal cumulated volume and surface area; image recreated and based on [33].

Kowalczuk and Drzymala [33] describe the relationship between both systems assuming ideal spheres. Here, the energy E_i (J) of a single granule (i) can be calculated according to equation 1, where σ is the surface tension (J/m^2) and A_i is the surface (m^2).

$$E_i = \sigma * A_i \qquad 1$$

The total energy E_{poly} of a poly-dispersed system equals the sum of all energies from each size class i and can be obtained by equation 2.

$$E_{poly} = \sum_{i=1}^{N} E_i = \sigma * \sum_{i=1}^{N} n_{\,i} * A_i \qquad 2$$

The surface area A_i of a single spherical body is as follows:

$$A_i = \pi * {d_i}^2 \qquad 3$$

Regarding a monodisperse granule system with identical granule size d_{mono} (monodisperse system), the energy E_{mono} is:

$$E_{mono} = \sigma * A_{mono} * n_{mono} = \sigma * \pi * d_{mono}^2 * n_{mono} \qquad 4$$

Assuming that the poly- and monodisperse systems are identical in terms of their surface areas and thus also in their energies ($E_{mono} = E_{poly}$), then equations 2 and 4 lead to:

$$n_{mono} * {d_{mono}}^2 = \sum_{i=1}^{N} n_i * {d_i}^2 \qquad 5$$

Kowalczuk and Drzymala [33] state that the number n_{mono} of identical spheres (monodisperse) is equivalent to the ratio of the total volume of a poly-dispersed system and the total volume of a monodispersed granule system ($V_{poly} = n_{mono} \cdot V_{mono}$), following:

$$n_{mono} = \frac{V_{poly}}{V_{mono}} = \frac{\sum V_i}{V_{mono}} = \frac{\frac{\pi}{6} * \sum_{i=1}^{N} n_i * {d_i}^3}{\frac{\pi}{6} * {d_{mono}}^3} = \frac{\sum_{i=1}^{N} n_i * {d_i}^3}{{d_{mono}}^3} \qquad 6$$

Inserting equation 6 into equation 5 provides the relationship between a poly- and a mono-dispersed system following:

$$\frac{\sum_{i=1}^{N} n_i * {d_i}^3}{{d_{mono}}^3} * {d_{mono}}^2 = \sum_{i=1}^{N} n_i * {d_i}^2 \qquad 7$$

A reorganisation of equation 7 leads to the known Sauter mean diameter d_{mono} (Equation 8)

$$d_{mono} = \frac{\sum_{i=1}^{N} n_i * {d_i}^3}{\sum_{i=1}^{N} n_i * {d_i}^2} \qquad 8$$

It can be derived from equation 8 that Sauter's mean diameter is the ratio between the total volume and the total surface of granule size distribution. The parameter d_{mono} is also commonly expressed as $d_{3,2}$ [34] or $d_{[3,2]}$ [35].

Equation 8 can also be used to calculate the de Brouckere mean diameter $d_{[4,3]}$, also known as volume moment mean diameter. The de Brouckere mean diameter can be calculated by changing the exponents in the numerator to d^4 and the denominator to d^3. This way, large granules are more considered in the mean diameter than smaller ones, as larger granules have high volumes, but their amount in the size distribution is comparably low. Conversely, fine granules are high in numbers but low in volume. The de Brouckere diameter is, according to Wang et al. [36] and Hofmann [37] very sensitive to coarse spheres.

3.1.3.3 A comparison of different mean size diameters and their application

The previous sections presented different mean diameters. These diameters will be explained with an exemplary granule size distribution (Figure 8) adapted from [38]. In a simple example, the granule size distribution consists of only three different granule sizes and is assumed to be spherical.

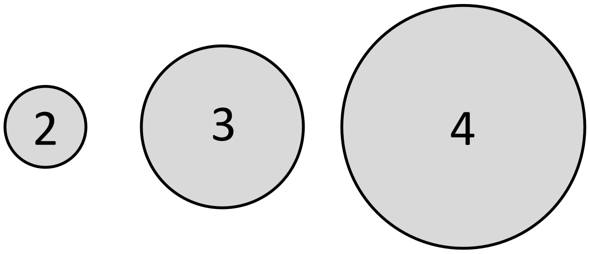

Figure 8: Exemplary granule size distribution consists of three different granule sizes: 2, 3 and 4. The image is created based on the information provided in the literature [38].

The definition of various mean diameters is based on the outcomes of Mugele and Evans [39], where the mean diameter of a distribution can be described by considering the frequency of occurring particles n_i in a size class i with the average diameter d_i [40] following:

$$d_{[p,\mathrm{q}]} = \left(\frac{\sum_{i=1}^{N} d_i^p * n_i}{\sum_{i=1}^{N} d_i^q * n_i}\right)^{\frac{1}{\mathrm{p-q}}} \qquad 9$$

The number mean diameter $d_{[1,0]}$ is the average mean diameter from all spherical objects in the exemplary granules distribution (Figure 8) and can be calculated according to equation 9, following:

$$d_{[1,0]} = \left(\frac{\sum d_i^1 * n_i}{\sum d_i^0 * n_i}\right)^{\frac{1}{1-0}} = \left(\frac{\sum d_i * n_i}{\sum n_i}\right)^{\frac{1}{1}} = \frac{(2*1)+(3*1)+(4*1)}{3} = 3 \qquad 10$$

The surface mean diameter $d_{[2,0]}$ is calculated according to equation 9 and weights the diameter in terms of their surfaces. Larger surfaces contribute more to the mean diameter (equation 11). Therefore, considering the surface of the individual granules (Figure 8) gives rise to a higher mean diameter.

$$d_{[2,0]} = \left(\frac{\sum d_i^2 * n_i}{\sum d_i^0 * n_i}\right)^{\frac{1}{2-0}} = \left(\frac{\sum {d_i}^2 * n_i}{\sum n_i}\right)^{\frac{1}{2}} = \sqrt[2]{\frac{(2)^2*1+(3)^2*1+(4)^2*1}{3}} = 3.11 \qquad 11$$

The same applies to the volume mean diameter $d_{[3,0]}$, following

$$d_{[3,0]} = \left(\frac{\sum d_i^3 * n_i}{\sum d_i^0 * n_i}\right)^{\frac{1}{3-0}} = \left(\frac{\sum {d_i}^3 * n_i}{\sum n_i}\right)^{\frac{1}{3}} = \sqrt[3]{\frac{(2)^3*1+(3)^3*1+(4)^3*1}{3}} = 3.21 \qquad 12$$

The Sauter mean diameter and the de Brouckere mean diameter explain the central point of the frequency where both mean diameters are located [38]. These are, in fact, the centre of the magnitude of the individual distributions [38]. The advantage of both mean diameters is that the exact number of particles in the size distribution is unimportant [38]. Both mean diameters $d_{[3,2]}$ and $d_{[4,3]}$ are strongly influenced by large diameters inside a size distribution, even when these large diameters are low in number [41]. The Sauter mean diameter can be calculated with equation 9.

$$d_{[3,2]} = \left(\frac{\sum d_i^3 * n_i}{\sum d_i^2 * n_i}\right)^{\frac{1}{3-2}} = \left(\frac{\sum {d_i}^3 * n_i}{\sum {d_i}^2 * n_i}\right)^{\frac{1}{1}} = \frac{(2)^3 * 1 + (3)^3 * 1 + (4)^3 * 1}{(2)^2 * 1 + (3)^2 * 1 + (4)^2 * 1} = 3.41 \qquad 13$$

Likewise, for the de Brouckere mean diameter.

$$d_{[4,3]} = \left(\frac{\sum d_i^4 * n_i}{\sum d_i^3 * n_i}\right)^{\frac{1}{4-3}} = \left(\frac{\sum {d_i}^4 * n_i}{\sum {d_i}^3 * n_i}\right)^{\frac{1}{1}} = \frac{(2)^4 * 1 + (3)^4 * 1 + (4)^4 * 1}{(2)^3 * 1 + (3)^3 * 1 + (4)^3 * 1} = 3.57 \qquad 14$$

The application of the above mean diameters is listed by Mugele and Evans [39], where the Sauter mean diameter $d_{[3,2]}$ is used for efficiency studies, mass transfer and reaction. Beyond this, more applications can be found in the literature. For instance, the Sauter mean diameter $d_{[3,2]}$ is used to describe the mean diameter of bubbles using frothers in a liquid [42] or mean droplet size in atomized fuel sprays [43]. Humby et al. [44] considered a set of mean diameters, such as $d_{[1,0]}$, $d_{[2,1]}$, $d_{[3,2]}$ and $d_{[4,3]}$, to find a suitable relationship between mean diameter and minimal orifice diameter in the domain of granules flow. In another study, the average mean diameter $d_{[1,0]}$ is selected to investigate the properties of Jatropha fruits [45].

3.2 The angle of repose of bulk materials

3.2.1 Definition of the angle of repose

The angle of repose is defined as the maximal angle between a horizontal plane and the inclined surface of a piled-up material under unconfined conditions. The maximal angle is reached by bulking up the bulk material before the material reaches an unstable state, followed by material relaxation through an avalanche on the pile's surface. The meaning of the angle of repose is related to the measurement procedure [46]. For instance, a static angle of repose is the maximal angle before an avalanche occurs, i.e., at rest (see following chapter) (Figure 9, a). Besides this, a dynamic angle of repose is known, describing various angles in motion typically measured with a rotating drum at defined speed (Figure 9, b) [47]. Another angle of repose is the so-called drained angle, measurable at the end of a discharged flat-bottomed container (Figure 9, c). Here, the drained angle is the angle of the occupied material in the dead zones inside the container, i.e. the material between the inner cylindrical container wall and the perimeter of the orifice [48].

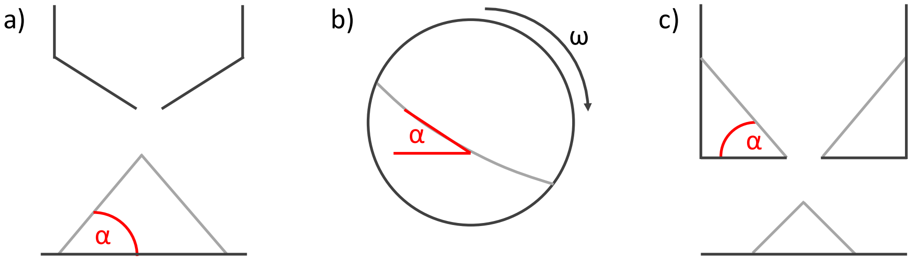

Figure 9: a) The static angle of repose, b) the dynamic angle of repose determined from a rotating drum and c) the drained angle within a flat-bottomed cylinder.

The angle of repose is explained in Figure 10. The normal force F_N acting on the surface is directly linked to the gravitational force F_G ($F_G = m \cdot g$) and the angle α between the horizontal plane and the inclined surface following:

$$F_N = F_G \cos\alpha \qquad 15$$

Perpendicular to the normal force F_N, the downhill force F_{DH} acts along the inclined surface.

$$F_{DH} = F_G \sin\alpha \qquad 16$$

The angle of repose is defined as the maximal angle α before the surface of a pile collapses. Considering this aspect, the maximal angle α is reached in Figure 10 when the downhill force F_{DH} equals the friction force F_R arising, for instance, from surface asperities between the object and the inclined surface.

$$F_R = F_{DH} \qquad 17$$

The magnitude of the friction force F_R is linked to the normal force F_N and the friction coefficient μ.

$$F_R = \mu F_N \qquad 18$$

Considering equations 15, 16 and 18 and inserting them into 17:

$$\mu F_G \cos\alpha = F_G \sin\alpha \qquad 19$$

Solving for the friction coefficient μ, then:

$$\mu = \frac{F_G \sin\alpha}{F_G \cos\alpha} = \tan\alpha \qquad 20$$

It is visible from equation 20 that the maximal friction coefficient μ can be directly acquired from the angle of repose of a piled-up material (before sliding). In reality, the angle of repose of granules is created from an interplay of many parameters, such as granule size (see chapter 3.2.3). Hence, equation 20 describes an effective friction coefficient. However, equation 20 is widely applied in the scientific community to calculate the friction coefficient μ of bulk materials, independent of their nature [46,49–52].

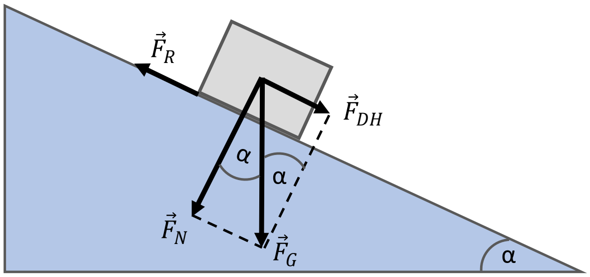

Figure 10: Forces acting on the surface of an inclined plane.

3.2.2 Measurement and determination of the angle of repose

The determination of the angle of repose is described in ASTM D6393-21 [53]. The measurement is briefly summarized: A mass m of the powder is filled into a funnel. The bulk material passes an orifice under vibration and falls onto a horizontal plate. Then, the pile height is measured when the material is discharged from the funnel. The angle of repose is calculated with the diameter D of the base and the height H of the pile (equation 21).

$$\alpha = \tan^{-1}\left(\frac{H}{0.5D}\right) \qquad 21$$

The method itself is simple. However, there are many ways to create a pile of bulk material. Figure 11 shows four possibilities of measurement setups to determine the angle of repose. The first version in Figure 11 (a) consists of a flat-bottomed container and a horizontal plane. The material discharges from the container on a flat surface. Then, the diameter D and the height H must be measured of the created heap on the horizontal plane. This method can also determine the drained angle of repose when the container is completely discharged, as depicted in Figure 11 (a). Figure 11 (b) resembles the measurement approach of ASTM D6393-21 [53]. The piling method uses a funnel and a base plate with known diameter D below the funnel (Figure 11, b). The material falls on top of the plate and creates a pile with a conical shape. The advantage of this method is a predefined circular diameter D of the base plate (Figure 11, b). This way, the angle of repose can be calculated by measuring only one parameter, the height H of the pile, and using equation 21. The submerged method creates a conical pile shape on a base plate inside a container by reducing the overall bulk-filled level (Figure 11, c). The pouring method test is based on the flowability of the inserted material (Figure 11, d). A discrete amount of mass is inside the hollow cylinder. The cylinder is lifted, and the material flows on the surface of the horizontal plane, creating a pile of the bulk material similar to Figure 11 (a). The angle of repose is then determined by measuring the diameter of the pile D and it’s height H. Further information regarding the pouring method can be found in [54]. Even more measurement setups exist, such as the tilting box method [55] and the parallel wall experiment [56].

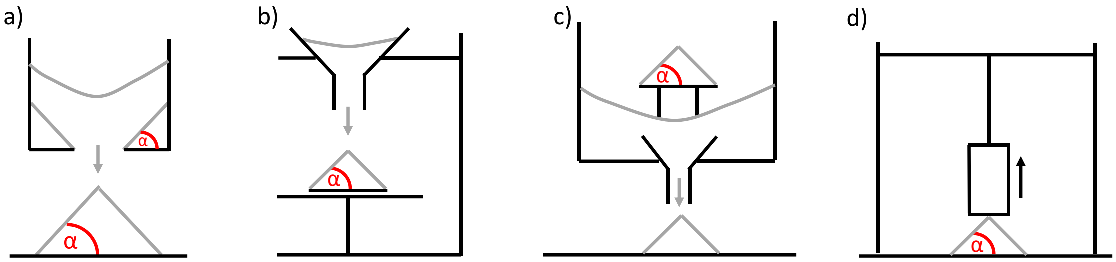

Figure 11: Various methods for determining the angle of repose, a) emptying method, b) piling method, c) submerging method and d) pouring method. The image is adapted from [57]. The grey arrows indicate the movement of the powder on the surface. The black arrow indicates the movement of the apparatus in d).

A problem arises in defining a representative angle of repose for bulk materials. In reality, the cone surface is uneven and changes radially from the sides to the centre of the cone. The problem of defining the correct repose angle has been illustrated by Wójcik et al. [57]. How the tangential line is applied on the cone surface changes the slope and the determined angle of repose. This effect is even more pronounced for very fine particles leading to irregular heap shapes, as illustrated by Lumay et al. [58]. The challenge to determine a representative slope of the pile demands for more advanced techniques. One approach is to take a projection of a cone as a 2D image and convert the irregular shape to an ideal triangular area with the help of image processing software [58]. This method suppresses the problem of how to correctly apply the tangential line and defines the angle of repose through a normalized triangular area. A comparison between the projected heap and the typical linear fit was investigated for snow by Willibald et al. [59]. The results state a higher angle of repose for the projected cone method. Independent of the applied determination method, the bulk material properties play a crucial role in the magnitude of the angle of repose.

Li et al. [60] determined the angle of repose using image processing software. In the first step, a heap is created on a base plate. Then, a camera takes an image of the static heap. The surface line of the heap projection is described with pixels containing discrete positions in the 2D image. In the next step, a linear fit is applied to the surface line using the discrete pixel locations. The correlation coefficient is calculated for a range of linear fits starting from the lower corner towards the centre of the heap. A correlation coefficient close to 1 yields the final angle of repose, considering the slope of the final linear fit [60].

Furthermore, Müller et al. [61] apply the following procedure to describe the outline shape of a piled-up material acquired from DEM simulations. In this approach, the image is cropped in two parts, i.e., left and right. A simple linear regression determines the angle of repose for both sides based on the cone surface's pixels. Notably, the cone is partly cropped to reduce the effect of the lower end of the cone. An iteration process similar to Li et al. [60] calculates the slope for each pixel on the surface line. The highest slope represents the angle of repose for one side. This method is applied on both sides. The final angle of repose is the average of both sides. In a second step, Mueller et al. [61] determine the angle of repose with a non-linear fit function based on a Newton-Gauss-Algorithm. The non-linear fit is likewise applied to each side of the image. The acquired angle of repose differs in dependency of the applied fit.

In another study, Chen et al. [62] created various conical heaps with DEM simulations. The angle of repose is then determined of these created heaps. Like in the previous approaches, the angle of repose is calculated from the particle positions on the cone's surface. However, the focus lies on the middle part of the cone by omitting a lower and upper portion of the piled heap. The middle part is divided into three parts, whose angles are determined individually. The average of the three sections is the angle of repose (Figure 12).

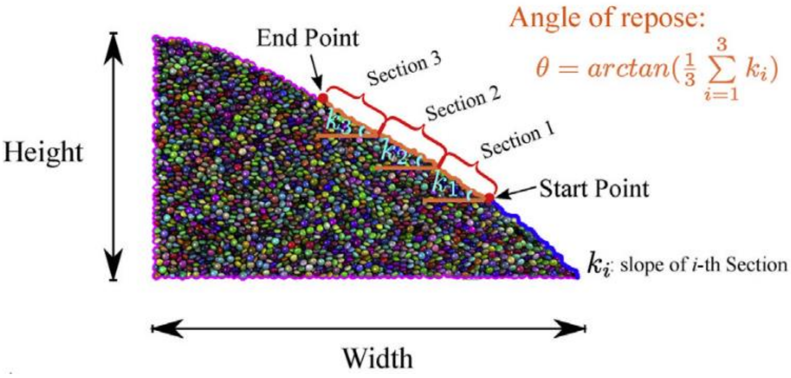

Figure 12: An image from a heap created with DEM simulations. The angle of repose is calculated with three sections. The image is taken from [62].

3.2.3 Influences on the angle of repose

Various parameters related to the bulk materials' properties affect the angle of repose. The isolation of these physical quantities is challenging. By manipulating one physical quantity, other properties change likewise. For instance, a change of the particle diameters in a polydisperse granules system also influences the bulk density of the material [63] and therefore the angle of repose.

Table 1: Influences on the angle of repose based on literature research.

External parameters	**Internal parameters**
Temperature	Size and size distribution
Gravity	Surface roughness (Friction)
Measurement setup (e.g., plate size)	Density (e.g., bulk density)
	Shape (e.g., sphericity)
	Cohesion
	Moisture

3.2.3.1 External parameters affecting the angle of repose

In terms of external parameters, the temperature influences the angle of repose. Willibald et al. [59] measured the angles of repose of different snowflake types, which differed in size and shape, over a broad range of temperatures. The outcomes show that the angle of repose is nearly constant for temperatures below -22 °C. Between -15 and -2 °C, the angle of repose increases, attributed to an increasing cohesive effect between snowflakes. An Arrhenius law expressed the temperature influence on the angle of repose. Additionally, Willibald et al. [59] stated that the snowflakes' shape also influenced the angle of repose.

Gravity influences the magnitude of the forces in the force network inside the pile material. A numerical investigation with DEM simulations by Chen et al. [64] showed that the force network scales linearly with increasing gravity. However, the ratio of the normal to tangential forces remains constant, i.e. gravity does not affect the angle of repose measurements. The DEM simulations neglected the influences of cohesive forces. Another investigation included this aspect and showed a significant impact on the measured angle of repose with decreasing gravity [50]. The main reason is the change in the cohesive forces' predominance as the gravity decreases. In other words, the magnitude of the cohesive forces is independent of gravity, while the weight of a singular particle is affected by gravity (see chapter 3.4). This relationship also affects the magnitude and frequency of avalanches [65].

Besides temperature and gravity, the measurement setup also influences the measured angle of repose (see also chapter 3.2.2). Miura et al. [66] studied various aspects impacting the angle of repose. For instance, the results show a minimal reduction of the measured angle of repose as the mass on a plate increases. This result is explained by a change in the internal friction with modifications in the confining pressures. Furthermore, the surface roughness of the base plate affects the measured angle of repose. The angle of repose increased nearly linearly with the surface roughness of the base plate. Therefore, Miura et al. [66] proposed a modification of the standard angle of repose measurements to avoid an influence by the base plate roughness. An influence by the base plate material and the falling height of the material onto the base plate is reported by Madrid et al. [67].

3.2.3.2 Internal parameters affecting the angle of repose

Assuming a constant measurement procedure, a change in the angle of repose occurs entirely by the nature of the materials, i.e., by the bulk properties. One of these properties is the granular size and size distribution. Lumay et al. [58] investigated the influences of the granular size on the static and dynamic angle of repose. In both cases, the angle of repose significantly increases when the powder grain size is below 70 µm. Regarding a polydisperse powder system, the results stated an optimal relationship with the d_{10} diameter (see chapter 3.1.3.1), implying a predominant influence on the angle of repose by the smallest particles in the granule system. The same is also found for various sizes of coal powders [68] and with DEM simulations [69].

The shape of the particles and granular materials affect the angle of repose [70]. For instance, a DEM study showed a difference in the angle of repose caused by the interlocking of the agglomerated particles with irregular shapes [71]. A similar approach with non-spherical granules has been reported by Khanal et al. [72]. Fu et al. [73] state an increase in the angle of repose with increasing particle angularity, i.e. less sphericity, caused by particle interlocking promoted by the particle edges. The effect of interlocking is in general increased by the particle's shape and the surface roughness of the particle or granular material [71]. The surface roughness can be described as a topographical irregularity caused by small asperities on the surface, which are smaller than the overall size of the particles or granules. The surface roughness of materials affects surface-related phenomena such as friction or wear.

In the case of hygroscopic powders, such as lactose or pharmaceutical powders, the moisture significantly influences the angle of repose. Studies show a common picture: the angle of repose increases with increasing moisture content [49,51,74]. The increase in the angle of repose is caused by the increase of cohesion inside the system (see chapter 3.4). Elekes and Parteli [50] further studied the influence of cohesion with the help of DEM simulations. Elekes and Parteli [50] assumed that the van der Waals forces are the dominant forces inside a dry granule system. An increase in the influence of the interparticle attraction by varying the particle diameters showed a non-linear evolution of the friction coefficient calculated from the angle of repose. Elekes and Parteli [50] expressed the interparticle attraction with the granular Bond number (see chapter 3.4) and stated a significant increase for granular Bond numbers higher than 100. The relationship is described with equation 22, where $\mu_{eff,\infty}$ is the effective infinite friction coefficient of the bulk material, Bo_g is the granular Bond number, and β is a fitting parameter. The effective infinite friction coefficient is for very big granules nearly independent of particle size, i.e., cohesive forces are low compared to the gravitational force.

$$\theta \approx \tan^{-1}\left\{\mu_{eff,\infty} \cdot \left[1 + \beta\sqrt{Bo_g}\right]\right\} \qquad 22$$

3.3 Flow of granules through an orifice

The flow of granules is defined as the movement of solid particles in vacuum or inside a fluid such as air or water. From a macroscopic point of view, a granule system can behave like a solid and fluid depending on external conditions. Jaeger et al. [75] explain this phenomenon with a sand pile at rest and below the maximal angle of repose. The stresses induced by the gravitational forces on the sand pile's surface are not big enough to provoke a granule flow. As a result, the granular material behaves like a solid. However, when the sand pile is tilted, i.e., increasing the angle, the granular material flows as an avalanche on the sand pile's surface. The granule system behaves like a liquid. This simple example describes that a granular material flows when the stress inside the system exceeds a yield stress similar to a Bingham fluid.

Regarding the flow of granular materials from a silo, the yield stress to inhibit flow is commonly overcome by pure gravitational forces acting in the vertical direction towards the orifice. However, many parameters affect the flow of a granule system. Therefore, this section provides insight into granule flow in more detail.

3.3.1 Mass flow rate measurements before the Beverloo Law

Gotthilf Heinrich Ludwig Hagen initially studied the flow of granules in 1852 by investigating the flow of dry sand for various circular orifice sizes [76,77]. Based on the findings, Hagen [76] provided the first qualitative understanding of the mass flow and postulated the first model to predict the mass flow rate for sand (equation 23).

$$\dot{m} = 2r^2\pi\,\rho\sqrt{gh} \qquad 23$$

Here, r is the radius of the circular orifice, and ρ is the density of the sand. Furthermore, g is the gravitational acceleration, and h is the falling height of a single granule above the orifice. Hagen [76] observed an influence of granules at the outer rim of the orifice, hindering the flow of granules and causing a decrease in the actual radius of the orifice to an effective orifice radius. In addition, Hagen [76] expected an increase in the mass flow rate with the orifice radius r, following $\dot{m} \sim r^3$. However, the results showed an increase of $r^{2.5}$, visible in equation 23, for the case that the falling height h equals the radius r.

Franklin and Johanson [78] investigated the mass flow rate for materials such as coal, puffed rice or glass beads with a hopper of different internal angles θ. The outcomes showed that the mass flow rate with horizontal orifices has to be adjusted depending on the internal angle θ and the kinetic angle of repose α of the material (Equation 24). The kinetic angle α is the slope of a material's surface with continuous movement, e.g., in a rotating drum.

$$\dot{m}_\theta = \dot{m}\frac{\cos\alpha + \cos\theta}{\cos\alpha + 1} \qquad 24$$

Many years later, Fowler and Glastonbury [79] continued in the year 1958 the investigations of Franklin and Johanson [78] (1955). Fowler and Glastonbury [79] focused on measurements with various orifice sizes and shapes, such as circular, triangular and hexagonal openings. The outcomes with various kinds of material, such as sand, sugar and organic seeds, yielded equation 25.

$$\dot{m} = 14.56\rho_b A\sqrt{2gD_h}\left[\frac{D_h}{d_s}\right]^{0.185} \qquad 25$$

Here, A expresses the area of the orifice, ρ_b is the bulk density of the material, and d_s is the spherical diameter of the material. The variable D_h is the hydraulic diameter of the orifice and describes the ratio between orifice surface A and the perimeter P of the orifice (4A/P). Notably, D_h is influenced by orifice shape and size.

3.3.2 The Beverloo law

Three years later (1961), Beverloo et al. [7] continued the investigations of Fowler and Glastonbury [79] by investigating the mass flow rate of various organic seeds. Based on the findings, Beverloo et al. [7] proposed an empirical model to predict the mass flow rate through a flat-bottomed orifice, which will be described in the following.

When bulk material passes through an orifice, it is assumed that the granules within a powder bed are falling from an arch above the orifice and that the resulting mass flow rate is independent of the pressure above the arch (Figure 13) [80]. This independence will be further discussed at a later stage.

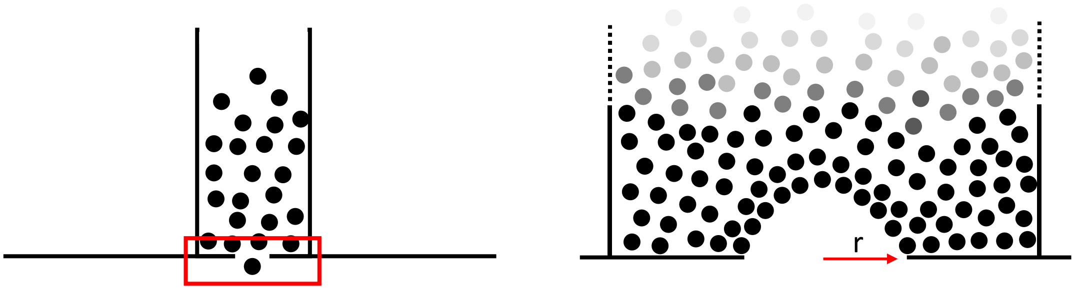

Sketch of flowability measurement

Sketch of the opening

Figure 13: Measurement of the mass flow rate with a flat-bottomed orifice (left); Close-up of the granule structure above the orifice and inside the cylinder (D = 2r) (right). D is the orifice diameter and r is the orifice radius.

The mass flow rate of granules arises from the assumption that the arch collapses and that the granules fall purely under the effect of gravity [81]. Assuming free-falling granules from the top position in the arch, the granules reach the maximal velocity following [82]:

$$v \sim \sqrt{gD} \qquad 26$$

For a material flowing through a vertical tube with a cross-sectional area A, the volume flow rate can be expressed by:

$$\dot{V} = \frac{dV}{dt} = \frac{d}{dt}(A\mathrm{h}) = A\frac{d}{dt}\mathrm{h} = Av \qquad 27$$

Here, V expresses the volume containing an arbitrary amount of granular material, A is the surface area of the orifice, t is the time, h is the distance, and v is the velocity of the granules. Combining equations 26 and 27 yields equation 28.

$$\dot{V} \sim A\sqrt{gD} \qquad 28$$

The mass of granular material in a volume depends on the granules packing density. Unlike a liquid, which can fully occupy a volume and is considered to be incompressible, granular materials inside a volume are compressible as the intergranular voids, filled with air, are distributed within a powder bulk. The ability to occupy interstitial voids, e.g. voids by smaller granules, is linked to the granule size distribution [83]. Generally, the packing is assumed to be in loose, i.e., in an uncompressed state above the orifice and is described by the bulk density ρ_b. The mass flow rate can then be described by:

$$\dot{m} \sim \rho_b \dot{V} \qquad 29$$

Inserting equation 28 into equation 29 yields the following equation 30.

$$\dot{m} \sim \rho_b A\sqrt{gD} \qquad 30$$

Beverloo et al. [7] state that the influence of the orifice is proportional to the square of the orifice diameter D. Replacing the orifice area A with D^2 leads to equation 31.

$$\dot{m} \sim \rho_b D^2\sqrt{gD} \qquad 31$$

Rewriting equation 31 states that the mass flow rate is proportional to $D^{2.5}$:

$$\dot{m} \sim \rho_b \sqrt{g}\, D^{2.5} \qquad 32$$

Beverloo et al. [7] found experimentally, for various materials, higher exponents in the ranges of $D^{2.7}$ to $D^{3.1}$ and stated a zone at the outer rim of the orifice, where the bulk material is at rest and blocks the free flow of the bulk material. This phenomenon was first observed by Hagen [76]. The zone is proportional to the size diameter d of the particles, expressed as kd, reducing the orifice diameter D to an effective orifice diameter D_{eff}, following:

$$\dot{m} \sim \rho_b \sqrt{g}\, {D_{eff}}^{2.5} \qquad 33$$

Which is equal to

$$\dot{m} \sim \rho_b \sqrt{g}\, (D - kd)^{2.5} \qquad 34$$

A fitting parameter C includes other effects on the mass flow, such as the orifice geometry, which yields the final form of the Beverloo law:

$$\dot{m} = C \rho_b \sqrt{g}\, (D - kd)^{2.5} \qquad 35$$

Equation 35 describes the observations stated by Hagen [76] over 170 years ago. Therefore, the Beverloo law is in some literature called Hagen-Beverloo law to acknowledge the early contributions [84,85]. The empirical investigations by Beverloo et al. [7] with different kinds of organic seeds provided C values ranging between 0.55 and 0.65. Parameter k ranges between 1 and 3.

Literature does not provide a unique picture of the connection between the fitting parameters, material properties or experimental conditions. It has been shown that C depends on the hopper geometry [86] and powder properties such as the friction coefficient [87]. The fitting parameter k is influenced by powder properties such as the attraction forces between particles [9,88] and particle shape [89,90].

3.3.2.1 The static and dynamic pressure profiles in a hopper

This section focuses on the basic principles of the pressure profiles inside a hopper. When pouring granular material inside a container, the pressure at the orifice is expected to increase linearly with the filling height. However, an experimental study by Janssen [91] showed a linear pressure increase followed by a pressure saturation with increasing filling height. The reason is that in a static state, a portion of forces in the granule media is passed by solid friction from particle to particle in a random contact network to the lateral walls of the silo (Figure 14)[92]. This results in normal and lateral pressure profiles along the filling height, taking an asymptotical exponential law at an ascendant distance above the outlet (Figure 15, a). Beyond this saturation pressure, the further increase of mass inside the hopper does not affect the pressure near the outlet. This effect is known as the Janssen effect.

Bertho et al. [93] verified the Janssen effect for moving walls and calculated vertical stress inside the powder bed with equation 36.

$$\sigma_v = \rho \eta g \lambda (1 - e^{-\frac{H}{\lambda}}) \qquad 36$$

H is the total height of the powder bed inside the hopper, ρ is the bulk density, η is the packing fraction, and λ is a characteristic length scale. The characteristic length scale λ can be determined by considering the hopper geometry and the granule properties.

In the case of a container with a squared cross-section, the characteristic length λ can be approximated with equation 37 [94], where W is the width, and L is the length of the container of a quasi-2D container. K is the lateral stress ratio (Equation 39), and μ_w is the wall friction coefficient arising from the ratio between the wall shear stress τ_w and the resulting lateral wall stress σ_w (Figure 14,b).

$$\lambda = \frac{WL}{2(W+L)}\frac{1}{\mu_w K} \qquad 37$$

For a cylinder, it takes the form of equation 38 [95], with R being the radius of the cylindric container.

$$\lambda = \frac{R}{2\mu_w K} \qquad 38$$

The ratio between the lateral stresses σ_h and the normal stresses σ_v inside a powder bed is described by the stress ratio K (Figure 14, a) and can be calculated with equation 39. It is stated that the stress ratio parameter K ranges between 0.3 and 0.6 and can be determined from shear experiments [96].

$$K = \frac{\sigma_h}{\sigma_v} \qquad 39$$

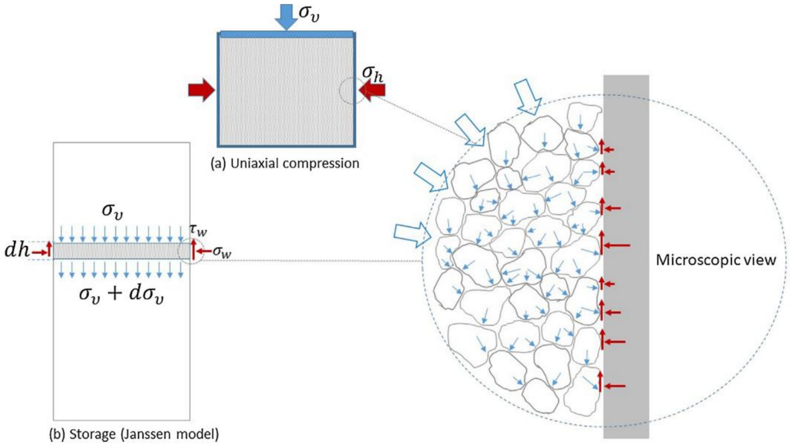

Figure 14: The stress distribution in a powder bed inside a tube. (a) and (b) represent an idealized schematic view of stresses inside the vessel. On the right side, a microscopic distribution of forces is shown. Forces induced by particles presented (blue) and resulting forces on the lateral walls (red). The image is taken from [97].

The evolution of the wall and the vertical mean stress inside a conical container is explained in the following based on Schulze [96] (Figure 15). When a container is filled with granular material, the vertical and wall stress increases inside the powder bed from the top towards the bottom, leading to an asymptotic stress profile. Maximal stress is reached at the transition of the cylindrical to conical container shape. Beyond this point, the wall and vertical stresses decrease and reach approximately zero at the outlet (Figure 15, a).

During the flow of a granular material out of the container (Figure 15, b), the stresses are similar above the conic container shape. Below this, the discharge leads to a converging flow zone, where the bulk material is compressed horizontally. In this stage, the material faces a vertical dilation. This effect leads to higher wall stresses, forming arching lines in the lower region. In the lower segment of the silo, the stresses decrease towards the outlet.

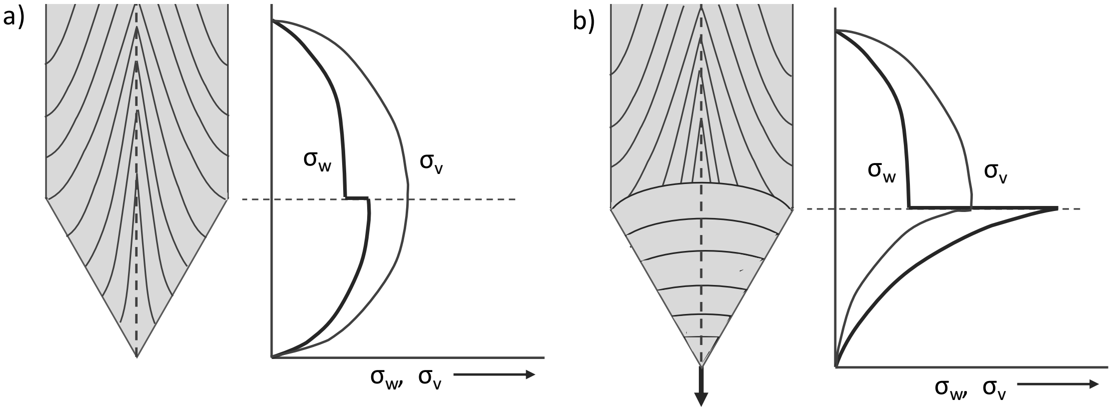

Figure 15: Image shows schematically the stress profiles in (a) static state after filling and (b) during discharging from a silo. Image is recreated and based on [96].

3.3.2.2 The free-falling arch theory – the velocity of granules near the outlet

The Beverloo law (equation 35) is based on the free-falling arch theory and states that particles above the outlet accelerate purely from gravity to reach the highest velocity at the outlet. The velocity of a single granule results from the height of the fall. This theory is accepted among researchers and is simultaneously one of the most discussed scientific topics in the field. Many investigations have been performed to describe and understand the principle of the free-falling arch theory.

Brown and Richards [98] describe the arch surface with a minimum energy theory, assuming that the pressure below the arch is low and the material above the arch is exposed to stress. The theoretical approach describes the minimal falling height r from a radial arch depending on the height of the apex r_0 below the orifice.

Vivanco et al. [99] studied the force distribution with a photoelastic material inside a transparent hopper between crossed polarizers. Vivanco et al. [99] state that flowing particles create force networks through contact points, which are formed and destroyed during the flow of particles. This outcome was observed for small orifice sizes, where jamming of the orifice typically occurs. For these small orifice sizes, the lifespan of the force networks indicated a boundary layer between a stress and a stress-free region above the outlet. Vivanco et al. [99] concluded that this boundary layer resembles the free-falling arch, which was not present for larger orifice sizes D.

Further studies have been done by Wan et al. [100] by investigating the effect of an increase in the free-falling arch with the help of DEM simulations. The results state the Beverloo law's validity as long there is a presence of an arch during the flow. In addition, the continuous increase of the arch radius resulted in a higher mean velocity of the bulk material. Similar results were stated by Lin et al. [82], showing that the arch's height depends on the orifice diameter, which was also postulated by Hagen [76]. Furthermore, Lin et al. [82] noticed that the shape of the arch is different compared to the typical idealized free-falling arch structure.

Dorbolo et al. [101] performed experimental studies to track the movement of glass beads with a camera under different gravitational influences in a centrifuge. The change of the gravitational constant with a centrifuge states a dependency on the velocity of the granules, i.e. $v \sim \sqrt{g^*}$, where g^* is the changed gravitational acceleration of $1 \leq g^* \leq 20$. With the help of the acquired images, the results proved the existence of a semi-circular arch above the outlet, only valid for higher orifice diameter D to granular diameter d ratios (D/d > 10).

<u>The velocity of the granules near the outlet</u>

The particles inside a cylindrical tube have a plug flow-like movement towards the outlet [102]. This holds as long as the granules are above one tube diameter from the flat-bottomed orifice. Below this threshold, the axial velocity monotonously increases, leading to a parabolic shape flow with the maximum velocity in the centre of the hopper [102].

The velocity of single granules mainly depends on the orifice size, the radial position above the outlet and the falling height. A study by Janda et al. [103] assumes that a parabolic arch above the outlet is responsible for the parabolic velocity profile. Based on this assumption, Janda et al. [103] calculated the velocity according to equation 40, where R is the radius of the circular orifice and x is the local radial position.

$$v(x) = \sqrt{2gR}\sqrt{1 - \left(\frac{x}{R}\right)^2} \qquad 40$$

In an experimental study, Doboro et al. [101] investigated the velocity profiles of glass beads in a flat-bottomed hopper. They proposed an equation to calculate the velocity of a single sphere along the radial position for a semi-circular flow (equation. 41). Here, $v_y(0)$ is the maximal velocity in the centre of the orifice, D is the orifice diameter, and x is the local radial position from the orifice centre.

$$v_y(x) = v_y(0)\sqrt{D^2 - x^2} \qquad 41$$

3.3.2.3 The jamming effect at the outlet

According to Péter et al. [104], jamming is the transition from flowing of particles to a motionless state near the outlet. These particles form an arch consisting of a set of stabilized particles above the outlet [105]. The arch collapses when a single particle is removed from the arch. The jamming phenomenon is influenced by the interactions of the material at the outlet and the packing quality of the filled system [106]. These jamming transitions are typically investigated by calculating a dimensionless ratio of the nominal orifice diameter D and the particle diameter d.

Mankoc et al. [81] state a critical flow regime for ratios lower than five (D/d < 5). In this regime, jamming is likely to occur during the flow. Liu et al. [107] experimentally investigated the critical orifice size and jamming during discharge of two-dimensional silos. The results show an increased probability of jamming when the dimensionless ratio is below 4.5. Similar values are found for polyethene discs with horizontal conveyor belts with a ratio of lower than 6 [108] and DEM simulations below 4 [109].

3.3.2.4 Contributions beyond the Beverloo Law

Over the years, many researchers modified the Beverloo Law to consider other influences on the mass flow. This chapter focuses on a few modifications.

A fundamental parameter of the Beverloo law is the reduced orifice size diameter directly related to the particle diameter (D-kd). The diameter is an important criterion for experimental studies of a granule system. In literature exists a broad range of different mean diameters (see chapter 3.1.3.3) to describe a polydisperse system. For instance, Humby et al. [44] studied the effect of the minimal orifice diameter (D_{min}) by considering various mean diameters for a binary mixture. The results showed the best correlation between the volume moment mean diameter (de Brouckere) and the minimal orifice diameter. Other diameters showed less promising results. A supplementary investigation by Gundogdu [110] with polydisperse materials states that the median diameter d_{50} may be the most suitable diameter. However, this might not be true for cohesive powders. Other experimental studies consider d_{50} [89,111], the surface volume mean diameter [9,68,112] (Sauter mean diameter, see chapter 3.1.3.2), or the volume moment mean diameter (de Brouckere) [110,113].

Tangri et al. [114] investigated the effect of elongated objects on the mass flow numerically, passing a rectangular orifice with a length L and width W. Based on the DEM study, Tangri et al. [114] proposed a modified version of the Beverloo law by considering the particle sphericity ψ following

$$\dot{m} = \left(\frac{4}{\pi} 2^{0.5}\, C\right) \rho_b\, g^{0.5}\, (L - k_1 \psi d_l)(\mathrm{W} - k_1 \psi d_l)^{1.5} \tag{42}$$

The parameter k_1 equals a fitting parameter similar to the one inside the Beverloo law, and d_l is the maximal length of the particle.

Experimental studies by Medina et al. [115] also showed the application of the Beverloo law for lateral side holes under consideration of the occupied angle inside the sidewalls. A mass flow rate was observed when the occupied angle α was higher than the angle θ_r inside the sidewalls (the wall's outer edge to the inner upper orifice edge). Notably, the flow stopped when the depth of the wall exceeded the occupied angle of material inside the sidewall aperture ($\alpha \approx \theta_r$).

$$\dot{m} = C\rho_b\sqrt{g}(D - kd)^{\frac{5}{2}}(\alpha - \theta_r) \tag{43}$$

Anand et al. [88] performed simulations with DEM for rectangular orifices to understand the impact of the cohesive forces of particles smaller than 100 µm on the mass flow rate. In simulations, the cohesiveness of investigated powders is expressed with the help of the granular Bond number. This unitless number describes the ratio between the cohesive forces and the gravitational force between particles (more in chapter chapter 3.4.3). Anand et al. [88] included the exponential increase of the parameter k in relation to an increasing granular Bond number in the Beverloo law with a rectangular orifice shape.

$$\dot{m} = C\rho_b\sqrt{g}(L - 1.9e^{0.39Bo}d_p)(W - 1.9e^{0.39Bo}d_p)^{3/2} \qquad 44$$

3.3.3 Parameters influencing the mass flow rate of bulk materials through orifices

The flowability of granules expressed as the mass flow rate through orifices is an essential parameter in the powder metallurgy industry. The properties of granules directly influence the mass flow rate, which also affects the cavity filling within the compression cycle. The mass flow rate of hard metal granules can be measured, for instance, with a Hall-Flow meter according to ASTM B213 standard [116]. Significant advantages of the Hall-Flow meter device are easy handling and short measurement times. Comparing mass flow rates of various batches provides information about inadequate granule characteristics, which might cause problems in the filling step. Knowing the influencing parameters on the mass flow rate provides the potential to tailor granules with optimal mass flow characteristics.

Table 2 provides an overview of the influencing parameters affecting the mass flow rate, which can be divided into two essential groups: external parameters, i.e., experimental design and internal parameters, i.e., intrinsic properties of the bulk material such as the density. It can be seen that Table 2 generally resembles Table 1 (see chapter 3.2.3). Parameters affecting the mass flow (Table 2) and parameters affecting the angle of repose (Table 1) are both important to derive flow properties from angle of repose measurements. In other words, influences on the mass flow rate from hoppers also affect the angle of repose and vice versa. Some parameters are further explained in the following paragraphs.

Table 2: Overview of parameters affecting the mass flow.

External parameters	**Internal parameters**
Hopper geometry (e.g., orifice shape)	Size and size distribution
Airflow	Surface roughness and friction
Gravity	Density (e.g., bulk density)
Vibration	Morphology (e.g., sphericity)
Temperature	Cohesion
Relative humidity / Moisture	
Temperature	

3.3.3.1 External parameters affecting the mass flow

One of the external parameters affecting the mass flow is air. Huang et al. [111] investigated the influence of introduced air near the outlet of a conical hopper. The measurement setup is displayed in Figure 16 (left), showing three different air inlet positions: A, B and C. A variation of the active air streams showed that the mass flow rate depends on the inlet positions. The highest mass flow rate was acquired when the air steam entered the hopper from all three inlet positions. Aside from this, the findings state a significant influence on the magnitude of the mass flow rate by the amount of introduced air stream (Figure 16, right). The air stream significantly changes the mass flow rate. A jamming effect occurs when the air stream is not optimally applied to the granule system. Increasing the air stream into the bulk system leads to a maximal mass flow rate (Figure 16, right). Beyond the maximum, the mass flow rate decreases with a further increase in the air stream.

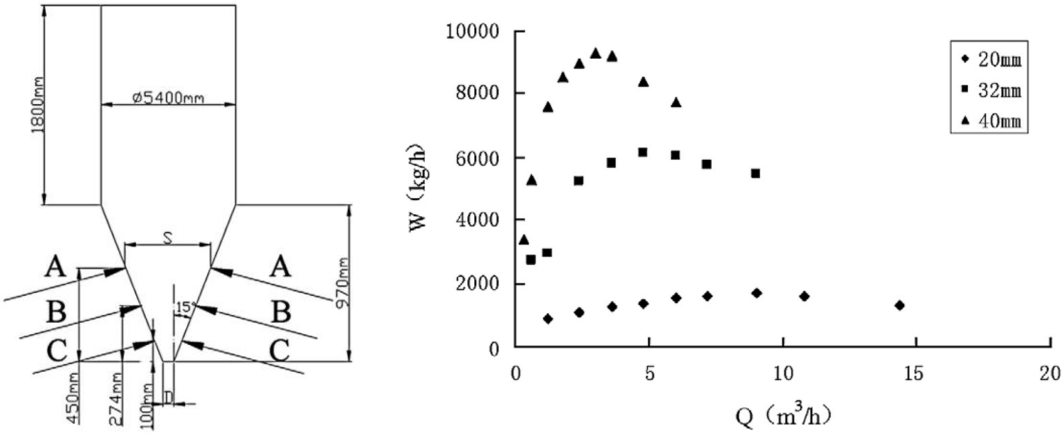

Figure 16: Airstream inlet positions of the conical hopper (left). Mass flow rate W of powder in dependency of the gas flow rate Q for different orifice sizes (right). The aeration is performed by all three inlets A, B and C. Both images are taken from [111].

Besides the airflow, the magnitude of the gravitational acceleration influences the mass flow rate. Based on the Beverloo law (equation 35), the mass flow rate scales with the square root of the gravitational acceleration ($\sqrt{g}$). The effect of gravitational acceleration on the mass flow rate can be studied at a laboratory scale with centrifugal measurements. Mathews and Wu [117] used a centrifuge, showing that the mass flow rate increases with rising gravitational acceleration, which aligns with the Beverloo Law.

Mechanical vibration in the form of shaking may be induced into a powder bed by performing, for instance, a periodical movement of a filling shoe on top of a powder bed inside a cavity. The periodical filling shoe movement introduces stress in the upper granules layer, provoking a rearrangement process, locally increasing the mass and density inside the cavity [118]. Studies on a laboratory scale with additional application of vibrators on a filling shoe showed an increased packing density of up to 16 % for various materials and frequencies [119]. Kumar et al. [120] studied the effect of oscillatory vibration on the mass flow rate with the help of DEM simulations. Here, an increase in either amplitude or frequency leads to a higher mass flow rate.

External parameters like temperature and relative humidity can also belong to internal parameters. The reason is that temperature and relative humidity change the characteristics of the bulk material from the outside. In the case of relative humidity, water can condense on the particle surface, increasing the moisture content of the bulk and affecting the flow [121] due to changed particle-particle interactions.

3.3.3.2 Internal parameters influencing the flow of granules

The internal parameters, i.e., the material's intrinsic properties, affect the mass flow rate. Table 2 shows a set of such parameters. The influence of the size distribution of polydisperse materials, the granule or particle size of a monodisperse material and the granule's shape have been described in chapter 3.3.2.4.

Besides the size of the particles and granules, the density of the materials plays an important role. Here, different kinds of densities can be found in literature, such as theoretical density, pycnometer density, bulk density, packing density (packing fraction) and tapped density. The bulk density is also known as the apparent density of powder-like materials, describing the granule's mass in a defined volume, including the interstitial voids between granules [122]. The pycnometer density provides information about the maximal density of a granule or powder material and is also known as the theoretical density [122]. A gas pycnometer with inert gas is used to determine the pycnometer density [123]. The ratio between the bulk density and the pycnometer density provides information about the packing and the amount of voids inside the bulk (porosity), expressed as the packing density [124].

It can be derived from the Beverloo law (equation 35) that the mass flow rate scales linearly with the bulk density. Higher (absolute) bulk densities are acquired in two ways: First, a change in the pycnometer density, or second, an increase in the packing density. Studies by Huang et al. [125] with simulations showed an increase in the flow rate with rising packing densities, reaching a maximal mass flow rate for packing densities between 0.5 and 0.7. Beyond this packing densities, the mass flow rate decreases. A change in the bulk density and packing density can be achieved by modifying the granule size distribution to reach ideally packed densities and is well-studied for bimodal spherical systems (see Figure 17) [126–128].

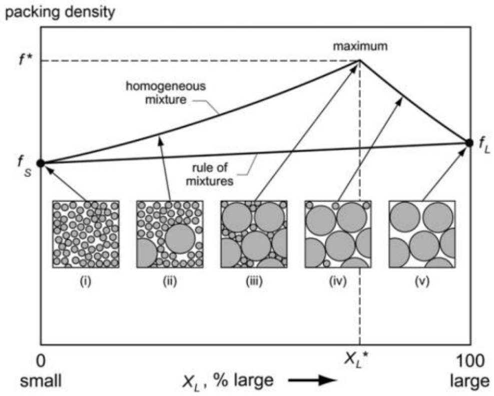

Figure 17: Packing density for various mixings of small and large spheres. The image is taken from [129].

Generally, the moisture content inside the bulk material is an essential factor for water-sensitive materials, i.e. hygroscopic materials and materials, which are negatively influenced by degradation [130]. The moisture content inside the bulk materials can arise from exposure to the humidity in the air (see chapter 3.3.3.1). Studies by Lumay et al. [131] with lactose powder showed a negative effect on the flow properties at elevated relative humidities. Iqbal and Fitzpatrick [132] showed a decrease in flowability of organic materials exposed to various relative humidities and temperatures. A DEM study by Dai et al. [133] showed the influence of the moisture content of wet coal powders. Here, the mass flow rate decreases nearly linearly with the increase of the moisture content inside the powder.

The interparticle friction significantly affects the mass flow rate. The influence of friction is expressed with the friction coefficient from angle of repose or shear measurements. Both measurements will be explained at a later stage. Generally, with an increased friction coefficient, a decrease in the mass flow rate is observed [134]. DEM simulations by Kobylka et al. [135] found that the friction between particles influences the arch structure above the outlet. Larger arches resulted from higher friction coefficients. It is important to remember that the arch's size directly affects the velocity of falling particles and also the mass flow rate.

3.4 Cohesive effects between spherical particles and the granular Bond number

When particles are in contact, an attractive force exists between particles, holding the bodies together [136]. This adhesion is commonly described by cohesion, which describes the attraction between particles in a bulk system [137]. The attraction between spherical objects can arise from different sources and is significantly influenced by the nature of the bulk system. Table 3 provides an overview of various forces affecting the cohesive forces. One of these cohesive forces is the van der Waals force, which is assumed to be the dominant force for hard metal powders [138]. This force will be described in the next chapter. This chapter focuses on the capillary and electrostatic forces.

Table 3: Various sources causing cohesion between particles, based on [139,140].

Cohesion
Capillary force (e.g., liquid bridges)
Van der Waals force
Electrostatic forces (e.g., tribocharging)
Magnetic force

The moisture inside the powder bed affects the cohesive forces. Depending on the amount of moisture, water layers in the form of liquid bridges between the granules are created, bonding the particles together (Figure 18) [141]. The creation of liquid bridges depends on the geometry of solids and contact points, surface free energy, the separation distance of particles, surface topography, and the liquid bridge's size influenced by the liquid's surface tension [142]. The liquid bridge must be overcome to provoke a movement from particles into local free spaces [143].

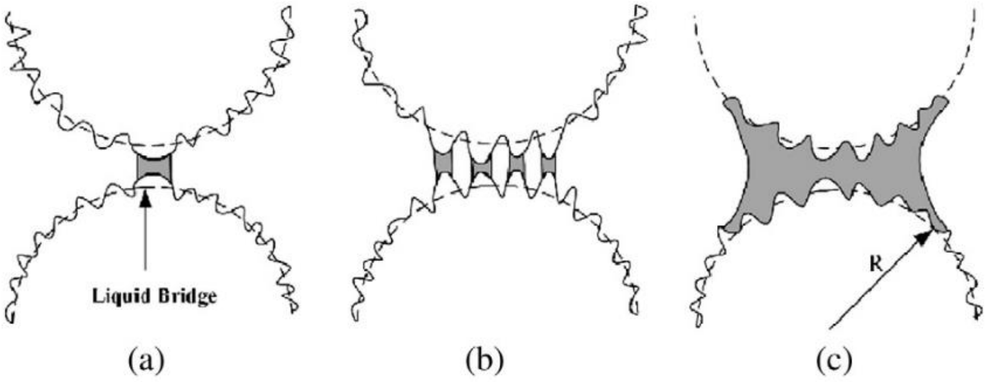

Figure 18: Different states of moisture contents forming liquid bridges, (a) liquid bridges with the closest contact, (b) several liquid bridges and (c) forming capillaries over a bigger surface. The image is taken from [141].

When dry granular materials flow, a triboelectric effect at the granule surface creates electrostatic charges [144]. These electrostatic charges are generated by friction between surfaces in contact during a movement. Burgo et al. [145] showed that the triboelectric effect influences the friction coefficient between materials. Rescaglio et al. [146] studied the influence of moisture inside a powder system on the triboelectric effect. The findings showed that an increase in the relative air humidity positively affected packing dynamics and enhanced powder flowability. The positive effect arises from decreasing electrostatic charges with increasing moisture inside the bulk material. An optimal amount of relative air humidity was observed. Beyond this, the creation of liquid bridges negatively affects the flowability.

3.4.1 Van der Waals forces

The Lennard-Jones potential can describe the interaction between two approaching bodies, considering equation 45 [147].

$$w(r) = 4\varepsilon\left[\left(\frac{\sigma}{r}\right)^{12} - \left(\frac{\sigma}{r}\right)^{6}\right] \quad 45$$

where ε describes the depth of the energy potential, σ is the distance between the body at which the potential sign changes (r = σ) and r is the interbody distance [148]. The first term describes the repulsive part, while the second term is the attractive part, attributed to the van der Waals forces, which are weak electrostatic forces that arise from fluctuations in molecules' electric dipole moments [149]. The van der Waals forces are affected by the material's properties and the shape of the approaching bodies [149].

It can be seen from equation 45 that the interaction depends on the distance r between the interacting bodies and is illustrated in Figure 19. At the interbody distance r_0, the energy potential is 0, while strong repulsive forces are present. The increase in the interbody distance r leads to a minimum energy potential $w(r_e)$ at which the interacting force is zero, the equilibrium position. The energy potential increases beyond the interbody distance r_e, and the attractive force reaches a maximum at the distance r_s.

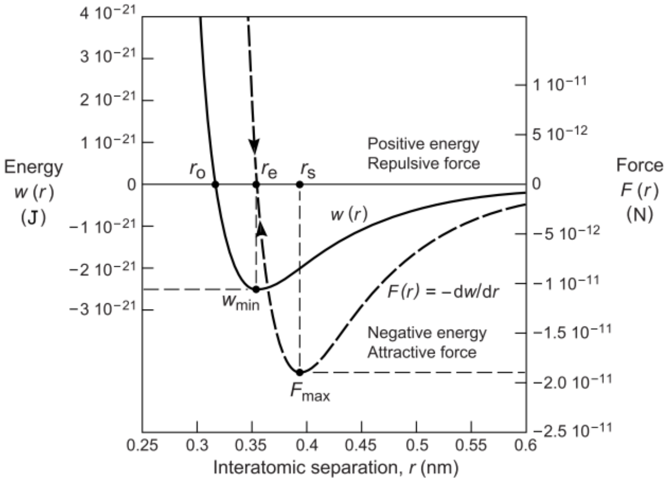

Figure 19: The interaction energy between two atoms in function of the separation distance r. The image is taken from [147].

Regarding two spherical objects being close to each other, as in the case of two granules from a granular system, the van der Waals force can be calculated with equation 46 [150]. Here, R is the radius of the spherical objects, d is the particle diameter, A is the Hamaker constant, and z_0 is the distance between the two spherical particles.

$$\mathrm{F}(z_0) = \frac{A}{6{z_0}^2}\left(\frac{R_1 R_2}{R_1 + R_2}\right) = \frac{A}{12{z_0}^2}\left(\frac{d_1 d_2}{d_1 + d_2}\right) \quad 46$$

For granular materials, z_0 is typically considered 0.4 nm [138,151]. The Hamaker constant A is linked to materials properties, such as the dielectric constant [152], and can be calculated according to equation 47 [147], where D_0 is the cut-off distance, also known as the minimum separation distance [153]. In the case of granular materials, the cut-off distance is assumed to be 0.165 nm [154,155] providing an adequate approximation of the Hamaker constants or surface energy γ when one of these parameters is known [147]. The surface energy γ is the dispersive energy of the solid material. The surface energy of solids can be experimentally determined with the contact angle method, which is explained in chapter 3.4.2.

$$A = 24\pi D_0^2 \gamma \qquad 47$$

In many cases, the granular materials have rough surfaces, arising from asperities on the surface influencing the contact points and effectively the van der Waals force. Xie [156] extended equation 46, considering also asperities on smooth spheres. Here, the asperity radius r describes half-shaped spheres situated on larger spheres.

$$F_{vdw} = \frac{A}{12\,(\mathrm{z}_0 + \mathrm{r})^2}\left(\frac{d_1 d_2}{d_1 + d_2}\right) + \frac{A}{12{z_0}^2}\left(\frac{2d_1 r}{d_1 + 2r}\right) \qquad 48$$

Rumpf [157] presents a model to calculate the van der Waals forces with equation 49 between a sphere and a planar surface. Here, D is the particle diameter, and d is the asperity diameter, assuming the shape of a sphere.

$$F_{vdw} = \frac{A}{12}\left[\frac{d}{z_0^2} + \frac{D}{\left(\frac{d}{2} + z_0^2\right)^2}\right] \qquad 49$$

Chen et al. [158] proposed a model considering the surface coverage (guest) particles on the surface of the bigger (host) particles (equation 50).

$$F_{vdw} = \frac{A}{12\,z_0^2}\left[\left(\frac{3dD}{d + D}\right) + \frac{D}{2(H_0/z_0)^2}\right] \qquad 50$$

Here, the host distance between the guest d_g and host particle d_p is expressed by equation 51. The SAC parameter describes the surface area coverage on the surface of the host particle with smaller guest particles.

$$H_0 = \sqrt{(D + d)^2 - \frac{1.21}{SAC}d_g^2} - d_p \qquad 51$$

In terms of surface roughness, Lu et al. [9] propose a modification of previously presented models by incorporating the approach of Rabinovich [159] to consider the surface roughness of granular materials with $r = 1.48R_{rms}$ (equation 52). R_{rms} is the mean root square of the surface roughness of particles and can be measured with atomic force microscopy (AFM). The parameter d' equals $2rd_p/d_p + 2r$.

$$F_{vdw} = \frac{Ad_p}{24\,(z_0 + 2.96R_{rms})^2} + \frac{Ad'}{6(z_0 + 1.48R_{rms})^2} + \frac{1.48R_{rms}A}{12z_0^2} \qquad 52$$

3.4.2 The surface energy of solids

When a liquid drop forms on the surface of a flat, smooth solid, the contact angle θ arises from an energy equilibrium between the solid γ_S and liquid γ_L surface tensions and the interfacial tension γ_{SL} at the contact interface (Figure 20). The interface tension γ_{SL} depends on the surface tensions of solid γ_S and liquid γ_L and is expressed by the Young equation [160], following:

$$\gamma_S = \gamma_{SL} + \gamma_L \cos\theta \qquad 53$$

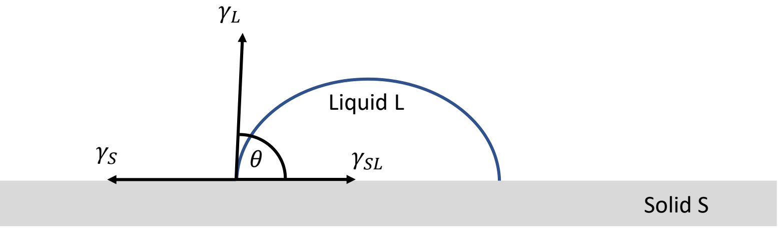

Figure 20: Drop of a liquid L on a solid surface S creating a contact angle θ. *The image is created and based on [161].*

A supplementary work is required to separate the liquid drop from the solid's surface. When both phases are separated, the interface energy γ_{SL} vanishes, creating two new surfaces. This required work is defined as the work of adhesion W_{SL} and is described by the Dupré equation [162].

$$W_{SL} = \gamma_S + \gamma_L - \gamma_{SL} \qquad 54$$

Studying the work of adhesion W_{SL} is challenging as the surface tension of the solid γ_S, liquid γ_L, and at the interface γ_{SL} has to be known. The combination of Young (equation 53) and Dupré (equation 54) simplifies the determination of the work of adhesion W_{SL}, yielding the Young-Dupré equation 55. The work of adhesion W_{SL} can be accessed by measuring the contact angle θ on a solid surface when the liquid surface tension γ_L is known. However, the Young-Dupré equation does not provide any information about the surface energy of the solid.

$$W_{SL} = \gamma_L (1 + \cos\theta) \qquad 55$$

A study by Fowkes [163] focused on the influences of dispersive force interactions in the interface of solid and liquid. Fowkes [163] assumed that the work of adhesion is mainly influenced by dispersive forces and replaced the work of adhesion W_{SL} inside the Dupré equation with a geometric mean approximation (equation 56) of the dispersive forces of the solid (γ_S^d) and liquid (γ_L^d).

$$\gamma_{SL} = \gamma_S + \gamma_L - 2\sqrt{\gamma_S^d \gamma_L^d} \qquad 56$$

Continued studies by Owens and Wendt [164] and by Kaelble and Uy [165] also considered the solid (γ_S^p) and liquid (γ_L^p) polar parts in equation 56, following:

$$\gamma_{SL} = \gamma_S + \gamma_L - 2\sqrt{\gamma_S^d \gamma_L^d} - 2\sqrt{\gamma_S^p \gamma_L^p} \qquad 57$$

Considering the Young-Dupré equation 55, equation 57 can be modified into equation 58.

$$\gamma_L \ (1 + \cos\theta) = 2\sqrt{\gamma_S^d \gamma_L^d} + 2\sqrt{\gamma_S^p \gamma_L^p} \qquad 58$$

Rewriting equation 58 into a linear form yields equation 59. The expression is today known as the OWRK (Owens, Wendt, Rabel and Kaelble) equation.

$$\frac{\gamma_L \ (1 + \cos\theta)}{2\sqrt{\gamma_L^d}} = \sqrt{\gamma_S^p} \cdot \sqrt{\frac{\gamma_L^p}{\gamma_L^d}} + \sqrt{\gamma_S^d} \qquad 59$$

Equation 59 can experimentally estimate the solid part's polar and dispersive surface energy by plotting the left side of the equation on the ordinate. The abscissa is the rooted polar to disperse liquid ratio (Figure 21). Determining the contact angle θ with various liquids on the same material is suggested, where the liquids' polar and dispersive surface tensions γ_L are known. Based on the experimental results, the polar surface tension γ_S^p of the solid is represented by the slope, whereas the intercept is the solid's dispersive surface tension γ_S^d. The sum of polar and dispersive energies is the total surface energy of the solid γ_S.

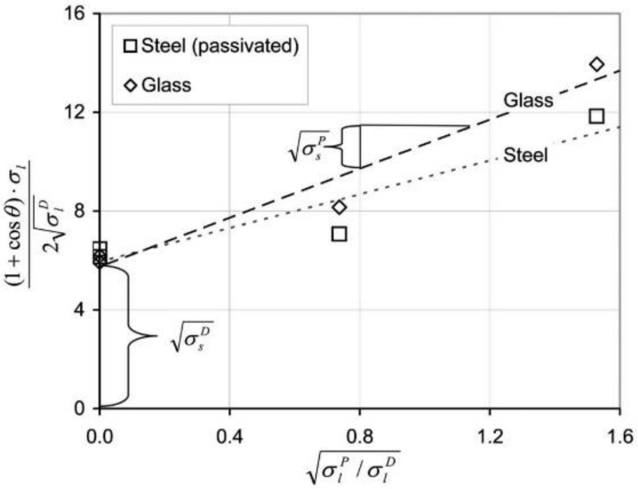

Figure 21: Plot of the OWRK method for two different materials. The image is taken from [166]. In this graphic, the surface tensions are expressed by the symbol σ.

3.4.3 Granular Bond number

The granular Bond number (Bo_g) is used for granules to describe the ratio of the cohesive forces (F_c) interacting between two granules and the weight of a single granule (F_g) (equation 60) [138], where the cohesive force is assumed to be solely caused by the van der Waals forces (F_{vdW}) of fine dry powders. However, other forces such as capillary forces and electrostatic forces contribute to the overall cohesive force [151][167] . In other words, the cohesive force is the sum of different powder-related attraction forces. In the case of dry, uncharged powders, the dominant cohesive forces are expected to be the van der Waals forces, as studied, for instance, by Lu et al. [9].

$$Bo_g = \frac{F_{vdW}}{F_g} \tag{60}$$

The granular Bond number describes macroscopic phenomena related to cohesion, such as porosity inside the bulk material [168], angle of repose [169] (more in chapter 3.2), flowing transitions in shear cells [170] or spreadability and packing of powders for additive manufacturing applications [171].

The gravitational force from a single granule can be calculated with equation 61, assuming a spherical shape. Based on equation 61, the granular Bond number is directly linked to the size of the granules within the bulk system.

$$F_g = \frac{1}{6}\pi d^3 \rho\, g \tag{61}$$

Other materials sensitive to moisture will likely create liquid bridges between granules. In this case, also, capillary forces have to be considered. For instance, Anand et al. [88] incorporated the capillary force inside the Bond number with DEM simulations. The results showed a significant influence on the flow of the simulated material.

3.5 Rheological properties of bulk solids

3.5.1 Rheology of granule's flow - inertial number and µ(I)-rheology

Granular materials can behave like a solid (sand pile), as a liquid (discharge from a silo) and even similar to a gas when the introduced stresses are sufficiently large [172]. In a liquid state, the granular material flows in a dense intermediate flow state, meaning that the packing density is near a maximal packing density during the flow, and the granules interact through contact and collisions [173]. According to Jop et al. [172], a granular liquid has two essential characteristics: a complex dependency on the shear rate during the flow and a yield criterion. Below the yield criterion, the shear stresses are insufficient to introduce a movement of granules. Both characteristics imply similarities between granular materials and visco-plastic fluids, such as Bingham fluids [172].

An extensive study has been performed to understand all three states by comparing various measurement systems, such as simple plane shear flows (e.g. with rotational rheometers), inclined plane flows, and the flow of granules in rotating drums [174]. Based on the outcomes, a local rheological model was proposed to describe the granular flow of simple shear flows – the so-called µ(I) rheology. The following explanations are adapted from [174]. The flow of a granule depends on the strain tensor, which is influenced by the shear rate $\dot{\gamma}$ and on the stress tensors affected by the normal stress P and the shear stress τ [174]. These parameters define two dimensionless numbers describing the flow of bulk materials [174]. One is the effective friction coefficient:

$$\mu_{eff} = \frac{\tau}{P} \tag{62}$$

and the other is the inertial number I:

$$I = \frac{\dot{\gamma} d}{\sqrt{P/\rho}} \qquad 63$$

The inertial number I arises from the ratio of the confinement timescale T_p and the deformation time T_γ.

$$I = \frac{T_p}{T_\gamma} \qquad 64$$

Here, the deformation timescale T_γ follows:

$$T_\gamma = \frac{1}{\dot{\gamma}} \qquad 65$$

And the confinement timescale T_p is:

$$T_p = d\sqrt{\frac{\rho}{P}} \qquad 66$$

Both times scales T_γ and T_p can be explained by Figure 22. Considering two layers of granules, the time scale T_γ can be understood as the time for the upper layer to move the distance d. This time scale T_γ scales with the shear rate $\dot{\gamma}$. The parameter T_p is the time needed to push a granule upwards and downwards into the next interstitial void [174]. Both timescales T_γ and T_p are directly linked to the velocity, as shown in Figure 22. A change in a granule's position by an upward and downward movement implies that the volume faction ϕ, i.e., the bulk density, is also affected by the inertial number I [174].

The inertial number I provides information about different flow regimes. In case the inertial number I is small, typically called the "quasi-static" regime, the movement of granules in the upper layer is slow while the confinement time is low. In this case, the inertia of granules is unimportant for the flow of granules. On the other side, in the case of a high shear rate, the inertial number I is high the particles interact through collisions, and the particle inertia affects the flow, the so-called inertial regime [174].

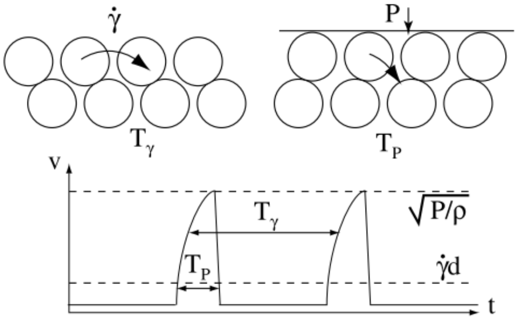

Figure 22: Illustration to describe the physical principle of the time deformation T_γ and the timescale of confinement T_p of the inertial number I. The image is taken from [174]

3.5.1.1 The flow regimes of bulk systems and constitutive laws

Investigating the effective friction coefficient µ over a broad range of inertial numbers I, the flow of granular materials occurring in a rotating drum, on an inclined plane, during annular shear flow and during simple plane shear measurements can be classified in three different flow regimes (Figure 30) [174]. First, the quasi-static regime is present for inertial numbers close to "zero". In this regime, the effective friction coefficient is independent of the shear rate. Secondly, the quasi-static regime becomes rate-dependent with increasing shear rate, the so-called dense flow regime. Thirdly, the further increase of the inertial number I leads to a more dilutive and collisional regime. The flow regime transitions are influenced by the applied normal pressure P and the shear rate [174].

A numerical study by Cruz et al. [173] found the same flow pattern and described quantitative transitions for each flow regime, also indicated in Figure 23. The transition of the critical state, also known as the quasi-static regime, to the dense flow, occurs at inertial numbers above I = 10^{-3}, depending on the system [173]. Finally, the dense flow regime transitions to the collisional flow regime, also known as the inertial regime, at I = 10^{-1}, fully describable by collisional kinetic theories [173]. In this regime, a considerable amount of kinetic energy is dissipated through collisions [173][175].

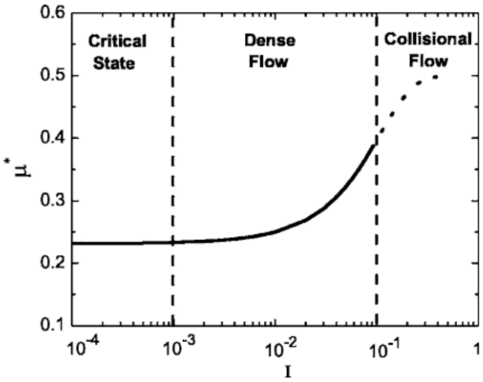

Figure 23: Flow regimes of granule flow for various inertial numbers I and effective friction coefficients μ^*. The critical state regime equals the quasi-static regime. The image is taken from [173].

Cruz et al. [173] investigated the change of the packing density η for increasing inertial numbers I and found a linear decrease from the maximal packing density ρ_{max}, described by:

$$\eta(I) = \eta_{max} - aI \qquad 67$$

, where a is a fitting parameter. In Cruz et al. [174] simulations, the fitting parameter a is nearly 0.3.

The same was investigated for the effective friction coefficient. For flow at very small inertial numbers I, the packing density η is close to the maximal packing density η_{max}, while the effective friction coefficient μ is at its minimum (Figure 23). With increasing I, the effective friction coefficient μ increases linearly until it saturates, caused by an increased dilation of the material in the collisional regime (Figure 23, dashed line) [173]. The linear increase is mathematically described for the dense flow regime as follows:

$$\mu = \mu_{min} + bI \qquad 68$$

, where b is a fitting parameter (b = 1.1 in [173]). The magnitude of the minimal effective friction coefficient μ_{min} exists mainly in the quasi-static flow regime and depends on the materials' characteristics. According to Cruz et al. [173], the minimal effective friction coefficient μ_{min} corresponds to the friction coefficient of the material found for simple shear tests (see chapter 3.5.2). A similar result is stated by Degiuli and Wyart [175], where the minimal effective friction coefficient is describable by the angle of repose (see chapter 3.2).

3.5.1.2 Monotonic and non-monotonic flows

When flow curves of granular materials are studied, for instance with a rotational rheometer, different torque evolutions can be acquired. Dijksman et al. [176] illustrate various flow curves and discuss these regarding the shear stress and rotation speed Ω. The simplest one is presented in Figure 24 (a)**.** In this monotonic flow curve, the measured shear stress decreases when the rotation speed decreases, leading finally to the yield stress, where the stress appears independent of the rotation speed (quasi-static regime). Secondly, the non-monotonic flow curve's characteristic is that at a finite rotation speed, the shear stress decreases towards minimal shear stress (Figure 24, b) with a negative slope. The negative slope in a non-monotonic flow curve at intermediate shear rates is assumed to be caused by to two zones in the material [176]. In these zones, the materials face low and high shear rates, leading to shear bands inside a granular bed [176]. A study by Van der Elst [177] showed that the evolution of shear bands is material-dependent and changes with increasing shear rates.

Dijksman et al. [176] studied the vibration's influence on flow curves' evolution considering the measured torque. The experimental study showed the existence of a third kind of flow curve. An increase in the toque is observed starting from very low rotation speeds (Figure 24, c). After reaching a (first) maximum torque, the flow curves follow a non-monotonic evolution similar to Figure 24,b. Dijksman et al. [176] found that the magnitude of vibration significantly affects the torque at low shear rates.

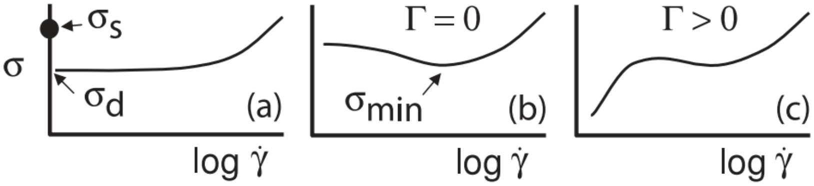

Figure 24: Flow curves of granular media. Shear stress σ in dependency on the logarithmic shear rate γ. (a) Monotonic flow curve with differing static σ_s and dynamic σ_d yield stress - in analogy to [174]. (b) Nonmonotonic flow curve without vibration Γ and (c) flow curve acquired with vibration strength Γ in the study of Dijksman et al. [176]. The image is taken from [176].

3.5.2 Shear measurements of solid materials with plate-cup shear cells

Polydisperse granular systems like lactose or sand consist of many different particle sizes. The enormous number of particles with varying sizes in a discrete volume makes it impossible to understand the influence of each particle. Such influences can be investigated with computational calculations, e.g. DEM or CFD-DEM [96].

Typically, the flow of granular materials is described as the flow of a continuum, where the number of contact points in a volume element is assumed to be large enough, and individual interactions from contact points are less important [96]. In this case, the stress occurring from deformation is expected to be homogenously distributed inside the bulk material, although the particles are locally closer or more distant [96].

The shear cell introduced by Jenike [178] is a measurement system to describe the flow of granules. The measurement principle is described in ASTM D6128-06 [179]. Nowadays, other shear cell testers can be used to measure powder properties, such as the Schulze shear ring shear tester [180]. Salehi et al. [181] compared various shear testers.

The measurement principle is comparable to common viscosity measurements of gels and fluids and is described here based on Schulze [96]. A bulk material is placed between two plates; the lower plate is fixed, and the upper plate is movable. When a normal force F is applied to the system, the bulk material envisages a normal stress σ, depending on the contact area A [96].

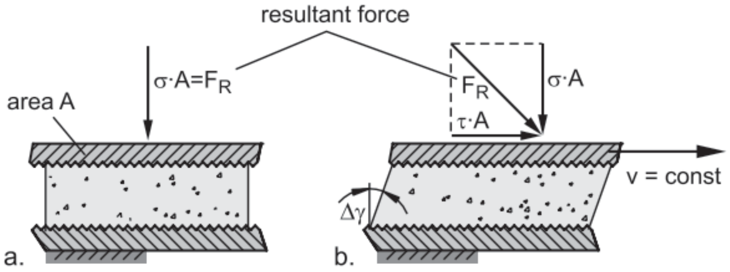

Figure 25: a) Granular material under load with an applied normal stress σ; b) shear deformation γ with constant velocity v. The graph is schematic. The image is taken from [96].

When a loose bulk material between two plates envisages a shear deformation γ by moving the upper plate (Figure 25, b), the introduced shear leads to particle movement. This particle movement transports small particles into (relatively) larger interparticle voids, increasing the bulk density of the powder system. The densification of a powder affects the shear stress in the function of time (Figure 26, a). As a result, the powder is plastically deformed while the upper plate moves. This deformation is permanent and remains even after unloading the bulk material from the measurement.

With increasing measuring time (Figure 26, a), the shear stress flattens, reaching a stress plateau. Beyond this point, the shear stress and the bulk density are nearly constant called the “steady-state flow”. In this state, the shear stress is constant and independent of time. The magnitude of the steady state, i.e., the shear stress is proportional to the applied normal stress and is influenced by the material's intrinsic properties. According to Schulze [96], this density and stress evolution is typical for powders in an “under-consolidated” state (Figure 26, a).

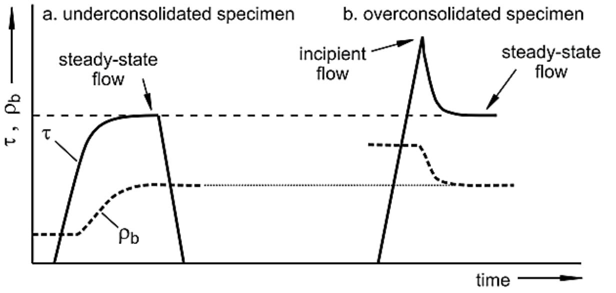

Figure 26: Evolution of the shear stress and bulk density for two different states, a) underconsolidated powder sample and b) overconsolidated powder sample. The image is taken from [96].

The shear stress and bulk density curve differ by exchanging a loose bulk material with a highly dense material (Figure 26, b). In the so-called “over-consolidated state”, the particles are closer to each other, having an increased bulk density and enhanced particle-particle interaction. With begin of a shear experiment, the shear stress increases linearly with advancing measurement time. In an "over-consolidated state", high shear stresses are needed to overcome the high particle-particle interactions to introduce particle movement below the moving plate (incipient flow) (Figure 26, b). The start of the particle movement is called "yielding". Once yielded, the particles move within a small shear zone below the plate [96]. The shearing in the shear zone below the plate reduces the bulk density and decreases particle-particle interactions. The further increase of the shear deformation γ in the function of time leads to a further decrease of the shear stress reaching a steady state flow (Figure 26, b).

Measurement principle

The description of the measurement principle is adapted from Schulze [96]. First, a measurement is prepared by placing a granular material between two plates. Then a normal stress σ_{pre} is applied on top of the powder bed. In the next step, the material is sheared. The shear stress τ increases linearly with time. During this step, the powder bed faces an elastic deformation. The elastic deformation remains until the shear stress flattens, reaching the constant shear stress (steady flow) at a specific shear stress τ_{pre} (Figure 27 a, c). In this state, the material is sheared with constant shear stress and constant normal stress (bulk density remains constant).

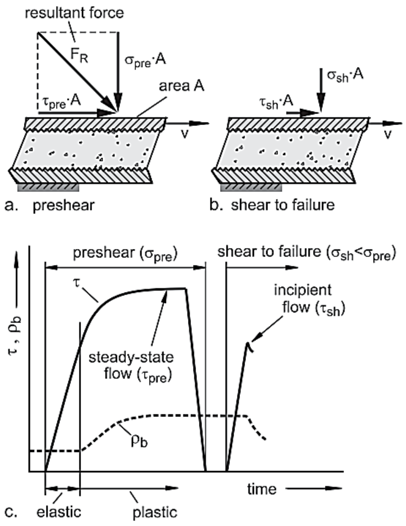

Figure 27: Bulk density ρ_b and shear stress τ for a single measurement, a) preshear of bulk material, b) shear to failure, c) measured quantities over time. The image is taken from [96].

In the next step, the shear to failure is measured by moving the upper plate relative to the lower plate (Figure 27 b). The shear to failure is measured with normal stresses $\sigma_{sh,}$ being lower than the preshear normal stresses σ_{pre} ($\sigma_{pre} > \sigma_{sh}$). For a given normal stress σ_{sh}, the shear stress τ_{sh} increases until the bulk system starts to move, the so-called "incipient flow". When the system starts to flow, the material dilates, and the density decreases. The incipient flow of the bulk material is characteristic of a given preshear σ_{pre}, applied normal stress σ_{sh} and bulk density. Both stresses (σ_{sh} and τ_{sh}) of the incipient flow are plotted in a diagram (Figure 28) [96], also called yield locus (dashed line in Figure 28).

The measured shear stresses for various applied normal stresses are related to the powder properties, providing important information about the material's nature. For example, in the case of a cohesive powder (Figure 28, a), higher shear stresses τ_{sh} are needed to introduce an incipient flow, whereas a cohesionless material needs smaller shear stresses τ_{sh} to start an incipient flow (Figure 28, b).

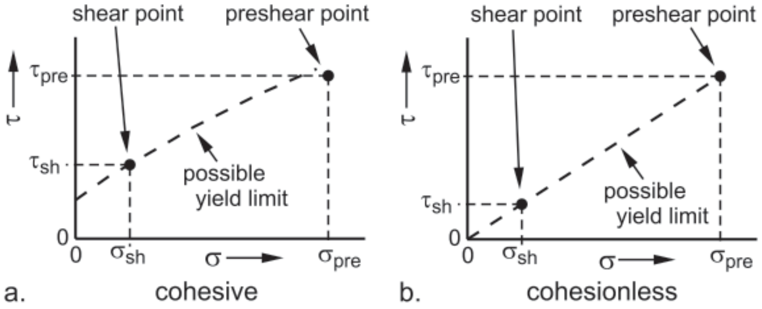

Figure 28: Different behaviours of cohesive (a) and cohesionless (b) materials under various normal stresses at one shear rate. The image is taken from [96].

The study of granules with shear cells can be used to acquire information about the bulk properties based on the acquired yield locus. Typically, the yield locus is determined from several measurements and every point expresses the incipient flow of the granule system. A linear line is applied to the yield locus to acquire the friction coefficient μ from the slope and the yield stress τ_0 from the intercept. This relationship is described by the Mohr-Coulomb model:

$$\tau = \sigma \mu + \tau_0 \qquad 69$$

where σ is the applied normal stress. The yield stress τ_0, also called shear strength, is often referred to the cohesion inside the material [182,183].

Carson and Wilms [184] note that the yield locus takes a form of a curve, which is even pronounced for smaller normal stresses σ. However, it is stated that there is no theoretical basis for the description of the yield locus. A common way is a best-fit approach to describe the evolution of the shear points in Figure 28, which might be a curve or straight linear fit [184].

3.5.3 Rheological measurement with vanes

Besides plate rheometer measurements, vane (Figure 29) or bob geometries can access the rheological properties of fluids and granular materials. Typically, both geometries are immersed inside a fluid or a bulk material. Barnes and Nguyen [185] list many applications of vane geometries. For instance, vane geometries can be used to investigate the yield stress of frozen yoghurt [186] or various tomato concentrates [187].

Barnes and Carnali [188] state several advantages of a vane geometry compared to a bob geometry. One of these advantages is that the vane geometry induces only minor disturbances during the immersion process [189]. A comparative study with several rheometers and measurement geometries has been conducted by Haist et al. [190].

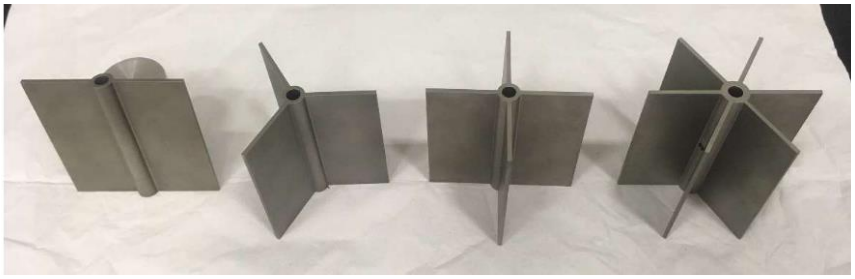

Figure 29: Various vane geometries for slurry measurements. The image is taken from [191].

3.5.3.1 Torque to shear stress relationship for a vane geometry in fluids

When measuring the rheological properties of a fluid, the vane geometry is completely immersed in the fluid. Then, the vane rotates, and the torque is measured. While the vane geometry rotates, the fluid's movement depends on the applied shear stresses at the geometry's surface.

The torque to stress relationship has been described by Nguyen and Boger [189] for a four-bladed vane, considering the geometrical contribution to the measured torque. In the case of a vane geometry with rectangular-shaped blades, the torque T_m and the yield stress τ_0 are described as

$$T_m = K\, \tau_0 \tag{70}$$

where K is the geometrical factor linked to the vane geometry. According to Nguyen and Boger [189], the total torque is the sum of the torque caused by the shear stress at the lateral area A_s and upper and lower area A_s ($T_m = T_s + 2\, T_e$). Here, T_s is the lateral contribution to the measured torque at the outer rim of the rotor blades, i.e., the lateral edge of the rotor blade. Second, T_e corresponds to the upper and lower-end torque, when the four-bladed vane is completely submerged.

The following equations are adapted from [191]. The lateral torque T_s can be calculated with

$$T_s = \tau_s\, A_s\, \frac{D}{2} = \tau_s\, (\pi D H)\, \frac{D}{2} = \tau_s\, \frac{\pi D^2 H}{2} \tag{71}$$

where D and H are the diameter and height of the vane geometry, respectively. The upper and lower end torque T_e is calculated with

$$T_e = \tau_e\, A_e = \int_0^R \tau_e\, 2\pi r dr \cdot r = 2\pi \int_0^{D/2} \tau_e\, r^2\, dr \tag{72}$$

where R is the vane radius (R = D/2), and r is the radial position on radius R. Both equations 71 and 72 are combined following equation 70, then

$$T_m = T_s + 2T_e = \tau_s\, \frac{\pi D^2 H}{2} + 4\pi \int_0^{D/2} \tau_e\, r^2\, dr \tag{73}$$

Assuming that the maximal torque is on the surface of the vane geometry, then the lateral shear stress τ_s and the shear stress τ_e from the upper and lower end equals the yield stress τ_0, following:

$$T_m = \tau_0 \frac{\pi D^2 H}{2} + 4\pi \int_0^{\frac{D}{2}} \tau_0 \, r^2 \, dr = \tau_0 \left[\left(\frac{\pi D^3}{2} \right) \left(\frac{H}{D} + \frac{1}{3} \right) \right] \qquad 74$$

Equation 74 equals the equation provided by Nguyen and Boger [189]. Equation 74 can be used to calculate the maximal yield stress τ_0 with the measured torque T_m.

$$\tau_0 = \frac{T_m}{\left[\left(\frac{\pi D^3}{2} \right) \left(\frac{H}{D} + \frac{1}{3} \right) \right]} \qquad 75$$

Equation 75 assumes that the shear stress around the cylindrical area is uniform. In case the shear zone is non-uniform, as found for clay [192], Nguyen and Boger [189] proposed a correction factor for the upper and lower-end shear stress. The approach assumes that the stress follows a relationship of $\tau_0(r/R)^m$ for $r \leq R$ at the lower end area, where m is a constant for a given vane.

$$T_m = \tau_0 \left[\left(\frac{\pi D^3}{2} \right) \left(\frac{H}{D} + \frac{1}{m+3} \right) \right] \qquad 76$$

Based on equation 76, it is assumed that m is independent of the vane height H and depends solely on the vane blade diameter D. Assad et al. [193] addressed this topic by varying H/D ratios for various vane shapes and stated that m equals 1 for a cylindrical vane geometry.

Previous equations assume a uniform stress distribution and that the maximal shear occurs on the shearing end surfaces of the rotating vanes. Experimental studies show that the actual shearing appears at a slightly larger diameter D_s than the nominal vane blade diameter D [194,195]. This effect was investigated by Keentok et al. [194] by combining finite element methods (FEM) with an experimental study with various Bingham fluids. The study expresses the shear zone as the ratio between the nominal vane blade diameter D and the measured shear zone diameter D_s. The results state that the shear zone depends on the inserted material; for Shell Retinax A, the D_s/D is 1.032 ± 0.003, and for a Duckhams LBM 10 D_s/D equals 1.002 ± 0.002.

3.5.3.2 Torque to shear stress relationship for a vane geometry in granular materials

Characterizing granular materials in terms of their rheological properties with a vane geometry is a challenging task, as the total torque T_m depends on the material's level of mobilization and the local shear [196]. Furthermore, the mobilization and local shear level depend on the material's properties and the measurement conditions such as the bulk density, the applied normal stresses, and the velocity gradient [197].

Poloski et al. [198] described a shear strength model for powders, granular materials and slurries with a vane geometry based on the outcomes of Shinohara [199] and Shinohara and Tanaka [200]. The shear strength model assumes that the shearing at the vane blade edges causes slip movement of bulk materials. Typically vane geometries have a cylindrical surface in motion, as stated in [194]. Then, the total differential torque dT_m occurring at the edge of a vane blade with radius r can be calculated, assuming that the force is acting on the differential area dA on the cylindrical slip surface:

$$dT_m = \tau r dA \qquad 77$$

The cohesive forces and interparticle friction influence the magnitude of the shear strength τ, which is a function of the normal stress and the structure inside the powder bed [198]. The shear stress contributions from the top and bottom ($\tau_{z\theta}$) as well as from the sides ($\tau_{r\theta}$) can be described by the following equations given by Shinohara [199]:

$$\tau_{z\theta} = C^f \sigma_v + C^c F \tag{78}$$

And

$$\tau_{r\theta} = C^f \sigma_h + C^c F \tag{79}$$

where σ_v and σ_h are the radial and axial normal stresses perpendicular to the shear planes around the vane. The parameter C^f is the coefficient of internal friction caused by geometrical interlocking and resistance against movement on the solid particle surface [199,200]. Furthermore, C^c expresses the contact points in a unit area, whereas F indicates the cohesive forces arising at the contact points [199,200]. Cohesive forces are composed of several forces, such as van der Waals, electrostatic, liquid, and solid bridging, which depend on the bulk material characteristics.

Poloski et al. [198] derived equations 78 and 79 from a tensile strength model [200], applied to each vane surface area. Substituting equation 77 into equations 78 and 79 yields:

$$dT_{m,z\theta} = C^f \sigma_v R\, dA + C^c F R\, dA \tag{80}$$

And

$$dT_{m,r\theta} = C^f \sigma_h R\, dA + C^c F R\, dA \tag{81}$$

The stresses σ_v, and σ_h are the stresses acting in the vertical and horizontal directions, arising from the powder bed around the vane, indicating that the powder bed height and the vane immersion inside the powder bed are crucial parameters.

It is essential to be reminded that the pressure acting on a vane does not increase linearly with increasing immersion depth (chapter 3.3.2.1). The main principle is that the forces are forwarded to the lateral walls through a contact force network [201], creating a pressure saturation at a specific depth, which depends on the granule's characteristic, the so-called Janssen effect [91]. Poloski et al. [198] used the Janssen equation to consider the vertical stress acting on the vane. Following this line of thought, σ_v in equation 80 is replaced by equation 36 (chapter 3.3.2.1), and σ_h equals $K\sigma_v$ (equation 39). The top, sides and bottom surfaces contribute to the total torque and can be calculated by integration of equations 80 and 81, yielding:

$$\begin{aligned} T = {} & 2\pi C^f \rho\eta g K \left[H + \lambda \left(e^{-\left(\frac{H - h^{top}}{\lambda}\right)} - e^{-\left(\frac{h^{top}}{\lambda}\right)} \right) \right] R^2 \\ & + \frac{2\pi C^f \rho\eta g}{3} \left[2 - e^{-\left(\frac{H - h^{top}}{\lambda}\right)} - e^{-\left(\frac{h^{top}}{\lambda}\right)} \right] R^3 \\ & + 4\pi C^c F R^3 \left(\frac{H}{2R} + \frac{1}{3} \right) \end{aligned} \tag{82}$$

Here, H is the vane height, and R is the vane radius. It is essential to point out that equation 82 is adapted to the previously stated version of the Janssen equation in chapter 3.3.2.1.

Daniel et al. [196] used the shear strength model of Poloski et al. [198] to study the different torque contributions for cohesionless glass beads and various immersion depths up to 90 mm with a vane geometry . In a preliminary step, Daniel et al. [196] discussed that the shear strength model applies when the bulk material obeys the Janssen effect, i.e. for static or dynamic cases, when the torque is independent of the vane rotation rate. At higher vane speeds, the bulk density changes, leading to a modification of the force network between the granules, resulting in difficulties to acquire precises stress distributions. The outcomes show that the torque is directly linked to the immersion depth (Figure 30), i.e., the deeper the immersion depth, the higher the measured torque. The same applies to the vane rotation speed, i.e., higher rotation speeds tend to increase the torque. Notably, Daniel et al. [196] concluded that the torque contribution by the vane shaft could reach up to 25% of the torque for the maximal immersion depth of 90 mm (quasi-static regime).

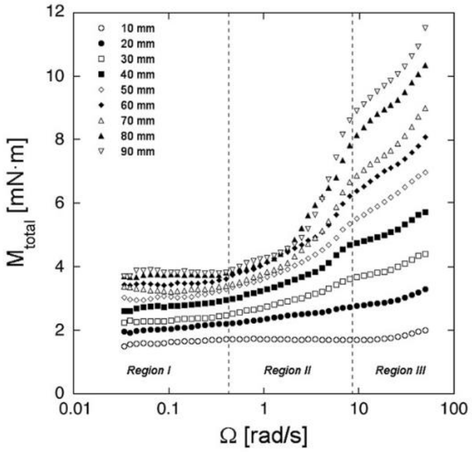

Figure 30: Total torque of a vane geometry immersed in glass beads for various immersion depths in the function of the vane velocity. The image is taken from [196].

4 Measurement devices and methodology

This chapter describes the used experimental devices in detail.

4.1 Mass flow rate

The mass flow rate $\dot{m}$ is measured experimentally with the device GranuFlow from Granutools (Figure 31, left). The measurement setup consists of a cylindrical tube (inner diameter of 47.6 mm), placed on a disc with various orifice sizes. A scale with a glass vessel is placed below the orifice (Figure 31, right). The orifice diameters D ranges from 1 to 16 mm. The scale below the orifice is connected to a computer. The software tracks the mass change with a fixed frequency of nearly 2 Hz. The measurement frequency is not changeable and is predefined by the manufacturer.

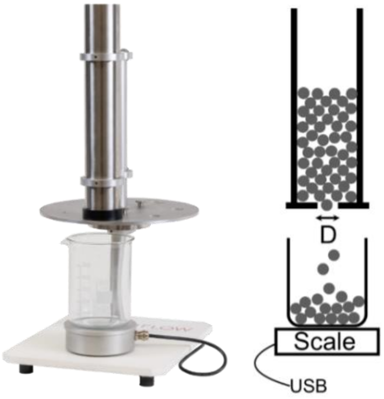

Figure 31: Measurement device GranuFlow from Granutools (left), the experimental sketch of the device (right). Both images are taken from [202].

Determination of the minimal orifice diameter

The minimal orifice diameter D_{min} is determined from the first occurrence of a jammed state. The GranuFlow setup is modified (Figure 32) by adding a self-made adjustable orifice. First, a conical support has been designed with the online software Onshape, 3D-printed with the Original Prusa i3 MK3S+ (see chapter 4.12). The backside of the support consists of a small aperture to insert a diaphragm. Then, the diaphragm, the support and the cylindrical tube have been assembled and placed on the metallic disc of the GranuFlow device. Furthermore, the support has been centred above the largest orifice with diameter D of 8 mm to ensure that jamming occurs entirely from the diaphragm.

A mass of nearly 50 g is inserted inside the tube. The measurement starts by opening the diaphragm. The granular material falls through the created orifice. In the next step, the diaphragm is slowly closed to reduce the orifice size. The measurement is stopped when the granular material blocks the orifice entirely, i.e., the $\dot{m} = 0$. The tube is emptied, and the orifice diameter is visually measured.

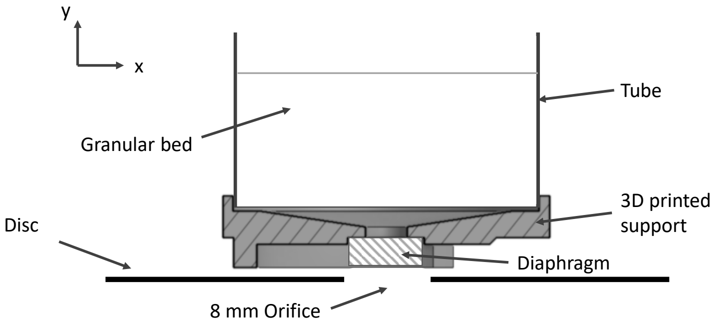

Figure 32: Close-up schematic experimental setup to measure the minimal orifice diameter; image shows a cross-section view of the 3D printed part and the lens diaphragm.

The determination of the orifice diameter is challenging. The idea is to use a small microscope Koolerton (1080p, 2MP) below the orifice. A graph paper is placed on the backside of the metallic disc and right next to the 8 mm orifice to act as a reference.

This approach led to three essential problems. First, the graph paper is insufficient to be used as a reference for very small orifice sizes. The graph paper's line thickness, combined with the high magnification of the microscope, caused problems determining a correct reference distance between two lines. Second, the distance in the y-direction between the microscope's objective and the graph paper and between the diaphragm is different (Figure 32). This effect leads to a measurement error by adjustment of the focus. This impact might be small but not neglectable. Thirdly, when placing the microscope below the jammed orifice, small-induced vibrations are sufficient to overcome bonds in the jammed state, causing granular material to fall inside the microscope's objective. This effect resulted in a jammed gear drive of the microscope, unable to change the magnification. Consequently, this approach was omitted.

The final approach to determine the minimal orifice diameter D_{min} is to measure the orifice diameter with a microscope (chapter 4.10). Figure 33 shows an image of the diaphragm after a measurement. It can be seen that the shape resembles an octagon. The black orifice area is considered to determine an equivalent circle diameter (ECD), which resembles a circular orifice with a minimal orifice diameter D_{min}.

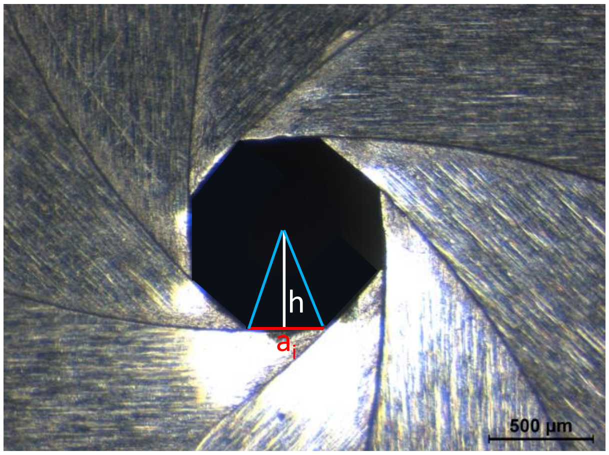

Figure 33: Exemplary image of the measured minimal orifice diameter. The length h towards the centre and the length a_i are manually added for illustration purposes. The black area represents the octagon orifice area A_O.

All sides of the octagon orifice (diaphragm) are measured to calculate an orifice area A_O. Assuming that the area A_O equals a circular area A_C, an equivalent circle diameter (ECD) can be calculated as follows:

$$A_O = A_C \tag{83}$$

Then:

$$\sum_{i=1}^{8} \frac{a_i}{2} h = \pi \left(\frac{D_{min}}{2}\right)^2 \tag{84}$$

where h is the distance from the diaphragm edge towards the centre of the octagon and a_i is the length of one side (Figure 33). Then, the ECD can be calculated as follows:

$$ECD = D_{min} = 2\sqrt{\frac{\left(\sum_{i=1}^{8} \frac{a_i}{2} h\right)}{\pi}} \tag{85}$$

The ECD describes the orifice diameter D_{min} equivalent to the diameter of a circular area.

It can be seen from Figure 33 that the edges of the small blades inside the diaphragm are curved. These curved shapes change the octagon to a circle with increasing orifice area A_O (the black area inside Figure 33). Preliminary tests showed that the transition from an octagon to a circular shape is reached when h is nearly 2 mm. Hence, equation 85 is used when h is lower than 2 mm. Beyond 2 mm, the diameter of the circular area is directly measured with the microscope.

4.2 Bulk and tap density

The bulk and tap densities are measured with the GranuPack device from Granutools. The measurement device has a cylindrical tube, a magnetic distance sensor and a motor below the tube (Figure 34). First, a smaller cylindrical tube is placed inside a larger tube into which the material is poured. Next, the inner cylinder moves up to erase any historical pre-orientation and packing in the powder bed. After the complete vertical movement of the inner cylinder, the so-called Diavolo is placed slightly on top of the powder bed. The sensor provides the possibility to track the powder height h automatically.

The necessary mass m for one measurement is calculated with the bulk density $\rho_{c,bulk}$. This density is determined with the Hall Flow meter (ASTM B212, ISO 3923), a conventional measurement system. The needed mass can be calculated with equation 86, with a volume V of 35 cm^3. The given volume is the recommended volume by the manufacturer. The measurement starts, inducing a periodical movement of the cylinder (tapping). The tapping height of the material corresponds to 1 mm (Δz).

$$m = V * \rho_{c,bulk} \tag{86}$$

The first density (n=0) is the bulk density ρ_{bulk}. The measurement ends after 500 taps (n = 500). The tap frequency changes from 1 Hz to 2 Hz after the 100th tap. This change in the tapping frequency is the standard Granutools measurement procedure. The tapped density ρ_{tap} is defined as the density at the end of the measurement, i.e., after 500 taps. The measurement is repeated at least two times.

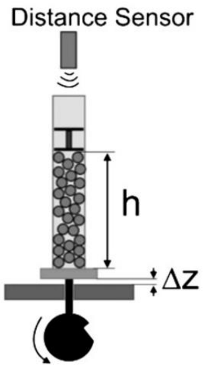

Figure 34: Measurement principle of the Granupack device. Image taken from [58].

4.3 Pycnometer density

The pycnometer density ρ_{pyc} is measured with the device AccuPyc II, type 1340, by Micromeretics. The measurement principle is based on the gas displacement principle [203]. The measurement device consists of two vessels of equal size. First, a small but known mass of granules is poured into one vessel. The vessel is then sealed and filled with inert gas, such as helium or nitrogen. In the next step, the inert gas is transferred into the second vessel to calculate the solids volume. The ratio between the solids volume and inserted mass yields the pycnometer density. The pycnometer density should be close to the theoretical density of the material in case all voids are accessible. The measurement is repeated several times and provides an average pycnometer density.

Figure 35: Measurement apparatus to measure the pycnometer density.

4.4 Granules size distribution

The granule size distribution is measured through laser diffraction with the measurement device Mastersizer 3000 from Malvern Panalytical. A small amount (5-15 g) of granules is used for each measurement. The measurement is repeated at least two times.

Figure 36: Laser diffraction measurement device Mastersizer 3000.

4.5 Moisture

The moisture inside the powder bulk is measured with the thermo-gravitational scale MA40 of Sartorius. The moisture loss is measured using a 5 g +- 0.5 g granular material and heating the granules to a temperature of 80°C. The initial and end mass is used to calculate the humidity in wt.-%. Furthermore, the measurement device measures the change in mass.

Figure 37: Thermal balance to measure the moisture content of granular materials.

4.6 Sieving

Granular materials are sieved to acquire defined granule size distributions. Here, a sieving machine by Retsch (Siebturm AS200) is selected with different stacked sieves (Figure 38). After stacking the sieves, roughly 400 g of granular material is poured into the top sieve. The sieving duration is one minute with an amplitude of 2 mm.

Figure 38: Sieving apparatus with sieves.

The selected meshes in Table 4 differ from granular material to granular material in this study, i.e., from reference batch to reference batch. Notably, everything below 63 µm is considered dust in this study.

Table 4: Used sieving meshes to sieve hard metal granular materials.

Mesh (µm)
>315
280
250
224
200
180
150
125
100
63
<63

4.7 Rheological measurements

The granular material's rheological properties are measured with the rotational rheometer Haake Mars II from Thermofisher. Two different types of geometries are used: (1) rotor-cup and (2) plate-cup. The measurement procedures are explained in the corresponding chapters.

Figure 39: Haake Mars II from Thermo Fisher

4.8 Contact angle measurement

The sessile drop technique is used to determine the surface energy of the solids, namely pure tungsten carbide (WC), cobalt (Co) and organic binder. First, a sample is cut from dense tungsten carbide. The part is embedded into a two-component adhesive in the next step. After the curing, the surface of the solid is polished. The same procedure is done for a pure cobalt part. In the case of the organic binder, small masses are compressed into a small block. Then, the contact angle measurements for tungsten carbide and cobalt are done on the polished surface, while a smooth and flat surface is selected for the organic binder from the compressed block.

The contact angle measurements are performed with the device OCA 15EC from dataphysics (Figure 40). Drops are created with various liquids, such as deionized water, dodecane and glycerine. It is known from the literature that the drop's volume influences the contact angle measurement [204]. Therefore, defined drop sizes of 2 cl are created with an Eppendorf pipette. After the creation of the drop, the camera's focus is adjusted. The software automatically detects the drop and calculates the contact angle on both sides. The average of both sides is considered.

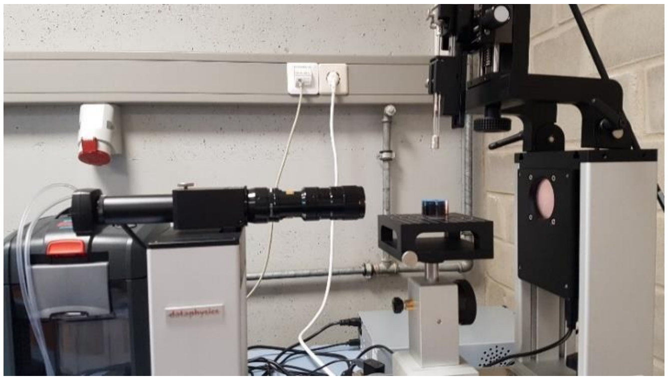

Figure 40: Contact angle measurement device with a camera on the left side and a backlight. In between, an embedded sample on a movable plate.

The solids' dispersive and polar surface energies are determined from the liquid's polar and dispersive surface tensions based on the OWRK method (see chapter 3.4.2). The polar and dispersive energies of the selected liquids can be found in Table 5.

Table 5: Selected liquids for the sessile drop method.

Liquid	**Polar surface energy γ_L^p (mJ/m^2)**	**Dispersive surface energy γ_L^d (mJ/m^2)**	**Total surface energy γ_L (mJ/m^2)**
Dodecane* [205]	0	24.93	24.93
Deionized water [206]	50.20	22.00	72.20
Glycerine [207]	29.70	33.60	63.30

*Dodecane has only dispersive surface energies according to [208].

4.9 Scanning electron microscope (SEM)

The scanning electron microscope (SEM) JSM-IT300LV from Joel takes images from the granular materials (Figure 41) at different magnifications to show differences between selected granular materials.

Figure 41: Image from the scanning electron microscope JEOL JSM-IT300LV.

4.10 Optical light microscope

The optical microscope MZ6, in combination with a camera DFC320 from Leica, is used to take images. The maximal magnification is 40x.

Figure 42: Microscope MZ6 with DFC320. Microscope is connected to a PC (not shown here).

4.11 Atomic Force Microscopy (AFM)

An atomic force microscope (AFM) from Veeco is used to measure the adhesive forces acting between granules (Figure 43). A single granule is glued with an electrical and thermally conductive resin by EPOTEK (two-component adhesive, type E2101) on a tipless cantilever (All-in-one, type AIO-TL-10, by BudgetSensors), with a spring constant of 0.2 N/m and a resonance frequency of 15 kHz. The glueing step is challenging as the cantilever has dimensions of length L = 500 µm, width W = 30 µm and thickness TH = 2.7 µm. The attaching process is performed in a second AFM with a camera. Here, the cantilever moves down on a prepared epoxy resin droplet. When the cantilever enters the surface slightly, the movement is reversed. In the best case, a small drop of glue sticks to the cantilever. In the next step, the cantilever (and drop) touches the top of a single hard metal granule. The measurement is performed after curing the adhesive glue, i.e., after one day.

In the next step, the deflection of the laser observed by the photodiode detector is calibrated for the prepared cantilever with a sapphire sheet in contact mode. Here, the prepared cantilever approaches the surface slightly until the tip snaps to the surface. Again, the movement of the cantilever and the deflected laser is recorded. Finally, the calibration is done with the linear deformation of the cantilever. This step has to be done for every new cantilever. The AFM is flooded with nitrogen to suppress the influence of humidity on top of the sample's surface. The measurement is performed when the relative air humidity is lower than 10 %.

Figure 43: Schematic image from the atomic force microscope (AFM) inside a housing.

Approaching a substrate surface with a cantilever, the cantilever snaps-in by the attractive forces between the tip and the substrate (Figure 44, black line). The tip is in contact with the substrate. Then, the cantilever is retracted. The force needed to separate the cantilever is called the “pull-off” force and is linked to the properties of the material, i.e., cantilever and substrate.

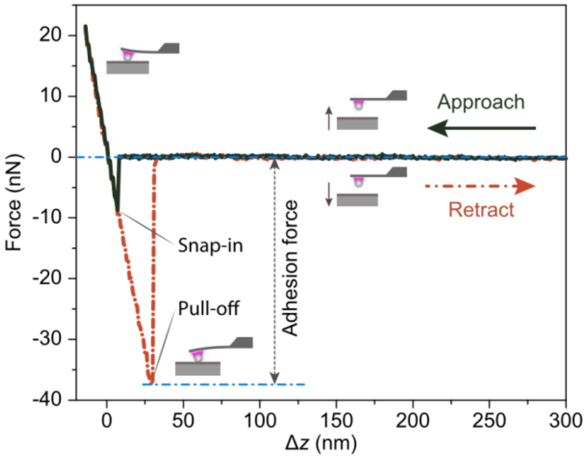

Figure 44: Exemplary AFM measurement of a substrate and a microbead probe [209].

The measured laser deflection is proportional to the cantilever's movement. The pull-off force can then be calculated with the maximal deflection of the laser, following:

$$F = k * \Delta e * \Gamma \tag{87}$$

where k is the stiffness of the cantilever, Δe is the difference of the laser deflection, and Γ is the sensitivity of the laser, coming from the calibration procedure (see above).

4.12 3D Printer

A set of rotor geometries for rheological measurements has been designed with the online platform Onshape. The geometries are saved as stl files and transferred to the 3D-printer Original Prusa i3 MK3S (Figure 45). The designed parts are manufactured with PLA filaments of 1.75 mm filament diameter. The extrusion nozzle has a diameter of 0.4 mm.

Figure 45: 3D-printer i3 MK3S by Prusa.

5 Determination of the angle of repose of hard metal granules

The measurement of the angle of repose (AOR) provides a possibility to get an insight into the flowability of granular materials and powders. Many different measurement techniques exist to measure the angle of repose of granular materials, such as rotating drums and the piling method (see also chapter 3.2). Both differ in the expression of the angle of repose, as the rotating drum usually describes the angle of repose in motion, also known as the dynamic angle of repose (AOR_d). Conversely, the piling method can be used to determine the static angle of repose (AOR_s). The static angle of repose describes the maximal angle before the cone's surface relaxes through an avalanche on the surface of the pile. When applying the piling method, material falls on top of a plate from a funnel. However, the measurement time affects the static angle of repose as any amount of mass discharged from the funnel may introduce, at some point an avalanche. This behaviour leads to a spread in the measured static angle of repose. Another challenge arises from the asymmetry of the created pile at the end of a measurement, leading to different angles, depending on the measurement position. Typically, the height H and the base width D of the pile are used to express the angle of repose.

In this study, the piling method is modified by integrating a dynamic image analysis procedure and a novel approach by moving the plate below the funnel. The results and technique will be discussed for hard metal granular materials. Parts of this chapter have been published [210].

5.1 Granular materials and properties

A hard metal granular material with 9 wt.-% cobalt is selected from the powder department of CERATIZIT Luxembourg S.à r.l.. This unsieved granular system referred to as “standard” or “SA”, is the basis for determining the angle of repose.

The granule size distribution influences the angle of repose. Therefore, measurements with well-defined granular systems are necessary. These granular systems are created by mechanical sieving (see chapter 4.6). Initially, 100 g of the standard sample was sieved to set the optimal sieving mesh. The outcome showed that the standard sample ranges between 224 and <63 µm (dust). Therefore, the standard sample is sieved with the corresponding sieves from chapter 4.6, following the nomenclature A/63-100, A/100-125, A/<125, A/125-150, A/150-200, A/200-224 and A/>224 µm. In the second and third steps, broader granule size distributions are considered: A/125-200, A/150-224 and A/125-224 µm.

Figure 46 shows the granules inside the unsieved sample SA. The images are acquired with a scanning electron microscope (SEM) (chapter 4.9). It can be seen from Figure 46 that the granular materials are nearly spherical and exhibit a rough surface.

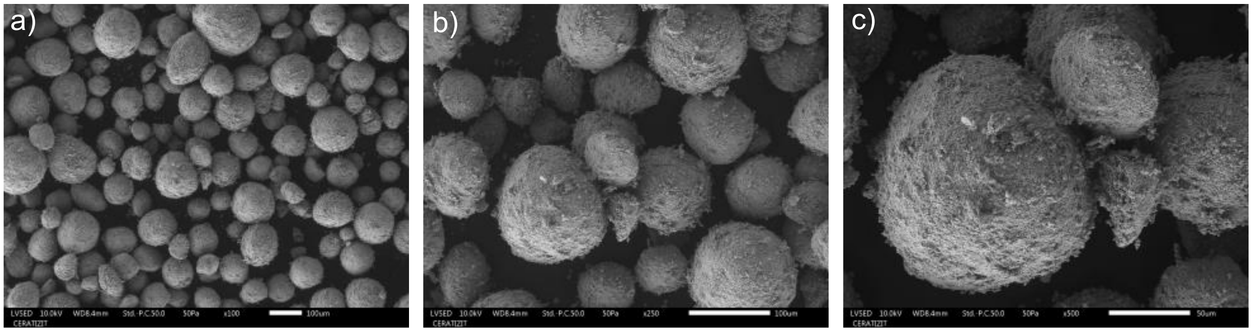

Figure 46: SEM images from the unsieved sample SA: a) x100, b) x250 and c) x500. Image is taken from [210].

Regarding shape and surface roughness, all sieved samples in Table 7 are expected to be similar to the granules shown in Figure 46, as all size classes originate from the unsieved sample SA. It can be seen from Figure 47 that the sieved samples differ in their granule diameter. Furthermore, the images show that the sieved samples have fewer fine particles attached to their surface. The wear causes the absence of finer particles on the surface as the granules are sheared against each other during the sieving process.

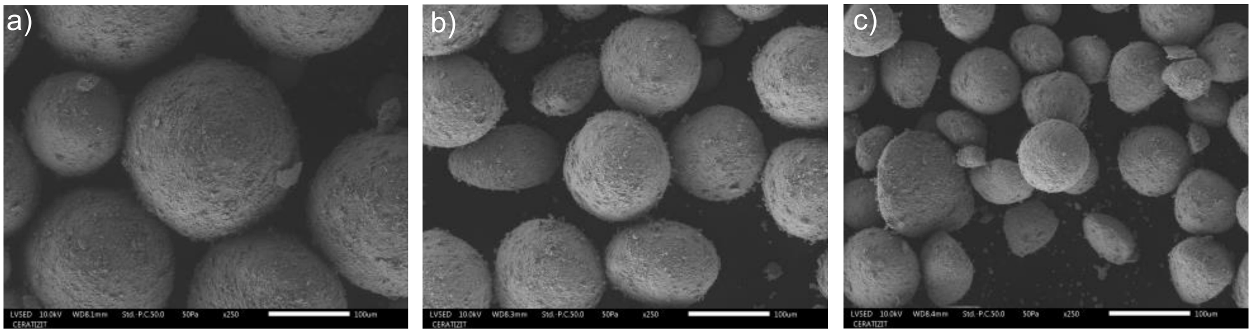

Figure 47: SEM images from three sieved samples with a magnification of x250: a) A/200-224, b) A/125-150, c) A/<125

5.1.1 Granule size distribution

The standard sample SA's and sieved samples' granule size distribution A/>224 to A/125-224 have been measured with laser diffraction (Mastersizer 3000 from Malvern analytics, chapter 3.1.3). The granule size distributions are shown in Figure 48. Figure 48 (left) clearly shows the differences in the granule size distributions, also visible in the shifts in the cumulative granule size distribution (Figure 48, right). Notably, sample A/<125 consists of very fine particles below 50 µm. A similar result can be found for the unsieved standard sample SA, composed of all granule sizes.

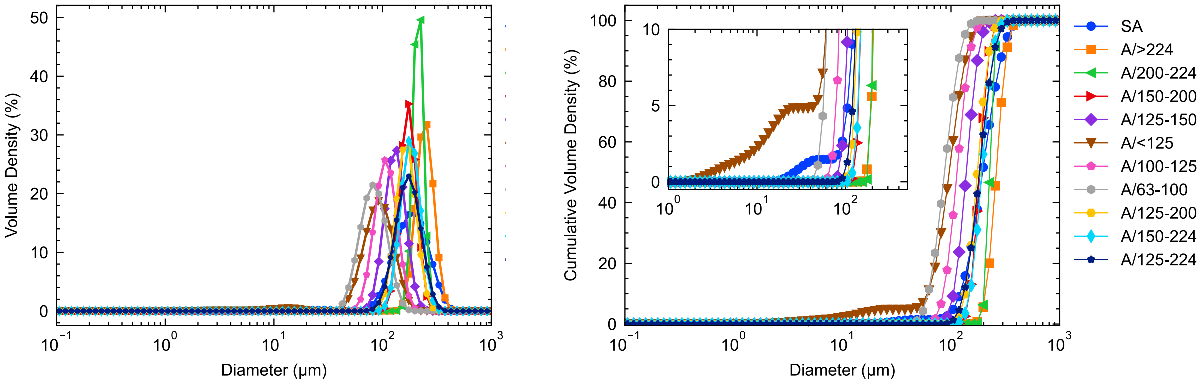

Figure 48 Averaged granule size distribution of samples SA and all sieved samples (left) and the cumulative granule size distribution (right). Both figures share the same legend.

Substantial diameters such as d_{10}, d_{50} and d_{90} are determined based on the cumulative granule size distribution (Figure 48, right). These diameters are listed in Table 6. The Sauter mean diameter $d_{[3,2]}$ and the de Brouckere diameter $d_{[4,3]}$ depend strongly on the individual granule sizes within the samples. Furthermore, based on the literature [36,37], the de Brouckere diameter $d_{[4,3]}$ is sensitive to coarser granules inside the distribution. Conversely, the Sauter mean diameter $d_{[3,2]}$ appears more sensitive to smaller particles inside the granule size distribution (see Table 6).

The span describes the difference between the d_{90} and d_{10}. The span is used to compare various granule size distributions (equation 88).

$$span = d_{90} - d_{10} \qquad 88$$

Low span numbers indicate a narrow size distribution. Broader size distributions, such as samples A/125-200, A/150-224 and A/125-224, show a slight increase in the span number. A more pronounced span can be found for sample SA containing all granule sizes.

Table 6: Diameters from laser diffraction measurements: d_{10}, d_{50}, d_{90}, Sauter mean diameter $d_{[3,2]}$ and de Brouckere $d_{[4,3]}$

Sample	d_{10} (µm)	d_{50} (µm)	d_{90} (µm)	$d_{[3,2]}$ (µm)	$d_{[4,3]}$ (µm)	span (µm)
SA	113 ± 3	183 ± 3	283 ± 5	159 ± 4	191 ± 3	170 ± 5
A/>224	193 ± 1	245 ± 2	307 ± 2	241 ± 2	249 ± 2	114 ± 2
A/200-224	188 ± 0	213 ± 0	239 ± 1	212 ± 1	214 ± 1	51 ± 1
A/150-200	139 ± 1	172 ± 1	212 ± 1	170 ± 1	175 ± 1	73 ± 1
A/125-150	99 ± 2	130 ± 1	171 ± 2	127 ± 1	132 ± 1	72 ± 3
A/<125	57 ± 1	90 ± 1	133 ± 1	54 ± 1	91 ± 1	76 ± 1
A/100-125	79 ± 2	106 ± 1	142 ± 1	104 ± 1	109 ± 1	63 ± 2
A/63-100	57 ± 1	82 ± 1	116 ± 1	79 ± 1	85 ± 1	59 ± 1
A/125-200	126 ± 2	164 ± 1	212 ± 2	161 ± 1	167 ± 1	86 ± 3
A/150-224	139 ± 4	180 ± 3	233 ± 2	177 ± 3	184 ± 3	94 ± 4
A/125-224	123 ± 5	171 ± 3	237 ± 1	165 ± 3	176 ± 3	114 ± 5

5.1.2 Moisture content inside granular materials

The powder's moisture was measured as described in chapter 4.5 and is presented in Table 7. It can be seen from the listed values that the moisture contents (MC) is very low, i.e. all below 0.26 %. Furthermore, it can be concluded from Table 7 that the moisture content varies among the granule size distributions and that there is no direct correlation between the size and the moisture content. Callahan et al. [211] proposed a classification to describe the hygroscopic properties of pharmaceutical powders. In accordance with this classification, the granular materials in Table 7 are non-hygroscopic. The non-hygroscopic classification is linked to the hydrophobic character of the organic binder inside the granules [212].

The influence of moisture content on mass flow and angle of repose measurements are generally unneglectable (see chapters 3.3.3.2 and 3.2.3.2). Comparing the measured moisture contents with the experimental study of Sun et al. [112], the presented moisture contents in Table 7 are close to the moisture contents of glass beads and lignite after a drying process at 105 °C. Sun et al. [112] omitted influences by moisture inside the material below 0.21 %. Similar ranges can be found in Table 7 without the application of heat. Hence, the influence of moisture in the granular materials is omitted, similar to Sun et al. [112].

Table 7: Moisture content (MC) for various granular materials

Sample	MC (wt.-%)
SA	0.26
A/>224	0.21
A/200-224	0.21
A/150-200	0.24
A/125-150	0.19
A/<125	0.24
A/100-125	0.23
A/63-100	0.25
A/125-200	0.22
A/150-224	0.16
A/125-224	0.22

5.1.3 Bulk, tap and pycnometer density of granular materials

The samples' bulk and tap density were measured according to the description in chapter 4.2. The pycnometer density was measured following chapter 4.3. Some representative densification curves of samples are presented in Figure 49. It can be seen that the most significant density change happens at an early stage, i.e., tap numbers below 50 and results in an asymptotic curve with increasing tap numbers.

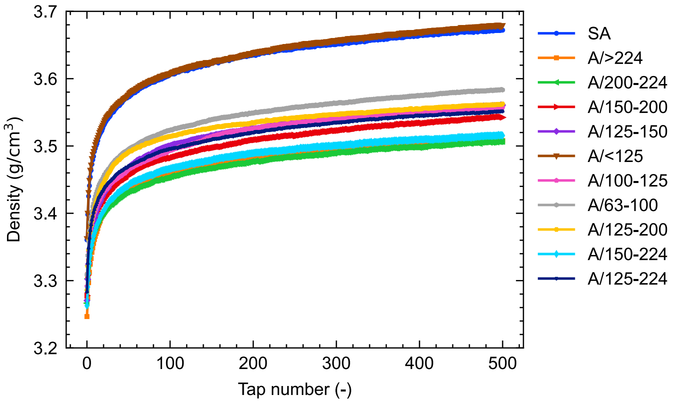

Figure 49: Densification of a single measurement of each sample to show noteworthy differences in bulk and tap densities.

The measured bulk, tap and pycnometer densities are listed in Table 8. It can be seen that the bulk densities are close to each other. Outstanding are samples SA and A/<125, with the highest bulk and tap densities. Besides this, minor fluctuations in the measured pycnometer densities can be observed (Table 8). It is important to remember that all samples are equal in their chemical composition, indicating that the presented bulk and tap densities in Table 8 are primarily influenced by the granule size distribution.

The bulk and pycnometer density ratio yields the packing fraction η (Table 8). Although the bulk and tap density show for some samples noteworthy differences, the packing fraction is nearly identical. This result aligns with the DEM simulations of Parteli et al. [213], showing that the packing fraction stays nearly constant for mean diameters larger than 30 µm. Schmidt et al. [214] found numerically a constant packing fraction for mean diameters above 100 µm. The calculated packing fractions of nearly 0.3 are considerably smaller than those of bimodal granular systems, ranging experimentally between 0.64 and 0.85 [215]. The ratio between the tap and bulk density is called Hausner ratio [216] and describes the degree of internal friction from a densification process [217] (Table 8). Hence, the flowability of the granular system is better the smaller Hausner ratio.

Table 8: Bulk, tap and pycnometer density of selected samples of type A. Errors stem from several measurements.

Sample	Bulk density (g/cm^3)	Tap density (g/cm^3)	Pycnometer density (g/cm^3)	Packing fraction η (-)	Hausner ratio (-)
SA	3.36 ± 0.01	3.67 ± 0.01	11.50 ± 0.01	0.29 ± 0.01	1.093 ± 0.004
A/>224	3.25 ± 0.01	3.51 ± 0.01	11.50 ± 0.01	0.28 ± 0.01	1.080 ± 0.005
A/200-224	3.27 ± 0.01	3.51 ± 0.01	11.52 ± 0.01	0.28 ± 0.01	1.074 ± 0.004
A/150-200	3.28 ± 0.01	3.53 ± 0.01	11.52 ± 0.01	0.28 ± 0.01	1.077 ± 0.004
A/125-150	3.27 ± 0.01	3.55 ± 0.01	11.52 ± 0.01	0.28 ± 0.01	1.085 ± 0.005
A/<125	3.36 ± 0.01	3.67 ± 0.01	11.53 ± 0.01	0.29 ± 0.01	1.091 ± 0.004
A/100-125	3.29 ± 0.01	3.55 ± 0.01	11.52 ± 0.01	0.29 ± 0.01	1.079 ± 0.004
A/63-100	3.30 ± 0.01	3.58 ± 0.01	11.51 ± 0.01	0.29 ± 0.01	1.086 ± 0.004
A/125-200	3.29 ± 0.01	3.56 ± 0.01	11.51 ± 0.01	0.29 ± 0.01	1.084 ± 0.004
A/150-224	3.26 ± 0.01	3.52 ± 0.01	11.52 ± 0.01	0.28 ± 0.01	1.078 ± 0.005
A/125-224	3.28 ± 0.01	3.55 ± 0.01	11.51 ± 0.01	0.29 ± 0.01	1.082 ± 0.004

5.2 A novel approach to measure the angle of repose

The angle of repose is determined with a new measurement setup, shown in Figure 50. The measurement device consists of a scaffold and four sliders. A symmetric funnel manufactured from inox steel is attached to a slider with an inner angle of 30° and outlet diameter of 2 mm. The inner funnel surface is ground to avoid negative influences on the mass flow, such as outlet clogging or funnel flow pattern. The distance between the funnel outlet and a round-shaped 80 mm base plate is set at 16.2 mm. The distance of 87.2 cm between the base plate centre and the camera lens is kept constant throughout all measurements.

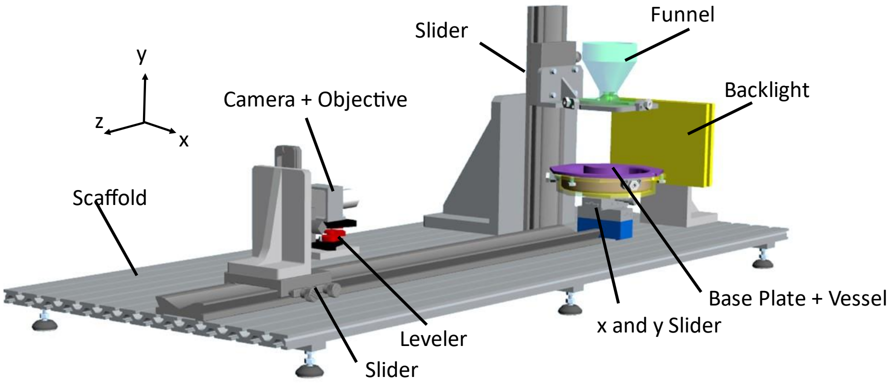

Figure 50: Measurement setup for the determination of the angle of repose of hard metal granules. Image is taken from [210].

The base plate is mounted on a second slider to change the position in the x-axis direction below the funnel orifice. The angle of repose is measured at different plate positions, evenly distributed around the plate with a step of 0.5 mm. The actual base plate position on the x-axis is measured with a calliper and a precision of 0.01 mm. The displacement of the base plate from the centre induces a wanted skewness of the conical heap on the base plate (Figure 51). More precisely, the skewness leads to a preferred sliding of a layer of granules from the cone's tip in the form of avalanches. The angle of repose is measured three times for each position, making for a single granular sample a total of 27 measurements. Noteworthy, the measurement position of the base plate is fixed during measurements and is shifted after the third subsequent measurement.

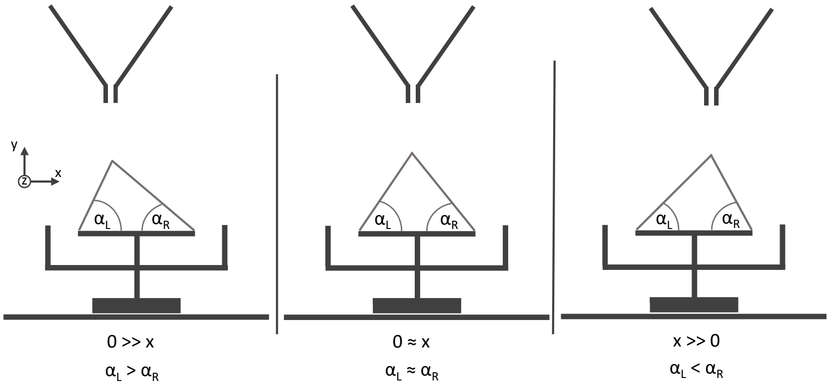

Figure 51: Skewness of the conical heap (left and right) and an ideal symmetric conical heap in dependency on the plate position. Image is taken from [210].

The measurements are performed in an air-conditioned room. The temperature ranges between 21 to 23 °C. The relative humidity in the air is influenced mainly by the weather conditions. Moisture influences are reduced by storing the granular materials inside plastic bottles or plastic bags inside buckets.

5.2.1 Image processing algorithm

The following chapters describe the underlying principles of the image processing algorithm. The objective is to describe the cone surface as precisely as possible by an edge detection function. The cone's edge is visible as a black line, being the transition from black to white pixels. A similar experimental study has been presented by Li et al. [60], where linear fittings of the surface line are used to determine a representative angle of repose for heaps at rest. In a previous study, Li et al. [218] discussed applying a global batch clustering method to detect the piled-up heap automatically. This method is also integrated into the follow-up experimental study of Li et al. [60].

5.2.1.1 Recording of data

The experimental setup in Figure 50 consists of an LED backlight to increase the brightness and the contrast between the background and the granular material. The granular materials are opaque and are visible as black cones in the acquired images. Measurement preparation begins with filling the funnel with one of the samples listed in chapter 5.1. The measurement starts by opening the orifice to introduce a continuous flow of granules onto the base plate. The continuous flow of granules leads to the bulking-up of the pile until avalanching occurs. In this state, the avalanching effect dominates. The bulking-up, permanent flow of the granules and the occurrence of avalanches are recorded with a full HD camera equipped with a 5-50 mm wide angle lens and a focal ratio of f/1.6. The frame rate is set to 5 fps, acting as a compromise between the stored data's size and the necessary number of images to detect reasonable changes in the angle of repose. The end of the measurement is reached when (1) the funnel is completely discharged, (2) the granular material from the vessel encounters the cone edge of the base plate (overfilling), or (3) a clogging effect inside the funnel occurs.

A single measurement records up to 1300 images per measurement, followed by image processing. Noteworthy, 35000 images are acquired from 27 measurements spread over various base plate positions. These images are saved in PNG format to acquire the angle of repose for a single granule sample.

5.2.1.2 Conditions for the image processing

In the early stage of the measurement, the continuous flow leads to bulking of the conical heap. During this phase and the overall measurement, avalanches exist. The existence of avalanches influences the measured angle of repose [219]. Consequently, it is necessary to provide restrictions and conditions for the following angle of repose calculation:

- Only images are considered after the bulking phase of the cone, i.e., after the first avalanche and the first granular material falling inside the vessel. The bulking phase ends when the granules reach the perimeter of the base plate. Therefore, the bulking phase is neglected in the proposed method.
- Images where granular materials on the base plate are in contact with granules from the vessel are discarded. The reason is an influence on the measured angle of repose. The size of the vessel and the granule properties mainly influence this effect. Noteworthy, this happens mainly at the end of the measurement.
- Tests during which clogging effects inside the funnel occur, are suppressed. When this happens, the whole measurement is discarded and repeated.

5.2.1.3 Steps of the image treatment

The image processing is split into two essential steps: image processing and the automatic angle of repose calculation. The image processing is performed with the Computer Vision library OpenCV [220] together with the data processing library SciPy [221]. The image processing starts by loading one image from the data set, followed by the application of bilateral filtering to minimize noise and, at the same time to keep sharp edges (Figure 52, a). In the second step, the image is changed to grey (Figure 52, b). In the following step, a binarization of the image is performed to convert the image to black and white (Figure 52, c). Then, the binarized image is reduced to a region of interest (ROI) (Figure 52, d). This step is essential to avoid any disturbances from the regions outside the LED backlight (see black areas next to the cone; Figure 52, a-c). The falling granular material leads to a rounded tip of the pile. The rounded tip and the base plate edges are omitted to determine the angle of repose. Finally, the angle of repose is determined from the ROI. The ROI contains the central body of the cone, i.e., the rounded tip and a few layers of the granules are excluded (Figure 52, e).

In the next step, the ROI is split horizontally into two separate images and is treated identically, as described in the following. From now on, the angles of repose for the left and right sides are called: alpha left α_L and alpha right α_R. The division of the ROI into two halves is essential for the sliding base plate approach. Here, the angles for both sides are equally calculated and, for simplicity reasons, only explained in the following for the left side (α_L). First, an edge detection function provides the x_i and y_i information from the pile's surface (Figure 52,f). Then, the first n pixels from the lower left corner are considered to apply a linear fit to calculate the slope m of the pile's surface. The angle of repose $\alpha_{L,n}$ for the discrete pixel number n and the slope m can be calculated following equation 89.

$$\alpha_{L,n} = \tan^{-1}(m) \qquad 89$$

It is important to note that the total amount of pixels n_{max} and the pixel number n changes from image to image, as the cone shape fluctuates during the measurement.

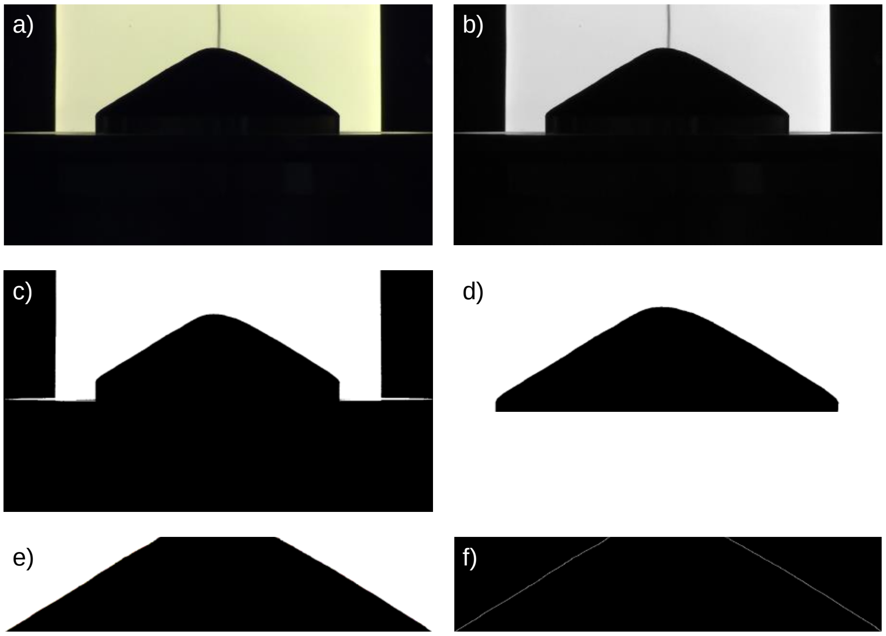

Figure 52: The various stages of the image processing: a) one original image, b) grey image, c) binarized image, d) ROI of the pile, e) ROI with sliced bottom and top of the pile, f) visible edge from edge detection function. Image is taken from [210].

5.2.1.4 Avalanche detection method

As previously stated, a continuous mass leads to bulking of the pile accompanied by avalanches. The avalanches are visible as local waves inside the 2D images, which occur unpredictably during the measurement. The bulking phase typically causes an increase in the angle of repose, while an avalanche leads to a decrease. Both cases are valid when the whole surface line of the pile is considered for the angle of repose evaluation. Consequently, in this approach, the effect of the avalanche is considered in the image processing, as the avalanche leads locally to an increased angle of repose.

In the first step, areas next to the base plate are controlled for the existence of discharging granular material (Figure 53, red boxes). Falling off the base plate happens when an avalanche exceeds the perimeter of the base plate. If granular materials are detected inside both areas, this image is omitted for the angle of repose calculation.

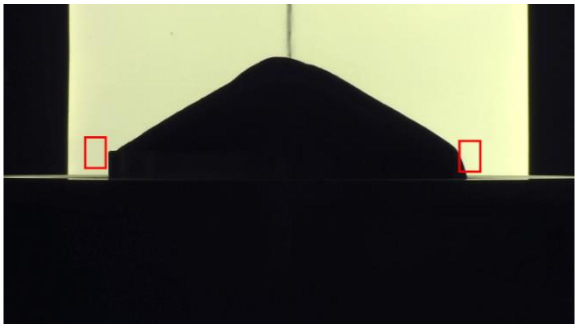

Figure 53: Exemplary original image with granular material next to the base plate. Red areas next to the base plate are manually added for illustration purposes. Image is taken from [210].

In this proposed approach, the idea of Li et al. [60] is implemented to calculate the slope with the x_i and y_i information through an iteration process. Furthermore, the iteration process is extended with further criteria. Figure 54 (left) shows a typical surface line created from x- and y-coordinates found from the edge detection function. The iteration for the given pixels starts in the lower left corner (Figure 54, right). The iteration starts at a minimum pixel number n_{min}, defined as 20% of the total pixel number n_{max}. For the iteration process, only 95 % of the total amount is considered to prevent any influences from the curved tip, i.e., the upper 5% are discarded. The iteration starts with the pixel number n_{min} and increases until the pixel number n reaches n_{max}. The slope is calculated for every iteration step of the pixel number n. It is important to remember that the total amount of pixels n_{max} depends on the actual image, influenced by bulking and avalanching, i.e., strongly influenced by the pile's shape. Consequently, n_{min} and n_{max} differ from image to image.

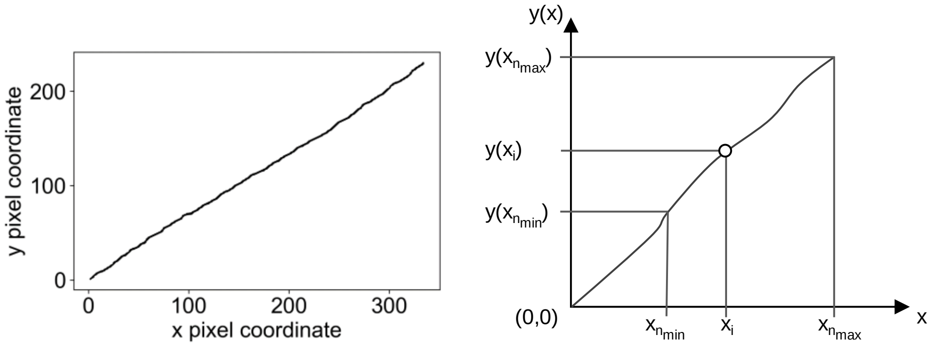

Figure 54: Surface line of a pile from the left side found by the edge detection function (left). Iteration process (right). Image is taken from [210].

This proposed approach uses the slope to determine a suitable range of pixels. The idea is to introduce the slope coefficient f, expressing the ratio of the slope m_n and the initial slope $m_{n_{min}}$, following:

$$f = \frac{m_n}{m_{n_{min}}} \quad (90)$$

A slope coefficient factor above or below 1 implies a slope change compared to the initial slope, indicating the presence of an avalanche or artefact. The presence of an avalanche is controlled by considering an upper m_{UL} and lower m_{LL} limit to describe the minimal and maximal deviation. While the slope coefficient f stays within limits, the iteration runs until the n_{min} reaches n_{max}. The smaller the difference between both limits, the more likely the slope coefficient f passes the given limits. Consequently, the size of the upper and lower limits describes the degree of sensitivity to avalanches and curved surfaces in the absence of avalanches. On the other side, excessive limits lead to ineffective classification, including less pronounced avalanches or surface irregularities of the heap. Initial measurements suggest that the slope coefficient should range between 5-10% around f. For the proposed approach, the limit is set to 6%. Besides this, Li´s criterion [60] is considered. Here, the correlation coefficient has to be higher than 0.96 during the iteration process. When this value is lower than 0.96, the iteration stops, similar to the boundary limits of the slope coefficient.

The angle of repose is then calculated with equation 89 and the slope from either the maximal pixels from the whole surface line or at an earlier stage with fewer pixels when boundaries are exceeded.

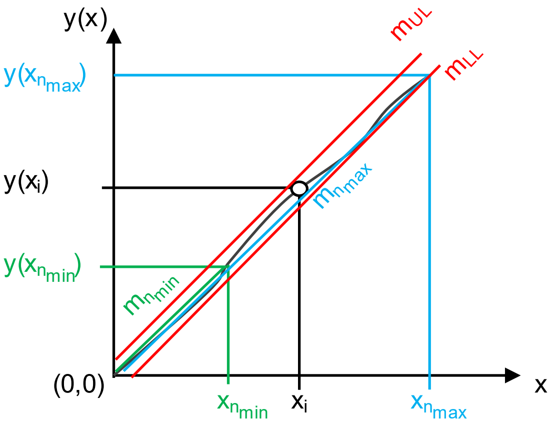

Figure 55: Schematic illustration of the upper and lower limits.

5.2.2 Data processing for data sets

Calculating the angle of repose for each image leads to a distribution of angles. Therefore, the beginning of the data processing is the search for significant outliers by using the 1.5-IQR method [222]. In this step, the data set is ordered. Then, the first and third quartiles are determined from the ordered list. The difference between both quartiles is described as the interquartile range (IQR). The IQR describes data scattering around the median value, the middle of the ordered data set. In the proposed approach, the IQR is increased by a factor of 1.5, as used by Kim et al. [223] and Pirson et al. [224], providing the upper and lower limits of considered AORs. Every angle exceeding these limits is excluded from the final AOR determination.

In the next step, the average is calculated based on the considered data for each measurement. Notably, the measurement is performed at least three times for every base plate position. The previously mentioned criteria lead to a minimal variation of the considered images, making it necessary to consider weighted averages.

5.2.3 The sliding base plate method

Compared to other angle of repose measurements found in the literature [46][225,226], the proposed method measures the pile angle for various base plate positions with reference to the funnel orifice. Consequently, it allows the plot of the acquired angles α_L and α_R in the function of the plate position (Figure 56). First, the angles α_L and α_R are fitted with a 4th-order polynomial fit. Polynomial fits of lower order described inadequately the evolution of α_L and α_R. Then, the intersection point of both polynomial fits is determined. It is expected to have a transition with a higher fit inclination near the intersection point. This inclination distorts the calculated AOR. Consequently, the angles of α_L and α_R near the intersection point are omitted. The average of the remaining angles yields the final AOR.

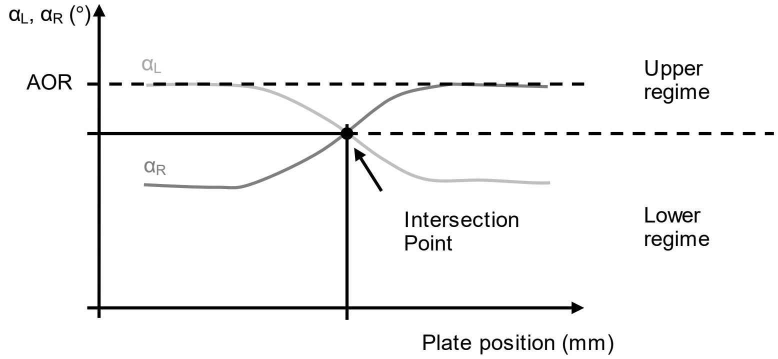

Figure 56: Schematic illustration to determine the angle of repose with the fits from the angles α_L and α_R for various plate positions. Image is taken from [210].

5.2.4 Validation of the approach with an artificial image and a reference cone

The novel approach is initially tested with two different methods. First, a symmetrical reference cone with a nominal angle of 32° is placed on top of the base plate (Figure 57). The program takes up to 250 images in the centre of the camera image, followed by the image processing treatment. The actual angle of the reference cone of 31.98° ± 0.04° has been measured with a Keyence VR-3200. Second, an artificial (digital) figure is created with a black triangular shape and a nominal angle on both sides of 32°. The artificial figure is treated with the proposed technique.

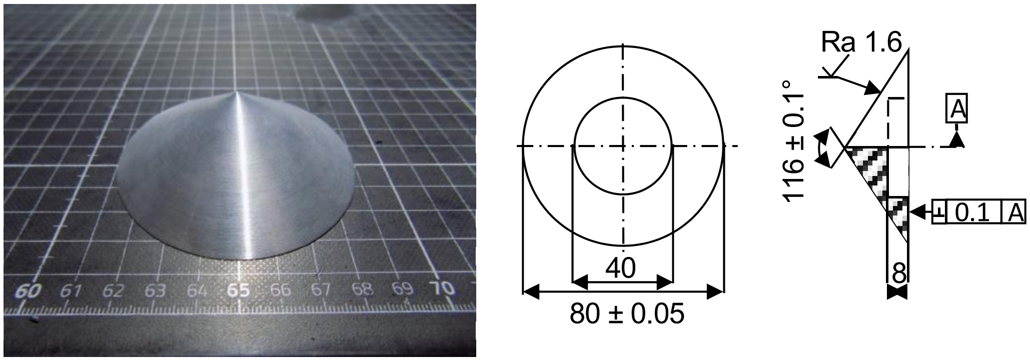

Figure 57: (left) manufactured metallic cone, (right) dimensions of the manufactured metallic cone. Image is taken from [210].

5.3 Results and Discussion

5.3.1 Verification of the proposed algorithm with the artificial image and the reference cone

In terms of the first method, the proposed image processing calculates from the set of images slightly smaller angles for α_L of 31.91° ± 0.01° and α_R of 31.89° ± 0.01° with respect to the measured reference angle of 31.98° ± 0.04°. For the second method, the proposed image processing algorithm is applied to an ideal triangular shape inside an image of the same resolution as the camera's images. Notably, the artificial image was not recorded by the camera. The results state an overall low measurement error of 0.002%, mainly caused by the size of the pixels and the step-like positioning to describe the transition from black edge to white background. A further increase in the artificial image resolution, leading to a decrease in the pixel size, might reduce the error further.

5.3.2 The angle of repose of granular materials

Figure 58 shows the results of the sliding base plate method. Clear intersection points can be found for the measured angles α_L and α_R for the listed samples in chapter 5.1. The intersection point is assumed to align the base plate and the orifice centre perfectly. Therefore, the intersection point is considered to calculate the angle of repose with the horizontal angles as follows: The first angles next to the intersection point are discarded and the average of the remaining angles yields the angle of repose (AOR) θ (Table 9).

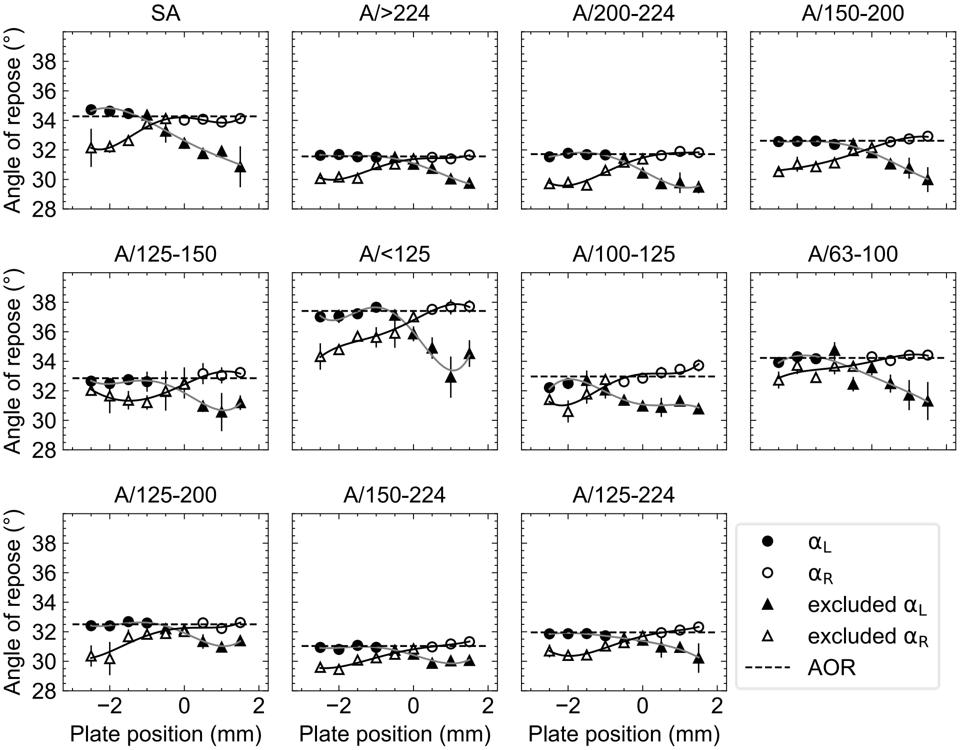

Figure 58: Measured angles in dependency of the plate position with respect to the orifice for a set of hard metal granular materials; displayed bars are the errors and, in some cases, smaller than the marker size.

As a benefit of this experimental method, the calculated angle of repose (AOR) appears insensitive to the centre position with respect to the funnel orifice, as the angles close to the intersection point are omitted (Table 9). It can be seen from Figure 58 that the angles left and right of the intersection are similar, i.e., for decentred base plate positions. Consequently, the proposed procedure can be reduced to a one-sided measurement, significantly reducing the measurement duration.

Table 9: Calculated angle of repose with the average of α_L and α_R. See text for more information.

Sample	AOR θ (°)
SA	34.3 ± 0.3
A/>224	31.6 ± 0.2
A/200-224	31.8 ± 0.2
A/150-200	32.6 ± 0.2
A/125-150	32.9 ± 0.2
A/<125	37.4 ± 0.3
A/100-125	32.9 ± 0.2
A/63-100	34.2 ± 0.1
A/125-200	32.5 ± 0.3
A/150-224	31.0 ± 0.2
A/125-224	32.0 ± 0.2

5.3.3 The influence of the granule properties on the angle of repose

Figure 59 (left) displays the angle of repose (AOR) in function of the d_{50} diameter. A decrease in the d_{50} diameter leads to an increased angle of repose, except for two outliers (SA and A/<125). These findings are in alignment with the study of Zhout et al. [69], Macho et al. [226], and Lumay et al. [58]: smaller diameters yield higher angles of repose. The two outliers, SA and A/<125, can be described by the granule size distribution shown in Figure 48. These two samples contain many fine particles (diameters below 65 µm). It is known [58] that fine particles significantly affect the angle of repose due to interparticle cohesive forces [50].

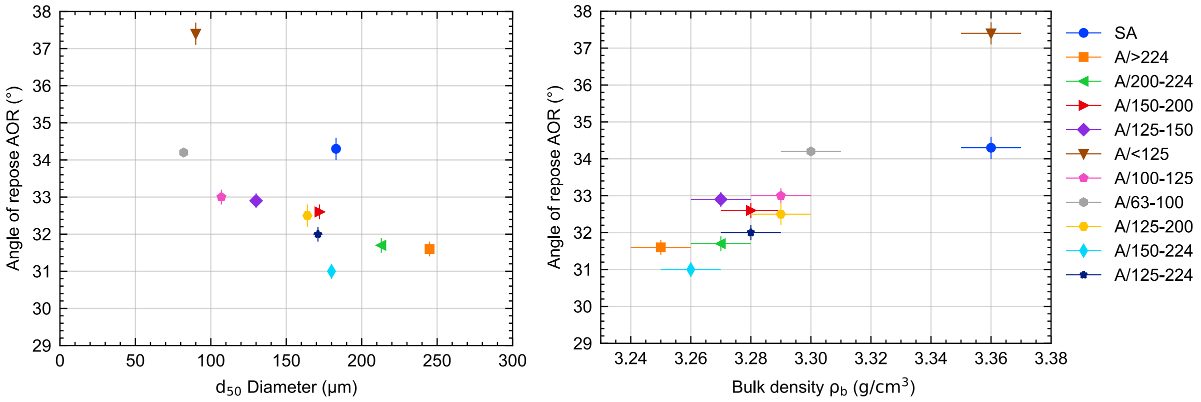

Figure 59: The angle of repose in dependency of the d_{50} diameter from the volumetric size distribution (left), angle of repose in dependency of the measured bulk density (right). Both figures share the same legend.

The size distribution (Figure 48) also influences other characteristic material parameters: the bulk density and the span. Therefore, these two parameters are expected to influence the angle of repose angle systematically. Figure 59 (right) shows the measured angle of repose in function of the bulk density (Table 8). It is visible that lower bulk densities lead tendentially to lower angles of repose. The granule size distribution primarily affects the bulk density, influencing the packing density, which is well understood for samples with bimodal distributions [126,128,227]. Depending on the granule size distribution, the interstitial voids between larger granules are filled, leading to higher bulk densities, explaining the increased densities for SA and A/<125, as these two samples contain very fine particles.

Figure 60 (right) displays the angle of repose in the function of the Hausner ratio. Again, similarities to the span and the bulk density can be found: a higher Hausner ratio leads to an increased repose angle. An experimental study by Santomaso et al. [228] showed a significant difference in the angle of repose of 25° to 41°, whereas the Hausner ratio was nearly constant. Santomaso et al. [228] concluded that the Hausner ratio might not be a suitable criterion, when the value is below 1.10.

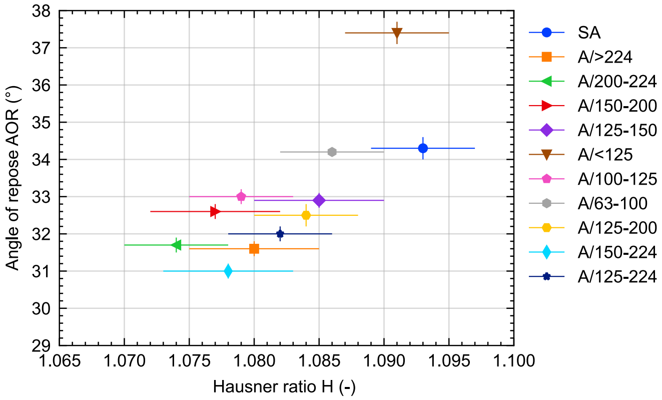

Figure 60: The angle of repose in the dependency of the Hausner ratio H for selected materials from chapter 5.1.

5.4 Influence of the lens distortion

The lens distortion on the measured angle of repose was investigated from images with a two-dimensional triangle in the centre position of the base plate. The lens distortion can be analyzed by performing a calibration, typically done using a chessboard with a known geometry as described in literature [229]. Here, two inputs are needed for the lens distortion calibration: (1) the length of a single square of the chessboard and (2) a set of images from the chessboard taken from different angles and distances [229]. With these inputs, the calibration parameters are determined and considered for every image to acquire an undistorted image. Notably, the calibration parameters depend highly on the quality of considered images.

The angles of both images, namely distorted and undistorted, are compared. The described calibration procedure leads to a slightly higher base angle of 0.1° for the acquired two-dimensional triangle images. However, a single angle measurement's standard deviation is nearly 0.4°. Therefore, the image distortion correction was omitted for the angle of repose determination.

5.5 Limits of the proposed approach

The angle of repose has been measured with granular materials of various mean diameters. Restrictions for the proposed method might occur for very cohesive powders, which form unevenly shaped piles [58]. The shape is influenced by the cohesive nature of the material, which leads to a higher angle of repose [50]. No undercuts or overhangs have been observed for the selected materials. Furthermore, the measurement device is currently limited to materials which can be discharged from the funnel with an orifice diameter of 2 mm, i.e., no clogging effect during the measurement. For very cohesive powders or systems with larger granule mean diameters, funnels with bigger orifice diameters must be considered. A bigger orifice diameter affects the mass flow rate discharged from the funnel and impacts the occurrences of avalanches.

Another aspect is that the pictures are taken at a single camera position. The calculated angle of repose is based on the side surface lines. Influences from covered surfaces are not respected, i.e., piles surface between the base plate and backlight and the surface between the camera and base plate. Measurements with more cameras around the base plate might be interesting, or a single camera rotating around the pile, as performed by others [57][225]. This will be subject of future investigations.

5.6 Summary and Conclusion

The angle of repose was measured for a set of hard metal granular materials. The presented technique proposes a way to determine the angle of repose with dynamic image analysis and the sliding base plate method. The proposed measurement technique can be described as follows: A camera takes images from conical heaps, visible as projections, for various base plate positions. The algorithm evaluates the angle of repose, also considering the surface avalanches. The algorithm is applied to every image taken during the heap formation on the base plate. The findings show that the presented approach, combined with a sliding base plate method, is insensitive to a decentred experimental setup. Furthermore, the relationship between the angle of repose and granule size diameter aligns with findings reported in literature. Therefore, it is assumed that this method is also applicable to other granular materials with similar characteristics.

6 The mass flow rate of hard metal granules in relation to an extended Bond number

This chapter compares the measured angle of repose for selected granular materials listed in chapter 5.1 with the mass flow rate through an orifice. First, the friction coefficient is calculated from the angle of repose. Next, the influence of the attractive forces on the friction coefficient and the mass flow rate is analysed for hard material-based granular systems. The influence on the mass flow rate by attractive forces is discussed in terms of the Beverloo Law and the fitting parameters C and k. Based on the acquired results, an extended granular Bond number is discussed, considering the friction arising not from the attractive forces. The extended granular Bond number might be useful for other powder-like systems. Parts of this chapter have been published [230].

6.1 The attractive forces between granular materials

The attractive forces between the granules influence the granule's flow (see chapters 3.3.3.2 and 3.4). It is essential to understand these influences for any powder and granular system, in our case, hard metal granular materials, as these are composed of different materials. One fundamental property is the Hamaker constant of these components, which influences the overall attractive forces between various granules differently. Two approaches are presented in the following.

6.1.1 The surface energy of the solid materials

The sessile drop technique is used to create drops on solid surfaces, as described in chapter 4.8. Using various liquids, solids' polar and dispersive surface energies are then determined following the OWRK method. Contact angle measurements are typically performed with water and diiodomethane [231,232]. The choice for both liquids lie in their chemical properties. The surface energy of water consists of a polar and a dispersive component, while the diiodomethane has only a dispersive component. Solids' polar and dispersive surface energies are then determined with a linear regression based on equation 59 and two data points representing two liquids (see also Figure 21, chapter 3.4.2). This technique has been used for various solids such as steel and polyurethane [233].

Table 10 shows the measured contact angles for selected liquids and for every solid material. It is important to note that dodecane thoroughly wetted every solid's surface. Therefore, a quantitative measurement of the contact angle is challenging. Nevertheless, the dodecane contact angle is assumed to be 2 ° with a high error.

Table 10: Measured contact angles measured with different liquids on various solids. Errors stem from multiple measurements. Error for dodecane is assumed, see text.

Sample	Deionized water (°)	Glycerine (°)	Dodecane (°)
WC	38 ± 1	33 ± 1	2 ± 2
Co	74 ± 1	74 ± 2	2 ± 2
Paraffin	109 ± 1	98 ± 1	2 ± 2

The measured contact angles from Table 10 are considered for the OWRK method, displayed in Figure 61. It is visible from Figure 61 that tungsten carbide (WC) is higher located in the graph, primarily influenced by its chemical property, i.e., high covalent bonds between atoms. On the other side, the surface energy of the organic binder is comparatively low.

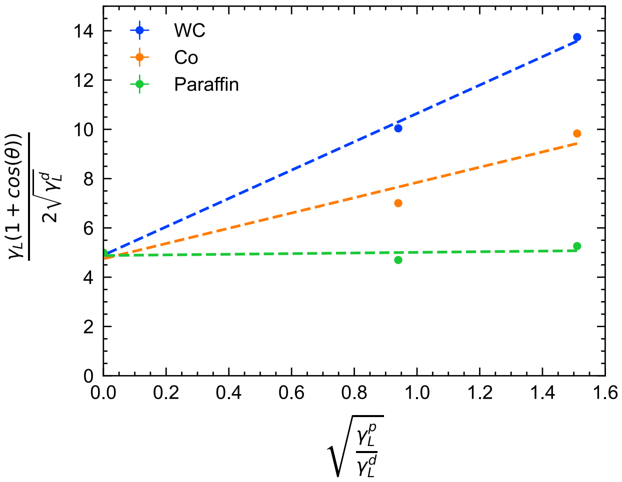

Figure 61: Calculated ratios for the OWRK method based on the measured contact angles for various liquids. The points from left to right are dodecane, glycerine and water. Error on the ordinate is neglected as the literature does not provide this information.

It is important to be reminded that the intersection with the abscissa corresponds to the disperse force $\gamma^{d,}$ and the slope is linked to the polar surface energy γ^{p} of the solid (chapter 3.4.2). The sum of both energies yields the total surface energy of the solid, listed in Table 11. It turns out that WC's measured total surface energy is nearly half compared to the surface energy found by Abd Rahman et al. [234]. The determined surface energy for the paraffin coincides well with the literature [235], as the polar part of paraffin is very low, and the dispersive energy is comparable high. Possible reasons for differing values compared to the literature are the surface quality of the investigated material, i.e., the surface roughness, as discussed by Packham [236]. Another influence arises from the cleansing of the solid surface [235]. In this experimental study, the surface was cleaned with acetone and dry wiped before a measurement.

Table 11: Measured polar and dispersive surface energies for various solids within a granular material. Linear fit according to the OWRK method. The linear fit is weighted according to their errors in the software origin.

Sample	Polar surface energy σ^p (mJ/m^2)	Dispersive surface energy σ^d (mJ/m^2)	Total surface energy σ (mJ/m^2)
WC	33 ± 2	25 ± 2	58 ± 3
Co	9 ± 5	22 ± 8	31 ± 9
Paraffin	0.1 ± 0.1	24 ± 4	24 ± 4

The measured dispersive surface energies σ^d from Table 11 are used to calculate the Hamaker constants A of WC, Co and paraffin, following equation 47 (chapter 3.4.1), where the cut-off distance D_0 is 0.165 nm [147]. It is important to be reminded that the granular materials from chapter 5.1 are composed of these three different materials. Israelachvili [147] describes the calculation of an effective Hamaker constant of two various materials through a geometric mean of the component's Hamaker constants. In the case of hard metal granules composed of three different materials, the multi-component Hamaker constant A_{123} follows:

$$A_{123} = \sqrt[3]{A_1 A_2 A_3} \qquad 91$$

where the index numbers 1, 2 and 3 correspond to the Hamaker constant of the individual materials WC, Co and Paraffin, respectively. This approach was applied by Capece et al. [154][237] for two-component systems created from mixing bulk materials, such as pharmaceutical and microcrystalline cellulose powders.

Equation 91 assumes that the individual Hamaker constants are equally distributed inside a granule. The resulting attractive forces between two granules strongly depend on the materials distributed on the surface of both granules in contact. Capece et al. [252] addressed this topic, considering the fractional surface area covered by the individual components on the surface of granules. In this approach, the Hamaker constant is weighted with factors v_x inside the geometric mean to acquire a multi-component Hamaker constant $\bar{A}_{123}$ influenced by the volumetric parts within a single granule, following:

$$\bar{A}_{123} = \sqrt[3]{(v_1 A_1)(v_2 A_2)(v_3 A_3)} \qquad 92$$

where v_1, v_2 and v_3 represent the volumetric part of each ingredient. Using equation 92, the calculated multi-component Hamaker constant yields (1.3 ± 0.1) 10^{-20} J. The multi-component Hamaker constant approximates a three-component system, i.e. for a single granule, and depends on the dispersive surface energies acquired from the contact angle measurements.

A problem arises from the assumption that the contact angle of dodecane of all solid materials is close to zero. According to Chibowski and Perea-Carpio [238], when a liquid's contact angle is nearly zero, the solid's dispersive surface energy is in the range of the surface tension of the liquid, which is a misleading conclusion. In other words, any liquid leading to a contact angle of (nearly) 0° and $\sqrt{\gamma_L^P/\gamma_L^D} = 0$ yields directly the surface energy of the solid. However, this can occur for various liquid materials with different surface energies. Considering this point, when omitting the dodecane in Figure 61, the multi-component Hamaker constant is nearly half, in the order of 0.6 10^{-20} J.

Determining the Hamaker constant based on the contact angle is challenging, and the provided approximation might not be suitable to describe precisely the Hamaker constant of a multi-component system. More Investigation is needed to confirm this approach. A more suitable way is to calculate a multi-component Hamaker constant from measured attractive forces between granules inside an atomic force microscopy (AFM).

6.1.2 Atomic force microscopy

Atomic force microscopy (AFM) (see chapter 4.11) is used to access the attraction between the granular materials directly. The preparation of the cantilever and the measurement conditions are described in chapter 4.11. Figure 62 displays two prepared cantilevers with different granule sizes from the unsieved sample SA. The AFM measurements are concentrated on the unsieved sample SA, as every other granular system (A1.1 to A3.1) comprises the same amount of tungsten carbide, cobalt and organic binder.

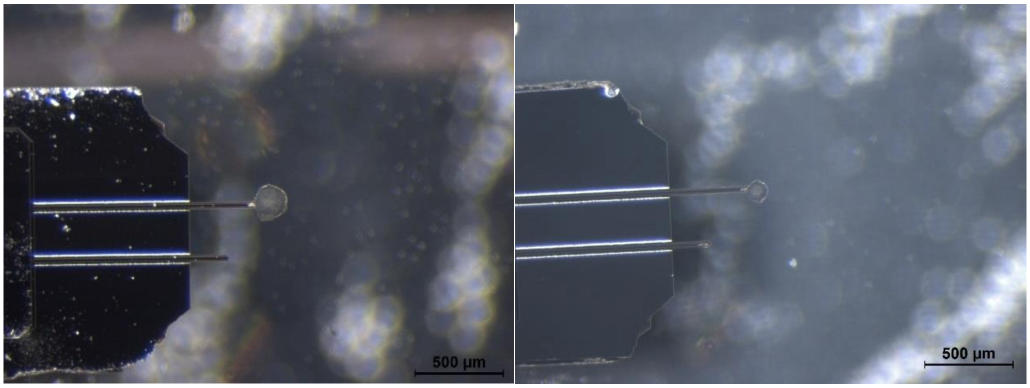

Figure 62: The images show an all-in-one cantilever from BudgetSensors with the attached granules on two cantilevers, 40x magnification.

The attractive forces are measured between a flat surface and a prepared cantilever. One of the reasons for this approach is the prevention of granule movement when the attractive forces between two granules act. Secondly, the attractive forces between granules are granule size dependent (see chapter 3.4.1). Therefore, it is likely in a set of different granule sizes that the attractive forces are measured between two different granules of different sizes, leading to a challenging approach, as both granule diameters have to be known. In this study, the flat surface is first created by compressing the granular material. Notably, the flat surface might be slightly uneven, as the applied pressure on the granules affects the surface topography of the flat surface. In the next step, the cantilever with the attached granule approaches the surface in a nitrogen atmosphere. The cantilever has a nominal resonance frequency of 15 kHz and a nominal stiffness constant of 0.2 N/m. Several measurements on twenty different locations are performed in contact mode. Finally, the maximal pull-off force is calculated with the maximal laser deflection following equation 87 (chapter 4.11).

The Hamaker constant A for the granular material, composed of a specific amount of WC, Co and organic binder, is then calculated as presented by Israelachvili [147] based on the pull-off force F acting over a distance D between a spherical object of diameter d_p and a planar surface, following equation 93:

$$\mathrm{A} = \frac{6FD^2}{\left({}^{d_p}/_2\right)} \qquad 93$$

The measurement of the pull-off forces with two different granule sizes (Figure 62) of 187 ± 2 µm and 113 ± 1 µm lead to two different Hamaker constants of (1.5 ± 0.2) 10^{-22} J and (3.2 ± 0.7) 10^{-22} J. These differences and the overall magnitude (10^{-22} J) arise mainly from the interplay between the surface roughness and the granule diameter. Other influences come from the deviation of the nominal cantilever stiffness given by the manufacturer, the multicomponent mixture of WC, Co and organic and a difference in the location of both granules' positions on each cantilever. Consequently, it is assumed that the Hamaker constant for the multi-component system is in the order of 2 10^{-22} J with an error of 100 %. This 2 10^{-22} J value is used to calculate the van der Waals forces in the determination of the granular Bond number.

6.1.3 The granular Bond number

The granular Bond number Bo_g is calculated following equation 60. Here, the cohesive forces arise solely from the van der Waals forces and are assumed to be the dominant attractive forces. Other influences, such as surface roughness, are neglected. The Hamaker constant (see previous chapter) is considered for the van der Waals forces between two spheres of diameter d_1 and d_2. Both spherical granule diameters are identical and expressed by the Sauter mean diameter $d_{[3,2]}$, describing the mean diameter of granular systems [154,155].

The gravitational force F_g is calculated based on equation 61 with the gravitational acceleration g and the mass m of a single granule. The mass is calculated with a granule's spherical volume and the multi-component system's density. Consequently, the measured pycnometer density ρ_{pyc} from Table 8 and the Sauter mean diameter $d_{[3,2]}$ is used to calculate the mass m, assuming that the granular materials are dense (no intragranular porosity). The ratio between the van der Waals forces and the gravitational force yields the granular Bond number and is listed for all granular systems in Table 12.

Table 12: Calculated granular Bond numbers for selected granular material from chapter 5; the error of the Bond number is 100%; see text in chapter 6.1.2

Sample	**Granular Bond number Bo_g (-)**
SA	0.04
A/>224	0.02
A/200-224	0.02
A/150-200	0.03
A/125-150	0.06
A/<125	0.30
A/100-125	0.08
A/63-100	0.14
A/125-200	0.03
A/150-224	0.03
A/125-224	0.03

6.2 Results and Discussion

6.2.1 The friction coefficient and particle size

The experimental setup presented in chapter 5.2 has been used to determine the angle of repose. These angles of repose are used to calculate the friction coefficient for each granular system of Table 9 with equation 94:

$$\mu = \tan(\theta) \tag{94}$$

and are listed in Table 13.

Table 13: Friction coefficients for selected hard metal granules, calculated with the angle of repose.

Sample	**Friction coefficient μ (-)**
SA	0.681 ± 0.008
A/>224	0.614 ± 0.005
A/200-224	0.619 ± 0.005
A/150-200	0.640 ± 0.005
A/125-150	0.645 ± 0.005
A/<125	0.765 ± 0.008
A/100-125	0.649 ± 0.005
A/63-100	0.680 ± 0.003
A/125-200	0.637 ± 0.007
A/150-224	0.602 ± 0.005
A/125-224	0.623 ± 0.005

Figure 63 shows the calculated friction coefficient from Table 13 in function of the Sauter mean diameter. As the angle of repose is linked to the granule diameter, an identical relationship can be found for the friction coefficient, aligning with the outcome of Lumay et al. [58], who reported a significant increase in the angle of repose θ for very small particles lower than 100 µm.

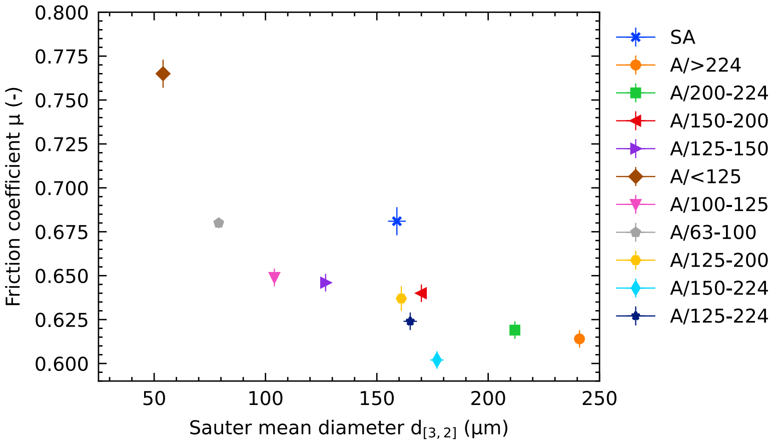

Figure 63: The friction coefficient μ in the function of the Sauter mean diameter $d_{[3,2]}$. Some error bars are smaller than the marker size.

6.2.2 Relationship between the friction coefficient and the granular Bond number

Figure 64 shows the friction coefficient and the granular Bond number (logarithmic). The results follow a linear relationship between the measured friction coefficient μ and the granular Bond number Bo_g, which can also be seen from the inset in Figure 64. The dashed line is a linear fit following:

$$\mu = \mu_{eff,\infty} + const * Bo_g \qquad 95$$

where $\mu_{eff,\infty} = 0.6$. The standard sample SA contains all granule sizes, leading to a broader size distribution than the other samples (A/>224 to A/125-224) and is therefore omitted for the fit. Elekes and Parteli [50] numerically investigated the friction coefficient change for a wide range of granular Bond numbers between 10^{-6} and 10^{5}. Their investigation shows a significant increase in the friction coefficient for granular Bond numbers above 10^{2}. The calculated granular Bond numbers for hard metal granules from Table 12 lie between 10^{2} and 10^{0} (see Figure 64). Consequently, the presented friction coefficients and granular Bond numbers in Figure 64 display only a small range of the friction coefficients shown in [50]. Within the presented limits, the findings agree with the results of Elekes and Parteli [50].

Besides this, Elekes and Parteli [50] presented a significant decrease in the attractive forces with increasing particle size, i.e. the granular Bond number decreases, yielding an effective infinite friction coefficient $\mu_{eff,\infty}$ for granular Bond numbers lower than 10^{-1}. Their findings showed that the friction coefficient remains nearly constant below this granular Bond number. A similar trend can be observed for the experimental data in Figure 64, expressed by the linear fit (Equation 95), also leading to an effective infinite friction coefficient $\mu_{eff,\infty}$. The magnitude of $\mu_{eff,\infty}$ is primarily affected by the granule composition, such as the type and amount of the tungsten carbide or organic binder.

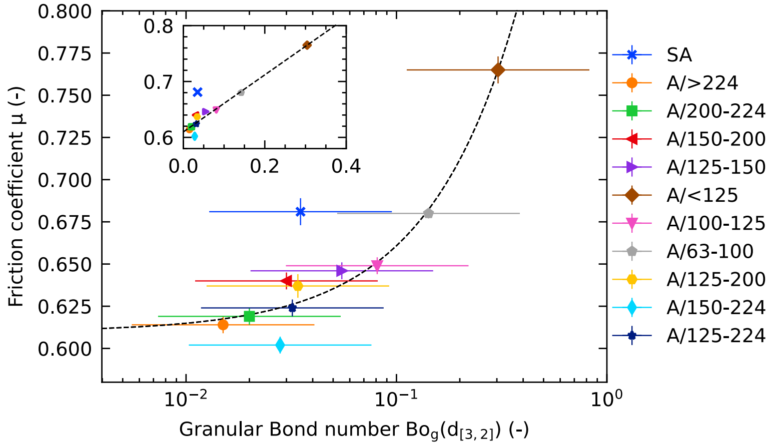

Figure 64: The friction coefficient μ in the function of the granular Bond number $Bo_g(d_{[3,2]})$. The inset shows the same data with a linear scale. The error bars are not present in the inset.

6.2.3 The mass flow rate of granular materials in function of the granular Bond number

Figure 65 displays the mass flow rate $\dot{m}$, experimentally measured with an orifice diameter of 5 mm, in function of the granular Bond number Bo_g. Similar trends were observed for other orifice sizes, i.e. 2 to 8 mm. Figure 65 displays an increasing mass flow rate (A/>224, A/200-224, A/150-224, A/150-200, A/125-224, A/125-200, on the left side), followed by a decrease in the mass flow rate (A/125-150, A/100-125, A/63-100, A/<125) with increasing granular Bond number. It is essential to be reminded that the decrease in the granular mean diameter mainly causes the increase in the granular Bond number. Moreover, the two data sets A/>224 to A/125-200 and A/125-150 to A/<125) are fitted with two power laws (Figure 65). The intersection point of both fits represents the granular Bond number at which a maximal mass flow rate can be reached for the selected granule system.

Two opposing relationships can describe the existence of a maximal mass flow rate. When the granule diameter decreases (increasing the granular Bond number), the mass flow rate rises for a specific orifice diameter D (equation 35, $\dot{m} \sim \left(D\text{-}kd_p\right)^{2.5}$). With a further decrease of the granule diameter, the influence of attractive forces increases until these forces become dominant over the gravitational force (compare equations 46 and 60). This effect increases the effective granule diameter ($d_{eff} = kd_p$) for a given orifice size D caused by the possible formation of agglomerates, leading to a higher hindrance of free flow. A similar finding of the interplay of granule size and the attraction forces, expressed by the granular Bond number, was concluded by Lu et al. [9].

The change of the AOR θ with respect to the granular Bond number is more significant (nearly 20%, Table 9) than the overall difference in the mass flow rate for the selected granules (nearly 10 %, Figure 65). This difference arises from the fact that the gravitational forces in the angle of repose measurements act mainly as a downhill force, and consequently, the weak attractive forces have a higher impact. Furthermore, in the mass flow rate measurements, the gravitational forces act vertically towards the orifice, and the attractive forces between granules have a less pronounced impact.

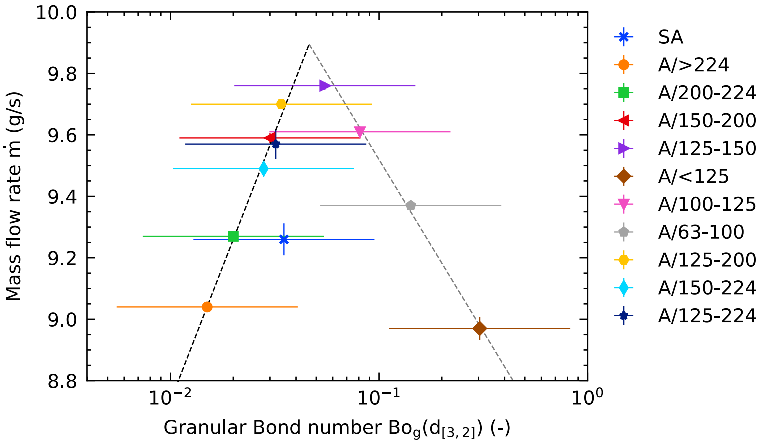

Figure 65: The mass flow rate $\dot{m}$, measured with an orifice diameter of 5 mm, in the function of the granular Bond number $Bo_g(d_{[3,2]})$. The dashed lines are power fits. Error bars might not be visible when smaller than the marker size.

6.2.4 The mass flow rate and the angle of repose

Figure 66 shows the mass flow rate $\dot{m}$, measured with an orifice diameter of 5 mm as a function of the angle of repose θ from Table 9. The values were categorized equally, as used in Figure 65. The dashed lines in Figure 66 represent the mass flow rate in function of the AOR θ calculated from the trend lines in Figure 65 and a linear fit created with the data from Table 12 and Table 13 ($\theta = f(Bo_g)$). This approach has been applied to both data categories (Bo_g > intersection point and Bo_g < intersection point). The maximal mass flow rate is represented by the intersection point of the dashed lines at an AOR θ of nearly 32.4°.

Generally, low AORs describe good flowability. However, Figure 66 shows that very low AORs fail to have high mass flow rates. As discussed in the previous chapter (6.2.3), the interparticle forces and the diameter of the granules influence the mass flow rate.

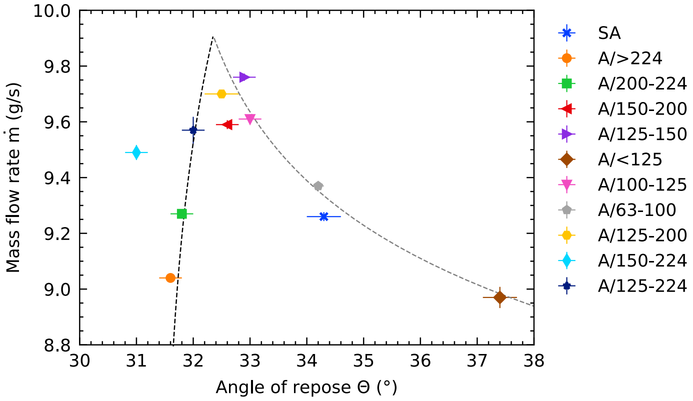

Figure 66: The mass flow rate $\dot{m}$ measured with an orifice diameter of 5 mm as a function of the AOR for selected granular materials.

6.2.5 The extended granular Bond number

Figure 67 shows a schematic comparison of Figure 64, Figure 65 and Figure 66 to show the two contradicting phenomena impacting the mass flow rate. First, Figure 67 (a) shows that as the AOR increases, the mass flow rate increases to the maximal mass flow rate $\dot{m}_{max}$ until AOR θ_t. This effect is connected to the decreasing granule diameter and increasing granular Bond number. Beyond AOR θ_t, the attractive forces (or any other forces) negatively affect the free flow of the granules, expressed by a decreasing mass flow rate as AOR θ increases (Figure 67, a). A similar relationship exists for the mass flow rate $\dot{m}$ and the granular Bond number, illustrated in Figure 67 (b).

As previously stated, the granular Bond number describes the ratio between the attractive forces (here: solely the van der Waals forces) and gravitational force. The maxima location in Figure 67 (a) (also Figure 66) and Figure 67 (b) (also Figure 65) is affected by the interplay between the increasing hindrance of the flow of granules and the decreasing granule diameter. The hindrance of the flow can arise from the van der Waals forces between the granules or geometrical restrictions, such as satellites or dust on granule surfaces or non-spherical granules and other aspects like humidity, etc. In addition, Lu et al. [9] and Anand et al. [88] have investigated the effect of cohesion, surface roughness and particle size, negatively affecting the flow.

Based on Figure 67, an extended granular Bond number is proposed, such as $Bo_{ex} = \delta\, Bo_{g}$, to acquire $Bo_{ex} = 1$ at the highest mass flow rate $\dot{m}_{max}$ location. This scaling will also impact the relationship between the AOR θ and the granular Bond number. Considering the extended Bond number Bo_{ex}, the data points in Figure 67 (c) will be shifted, while the effective infinite friction coefficient $\mu_{eff,\infty}$ remains unaffected. The reason is that $\mu_{eff,\infty}$ (and also the parameters k and C in the Beverloo law, equation 35) include all impacting parameters restraining the flow of granules through an orifice, e.g., the attractive forces. Consequently, the extended Bond number Bo_{ex} and the effective infinite friction coefficient $\mu_{eff,\infty}$ relate to a similar assembly of parameters impacting the flow granules.

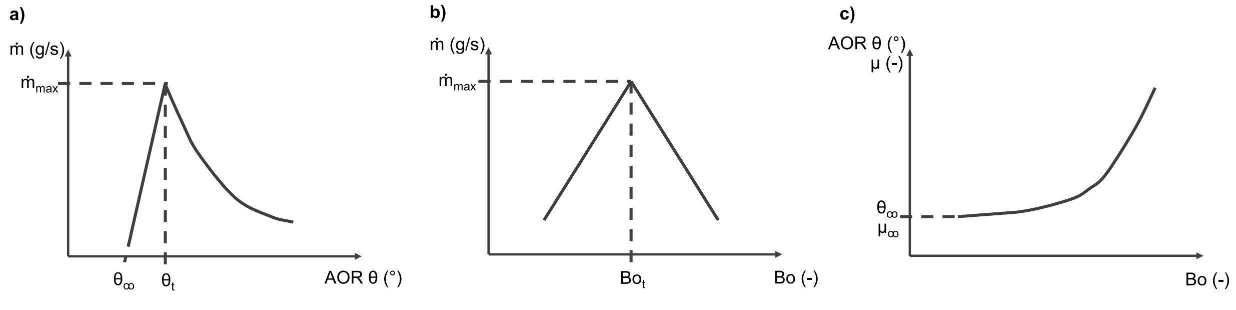

Figure 67: Schematic results from a) Figure 66, b) Figure 65 and c) Figure 64. Image is taken from [230].

6.3 Summary and Conclusion

The relationship between the angle of repose and the mass flow rate with different sizes of hard metal granules has been investigated. Various approaches to determine the Hamaker constant of the multi-component system are presented. Directly measuring the attractive forces with an AFM is a suitable technique. The Hamaker constant was determined from force measurements between a spherical granule attached to a cantilever and a flat surface. It was then used to calculate the granular Bond number. The findings show that the flow of granular materials is affected by two main parameters: the infinite friction coefficient and the granular Bond number. The friction coefficient contains all information that influences the flow of granules, such as the attractive forces arising from van der Waals forces or surface roughness effects. An extended granular Bond number Bo_{ex}, to acquire $Bo_{ex} = 1$, was proposed to consider these influences. Supplementary granular materials with differing chemical compositions have to be studied to investigate the application of the extended granular Bond number.

7 Rheological properties of hard metal granular materials

Rheological measurements provide insight into the macroscopic friction within a bed of granules under shear. The focus of this study lies on two different measurement techniques: rheological measurements with (1) a cup and vane as well as (2) a cup and plate combination. In terms of a cup and vane combination, various 3D-printed vane geometries have been created and tested with different granular materials. The influence of the vane height and diameter on the torque is presented. The effect of the immersion depth on the torque is investigated.

Cup-plate measurements have been performed to study the friction under shear. The shear stresses to introduce the flow are investigated for several normal pressures. The ratio between the shear stress and the normal pressure yields the friction coefficient, considered for the μ(I) rheology. The friction coefficient is studied for a range of shear rates with several hard metal granular materials. Furthermore, amplitude and frequency sweep tests are performed to study the viscoelastic properties of granular materials.

7.1 Methodology

7.1.1 Rotor-Cup measurements

Granular material behaves like a solid in a static state and like a liquid beyond the yield stress. It is envisaged to shear granular material with a rotor while submerged inside the bed of granules. The measured torque is directly proportional to the size of the rotor and the material inside the cylindrical cup. Various rotor geometries are created with a 3D printer using polylactic acid (PLA) filaments (chapter 4.12). The rotors are clamped on a 35 mm plate geometry (PP35 Ti) from Thermo Fisher. A metallic cup with a diameter of nearly 60 mm is used. A polymer insert with an inner diameter of nominal 40 mm is created with the 3D printer (chapter 4.12) to reduce the necessary material for each measurement (Figure 68).

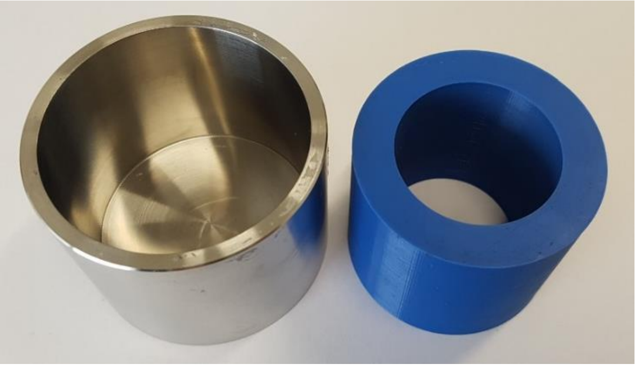

Figure 68: Metallic cup and the 3D printed insert.

Measurements with various rotor geometries are performed. An experimental study with various 3D-printed vane geometries revealed that material flow is mainly influenced by the number of rotor edges creating the circular perimeter and not by the internal rotor structure [239]. In this study, the amount of rotor blades is set to eight with a blade thickness h of 2 mm. The 3D-printed rotors and the plate geometry are clamped, followed by a calibration of the rotor inertia.

Several rotors have been constructed, varying in height H and diameter D. the nomenclature of the rotors is as follow: RCDxHy, where x and y take the corresponding lengths of height H and diameter D (RC denotes Rotor-Cup). For instance, a rotor of diameter 20 mm and height 10 mm has the nomenclature: RCD20H10.

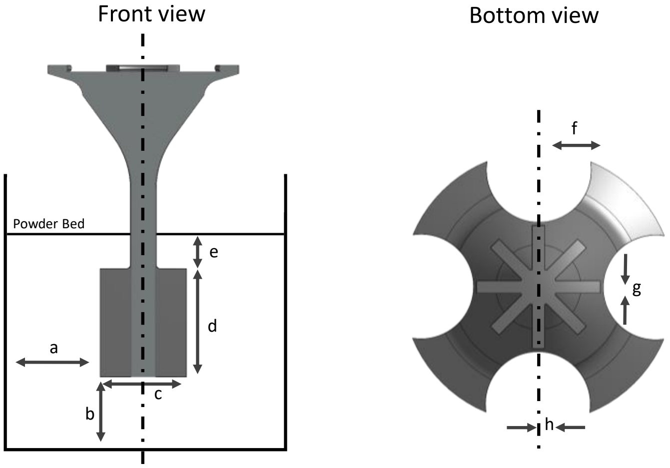

Figure 69: Schematic dimensions of a rotor geometry.

The necessary material to completely immerse the rotor depends on the granular material's bulk density and the rotor's position inside the cup. The mass for a measurement is estimated with equation 96. Here, a is the distance between the rotor blades and the inner cup wall, and b is the gap between the rotor's lower edge and the cup's bottom. Furthermore, c is the diameter, and d is the height of the rotor. The submerged level, i.e. the additional distance between the upper rotor edge and powder bed surface, is described by e. The rotor needs a critical thickness to withstand the torque inside the powder bed. Here, the rotor blade length is f and thickness g. The blades are attached to the cylindrical shaft, defined by the radius h. Furthermore, n is the number of rotor blades used for the measurements (here: eight). When the powder bed is aligned with the upper rotor edge, the powder bed above the rotor is zero, i.e. the variable e equals zero in equation 96.

$$m \approx \frac{\left(2\pi\,(\frac{c}{2}+a)^2\,(b+d+e)\right) - \,(\pi h^2 + nfg)}{\rho_b} \tag{96}$$

The measurement preparation is challenging. An appropriate preparation technique is to fill the cup after the rotor is placed in the desired measuring position (gap width). This approach is considered for any performed measurement. It is important to mention that the calculated mass from equation 96 is estimated to reach the set filling height. The final filling height is linked to the bulk density of the bulk material and depends, for instance, on the filling procedure inside the cup. A prehearing step with a rotation speed of 1/min is applied to the powder bed to suppress any influence of the filling process and guarantee the same initial conditions for all measurements.

All measurements are performed in controlled deformation (CD) mode. Preliminary tests showed that controlled shear stress (CS) measurements lead to unstable data, as the rotation speed is highly increased to reach the desired shear stresses. In any performed CS measurement, destruction of granules has been observed; therefore, controlled shear stress (CS) tests are omitted.

Measurements have been performed at different shear rates ranging between 10^{-5} to 100 to study different flow regimes with hard metal granular systems listed in chapter 5.1. These shear rates are in a similar range of measurements reported in literature for yield stress fluids [239]. Granular materials also exhibit yield stress characteristics (see chapter 3.5.2), which depend on the granule properties. The parameters are selected based on preliminary measurements for a single rotor geometry: RCD20H25. Further information can be found in the following paragraphs. The gap width b and the immersion depth e are 5 mm. The final immersion depth depends on the granule characteristic, calculated with equation 96. The distance between the perimeter of the rotor and the wall is 10 mm. Notably, the shear rate $\dot{\gamma}$ is defined as the velocity over the distance between two plates [240]. In this case, the velocity at the outer rotor perimeter is in relation to the distance between the rotor edge and the wall of the cup. The applied shear rate introduces stresses to move a granule layer, also called a shear band in granular materials, with a specific depth (shear zone) next to the rotor. The introduced stresses are transferred intergranularly through contact points. The exact velocity and stress gradient inside the granular bed towards the wall is unknown. This shear zone can be smaller than the overall gap width, as visualized, for instance, for yield stress fluids [239]. Hence, the presented sheared rate can be interpreted as an apparent shear rate. For simplicity reasons, the apparent shear rate is called the shear rate for all measurements, including plate-cup measurements.

7.1.2 Plate-Cup measurements

Tests with a plate geometry PP35 Ti (L07015, 35 mm diameter, flat) are performed with the Haake Mars II rotational rheometer from Thermo Fisher (chapter 4.7). A granule bed is created inside a circular cup with an insert of 35.5 mm and 10 mm high (Figure 70). The insert is inside a metallic cup. Preliminary measurements showed that the contact of the outer plate edge and inner side wall significantly influences the torque. Therefore, a nominal gap of 0.25 mm, between the plate's perimeter and the insert's inner wall was selected. Scraping with a ruler along the cup's surface creates a flat, even powder surface. The bulk density of the granule impacts the mass inside the cup. Two different kinds of measurements have been performed: (1) rotary plate measurements with different normal pressures, similar to Schulze [180] and (2) amplitude and frequency sweep tests.

Figure 70: Metallic cup and the 3D printed insert.

In both cases, the intergranular friction is in this research's interest, which is achieved by attaching granular material on the lower surface of the circular plate geometry with a double-sided adhesive tape (3M 9088 PET, double coated tape, extra sticky). The tape size of 38 mm is selected to cover the lower surface completely, preventing gaps between several tape sheets. The zero gap is set with the attached tape and cover. The cover thickness of the tape is in the order of 0.1 mm. The inertia of the plate and the tape is determined before each measurement (without attached granules). The reason was to prevent a detaching of granules during the inertia determination when using a plate-tape-granules combination. The error in inertia determination without attached granules is less important than the total coverage of the tape with granules. Preliminary tests with controlled shear stress (CS) showed similar problems to rotor-cup measurements. Therefore, measurements with controlled shear stress (CS) are omitted. Another aspect is the densification of the granule bed over the measurement time. With a fixed gap, the plate loses contact with the granule bed. Consequently, the measurements are performed with a force control (FC) to maintain the selected normal force, changing the gap size within a measurement. The selected force depends on the performed measurement.

Shear measurements consist of a preshearing step as described by Schulze [96]. The granule bed is typically sheared under load to acquire an over-consolidated bed. Preliminary measurements showed signs of granule destruction beyond a normal force of 6N. Hence, the pre-shearing force is set to 5 N, followed by shearing at normal forces between 0.5 and 2 N. Like rotor measurements from chapter 7.1.1, the shear rate $\dot{\gamma}$ is calculated with the plate's rotation velocity and the corresponding gap width between the plate and the bottom of the cup.

7.2 Results and Discussion

7.2.1 Application of 3D-printed rotor geometries

Applying 3D-printed rotor geometries offers fast and flexible opportunities to measure rheological properties over a range of shear rates. The shear rates in this study are small compared to other measurements, such as capillary measurements with inkjet inks [241], exceeding shear rates of 10^4. Regarding granular materials, testing a broad range of measurement parameters is essential to understand influences on the measured torque, for instance, duration of measurement t and shear rate $\dot{\gamma}$.

Tests with a rotor geometry (RCD20H25) are performed inside an immersed powder bed with different rotation speeds. The investigated material is the unsieved sample SA, consisting of every granular material from chapter 5.1. Figure 71 (left) displays the measured torque as a function of time for two different shear rates.

As time advances, the torque for both displayed shear rates increases and reaches a similar torque level, which appears to be constant. However, when shearing a granular material, it is expected that once overcoming the interlocking of single granules (yield) through local dilatation, the flow of granules begins, followed by a torque decrease, as found e.g. for TiO_2 pigment suspensions [242]. The constant torque level indicates that the material is sheared in an under-consolidated state, where the bulk density preferably increases locally until reaching a steady state [96]. Inside the shear zone of the steady-state flow exists a microscopic equilibrium between local dilatation (increase in torque) and contraction (decrease in torque) [243]. This interplay can be seen in the small fluctuations of the measured torque in the steady state regime (Figure 71, left, 0.08 s^{-1}).

Such a torque decline is absent in Figure 71 (left), even at very long measurement times. The densification and rearrangement of granules near the rotor surface appear absent, and only the interplay between microscopic dilatation and contraction exists, implying that the system is unaffected by the applied shear rates ($\dot{\gamma} < 0.8\ s^{-1}$) once the maximal torque level is reached. However, a change in the shear rate affects the time needed to reach the torque level: The higher the shear rate, the faster the torque level is reached. This observation also aligns with the literature [174], as the time of the granule shear deformation is inversely proportional to the shear rate ($t_{\dot{\gamma}} = 1/\dot{\gamma}$).

The same can be observed for the finest granular materials <125 from 5.1 (Figure 71, right). Considering both granular systems in Figure 71, the granule size negatively affects the torque increase towards the constant torque level. A granular system with a smaller diameter requires more time to reach the maximal torque. However, this outcome can not be entirely explained by the granular diameter, as other aspects, such as the bulk density or confinement pressure near the rotor surface, must be considered [174].

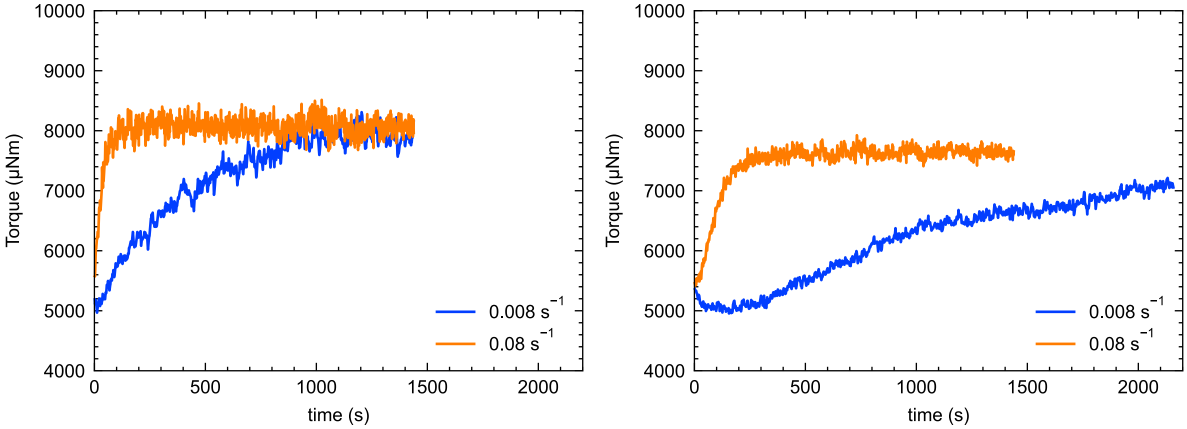

Figure 71: Torque-time dependency for two different shear rates and granules: sample SA (left) and A/<125 (right). The gap width b is set to 5 mm, with no material on the rotor (e= 0 mm).

7.2.1.1 Influence of the mass above the rotor on the measured torque

Tests at different gap widths b have been performed inside a cup filled with the unsieved sample SA (chapter 5.1) at low shear rates of 0.05 to 0.5 s^{-1}. Figure 72 presents the torque at a shear rate of 0.5 s^{-1} for a rotor geometry of 20 mm in diameter and 25 mm in height. The measurements started with a gap of 1 mm. The rotor is entirely immersed inside a powder bed of 400 g inside a metallic cup with an inner diameter of nearly 60 mm.

Figure 72 presents a linear decrease of the measured torque when the gap width increases. This decrease was also observed for any other shear rate between 0.05 and 0.5 s^{-1}. The results coincide with a similar observation of Daniel et al. [196] and Poloski et al. [198], showing that the torque linearly increases as the gap width decreases. The main reason for the decrease in torque is the shrinking lithostatic pressure (normal pressure) acting on all sides of the rotor as the rotor exits the granules bed.

Besides the rotor surface, the rotor shaft is in contact with the granular material during rotation, impacting the measured torque. The contact surface of the shaft with the material is directly linked to the powder bed level and immersion depth, which reduces when the gap width increases. The shaft contribution decays to zero when the powder bed level aligns with the upper edge of the rotor blades. The influence of the shaft on the measured torque is significant for immersed measurements, which can contribute up to 25 % of the total measured torque [196].

The experimental study by Daniel et al. [196] showed that the measured torque deviates from the linear fit as the immersion depth increases, explained by a pressure saturation above the rotor, also known as the Janssen effect (see chapter 3.3.2.1). This deviation is absent in Figure 72 as the selected gaps and the powder bed height are smaller than in Daniel et al.'s [196] experimental study. Notably, the Janssen effect is bulk material and wall friction dependent, which might be visible in Figure 72 when the mass inside the cup increases, i.e., above 400 g.

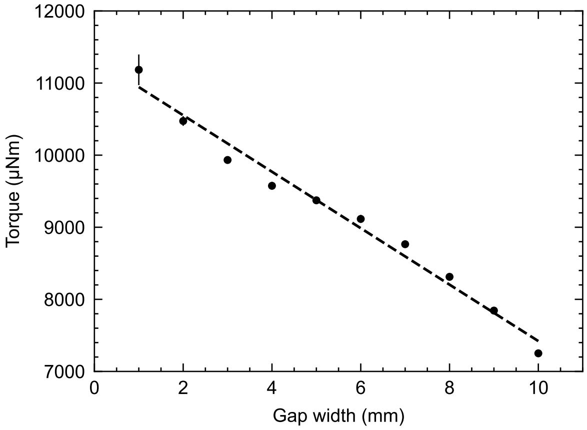

Figure 72: Influence of the gap width b (distance between the bottom and lower rotor edge) for a mass of 400 g inside the cup with sample SA at a shear rate of 0.5 s^{-1}, Rotor: RCD20H25, the linear fit is for guidance, three measurements per gap width, most error bars are smaller than the marker size

7.2.1.2 Influence of the gap width and a changing powder bed level

Measurements at various gap widths are performed in analogy to the previous chapter. In addition, the powder bed level is adapted to the rotor's upper edge to reduce the shaft's effect, i.e. zero contribution by the shaft on the measured torque. In other words, the powder bed level equals the upper rotor edge. Adding more granules to the metallic cup following equation 96 (chapter 7.1.1) compensates for the lack of granular material with an increasing gap width. Assuming no mass is on top of the rotor, the measured torque is impacted solely by the rotor's side and bottom surfaces. When the missing volume with increasing gap width is compensated by adding mass, the torque magnitude is expected to be identical and independent of the gap width as long as no other effects are present.

Figure 73 displays the average torques for various gap widths of granule sample SA. The measured torques at all gap widths are similar, approving the initial assumption. However, the torques fluctuate between 6500 and 7200 µNm. The measured toques are reproducible for a given gap width (marker size bigger than error bars). A possible reason for the spread in the measured torques might be the measurement preparation itself, e.g., filling procedure to equalize the missing volume with granules and granule distribution, i.e. uneven powder bed surface resulting in a density difference along the rotor height. The preparation effect was diminished by applying a constant shear rate of 5 s^{-1}, which might not have been compelling enough for this granular system.

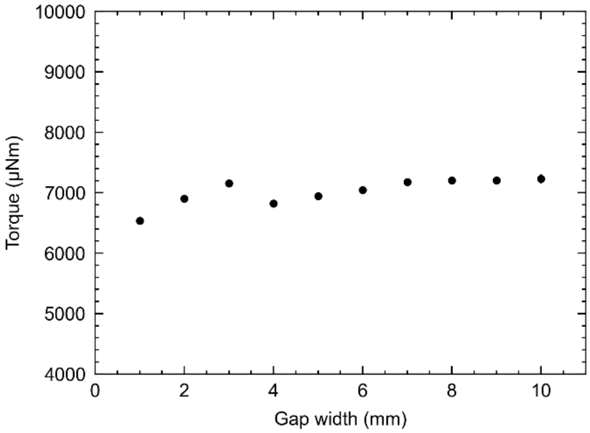

Figure 73: Torque measurements with the rotor RCD20H25 at various gap widths and a shear rate of 0.5 s^{-1}, data points represent an average of three measurements, error bars are smaller than the marker size.

7.2.1.3 Influence of the rotor geometry

Measurements with various rotor diameters D and heights H are investigated with granule sample SA at a constant gap width of 5mm. The cup size is reduced by inserting a 3D-printed insert into the metallic cup having an inner diameter of 40 mm. The shear stresses near the rotor surface for all rotor geometries are calculated as follows:

$$\tau = \frac{T}{\left(\frac{1}{3} + \frac{2H}{D}\right) \cdot \left(\frac{\pi D^3}{4}\right)} \qquad 97$$

The presented equation 97 is an adapted version of equation 75 by Ngyuen and Boger [189], assuming that the lower-end contributions are similar to the upper-end (top) surface contributions when a rotor is entirely immersed. The powder bed volume is aligned with the upper rotor edge in this experiment. Therefore, the top-end contributions are omitted in equation 97.

Figure 74 (left) displays the measured torque with a changing diameter D with constant height H. Equation 97 implies that the torque increases quadratically (D^2) with the rotor sides surface and cubically (D^3) with the lower-end surface. In the case that the rotor diameter D decreases to zero, the measured torque vanishes to zero. The measured data in Figure 74 (left) are fitted with a function of $T = aD^b$. It turns out that the measured torque increases with an exponent of nearly b= 2.02 (best fit). The outcome suggests that the rotor sides mainly contribute while the lower-end surface contributes insignificantly to the measured torque.

This assumption is supported by Figure 74 (right), showing the measured torque at constant rotor diameter D and changing height H. Considering equation 97, the torque is expected to increase linearly with growing rotor height H. However, it can be seen from Figure 74 (right) that the measured torque follows a quadratic trend of H^2 ($b \approx 1.98$) with an intercept representing the lower-end surface contribution [196]. This intercept is fairly pronounced and loses importance as the rotor height H increases.

The quadratic relationship seen in Figure 74 (right) is in line with the experimental study of Daniel et al. [196], showing that the total torque increases quadratically with the rotor height H for cohesionless glass beads. Considering the quadratic relationship on the torque in Figure 74 (right), the calculated shear stress is expected to increase linearly in the function of the rotor height H using equation 97. This increase shows that the shear stress is a function of the rotor height and the granular system's intrinsic properties, such as the friction coefficient and particle density [196].

The linear increase of the shear stress is equally expected for Figure 74 (left) when the torque increases to the power of three (b = 3). However, the contribution to the total torque by the end surface is insignificant, leading to constant shear stress using equation 97. A cubic increase of the torque is assumed to be measurable when similar measurements are performed at different immersion depths.

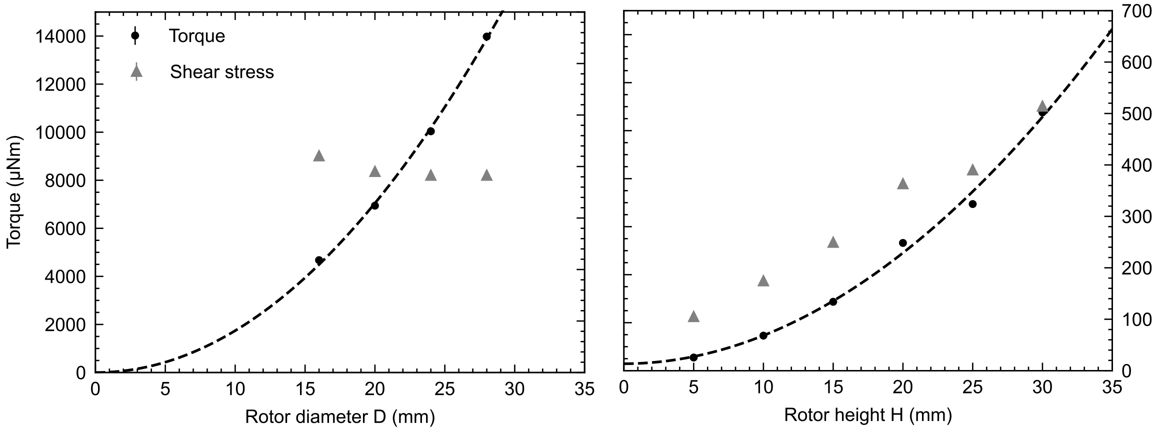

Figure 74: Measured torque at a shear rate of 1 s^{-1} and gap position b at 5 mm for various rotor diameters (left) and heights (right); Shear stresses for both graphs are calculated with equation 97. Inner cup diameter of 40 mm. The height (left) and diameter (right) are 25 mm and 20 mm, respectively. Error bars are smaller than the marker size. Displayed trend lines follow the equation: $y = ax^b$ (left) and $y = c+ax^b$ (right). Both graphs share a legend and axis.

7.2.2 Measurements with a plate geometry

Plate-cup measurements with various granules have been performed, as explained in chapter 7.1.2. The granular material has been sheared at constant normal force. When a granular material is sheared under constant load, the volume of the granule bed decreases, meaning that the gap width during the measurement has to be adjusted to maintain the envisaged normal force. Measurements with a plate geometry for various normal forces are displayed in Figure 75 (left). The normal forces are selected based on preliminary measurements to avoid granules' destruction.

It is visible from Figure 75 (left) that the torque increases sharply, followed by a sharp decline of the torque reaching a steady state, i.e. no change of the torque, as described by Schulze [96]. The sharp increase in torque arises from granules' movement against each other, causing the interlocking of granules. A suitable amount of shear stress is needed to overcome the interlocking through dilation [281] and to move the granules towards intergranular voids. The dilation of granules leads to an incipient flow (yielding) followed by a decreased measured torque towards a steady state. In this steady state, the measured torque is constant, and an equilibrium exists between dilation and contraction, similar to rotor measurements (see chapter 7.2.1.1).

The interlocking of granules in the early stage of the measurement depends on the bulk density below the plate surface affected by the applied normal forces. Higher normal forces lead to higher bulk densities; thus, higher shear stresses are needed to introduce flow (yielding), visible as higher measured torques in Figure 75 (left). Repetitive measurements of the same material in Figure 75 (right) show that the steady state is at a similar torque level.

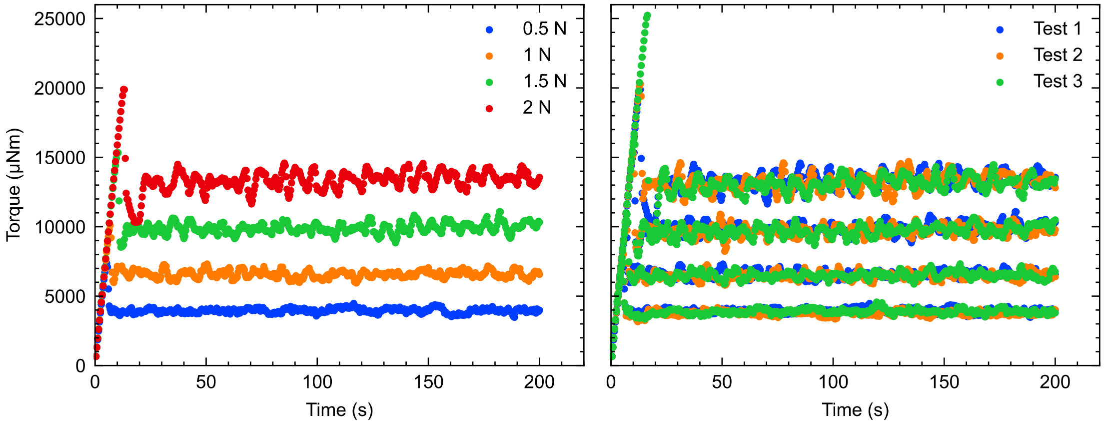

Figure 75: Measurement of the torque for various normal forces ranging between 0.5 and 2N (left). Repetitive measurements with the same applied normal forces (right). Both graphs share the same y-axis label. Unsieved sample SA. Shear rate of 0.1 s^{-1}.

The maximum shear stress at incipient flow is typically considered for bulk materials [96]. In this experimental study, the steady state is the focus of interest, which describes the flow of the granular material once yielded, as considered in the literature [244]. An average torque beyond the yielding is calculated for the different normal forces (100 to 200 s). The shear stress is calculated based on the averaged torque for two parallel plates, following [245]:

$$\tau = \frac{2T}{\pi R^3} \tag{98}$$

where R is the plate radius. The normal pressure σ acting on the granule bed is calculated using plate contact surface area A ($A = \pi R^2$) and the average normal force F_n. The shear stresses τ for a range of applied normal pressures σ are displayed in Figure 76 (left).

As expected, Figure 76 (left) shows that the shear stresses increase with applied normal pressures, typically forming an upward convex curve inside a τ-σ-diagram (see also chapter 3.5.2). Such an upward convex curve can not be observed in Figure 76 (left) for the applied normal pressures. A linear fit is applied to the data sets for conservatively estimating a friction coefficient for yielded flows in a steady state [216]. Considering the Mohr-Coulomb model (equation 69, chapter 3.5.2), the slope of the linear fits presents the friction coefficients μ, and the intercept is the yield stress τ_0 for steady-state flows.

Figure 76 (right) displays the friction coefficients μ in dependency of the Sauter mean diameters $d_{[3,2]}$ from Table 6. It appears that two effects affect the friction coefficient. First, as the mean diameter increases for narrow sieved samples, the friction coefficient μ increases linearly (A/63-100, ..., A/>224). Second, as the sieving fraction widens (A/125-200, A/150-224 and A/125-224), the friction coefficient increases, having similar Sauter mean diameters. Both outcomes imply that the mean diameter of granules is essential for narrow size distributions, while for broader size distributions also, packing phenomena come into play, increasing the friction coefficient when sheared. This effect is pronounced for the unsieved sample SA containing all granular diameters and showing the highest friction coefficient.

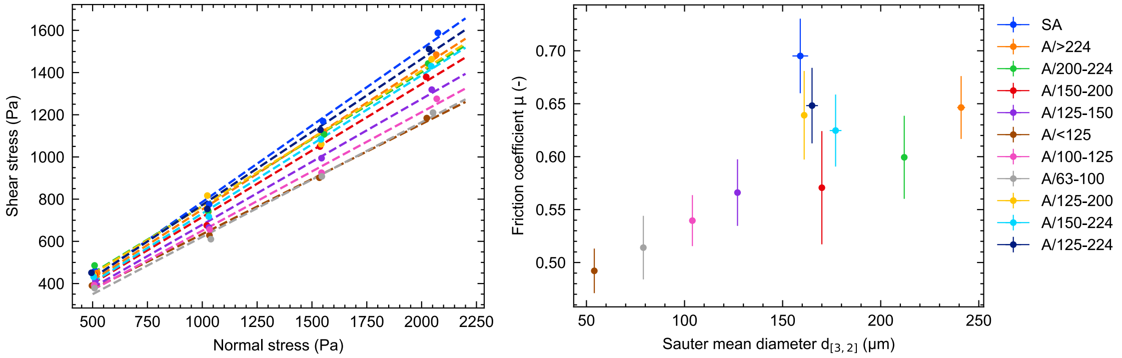

Figure 76: Shear stress in the function of normal pressures for various samples (left); The friction coefficient in the function of the Sauter mean diameter (right). Both graphs share the same legend.

7.2.3 The friction coefficients from the shear cell and angle of repose measurements

Figure 77 compares the friction coefficients acquired from shear measurements in Figure 68 and those from the angle of repose measurements in Figure 63 (chapter 6.2.1). It turns out that granular systems with small mean diameters appear to have small friction coefficients arising from shear measurements (A/125-150, A/100-125, A/63-100 and A/<125), which tend to have high friction coefficients measured with the angle of repose measurements. Samples A/>224 to A/150-200, A/125-200, A/150-224 and A/125-224 have similar friction coefficients ranging between 0.55 and 0.65, apparently independent of the applied technique.

The contrary relationship for samples with small diameter d is assumed to be caused by different phenomena effective during the measurements with the two different techniques. First, the friction coefficient from the angle of repose measurement arises from a bulking-up of the heap followed by avalanching effects on a free surface plane. The introduced flow, visible as an avalanche, is caused by exceeding the maximal angle of a specific granular system. The angle of repose and, thus, the friction coefficient derived from such a measurement technique appears more sensitive to present cohesive effects, i.e., van der Waals forces, as outlined in chapter 6.2.2. Most important, the AOR measurements yield a static friction coefficient when the appearing forces are just below the yield limit. This is not the case for the rheological measurements. Here, the friction coefficients are derived from a densified steady-state regime imposed by the applied shear rate and normal pressures. The material is beyond the yield limit, overcoming the static friction to introduce flow, where the friction coefficient appears less affected by cohesive effects but more influenced by phenomena related to granule properties, such as bulk density. The latter is visible for the unsieved sample SA, as it contains all granules, leading to an increased friction coefficient, which is well determined by both techniques.

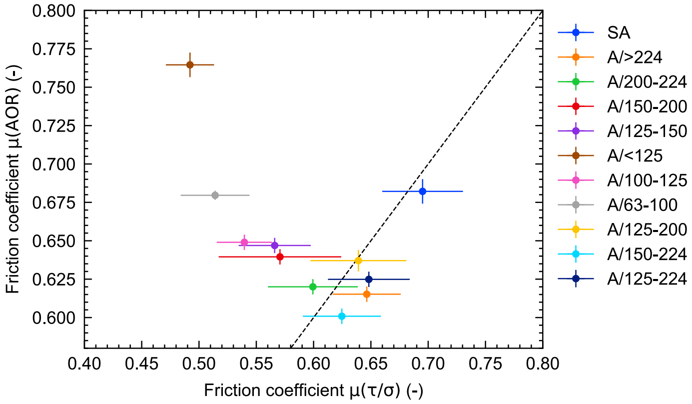

Figure 77: Comparison of the friction coefficient measured from the angle of repose AOR measurement and the friction coefficient from shear measurements. The line is for guidance only and follows y=x.

7.2.4 Amplitude sweep measurements with hard metal granules

Amplitude sweep tests, i.e. oscillatory measurements at a fixed frequency of 1 Hz have been performed over an extensive range of oscillation amplitudes (shear deformations γ). In preliminary measurements, suitable measurement parameters for hard metal granular materials have been elaborated. A force of 0.5 N has been selected to prevent any material destruction. Figure 78 displays the storage modulus G' and the loss modulus G" as a function of the shear deformation. It can be seen from Figure 78 that a linear viscoelastic region (LVE) at very low amplitudes exists, where the storage and loss modulus form a plateau. In the LVE, the layer of granules directly below the plate behaves like a solid (G' > G'' for $\gamma < 10^{-4}$), as the oscillatory movement is too small to create flow. The oscillatory movement implies that the movement of single granules resembles vibrations. In this state, single granules cannot overcome the direct neighbour by dilation as the shear deformation is too small. The single granules slide or roll back to the initial positions.

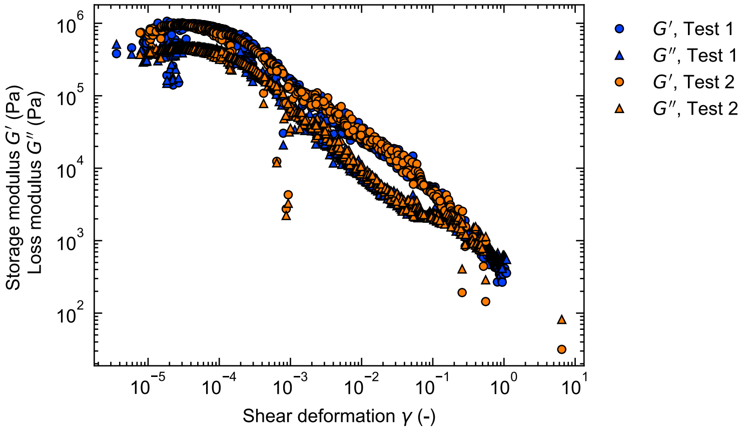

Figure 78: Amplitude sweep tests with the unsieved standard sample SA at 1 Hz.

With increasing shear deformation, the storage G' and loss modulus G'' decrease simultaneously ($\gamma > 10^{-4}$), indicating a change in the inner structure inside the granules' bed. The change in the inner structure can be interpreted as a yield point for the granular system. The introduced shear stress decreases over a small powder bed depth at such small shear deformations. In this thin layer, the granules move over a static shear band, leading to a slight densification of the granular material below the plate. The gap width decreases to maintain the envisaged force of 0.5 N. Notably, as the material begins rearranging and densifying, the storage modulus G’ is superior to the loss modulus G’’, indicating that the granular system behaves like a solid.

The beginning of the decline of G’ and G’’ near a shear deformation of 10^{-4} is assumed to be influenced by the granule properties, such as the granule mean diameter or the bulk density. Therefore, a granular system with a smaller granule mean diameter is expected to yield at smaller shear deformation. However, it can be seen from Figure 79 that this outcome is not evident; all curves are very similar in measured magnitudes of G’ and G’’ in dependency of the shear deformation. The materials are close to each other in terms of their mean diameters (Table 6) and densities (Table 8) and, thus, are not distinguishable.

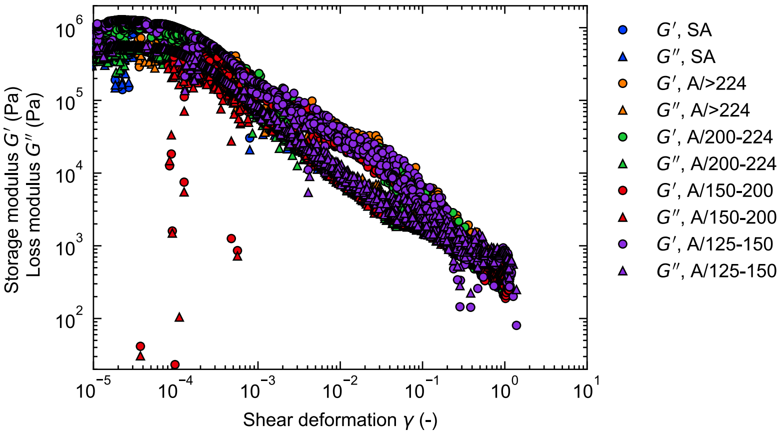

Figure 79: Amplitude sweep tests for various granular materials at 1 Hz.

Following the decreasing trend of G’ and G’’, a transition of G’ and G’’ at higher amplitudes (γ > 0.1) is visible, marking the increased flowability of the material as G’’ is above G’. In other words, the system behaves like a liquid (G’’ > G’). Here, interparticle friction plays a crucial role; energy dissipation through heat leads to deformation and destruction, visible as a ring at the outer region of the cup, where the shear stresses are the highest (Figure 80, left). Taking a closer look at Figure 80 (right), then exceeding the transition of G’ and G’’, the high amplitudes lead to a detaching or destruction of granules at the outer zone of the upper plate. Here, the attached granules are still visible in the centre of the plate. Hence, the flow region with shear deformation beyond the intersection (G’ < G’’) has to be carefully considered, as this region might not reflect entirely the granule properties.

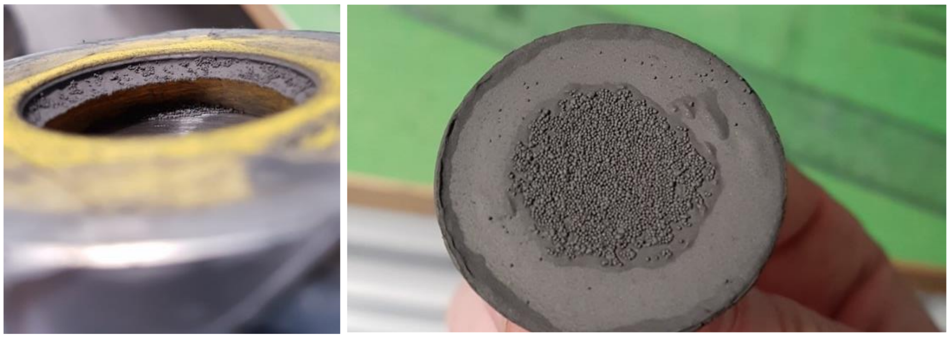

Figure 80: Destroyed granular material at the outer perimeter of the 3D printed insert (left) and the surface of the plate geometry with tape (right) at the end of an amplitude sweep measurement with the standard sample SA over a large range of shear deformation. Measurement points: 1000.

Additional measurements have been performed to verify the destruction of granular materials in the transitional regime ($G' < G''$). Several measurements have been performed over specific shear deformation ranges: 10^{-5}-10^{-1}, 10^{-1}-$5\cdot10^{-1}$, $5\cdot10^{-1}$-10^{0}, 10^{0}-$5\cdot10^{0}$. At the end of each measurement, the surface of the granule bed and the plate surface are visually evaluated. The granule bed's top surface is slightly moved to control for destructed granules at the inner cup wall and on the plate, similar to Figure 80. It can be seen from Figure 81 that the granules are destroyed for the largest shear deformation interval: 10^{0}-$5\cdot10^{0}$.

It is important to mention that the measurements shown in Figure 81 have been performed with 100 data points for each interval, whereas Figure 80 includes 1000 data points. The amount of data points significantly affects the measurement duration, i.e., more data points with a longer duration. The measurement duration impacts the time of the granule's movement below the plate, provoking the dry friction between granules and, hence, the destruction of granules. This can be seen when comparing Figure 80 and Figure 81 ($5\cdot10^{-1}$-10^{0}). In the case of Figure 80, the destruction of granules appeared at lower shear deformations inside the transitional regime, while in Figure 81, at larger shear deformations $5\cdot10^{-1}$-10^{0}. This outcome indicates that the measurement duration and large shear deformations lead to the destruction of granules.

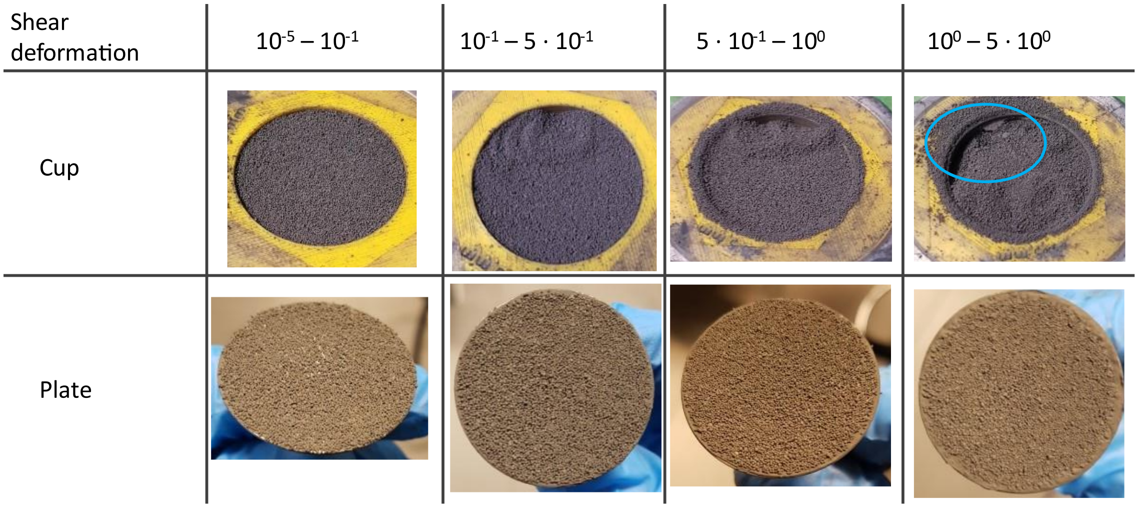

Figure 81: Images show various stages of the amplitude sweep tests. The blue circle shows the destruction of granules at the cup wall. For the same shear deformation interval, destructed and detached granules can be observed at the outer rim of the plate.

7.2.4.1 Amplitude sweep tests with pre-compaction

Amplitude sweep tests with a frequency of 1 Hz were performed with a precompacted granule bed in analogy to 7.2.4. This pre-compaction has been achieved by applying a normal force of 5.77 N. Afterwards, a normal force of 0.5 N has been maintained during the measurement. Figure 82 shows repetitive measurements of the unsieved sample SA. The outcome shows that the LVE is shifted towards higher storage and loss modulus G’ and G’’ in a precompacted state compared to a non-compacted state, as shown in Figure 78. The shift towards higher moduli with pre-compaction indicates that the bulk density of the granular system below the plate affects the storage G’ and loss modulus G’’ – which is expected.

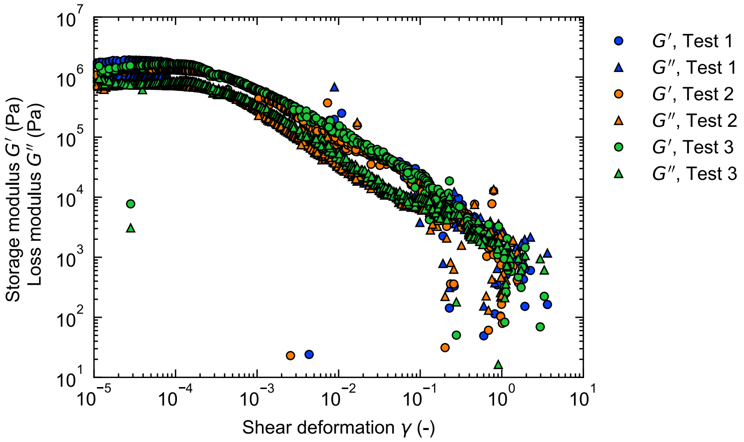

Figure 82: Storage and loss modulus of a precompacted powder at 5.77 N and measured at 0.5 N. Sample SA.

7.2.4.2 Amplitude sweep tests with different frequencies

Amplitude sweep tests with different frequencies have been performed and are displayed for the standard sample SA. The frequency is expected to affect the storage G’ and loss modulus G’’. Figure 83 displays the storage and loss modulus G’ and G’’ for three different frequencies: 1 Hz, 10 Hz, and 20 Hz.

Acquired data sets were displayed into free different subplots to show differences. Figure 83 displays the typical trends comparable to Figure 78: A LVE region followed by a decline towards an intersection of G’ and G’’. An increase of the frequency from 1 Hz to 10 Hz shifts the transition of G’ and G’’ from γ ≈ 0.6 to lower shear deformation, near γ ≈ 0.2. However, the exact transition point is problematic to determine as the transition takes place over a large shear deformation range. A further increase from 10 Hz to 20 Hz in the frequency minorly shifts the transition range towards lower shear deformation.

It is important to note that measurements at lower (f < 1 Hz) and higher (f > 20Hz) frequencies were also performed. The machine could not completely measure the shear deformation ranges beyond and below the displayed frequencies. This outcome is unexpected and can not be entirely explained. In any performed measurement with a frequency of 0.1 Hz, the measurement started following the typical G’ and G’’ curve, and then the rotation velocity increased uncontrollably. It was observed that this happens when G’ and G’’ decreased between a shear deformation of 10^{-4} to 10^{-3}.

On the other side, measurements with higher frequencies (f > 20 Hz) led to inconsistencies in the acquired data. It is assumed that high shear deformation with high frequencies leads to a failure in the shear plane between the granules stuck on the lower plate surface and those in slightly deep layers. This effect indicates the destruction caused by dry friction between granules or detaching of granular material from the tape, similar to Figure 80 (right).

As a result of the amplitude sweeps with different frequencies, no significant change of the absolute values of the elastic modules could be found. This is attributed to the small accessible (see above) frequency window. The shift of the cross-over of both moduli is too smeared out in order to be determined. It should be mentioned that this is not due to the measurement procedure. The reproducibility of the amplitude measurements (see e.g., Figure 79) is considerably high especially when one takes the filling process with all its peculiarities into account.

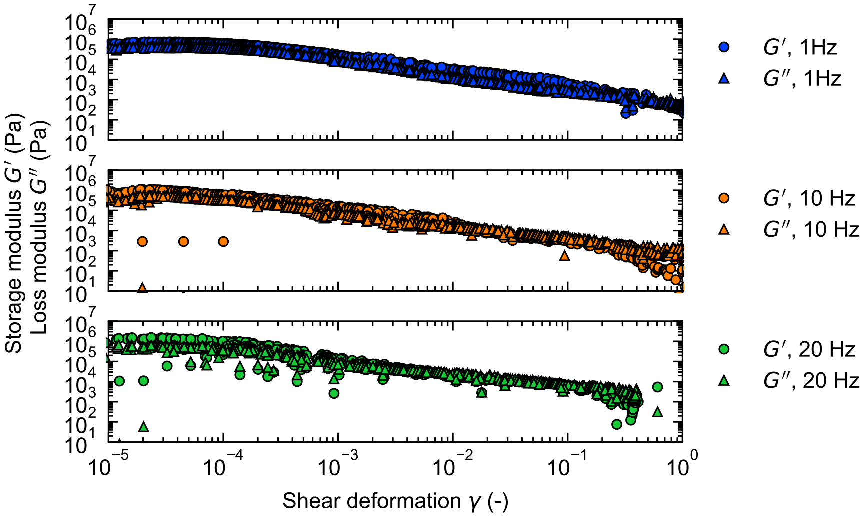

Figure 83: Amplitude sweep measurements with the unsieved sample SA for three frequencies:1, 10 and 20 Hz. The normal force of 0.5 N is maintained during the measurement.

7.2.5 Frequency sweep measurements with hard metal granules

The idea behind the frequency sweeps is as follows: if the LVE regime seen in the amplitude sweeps is the region where the granules only "vibrate", can a dynamic freezing be observed at higher frequencies.

Frequency sweep tests have been performed at a shear amplitude of $\gamma = 3\ 10^{-5}$ (LVE regime) selected based on the amplitude sweep measurements in previous paragraphs 7.2.4.1 and 7.2.4.1. The maximum frequency of 100 Hz has been selected based on the machine's instruction manual given by the manufacturer. The outcome for the unsieved sample SA (Figure 84) shows that both G' and G'' increase by nearly half of an order of magnitude as the frequency increases. Notably is the slight decrease in G' and G'' above frequencies of nearly 50 Hz. The slight decrease at higher frequencies could indicate the start of a dynamic freezing of the granules' vibrational movement but unfortunately, the accessible frequency range by the rheometer is too low to draw a definite conclusion.

It should be added that both experiments (frequency and amplitude sweep tests) can be compared regarding the plate velocities:

The velocity v of the rotor can be calculated with equation 99, where A is the shear deformation (amplitude), ω_0 is the angular velocity, r is the radius of the plate, and t is the time.

$$v = r\ A\ \omega_0 \cos(\omega_0 t) \qquad 99$$

The velocity is at its maximum when the cos(ωt) term equals 1. In this case, the maximal velocity follows.

$$v_{max} = r\ A\ \omega \qquad 100$$

Equation 100 can calculate the maximal amplitude A_A within the amplitude sweep tests when the maximal velocity v_{max} is equal in both experiments.

$$\mathrm{A}_f\ \omega_f r = A_A \omega_A r \qquad 101$$

Solving for the amplitude A_A, then equation 101 follows:

$$\mathrm{A}_A\ = \frac{A_f \omega_f}{\omega_A} \qquad 102$$

Equation 102 can be used to calculate the amplitude A_A at which the maximal velocity equals the maximal velocity in frequency sweep tests. Considering the measurement parameters in chapter 7.2.4 and this chapter and using equation 106 with ω_f equals (2π 100 Hz), A_f is $3\ 10^{-5}$ and ω_A is (2π 1 Hz), then A_A yields $3 \cdot 10^{-3}$. The magnitude of A_A shows in Figure 78 that G' and G'' are decreased, whereas Figure 84 shows the beginning of a decrease in G' and G''. It is important to note that the above calculation is an approximation as G' and G'' are also density-dependent, influenced by a precompaction step (see Figure 82).

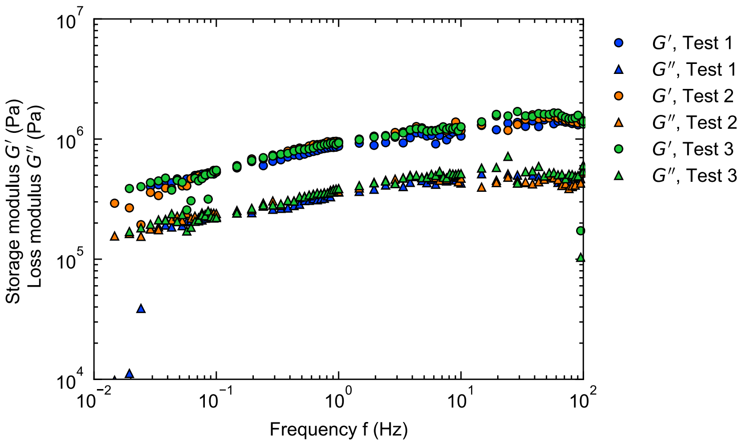

Figure 84: Storage and loss modulus G' ang G'' for various frequencies measured with the unsieved sample SA at an amplitude of 3 10^{-5}. A normal force of 0.5 N was selected.

7.2.6 Flow curves measured with a rotor geometry

The flow of granular materials is studied for a wide range of shear rates described in chapter 7.1.1. The shear stress τ is calculated from the measured torque with equation 103 [239]:

$$\tau = \frac{T}{2\pi R^2 H\left[\left(1-\frac{1{,}113}{N}\right)+\frac{R}{4H}\left(2.75-\frac{3}{\sqrt{N}}\right)\right]} \qquad 103$$

where R is the radius of the rotor, H is the height of the blades, and N is the number of rotor blades, assuming the material within the blades acts as a rigid material. Figure 85 (left) presents the shear stress as a function of the shear rate $\dot{\gamma}$. It is essential to mention that the stress magnitudes are related to the resistance to flow by the granular material and the inserted mass, calculated with equation 96, as the mass above the rotor significantly affects the measured torque (see Figure 72).

It can be seen from Figure 85 (left) that the shear stress τ follows a non-monotonic flow curve for all samples: an increase of the shear stress at very low shear rates ($10^{-2} \leq \dot{\gamma} \leq 10^{-1}$ s^{-1}), followed by a decrease in the shear stress, leading to a minimum ($\dot{\gamma} \approx 2 \cdot 10^1$ s^{-1}) and a sharp increase in shear stress ($\dot{\gamma} > 2 \cdot 10^1$ s^{-1}). Such a flow curve has been found for rotor-cup measurements coupled with vibrations [176]. However, it is evident that the presented shear stress increases at minimal shear rates ($10^{-2} \leq \dot{\gamma} \leq 10^{-1}$ s^{-1}) is mainly caused by the selected measurement parameters. The time needed to reach the steady state is strongly enhanced as the shear rate, and the granule mean diameter decrease, as presented in chapter 7.2.1. Hence, the data below a shear rate of 10^{-1} are omitted for further discussions.

With an increasing shear rate, the shear stress decreases towards a minimum shear stress, followed by a shear stress increase in Figure 85 (left). The decrease in shear stress is attributed to the appearance of spatial anisotropy of the granules [246]. The increasing collisions between granules provokes an alignment of granules as the shear rate increases. This change in the inner structure introduces a collapse of the granule force network, reducing the resistance to flow [246] by aligning granules or reducing the packing density [247]. The destruction in the force network occurs when the presented stresses pass the yield stresses inside the shear plane, creating a yielded region similar to an avalanche threshold, changing from a static to a dynamic state [248].

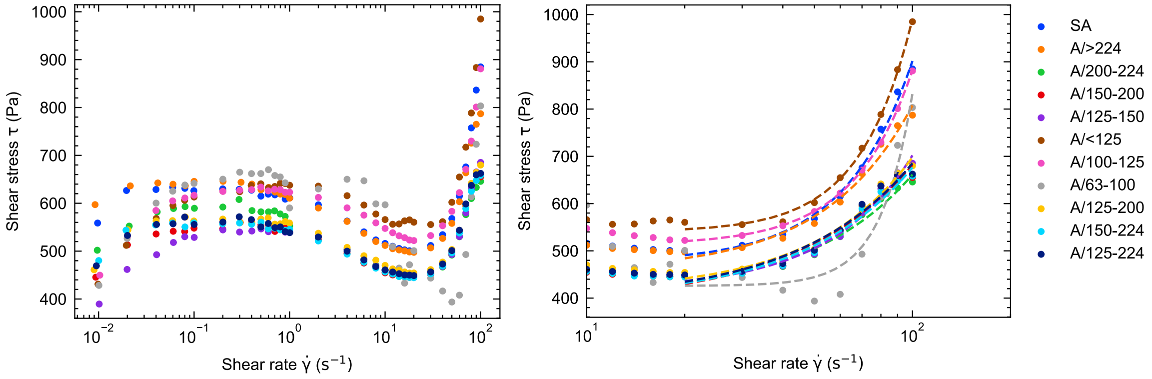

Figure 85: Shear stress calculated from the measured torque with the rotor RCD20H25 in the function of the shear rate (left); close-up of the shear stress (right). Fit equation: $\tau = \tau_0 + C\dot{\gamma}^n$*. Both graphs share the same legend. Measurements for samples 1.6 and 1.7 considered the tap density to calculate the mass. For others, the bulk density is considered.*

As the shear rate increases ($\dot{\gamma} > 2\cdot10^{1}\ \mathrm{s}^{-1}$), the shear zone grows [249], leading to a rise of collisions between granules caused by the exchange of momentums [248]. The increase in collisions results in a decrease in the packing fraction [244,250]. The increase in the shear stress depends on the packing fraction of the granular material [251]. In the case of lower granule packings, the shear stress increases quadratically ($n \approx 2$) with $\tau \sim \dot{\gamma}^n$, while at higher packing fractions n deviates from 2 towards lower values caused by dry frictions between granules [251], which leads to destruction of the granular material during the measurement (Figure 86). The similar relationship was also fund in another study with solids in a Newtonian fluid [252].

Several fits in the form of $\tau = \tau_0 + C\dot{\gamma}^n$ [246] have been applied to each data set in Figure 85 (right), starting from the lowest shear stress τ_0 (nearly 20 s^{-1}), where C depends on the granule properties. Hence, both are fitting parameters depending on the material's properties. The above equation was considered by Lu et al. [246] to describe the shear rate dependency of the shear stress at elevated shear rates in the inertia regime (collision regime). The focus of interest is the evolution of the exponent n. It turns out that the granular samples (A/>224,.., A/125-150, A/125-200, A/150-224 and A/125-224) with larger granule mean diameters range between 1.2 and 1.7 for n, while finer ones (A/<125 and A/100-125) and the unsieved sample SA range between 2 and 2.7. It can be seen from both graphs (Figure 85) that sample A/63-100 with the smallest diameter (Table 6) shows inconsistencies in the data, and the applied fit does not describe the trend well, yielding an exponent of n = 6. The difference in the exponent n for larger and smaller sets of granules (except A/63-100) implies that the shear stress evolution in the collisional regime is related to the granule characteristics, such as the granule diameter d, which is considered in the μ(I)-rheology.

Figure 86: Destroyed granules at the outer perimeter of the rotor geometry. Image taken after measuring the entire shear rate range of 10^{-2} to 100 s^{-1}. Sample: A/63-100. Rotor: RCD20H25.

7.2.7 The µ(I) rheology of hard metal granules with a rotor geometry

The µ(I)-rheology describes the friction coefficient change in the function of the inertial number I for different flow regimes: quasi-static, dense flow, and inertial regime (see chapter 3.5.1). The friction coefficient between single particles can not be determined from simple shear measurements; instead, an effective friction coefficient μ_{eff} is considered. The effective friction coefficient μ_{eff} of the bulk is described by the relation between the shear stress τ and the normal shear stress σ (or normal pressure P), see equation 69. The inertial number I is related to the granular size d, the granule density ρ_p, the shear rate $\dot{\gamma}$ and normal pressure P (equation 63).

Challenges arose in determining the lateral forces acting on the side plane of the rotor by the granular material inside the cup and, thus, determining a normal lateral pressure P (equivalent to the normal stress σ). A possible way to determine the pressure P is to investigate the pressure at different immersion depths with a pressure transducer in a static state [196]. Assuming that the pressure P in a static state equalizes the pressure P at very low shear rates in a quasi-static regime ($I \rightarrow 0$), then the effective friction coefficient μ_{eff} can be derived from Coulomb's friction law for cohesionless systems with $\mu_{eff} = \tau/P$. The shear stress τ can be calculated from the measured torque T, acting along the shear plane perpendicular to normal pressure P. Inserting a pressure sensor into the cup is not applicable as the sensor's presence affects the granules' flow around the rotor at elevated rotation speeds, as remarked by Daniel et al. [196].

Another approach deriving the normal pressures P acting vertically and radially on the rotor surfaces is considering the inserted mass where lithostatic pressure increase remains linear. A linear lithostatic pressure is present when the rotor immersion is small and stays superficial to the granule bed surface, and the pressure saturation caused by the Janssen effect is absent. The pressures P acting along the rotor surface can be estimated by splitting the total pressure P into axial and radial components caused by the mass above and next to the rotor surface. Assuming that the gravitational force from the mass above and next to the rotor acts entirely on the rotor surface, the maximal lithostatic pressure P_{max} can be approximated using equation 96 (chapter 7.1.1), neglecting the mass between the rotor blades and within the gap below the rotors lower edge and the bottom of the cup. Using equation 96 and considering the surface of the rotor, the maximal lithostatic pressure ranges between 1400 and 1600 Pa for all hard metal granular samples. These normal pressures are lower than the maximal normal pressure in the plate cup measurements of nearly 2100 Pa (see Figure 76, chapter 7.2.2). However, this approach estimates the pressures acting on the rotor surfaces insufficiently, as a portion of the lithostatic pressure is transferred laterally by intergranular contacts towards the wall of the cup. Hence, the normal pressure P acting on the rotor surface is lower than P_{max}.

The final approach is to estimate the normal pressure P acting on the rotor surface from the Coulomb friction model, assuming that the effective friction coefficient μ_{eff} equals the friction coefficient from plate cup measurements, presented in chapter 7.2.2. Both friction coefficients are set equal, assuming the granular systems are in both measurements in a quasi-static regime at low shear rates. Notably, in the quasi-static regime, the friction coefficient is independent of the shear rate $\dot{\gamma}$, i.e., the friction coefficient is constant. As described in the previous chapter, the applied measurement parameters led to inconsistencies at low shear rates (see Figure 85). Hence, both friction coefficients are set equal inside the quasi-static regime, between a shear rate of 0.1 and 0.5 s^{-1}, at which the friction coefficient is nearly constant. This provides pressures P lower than the maximal pressure P_{max}, ranging for the selected hard metal granules between 900 and 1300 Pa. These pressures P are considered to calculate the inertial number I for each sample, assuming the pressure is constant over the entire shear rate. As the pressure P is constant, the calculated friction coefficients beyond the quasi-static regime follow the non-monotonic curve of the shear stress (see Figure 85).

Figure 87 shows the friction coefficient in the function of the inertial number I for various granular materials. As expected, the curve evolution is identical to the stress curve in Figure 85. The three different regimes are visible in Figure 87. The quasistatic regime for $I \rightarrow 0$. Here, the same problem is present, as stated in chapter 7.2.6. In the dense flow regime, the decrease of friction coefficient starts beyond $I > 10^{-4}$, being nearly one order of magnitude lower than classified by Cruz et al. [173]. In the inertial regime, the increase in friction coefficient with shear rate begins at $I > 10^{-2,}$ aligning with the literature [174].

It is ambitious to assume that the pressure P acting on the rotor surface is constant beyond the quasi-static regime and that a change in the granule's structure inside the shear zone entirely causes the decrease in friction coefficient in the dense flow regime. This assumption holds when the immersion depth of z = 5mm is maintained throughout the measurement, and the shear zone is smaller than the diameter of the cup (no slip at the wall). However, a densification of the granular material above the rotor was observed at elevated shear rates, reducing the nominal immersion depth z and affecting the overall mass on top of the rotor, hence, the pressure P acting on the rotor surface.

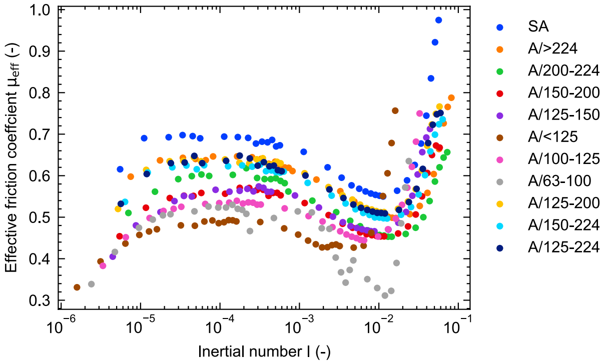

Figure 87: The effective friction coefficient μ_{eff} in the function of the inertial number I. Errors are not shown for visibility reasons. Relative errors from the friction coefficient vary between 5 and 10% depending on the sample. Inertial numbers consider pressures derived from friction coefficients. Hence, errors for the inertial numbers are between 5 and 10%, depending on the sample.

The friction coefficients and the inertial numbers in Figure 87 are normalized with the friction coefficients from plate cup measurements and the maximal inertial numbers at I = 10^{-1}, shown in Figure 88. The normalized data sets are presented in Figure 88. The most significant difference can be observed in the dense flow regime ($5 \cdot 10^{-2} < I/I_{max} < 2 \cdot 10^{-1}$), where smaller granular systems (A/<125 and A/100-125) lower decrease less in the normalized friction coefficients compared to larger granular systems (A/>224 and A/200-224) (except sample A/63-100). In the inertial regime, larger granular materials (A/>224 and A/200-224) tend to increase less, related to the higher mass of single granules.

The data sets are fitted with equation 104, omitting data below the normalized friction coefficients $\mu_{eff}/\mu = 1$ and normalized Inertial numbers $I/I_{max} < 2 \cdot 10^{-3}$. Equation 104 is based on the proposed constitutive law by Lu et al. [246], combining two fits to describe the shear weakening effect in the dense flow regime (first term) and the increase in the inertial regime (second term) over a broad shear rate range. The constitutive law is adapted to describe the non-monotonic flow curve of the normalized μ(I) rheology.

$$\frac{\mu_{eff}}{\mu} = \left(1 - \frac{1}{\left(K_1\, e^{\left(\left(\frac{I}{I_{max}}\right)^{K_2}\right)}\right)}\right) + K_3 \left(\frac{I}{I_{max}}\right)^{K_4} \qquad 104$$

The first term in equation 104 considers the constant normalized friction coefficient of 1 when $I/I_{max} \rightarrow 0$ (quasi-static regime). The shear weakening effect of the μ_{eff}/μ in the dense flow regime decreases exponentially, followed by an exponential increase inside the inertial regime (second term).

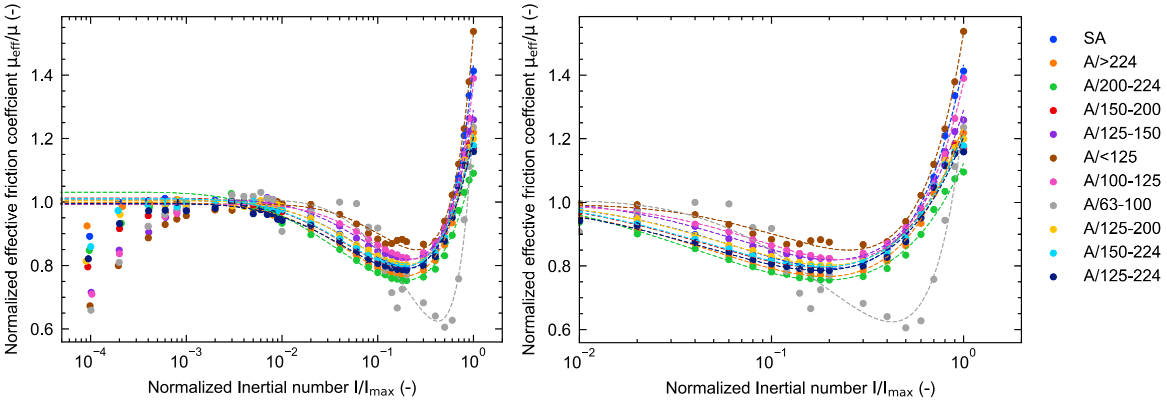

Figure 88:Normalized Inertial number calculated with the maximal inertial number at 10^{-1} (left). Close-up (right). Both figures share the same legend. Normalized friction coefficient calculated with the friction coefficient from plate-cup measurements. Errors are not shown for visibility reasons. Relative errors from the friction coefficient vary between 5 and 10% depending on the sample. Inertial numbers consider pressures derived from friction coefficients. Hence, errors for the inertial numbers are between 5 and 10%, depending on the sample. Fits omit data sets below normalized friction coefficients $\mu_{eff}/\mu = 1$ and normalized Inertial numbers $I/I_{max} < 2\cdot10^{-3}$. R^2 ranges between 0.92 and 1.

7.3 Conclusion and summary

Rheological measurements with various rotor geometries inside a cup and with a plate geometry have been investigated for a set of hard metal granular materials. The application of 3D-printed rotor geometries has been studied by varying the rotor diameter and height with changing immersion depths. The presented outcome aligns with the literature. Measurements with simple shear tests showed that the hard metal granular materials are sensitive to destruction, caused by the organic binder, making a unique measurement procedure necessary by limiting the normal force to low magnitudes. Amplitude sweep tests showed the existence of an LVE at very low shear rates, declining towards an intersection of G’ and G’’. Frequency sweeps tests in the LVE regime showed no crossing of G’ and G’’, indicating no dynamic phase change over a wide range of frequencies. Studying hard metal granular materials at low normal forces yielded the friction coefficient, which estimates the total pressure P acting on all sides of rotor geometry. This total pressure P was considered for calculating the inertial number I. The μ(I)-rheology showed a non-monotonic flow curve of the hard metal granular materials with a shear weakening effect resulting in a decrease in the friction coefficients at moderate inertial numbers I. The knowledge of such a shear weakening effect can be considered to increase the flowability of hard metal granular systems.

8 The mass flow rate of granular materials in relation to the Beverloo law

Chapters 5 and 6 showed that the friction coefficient, arising from the angle of repose, and the mass flow rate are influenced by the mean diameter of the granule size distribution and the attractive forces acting between granules. This chapter aims to approve previous outcomes by selecting two additional hard metal granules and granule systems with different characteristics, such as iron and inox granules.

Furthermore, this chapter focuses on understanding the influences on the parameters C and k. This is realized by measuring the mass flow rate with a cylindrical tube and flat-bottomed orifices for granular systems with varying particle size distributions. The fitting parameters C and k are determined from the acquired mass flow rates, and they are compared to the friction coefficient (from the angle of repose measurements) and to interparticle forces expressed by the granular Bond number, respectively. The outcomes are considered to propose an empirical model based on the Beverloo Law for hard metal granules. This empirical model is verified by considering an additional set of hard metal granular systems with different compositions, i.e., varying tungsten carbide and cobalt content.

It is important to note that parts of this chapter have been published recently [253].

8.1 Characterisation of granular materials

Various granular materials are selected and classified into two large sets. The first set contains two hard metal granular systems with different cobalt contents and types of WC. The selection complements the hard metal granules used in the previous investigations. These hard metal systems are referred to as B and C, respectively. Both hard metal granule systems are sieved. The selected sieving classes are determined from preliminary sieving. The hard metal granules listed in chapter 5.1 are also considered. For the sake of clarity, the nomenclature of sieved hard metal granule systems is also extended by letters A, B and C to distinguish between different hard metal compositions. Aside from hard metal granules, the first set contains various iron and inox granules of different sizes. All iron and inox granules are commercially acquired (Metallpulver24). The selected iron and inox granules differ in their granule's diameter. However, they do not originate from an unsieved sample. These samples are indicated by letters D and E, respectively.

Furthermore, commercial sand and corundum powder (white, F40) are also considered. In this study, both systems are described by the letters F and G, respectively.

The second data set contains hard metal granular materials containing different amounts of tungsten carbide, cobalt or nickel, and organic binder. These granules are considered to verify the proposed empirical model to estimate the mass flow rate.

8.1.1 The granular size distribution

The granule size distributions of the samples are measured with laser diffraction using the Mastersizer 3000 from Malvern (chapter 4.4). The acquired data are presented in Table 14 and Table 15. The column *sieving class* corresponds to the difference between two different sieving mesh sizes of the sievings provided from the upper and lower limits. The granule size distribution can be found in appendix 14.1.

Table 14: Different diameters based on the granule size distribution of selected granular materials. Diameters of type A can be found in Table 6.

Type	**Sample**	**d_{10} (µm)**	**d_{50} (µm)**	**d_{90} (µm)**	**$d_{[3,2]}$ (µm)**	**$d_{[4,3]}$ (µm)**
8.2 % Cobalt, Fine WC **B-HM2**	SB	101 ± 2	167 ± 3	265 ± 4	149 ± 2	176 ± 3
	B/>224	219 ± 1	258 ± 2	302 ± 3	256 ± 1	260 ± 2
	B/200-224	190 ± 1	215 ± 1	240 ± 3	214 ± 0	215 ± 1
	B/180-200	167 ± 1	190 ± 1	211 ± 1	189 ± 0	190 ± 1
	B/150-180	145 ± 1	166 ± 0	191 ± 2	165 ± 0	166 ± 1
	B/125-150	116 ± 1	139 ± 0	165 ± 2	138 ± 0	140 ± 1
	B/100-125	88 ± 1	111 ± 1	140 ± 1	109 ± 0	112 ± 0
	B/63-100	75 ± 1	81 ± 1	113 ± 1	78 ± 0	87 ± 3
30 % Co, Extra Coarse WC **C-HM3**	SC	135 ± 1	231 ± 1	374 ± 4	144 ± 3	243 ± 2
	C/>315	261 ± 1	360 ± 8	505 ± 16	350 ± 6	373 ± 9
	C/280-315	226 ± 2	277 ± 1	340 ± 1	274 ± 1	280 ± 1
	C/250-280	209 ± 3	249 ± 1	299 ± 1	247 ± 1	251 ± 1
	C/224-250	149 ± 2	209 ± 1	292 ± 1	202 ± 1	216 ± 1
	C/200-224	159 ± 2	200 ± 1	254 ± 2	197 ± 1	204 ± 1
	C/180-200	145 ± 1	183 ± 0	233 ± 1	181 ± 0	186 ± 1
	C/150-180	128 ± 1	159 ± 0	201 ± 1	157 ± 0	162 ± 1
	C/125-1500	100 ± 1	132 ± 0	175 ± 1	129 ± 0	134 ± 1
	C/100-125	71 ± 1	101 ± 0	137 ± 2	56 ± 1	101 ± 1
	C/63-100	47 ± 1	76 ± 1	107 ± 0	40 ± 0	75 ± 1
D-Iron	D/200-400	256 ± 2	318 ± 2	392 ± 1	314 ± 2	322 ± 2
	D/600-900	637 ± 2	770 ± 4	933 ± 7	763 ± 3	777 ± 4
	D/900-1200	923 ± 2	1080 ± 5	1260 ± 19	1080 ± 5	1100 ± 5
	D/1000-1700	1360 ± 8	1573 ± 5	1827 ± 3	1573 ± 5	1593 ± 5
E-Inox	E/200-400	331 ± 5	417 ± 5	525 ± 6	411 ± 6	423 ± 5
	E/700-1200	850 ± 5	1050 ±5	1360 ± 10	1050 ± 5	1080 ± 5
	E/1000-1700	1123 ± 3	1353 ± 5	1663 ± 10	1343 + 5	1373 ± 5
F-Sand	F/100-800	178 ± 3	275 ± 3	423 ± 3	260 ± 3	289 ± 3
G-Corundum	G/355-500	380 ± 3	506 ± 3	673 ± 4	495 ± 3	519 ± 3

*No sievings performed; HM = hard metal; sample names for iron, inox, sand and corundum granules are selected based on manufacturer information.

Table 15: Granular samples selected for the verification of the empirical model. The table lists important diameters.

Type	Sieving class	d_{10} (µm)	d_{50} (µm)	d_{90} (µm)	$d_{[3,2]}$ (µm)	$d_{[4,3]}$ (µm)
H-HM4	n.A*	115 ± 4	188 ± 5	300 ± 6	173 ± 7	199 ± 5
I-HM5		110 ± 3	182 ± 3	292 ± 3	112 ± 3	191 ± 3
J-HM6		133 ± 1	218 ± 2	330 ± 5	109 ± 3	223 ± 3
K-HM7		121 ± 2	199 ± 2	312 ± 2	161 ± 11	208 ± 2
L-HM8		165 ± 5	244 ± 6	355 ± 7	234 ± 6	254 ± 6
M-HM9		106 ± 3	179 ± 2	289 ± 0	161 ± 4	192 ± 2
N-HM10		113 ± 1	183 ± 1	290 ± 2	171 ± 1	194 ± 2
O-HM11		117 ± 2	199 ± 2	320 ± 3	147 ± 13	210 ± 2
P-HM12		105 ± 6	162 ± 6	247 ± 5	153 ± 7	170 ± 5
Q-HM13		126 ± 2	215 ± 1	348 ± 0	149 ± 2	226 ± 1
R-HM14		132 ± 1	223 ± 1	365 ± 2	134 ± 1	236 ± 1

*No sievings performed; “as-sprayed”.

8.1.2 Bulk Density, tap density and pycnometer density

The bulk and taping density has been measured with the measurement device GranuPack from Granutools (chapter 4.2). The materials' pycnometer density has been determined using the Accupyc II 1240 device from Micromeritics (chapter 4.3). The density curves can be found in appendix 14.2.

Table 16: Bulk, tap and pycnometer density of selected materials. The error is calculated from several measurements. Density values for samples of type A can be found in Table 8.

Sample	Bulk density ρ_b (g/cm^3)	Tap density ρ_{Tap} (g/cm^3)	Pycnometer density (g/cm^3)
SB	3.61 ± 0.01	3.96 ± 0.01	11.43
B/>224	3.54 ± 0.01	3.80 ± 0.01	11.48
B/200-224	3.48 ± 0.01	3.74 ± 0.01	11.44
B/180-200	3.47 ± 0.01	3.73 ± 0.01	11.44
B/150-180	3.46 ± 0.01	3.72 ± 0.01	11.45
B/125-150	3.45 ± 0.01	3.72 ± 0.01	11.43
B/100-125	3.42 ± 0.01	3.70 ± 0.01	11.41
B/63-100	3.40 ± 0.01	3.68 ± 0.01	11.36
SC	2.82 ± 0.01	3.07 ± 0.01	10.18
C/>315	2.85 ± 0.01	3.10 ± 0.01	10.34
C/280-315	2.82 ± 0.01	3.04 ± 0.01	10.24
C/250-280	2.79 ± 0.01	3.00 ± 0.01	10.21
C/224-250	2.77 ± 0.01	3.00 ± 0.01	10.17
C/200-224	2.69 ± 0.01	2.92 ± 0.01	10.22
C/180-200	2.66 ± 0.01	2.89 ± 0.01	10.16
C/150-180	2.62 ± 0.01	2.85 ± 0.01	10.14
C/125-1500	2.59 ± 0.01	2.81 ± 0.01	10.12
C/100-125	2.56 ± 0.01	2.79 ± 0.01	10.08
C/63-100	2.52 ± 0.01	2.75 ± 0.01	10.01
D/200-400	4.35 ± 0.01	4.57 ± 0.01	7.70
D/600-900	4.36 ± 0.01	4.64 ± 0.01	7.68
D/900-1200	4.33 ± 0.01	4.62 ± 0.01	7.70
D/1000-1700	4.20 ± 0.01	4.52 ± 0.01	7.68
E/200-400	4.46 ± 0.01	4.71 ± 0.01	7.65
E/700-1200	4.05 ± 0.01	4.42 ± 0.01	7.65
E/1000-1700	3.80 ± 0.03	4.12 ± 0.02	7.67
F/100-800	1.34 ± 0.01	1.49 ± 0.01	2.66
G/355-500	2.28 ± 0.01	2.46 ± 0.01	3.99

Table 17: Table shows the bulk, tap and pycnometer densities of hard metal granular materials for the empirical model. The error is calculated from two measurements.

Type	**Bulk density ρ_b (g/cm^3)**	**Tap density ρ_{Tap} (g/cm^3)**	**Pycnometer density (g/cm^3)**
H-HM4	3.54 ± 0.01	3.91 ± 0.01	11.42
I-HM5	3.43 ± 0.01	3.83 ± 0.01	11.42
J-HM6	3.10 ± 0.01	3.45 ± 0.01	10.82
K-HM7	3.20 ± 0.01	3.53 ± 0.01	10.92
L-HM8	3.30 ± 0.01	3.63 ± 0.01	10.74
M-HM9	3.12 ± 0.01	3.45 ± 0.01	10.50
N-HM10	3.42 ± 0.01	3.71 ± 0.01	11.28
O-HM11	2.76 ± 0.01	3.04 ± 0.01	9.93
P-HM12	3.19± 0.01	3.43 ± 0.01	10.95
Q-HM13	3.08 ± 0.01	3.40 ± 0.01	10.06
R-HM14	3.10 ± 0.01	3.41 ± 0.01	11.26

8.1.3 Morphology

Figure 89 shows the morphology of a few selected granular materials at the same magnification. It can be seen that the selected materials differ in size, surface roughness, and roundness. More images can be found in appendix 14.3.

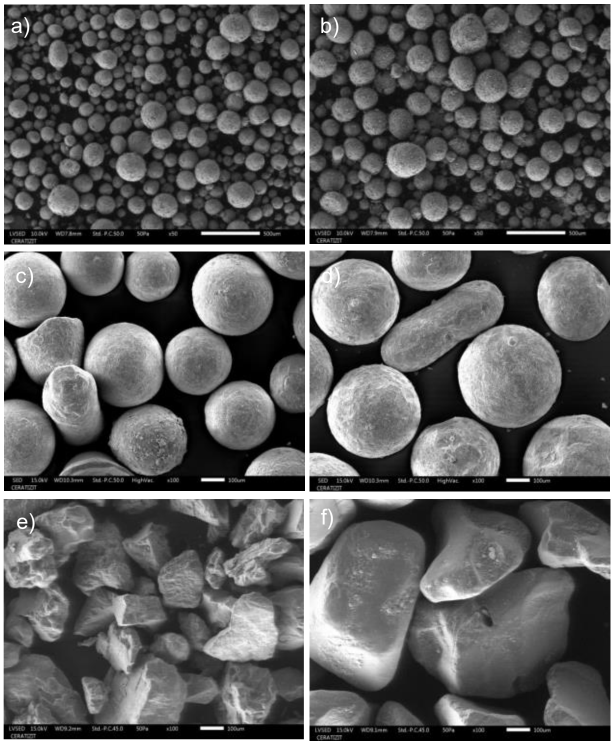

Figure 89: Images from selected powders at 100x magnification: a) SB, b) SC, c) D/200-400, d) E/200-400, e) F/100-800, and f) G/355-500.

8.2 Results and Discussion

8.2.1 The friction coefficient from the angle of repose measurements

The AORs of the selected granular systems from Table 14 have been determined with the proposed method in chapter 5. The friction coefficient for each granular system has then been calculated with the AOR (see chapter 3.2)

In the case of iron (D/200-400 - D/1200-1700) and inox (E/200-400 - E/1000-1700) granular systems, it turned out that the proposed method from chapter 5 was insufficient to determine the AOR. One of the reasons is the blocking effect for system with larges granules. Another reason is the continuous flow on the heap surface while the other side's surface remained static for decentred base plate positions. A similar behaviour of avalanching and static state was also observed in previous investigations (chapter 5.3.2) depending on the decentred position of the base plate. In the case of the finest iron and inox granules D/200-400 and E/200-400, the continuous mass flow along the heap surface resulted in smaller angles α_L than α_R (on the left side). This finding is displayed in Figure 90 for various base plate positions of granular system D/200-400. The same was observed for sample E/200-400. This outcome contradicts the findings presented in chapter 5, where α_L is higher than α_R. for the same base plate positions (left decentred positions). The effect was even more pronounced for larger granular systems of type D (D/600-900-D4) and E (E/700-1200 and E/1000-1700). Aside from this, a bouncing effect of granules on the base plate surface was observed, caused by an elastic collision between a single granule and a flat metallic surface, which prevented a bulking-up of the granules in the early phase of the measurement.

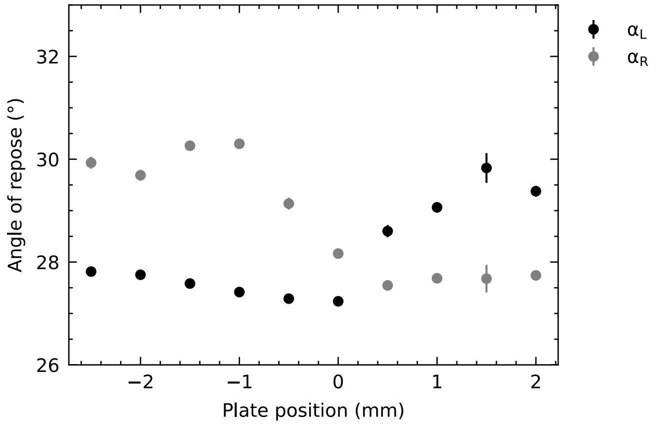

Figure 90: The angles of the finest iron sample D/200-400 for various base plate positions.

Two different phenomena were observed regarding samples sand (F/100-800) and corundum (G/355-500). For sample F/100-800, a continuous mass flow along the heap surface was observed once a maximal heap was formed, similar to samples D/200-400 and E/200-400. Sample G/355-500 showed a blocking effect of the orifice during the measurement. The blocking effect is explainable by the irregular shape of sample G/355-500 (see appendix 14.3), granule diameter and the orifice diameter of 2 mm. Based on these findings, the proposed method can not be entirely applied to the granular systems of type D to G.

To overcome the described experimental difficulties, the AOR, and thus the friction coefficient, has been approximated from a static heap for the systems D/200-400- D/1200-1700, E/200-400- E/1000-1700, F/100-800 and G/355-500. The heap has been created using a funnel with a larger orifice diameter placed above the base plate. The granular system has been discharged onto the base plate. An image has been taken from the static heap and repeated at least five times. The images for each data set are treated with the proposed algorithm from chapter 5. The static friction coefficient μ_s has been calculated with the static AOR (see chapter 3.2).

Figure 91 shows the friction coefficient in function of the Sauter mean diameter $d_{[3,2]}$ for all samples, including the ones already presented in chapter 6.2.1. Friction coefficients acquired from static heap AOR measurements are highlighted with a triangular marker. The hard metal granular systems are clustered and referred to as “A-HM1”, “B-HM2”, and “C-HM3”. These data sets contain samples with the same chemical composition, including unsieved and sieved samples from Table 6 and Table 14. The same is applied to samples of type D to G.

It can be seen from Figure 91 that smaller diameters tend to have higher friction coefficients, being in alignment with the outcomes in chapter 6.2.1. The high friction coefficients for samples F/100-800 and G/355-500 can be explained by the irregular shape of the granules (appendix 14.3), as such shapes are likely to interlock and increase the AOR and, thus, the friction coefficient [73]. As the diameter increases (>300 µm), the friction coefficients goes down and is nearly constant for samples of type D, explainable by the large granular sizes and smooth surfaces (appendix 14.3). Astonishingly, there is a significant difference in the friction coefficient for the samples of type E. Both samples E/700-1200 and E/1000-1700 have a larger granule diameter and are expected to have low friction coefficients compared to sample E/200-400, as discussed in chapter 6.2.1. However, such an outcome is not visible in Figure 91. The granule diameter does not explain the increased friction coefficient for these samples.

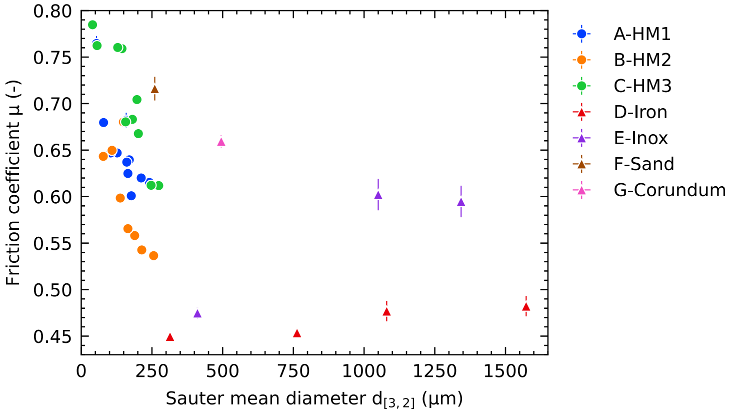

Figure 91: The friction coefficients µ from AOR measurements for different materials. Samples are classified according to their chemical composition and nature.

The friction coefficient for samples D/600-900 - D/1200-1700, E/700-1200 and E/1000-1700 must be critically discussed. A problem arises in correctly determining the AOR (even in a static state) by applying the proposed experimental method in chapter 5 to samples with increased granule diameters. As the granule diameter of these samples increases, the created heaps' surface line becomes more uneven and irregular as the granules' size and shape are more visible in the images (see Figure 92). Applying a linear fit with the proposed algorithm is insufficient to describe correctly such surface lines affecting the acquired AOR (and friction coefficients) significantly. This effect leads to under- or overestimation of the calculated friction coefficients. The proposed experimental method is suggested to be restricted to granular materials with granule diameters lower than 500 µm. This limit is an approximation based on the considered granule diameters listed in Table 14 and related to the current experimental setup.

Figure 92: Cropped exemplary images from the coarsest granular samples D/1200-1700 (left) and E/1000-1700 (right). Images are manually cropped to illustrate differences.

8.2.2 The mass flow rate of granular materials

The mass flow rates have been measured with the GranuFlow device from Granutools (see chapter 4.1). Figure 93 to Figure 96 shows the mass flow rates as a function of the orifice diameter D for all materials in Table 16. In terms of materials, such as iron and inox granules, additional measurements beyond the orifice size of 0.008 m are performed. All figures (Figure 93 to Figure 96) share a common trend: the larger the orifice diameter D, the higher the mass flow rate $\dot{m}$. The measured mass flow rates follow a trend (a guide to the eye) of $\dot{m} \sim D^{2.5}$.

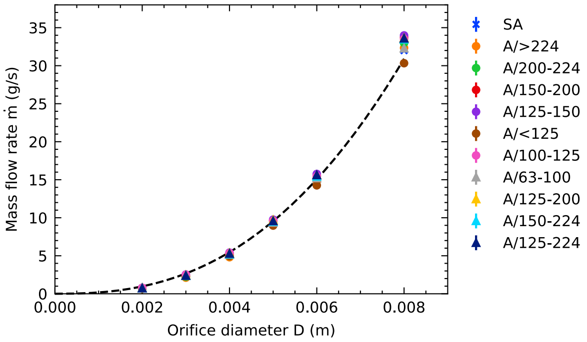

Figure 93: Mass flow rate of sieved and unsieved granular material with 9 % cobalt and submicron WC; trend lines are for guidance and follow the equation $\dot{m} = xD^{2.5}$.

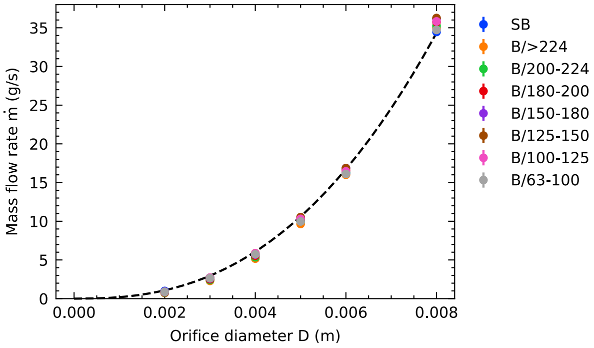

Figure 94: Mass flow rate of sieved and unsieved granular material with 8.2 % cobalt and fine WC; trend lines are for guidance and follow the equation $\dot{m} = xD^{2.5}$.

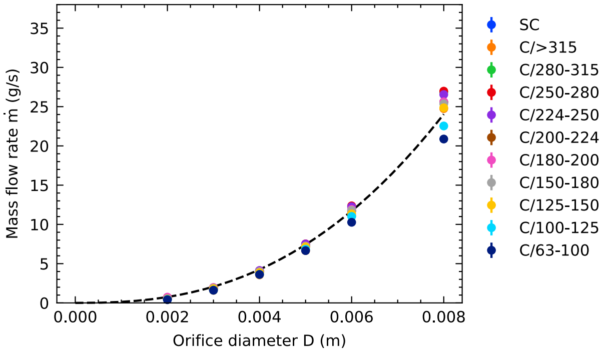

Figure 95: Mass flow rater of sieved and unsieved granular material with 30 % cobalt and extra coarse WC; trend lines are for guidance and follow the equation ṁ = xD$^{2.5}$.

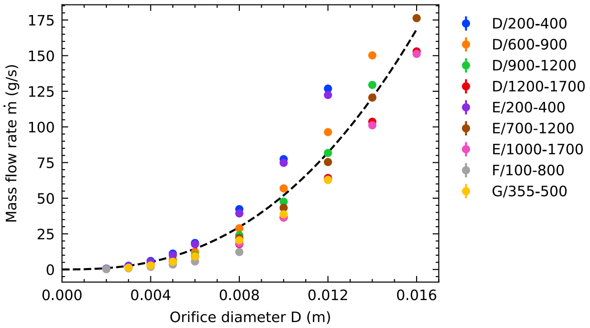

Figure 96: Mass flow rate of iron (D/200-400 – D/1200-1700), inox (E/200-400 – E/1000-1200), sand (F/100-800) and corundum (G/355-500) powders; trend lines are for guidance and follow the equation ṁ = xD$^{2.5}$.

8.2.3 The influence of the attractive forces on the mass flow rate for different materials

The influence of the attractive forces on the mass flow rate is investigated for hard metal granular systems with different chemical compositions, such as the amount of cobalt and tungsten carbide grain size. The granular Bond number expresses the magnitude of the attractive forces between two granules in relation to the gravitational force of a single granule. The granular Bond number is also considered in this chapter. It has been shown in 6.2.3 that the granular Bond number describes two different flow regimes related to the granule mean diameter: (1) an increase in the mass flow rate leading to a maximal mass flow rate with increasing granular Bond number, (2) followed by a decline of the mass flow rate related to an increase of attractive forces.

It is expected that similar influences are present for the granular systems SB and SC. The influence is investigated with sieved samples B/>224 to B/63-100 and C/>315 to C/63-100 with different granule mean diameters (Table 14). The granular Bond number Bo_g is calculated with equation 60 (chapter 3.4.3), considering the granule's pycnometer density from Table 16, the Sauter mean diameter from Table 14 and the Hamaker constant from 6.1.2. Notably, the Hamaker constant depends on the material. It is assumed that the Hamaker constants of sieved and unsieved systems of type B and C are similar to the Hamaker constant of type A (see chapter 6.1.2). Hence, the calculated magnitudes of the granular Bond number only depend on the materials' pycnometer density and granule mean diameter.

Figure 97 and Figure 98 present the mass flow rates measured with an orifice size D of 5 mm in the function of the granular Bond number Bo_g. As expected, similar trends are observed for other orifice sizes D of the same material (see appendix 14.4), aligning with the findings in chapter 6.2.3. Considering the outcomes from chapter 6.2.3, the intersection of the applied fits for types A and B are at similar granular Bond numbers at approximately $Bo_g \approx 0.5$ for a circular orifice diameter of 5 mm. In the case of type C, Figure 98 shows an intersection at lower granular Bond numbers (between 0.1 and 0.2) compared to samples of type A (Figure 65, chapter 6.2.3) and B (Figure 97). This shift is related to the granule composition. Samples of type C contain more cobalt and larger tungsten carbide grain sizes, leading to lower pycnometer densities (Table 16) and, at the same time, having rougher surfaces (appendix 14.3), hindering the mass flow rate by interlocking effects.

The intersection of both fits presented in Figure 65 (chapter 6.2.3), Figure 97 and Figure 98 defines the highest mass flow rate for a specific granular material (orifice diameter of 5 mm). The mean diameter for the highest mass flow rate can be estimated using equation 60, considering the pycnometer densities of the unsieved samples of type A, B and C in Table 8 and Table 16. It turns out that samples of type A and B lead to similar granule mean diameters of about 140 µm, while type C shows the maximum at a mean diameter of about 245 µm. This outcome shows that larger diameters are needed to reach a maximal mass flow rate for hard metal granules of type C, related to the granule properties.

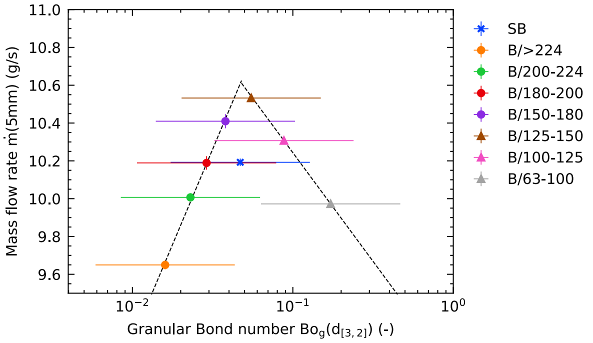

Figure 97: Mass flow rate measured with an orifice size of 5mm in the function of the granular Bond number. The samples are type B. Some errors are smaller than the marker size. Fits are power-law fits.

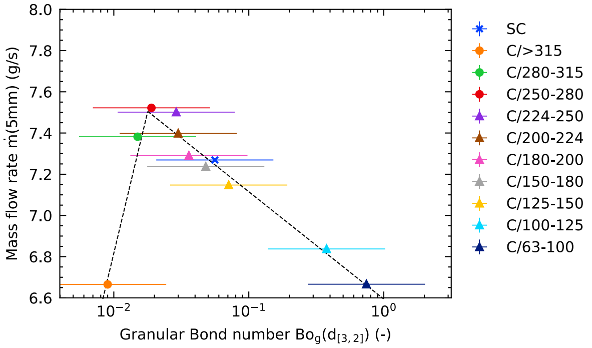

Figure 98: Mass flow rate measured with an orifice size of 5mm in the function of the granular Bond number. The samples are type C. Some errors are smaller than the marker size. Fits are power-law fits.

8.2.4 The effect of attractive forces on the mass flow rate on differing orifice sizes D

The influence of the attractive forces with differing orifice diameter D has been studied with the sieved samples of type B. Figure 99 to Figure 101 presents the mass flow rate for orifice diameters D ranging between 2 and 8 mm. Two power law fits are added in each of the shown graphs, similar to the previous chapter, yielding an intersection point for each figure. Notably, the unsieved sample SB is neglected for the fits as this sample contains every granule from B/>224 to B/63-100. It turns out that the intersections range between granular Bond numbers 0.04 and 0.05 and appear independent of the orifice diameter D, while the mass flow rate increases significantly with the orifice diameter D. A similar outcome is shown for other hard metal granular systems of type A and C in appendix 14.4.

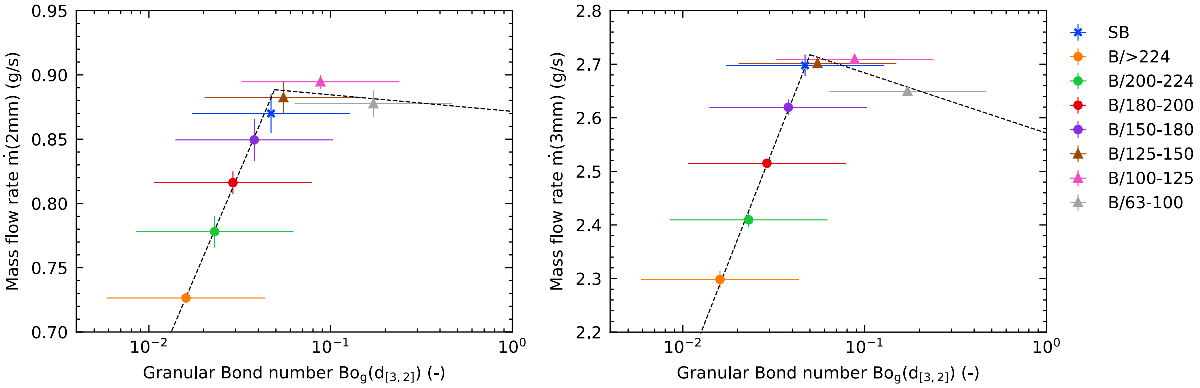

Figure 99: Mass flow rate for two different orifice sizes 2mm (left) and 3mm (right) in the function of the granular Bond number. Both graphs share the same legend. Samples of type B.

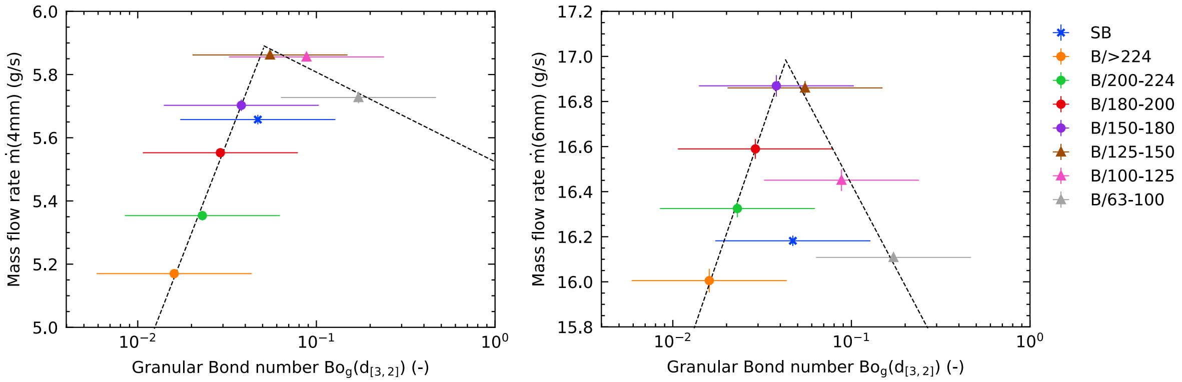

Figure 100: Mass flow rate for two different orifice sizes, 4 mm (left) and 6 mm (right), in the function of the granular Bond number. Both graphs share the same legend. Samples of type B.

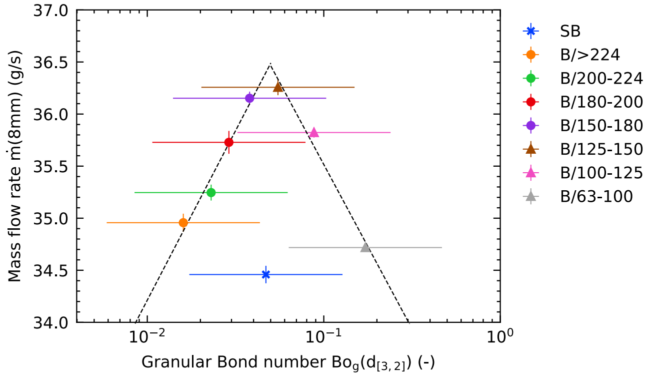

Figure 101: Mass flow rate for two different orifice sizes 8mm in the function of the granular Bond number. Samples of type B.

8.2.5 The minimal orifice diameter D_{min} and the fitting parameter k

The minimal orifice diameter D_{min} describes the smallest orifice diameter D at which blocking occurs. The minimal orifice diameter D_{min} can be determined in two ways: From an extrapolation approach using a linear form of the Beverloo law inside a plot of $\dot{m}^{0.4}(D)$. This is the standard method. Alternatively, the minimal orifice diameter D_{min} is accessed using an experimental setup, where the orifice diameter can be reduced until blocking is reached, as described in chapter 4.1. Both methods are discussed in the following.

8.2.5.1 Determination of the minimal orifice diameter D_{eff} with mass flow measurements

The minimal orifice diameter D_{min} is determined experimentally from mass flow rate measurements using various orifice diameters D. In the first step, the mass flow rates $\dot{m}$ are plotted in the form of $\dot{m}^{0.4}(D)$. Next, the Beverloo Law (equation 35) is brought into a linear form to apply a linear fit to the data set, following:

$$\dot{m}^{0.4} = C^{0.4}\rho_b^{0.4}g^{0.2}(D - kd) \tag{105}$$

The mass flow stops when the granules block the orifice D, which is satisfied when the term kd equals the orifice diameter D and the effective orifice diameter D_{eff} decays to zero ($D_{eff} \rightarrow 0$). Inside a plot of $\dot{m}^{0.4}(D)$, the minimal orifice diameter D_{min} corresponds to the intersection with the abscissa ($\dot{m}^{0.4} = 0$).

$$D_{eff}(\dot{m}^{0.4} = 0) = 0 = D - D_{min} \tag{106}$$

With

$$D_{min} = kd \tag{107}$$

It is visible from equation 107 that the granule diameter affects the magnitude of the minimal orifice diameter D_{min}. Hence, it is expected to have a relationship between both quantities. All samples' minimal orifice diameters D_{min} are displayed in the function of the Sauter mean diameter $d_{[3,2]}$ in Figure 102. The granular systems are clustered, as stated in chapter 8.2.1.

A linear fit is applied to the data set considering all data points. It turns out that the minimal orifice diameter D_{min} scales linearly for granular materials with mean diameters above 50 µm. This outcome is similar to results reported in literature [44], where a linear relationship with the de Brouckere diameter was found. It is assumed that the minimal orifice diameter D_{min} decays to zero when the granule diameter of a system further decreases [44]. Such an assumption can not be confirmed considering the presented data in Figure 102.

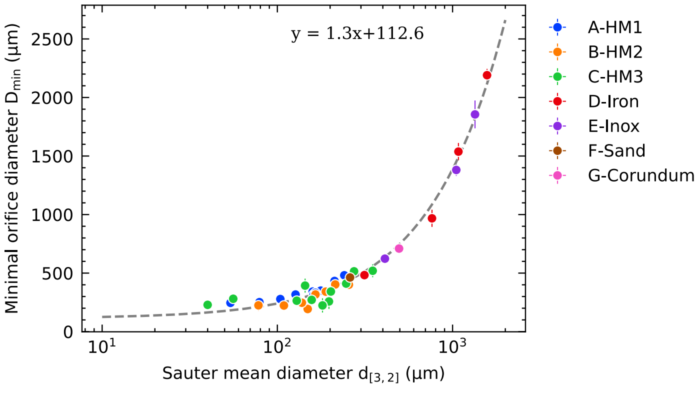

Figure 102: The minimal orifice diameter D_{eff} in the function of the Sauter mean diameter for all samples listed in Table 6 and Table 14. Some error bars are smaller than the marker size. $R^2 \approx 0.98$.

8.2.5.2 The equivalent circular diameter (ECD) from measurements with a diaphragm

The equivalent circle diameter ECD is measured as described in Chapter 4.1. Figure 103 displays the equivalent circle diameter ECD in the function of the Sauter mean diameter $d_{[3,2]}$ from Table 6 and Table 14. The finding shows a linear relationship between both quantities, similar to Figure 102. The slope's magnitude of 3.9 describes the ratio between the ECD and the Sauter mean diameter, as described in chapter 3.3.2.3. In other words, blocking of the orifice occurs when the orifice diameter is nearly four times the Sauter mean diameter. This value is in a similar range stated in the literature [107,109], influenced by the measurement setup.

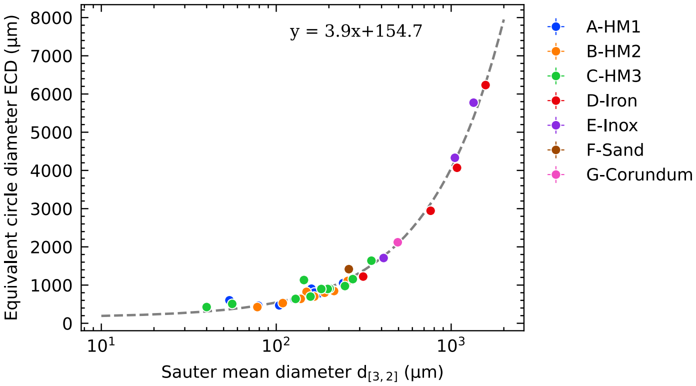

Figure 103: The equivalent circle diameter ECD of the diaphragm at which blocking occurred. The ECD in the function of the Sauter mean diameter. $R^2 \approx 0.99$.

Figure 104 presents the minimal orifice diameter D_{min} (Figure 102) in the function of the equivalent circle diameter ECD from Figure 103. This way, both data sets acquired from the two methods are compared. It can be seen from Figure 104 that a linear relationship exists between both diameters. The ECD appears to lead to larger orifice diameters than the minimal orifice diameters (D_{min}) acquired from mass flow rate measurements. Considering the slope of the applied linear fit, the minimal orifice diameter (D_{min}) is nearly 1/3 of the ECD.

The difference in both diameters arises from two different states: static and dynamic. First, the ECD describes the diameter at which the orifice is blocked, resulting from a static state ($\dot{m} = 0$). In a static state, granular materials block the orifice as an arch [73]. The radius of the arch equals the radius of the orifice, which is influenced by the material's properties. The granules inside the arch are in a force equilibrium between gravitational and frictional forces. A slight increase in the orifice diameter (D > ECD) leads to a collapse of the arch and initiates the material flow through the orifice driven by gravitational forces.

Second, the minimal orifice diameter D_{min} is determined from gravitational mass flow rate measurements referring to a dynamic state ($\dot{m} > 0$) and extrapolation to the static state. The diameter D_{min} describes the reduction of the nominal orifice diameter D during the material flow [7], influenced by dynamic frictions affected by the granule diameter d and all effects inside fitting parameter k, such as the shape of granules [89].

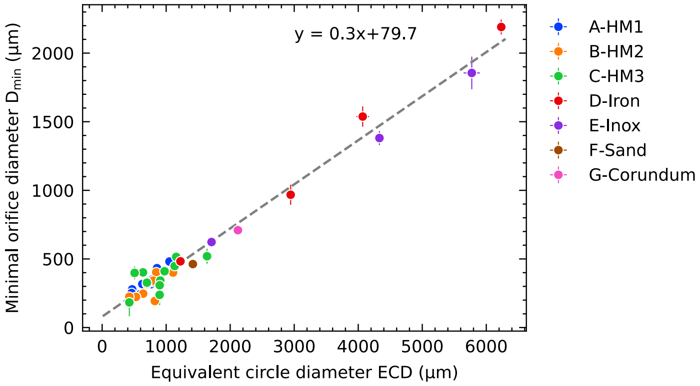

Figure 104: Minimal orifice diameter D_{min} in the function of the equivalent circle diameter ECD. Each data point represents one sample. Errors from ECD stem from several measurements.

8.2.5.3 The effect of attractive forces on the fitting parameter k

This study aims to understand the influences of the attractive forces on the fitting parameter k determined from a dynamical state ($\dot{m} > 0$). The fitting parameter k can be assessed by rearranging equation 107 to equation 108:

$$\mathrm{k} = \frac{D_{min}}{d} \qquad 108$$

The considered diameter, such as d_{50} or de Brouckere (chapter 3.1.3.1 and 3.1.3.2), significantly affects the magnitude of the calculated fitting parameter k. This study selects the Sauter mean diameter $d_{[3,2]}$ as this diameter is sensitive to finer granules in a broad polydisperse size distribution.

Literature shows that cohesive forces affect the fitting parameter k inside the Beverloo Law [88]. In the DEM study, the granular Bond number expresses the cohesive forces' magnitude relative to the gravitational forces (chapter 3.4.3). A similar influence can be studied for hard metal granules by considering the granular Bond numbers from chapter 8.2.3 and the fitting parameter k calculated with equation 108. As the Hamaker constant is identical for all hard metal granular samples, and the pycnometer density is nearly constant, a change in the granular Bond number is mainly caused by a change in the granule mean diameter. The influence of attractive forces will be first discussed for hard metal samples of type A listed in chapter 5.

Figure 105 displays the fitting parameter k in function of the granular Bond number of sample SA. It is visible from Figure 105 that the fitting parameter k is almost constant for a broad range of granular Bond numbers (A1.1, .., A1.3, A2.1, A2.2, A3.1) ranging between 0.01 and 0.04. As the granular Bond number exceeds 0.04, the fitting parameter k sharply increases (k > 2). The sharp increase in the fitting parameter k is explainable by the increasing attraction between granules (i.e. van der Waals forces), reducing over proportionally the nominal diameter D towards an effective orifice diameter (D_{eff} = D- kd) in the Beverloo law, affecting negatively the mass flow rate (see for instance Figure 97 and Figure 98, chapter 8.2.3).

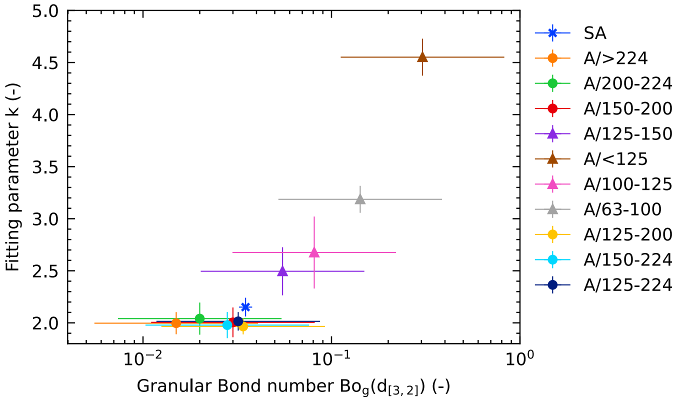

Figure 105: Fitting parameter k in the function of the granular Bond number for samples of type A. The granular Bond number increases as the granule mean diameter decreases.

A similar outcome can be observed when considering other hard metal granular materials of type B and C, as presented in Figure 106. A linear fit adequately describes the relationship between fitting parameter k and the granular Bond number for the presented data. The linear relationship differs from the findings of Anand et al. [88] acquired by DEM simulation, stating that the fitting parameter k increases exponentially ($k = 1.9e^{0.39Bo}$) with increasing granular Bond numbers. The main difference between both relationships, presented in Figure 106 and the results in literature [88] is related to the type of present cohesive forces. The cohesive forces in the DEM study of Anand et al. [88] arise solely from liquid bridging forces between wetted granules, while this study (Figure 106) focuses on the van der Waals forces acting between dry granules.

The presence of liquid bridge forces appears to influence the fitting parameter k stronger than van der Waals forces at higher granular Bond numbers. The exponential increase of fitting parameter k presented in [88] affects the mass flow through the orifice as the granules remain in a “dense” state, i.e. the granules remain close, while flowing through the orifice, increasing the effective diameter d (similar to an agglomerated state) and substantially decreasing the nominal orifice diameter D to an effective orifice diameter D_{eff}.

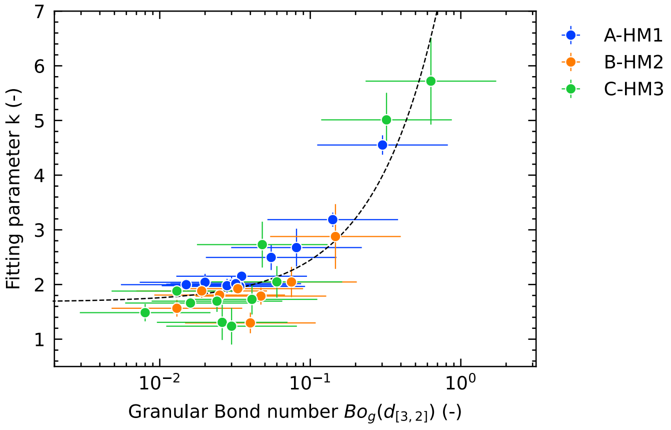

Figure 106: Fitting parameter k in the function of the granular Bond number for three kinds of hard metal granular materials of type A, B and C. The linear fit is y = mx+b and is here for guidance only.

Figure 106 shows that the fitting parameter k follows a linear relationship with the granular Bond number for three different hard metal granular materials. The main difference in the granular Bond number arises from a change in the mean diameter of granules. If other materials are studied, the Hamaker constant and the pycnometer density have to be known. Considering equation 60 (chapter 3.4.3), and assuming that the van der Waals forces are the only cohesive forces for dry uncharged granular systems, then the granular Bond number scales with the mean diameter of $\mathrm{Bo} \sim 1/\mathrm{d}^2$. The fitting parameter k can be described by a function of $f(1/d^2)$, presented in Figure 107. This approach approximates the influence of the mean diameter d on the fitting parameter k for all selected granular materials (A-HM1 to G/Corundum).

Like previous Figure 106, a linear fit adequately describes the relationship between fitting parameter k and the Sauter mean diameter in Figure 107. The linear fit is only applicable when the cohesive forces between the granules for samples of type E/Iron to G/Corundum are minimal with respect to the gravitational forces, i.e., very coarse granular materials. It can be seen from Figure 107 that the majority of the samples D/Iron to G/Corundum are close to the intercept of nearly 1.63. However, as the cohesion forces between granules increase with decreasing mean diameter, the fitting parameter k is expected to deviate from the fit for samples of type D/Iron to G/Corundum, as the van der Waals force is related to the Hamaker constant, which is a material-dependent property

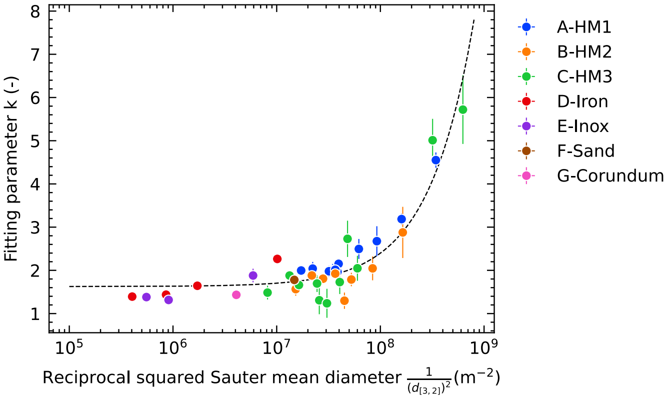

Figure 107: Fitting parameter k in the function of the reciprocal squared Sauter mean diameter. Linear fit of from y = mx+b with $m \approx 7.72 \cdot 10^{-9}$ and $b \approx 1.63$. $R^2 \approx 0.87$.

8.2.6 The fitting parameter C and the friction coefficient

The fitting parameter C can be determined from the slope of the mass flow rate $\dot{m}^{0.4}(D)$ considering the linear form of the Beverloo Law (equation 105) following:

$$C = \left(\frac{w}{g^{1/5} \cdot \rho_b}\right)^{5/2} \tag{109}$$

It can be seen from equation 109 that fitting parameter C is directly influenced by the linear increase (slope w) of the mass flow rate $\dot{m}^{0.4}(D)$ and the bulk density ρ_b of the granular system.

The friction coefficient μ from Figure 91 is considered to study the influence on the fitting parameter C for a range of granular materials. Figure 108 (left) shows the fitting parameter C of hard metal granular systems of type A, B and C in the function of friction coefficient μ measured with the AOR measurement. It can be seen from Figure 108 (left) that the fitting parameter ranges between 0.5 and 0.65, being in common bounds for flat-bottomed orifices [7,86,254]. Overall, the fitting parameter C decreases as the friction coefficient increases. This outcome appears intuitively as a higher friction coefficient impact negatively the granules flow, visible in a decrease of C. A DEM simulation study has also shown such an influence for friction coefficients between 0.125 and 0.875 [87]. Here, the fitting parameter C showed a non-linear decrease within these ranges as the friction coefficient increases [87].

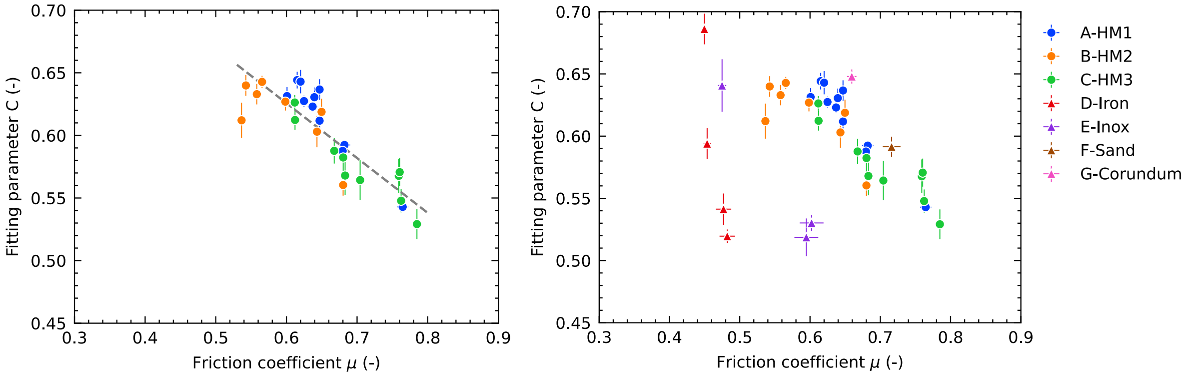

Figure 108: Fitting parameter C from mass flow rate measurements for hard metal granular systems (left) and all samples from Table 14, including samples D to G (right). A linear fit is applied in the form of y = mx+b (for guidance only). Some errors are smaller than the marker size. Friction coefficients determined from static heap measurement are indicated with triangular markers. The largest granular sample of type C (C/>315) is omitted in this graph as this granular system jammed the funnel orifice.

Figure 108 (left) shows that the fitting parameter C decreases linearly with the friction coefficient. When considering other granular systems (Figure 108, right), the friction coefficient μ does not entirely describe a change in the fitting parameter C for a range of materials. For instance, samples F and G consist of irregularly shaped granules (see annexe 14.3), leading to fitting parameters C above 0.59, while the friction coefficients μ range at similar magnitudes of hard metal granules. On the other side, granular material of type D consists of very spherical granules (see annexe 14.3). The fitting parameter C spreads over a broad range while the friction coefficient μ remains nearly constant for spherical granules. Both outcomes imply that the granules' shape does not significantly impact the fitting parameter C. However, the granules’ shape affects the friction coefficient μ from the angle of repose measurement [70].

It is important to remember that the fitting parameter C is influenced by the bulk density ρ_b of the granular material (equation 109). An influence on the outcome in Figure 108 (right) is that the measured bulk density ρ_b is unsuitable to describe the granule density during the flow through the orifice. The influence of the considered density was also briefly discussed in an experimental study [86] for different hopper types, as it is unclear which density is the most suitable to describe the granule density during the flow [255].

8.2.7 Verification of the empirical model for hard metal granules

The outcomes from chapter 8.2.5.3 and 8.2.6 are considered to estimate the mass flow rate for a new set of hard metal granular materials. These granules have been arbitrarily selected and consist of different amounts of tungsten carbide, a metallic binder such as nickel or cobalt and an organic binder. The bulk density and pycnometer density have been measured and listed in Table 17. The granular Bond number Bo_g is calculated assuming similar magnitudes of the Hamaker constant as presented in chapter 6.1.2, the pycnometer densities from Table 17 and the Sauter mean diameters from Table 15. The angle of repose is determined as presented in chapter 5. It is important to note that a reduced measurement procedure is performed over two base plate positions to determine the angle of repose. Then, the friction coefficient μ is calculated from the angle of repose.

Figure 105 and Figure 108 show that C(μ) and $k(Bo_g)$ follow a linear trend. Hence, linear fits are applied to the data sets presented in Figure 105 and Figure 108 (figures not shown here) following a best-fit approach considering the errors in the y and x directions. In the case of C in the function of the friction coefficient (Figure 108), the linear fit in the form of $C(\mu) = m_1\mu+b_1$, where m_1 is the slope and b_1 is the intercept, yields $m_2 = 0.93 \pm 0.03$ and $b_1 = -0.49 \pm 0.04$. The values are acquired from the software Origin, applying a linear fit using the FV method [256]. A linear fit is also applied to the graph of the fitting parameter k in the function of the granular Bond number, yielding the parameters inside the linear fit of $m_2 = 9.1 \pm 2.5$ and $b_2 = 1.6 \pm 0.1$.

The parameters m_1, m_2, b_1 and b_2 are used to estimate the mass flow rate with equation 110, considering all parameters inside the Beverloo law: the bulk density (Table 17), the Sauter mean diameter (Table 15), the orifice diameter D, the friction coefficient μ acquired from the new data set (see appendix Table 18).

$$\dot{m} = (m_1\mu + b_1)\rho_b\sqrt{g}\left(D - \left(m_2 Bo_g + b_2\right)d\right)^{2.5} \quad 110$$

Figure 109 presents the estimated mass flow rate $\dot{m}_{est}$ in function of the measured mass flow rate with an orifice diameter D of 6 mm as described in chapter 4.1. It is visible from Figure 109 that the estimated mass flow rates are close to the measured mass flow rates by using equation 110. However, the absolute errors calculated by error propagation are high, ranging between 0.3 and 0.6 g/s. The relative errors of the estimated mass flow rates range between 4.0 and 6.0 %. The magnitudes of the relative errors remain unchanged for other orifice diameters D, as all other parameters are constants in equation 110.

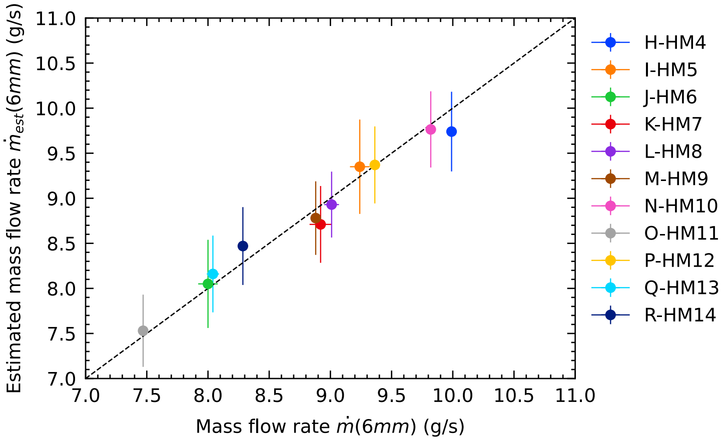

Figure 109: The estimated mass flow rate $\dot{m}_{ext}$ in function of the measured mass flow rate $\dot{m}$ for an orifice diameter of 6 mm. Errors in the measured mass flow rate stem from at least three measurements. The errors from the estimated mass flow rate stem from error propagation, neglecting errors for the gravitational acceleration g and nominal orifice diameter D. Some error bars are smaller than the marker size. The linear line follows y=x and is for guidance only.

The presented errors from Figure 109 can be compared with the literature in two different ways. First, the error of a single measurement stemming from error propagation. Second is the deviation from the ideal linear line (y=x), i.e., the spread of the estimated and measured mass flow rates. Regarding the error of a single estimated mass flow rate, the relative errors of 4 to 6 % in Figure 109 align with the errors of 4 % presented by Medina et al. [115], predicting the mass flow rate from lateral holes.

Calculating the deviation of the estimated and measured mass flows rates (Figure 109) reveals that both mass flow rates spread within ±4 % using equation 110. A spread of ±4 % is small compared to other studies. For instance, Tangri et al. [114] studied experimentally and numerically the influence of the elongated particles on the mass flow rate with simulations and proposed a modified Beverloo Law incorporating the sphericity of particles. The comparison of the estimated and experimental mass flow rates showed that the prediction error ranged between 10 and 20 %. In another study, predicting the mass flow rate with areated funnel-shaped hoppers leads to a spread of the estimated and measured mass flow rate of ±20 % [111]. Furthermore, a DEM study with a bend outlet shows a spread of the mass flow rates within ±8 %. Beverloo et al. [6] presented a spread of 5 % (averaged) and a maximal spread of 12.5 % for a broad range of materials.

The above comparison with literature shows that equation 110 can be used to estimate adequately the mass flow rate for a range of hard metal granule systems. The low spread of ±4 % in Figure 109 can be interpreted in two ways. First, a universal Hamaker constant of $2 \cdot 10^{-22}$ J describes well the Hamaker constant for a broad range of different hard metal compositions. This outcome indicates that the Hamaker constants of these different systems are very close. Second, as the Hamaker constant is identical for all mass flow rate estimations, all parameters inside the modified Beverloo law, such as fitting parameters C, k, and the bulk density and friction coefficient, are dominated by a change of the mean diameter of a granule size distribution. This outcome reveals that the mean diameter primarily affects the mass flow rate and is the dominant parameter to be changed to acquire an optimal mass flow.

It is essential to emphasise that equation 110 is restricted to hard metal granular systems. The error is expected to be higher when considering other materials, as the C(μ) relationship from Figure 104 fails to be linear (see chapter 8.2.6).

8.3 Conclusion and Summary

Measurements with various techniques are performed to understand influences on the mass flow of different granular materials, the friction coefficient and the minimal orifice diameter before jamming happens. The latter is investigated using a diaphragm (static) and through extrapolation of the mass flow rate measured from a cylinder with a flat-bottomed orifice (dynamic). The diameter acquired from the mass flow rate measurements resulted in smaller diameters than those acquired from a static state. In both cases, static and dynamic, the diameter of the jamming is directly related to the granule mean diameter of the granular system. Based on this information, it is possible to estimate the orifice diameter at which jamming occurs from a dynamic measurement.

The influence on the fitting parameters k and C has been investigated considering the granular Bond number and the friction coefficient, respectively. The influence on the fitting parameter C by the friction coefficient μ, determined with the angle of repose measurement, showed a unique picture: the higher the friction coefficient, the lower the fitting parameter C. However, a substantial decrease in the fitting parameter C over a small range of friction coefficients has been found for some granular materials, such as iron granules. The fitting parameter k strongly depends on the cohesive forces described by the granular Bond number, this finding is in line with literature.

The impact of the cohesive forces, expressed by the granular Bond number, on the mass flow rate has also been investigated. The granular Bond number is changed by sieving a reference sample into well-defined fractions with changing mean diameters. With increasing Bond numbers, an increase in the mass flow rate was found, reaching a maximal mass flow rate, which appeared to be independent of the orifice diameter. With increasing granular Bond number, a decrease in the mass flow rate was observed, related to the increasing dominance of the cohesive forces. The maximal flow rate is related to the granule properties, such as the mean diameter. This finding can be considered to optimise the mass flow rate of hard metal granular systems by varying the mean diameter of a polydisperse system. It is worth to mention that granular materials with different polydisperse distributions can have the same mean diameter.

The decrease of the fitting parameter C caused by the increasing friction coefficient and the impact of the granular Bond number on the fitting parameter k is considered to estimate the mass flow rate of hard metal granular materials. The mass flow rate can be adequately estimated for hard metal granular materials. It turns out that the friction coefficient cannot entirely describe the change in the fitting parameter C between different granular materials.

The focus of this study lies on hard metal granules. The relationship of C(μ) and k(Bo_g) of hard metal granules is considered to propose a modified empirical model based on the Beverloo Law. The proposed model is verified with a new set of hard metal granules. The estimated mass flow rates deviate within ±4% of the measured mass flow rates. Furthermore, the relative error of the estimated mass flow rate ranges between 4 and 6 %, which is similar to results reported in literature.

9 Conclusion

This study aims to understand and quantitatively describe the flow behaviour of hard metal granules through an orifice. One of the parameters influencing the mass flow rate is the friction coefficient. The friction coefficient can be determined from angle of repose and rheological measurements. The AOR measurements show that the presence of avalanches and misalignment of the outlet with respect to the base plate significantly affects the magnitude of the angle of repose. The effect of avalanching and misalignment has been minimized by developing a new technique based on the funnel method. The new technique uses a sliding base plate positioned between a camera and a backlight. The camera records granules' bulking and avalanching phase for various plate positions below the outlet. An algorithm, capable of detecting avalanches, was developed allowing to select only images for the final angle of repose calculation which do not present avalanches. The proposed technique enables the determination of the angle of repose for a broad range of hard metal granules.

Applying this technique to other granular systems, such as iron and inox with different mean diameters, showed problems in correctly determining the angle of repose. In the case of iron and inox granules, the elastic impact on the base plate in the initial phase of the measurement affected the bulking phase and the avalanching. The angle of repose of such systems was determined from a static heap and were evaluated using the presented image processing algorithm.

The influence of cohesive forces on the friction coefficient of hard metal granules has been a second main objective. It has been investigated by measuring the attractive forces with atomic force microscopy (AFM). As a result, an effective Hamaker constant could be calculated for a three-component system and used to estimate the attractive (cohesive) forces (here: van der Waals forces) acting between two hard metal granules. Based on these results, granular Bond numbers could be determined for all hard metal systems under study. It could be shown that there exists a clear relationship between the friction coefficient μ and the angle of repose for each granular system. Two outcomes need to be emphasized: First, decreasing the granular Bond number by increasing the granule's mean diameter leads to a minimal friction coefficient. Here, the influence of cohesion is very small, and therefore the friction coefficient is nearly constant. Second, decreasing the granule's diameter increases the granular Bond number which leads to an exponential increase of the friction coefficient. Both outcomes show that the friction coefficient arising from the angle of repose is composed of (1) a low friction coefficient for low Bond numbers and (2) a friction coefficient dominated by cohesive forces (here: van der Waals forces) for high Bond numbers.

The studies of the flow of the hard metal granules through orifices also depicted the influence of cohesive effects. The outcomes showed the presence of two different regions. In the first region, as the granular Bond number increases, decreasing the system's mean diameter increases the mass flow rate, leading to a maximal mass flow rate. As the granular Bond number increases further, the mass flow rate decreases. This is caused by the rise of the attractive forces, which increases the effective mean diameter, expressed by the kd inside the Beverloo law. The particle diameter belonging to the granular Bond number, at which the maximal mass flow rate occurs, is similar for two hard metal systems (A and B), while for one hard metal system (C) containing larger tungsten carbide particles and a higher amount of cobalt it is bigger. This knowledge helps to optimise the granules' mean diameter of a granule size distribution to reach a maximal mass flow rate. However, it is essential to note that different granule size distributions lead to an identical mean diameter.

The influences on fitting parameters C and k were studied. It turned out that the fitting parameter C was affected by the friction coefficient, while the fitting parameter k was influenced by the attractive forces. The relationship of C(μ) and k(Bo_g) were considered to estimate the mass flow rate for a new set of hard metal granules. Comparison of the estimated and measured mass flow rates showed a spread of 4 %, and the error of a single estimate was up to 6 %, being in alignment with the literature.

In order to supplement the above-mentioned investigations, rheological measurements with granular materials have been performed. Rotor-cup measurements as well as plate-cup measurements have been used to access dynamic friction coefficients. As expected, they differ from the static friction coefficients obtained from extrapolation of AOR measurements to infinite granule sizes. Further investigations would certainly shed more light on the link between both quantities.

10 Outlook

The following points are interesting to be further studied:

- Study the attractive forces between pure systems such as WC-WC, Co-Co and organic binder-organic binder systems and any interchangeable combination, such as WC-Co and WC-organic with AFM. The results can be used to calculate Hamaker constants and thus granular Bond numbers for a variety of materials.
- Investigation of the relationship between static and dynamic friction coefficients.

  Study of size and shear rate dependency of shear bands which are a dominating feature in powder rheology.
- Study of the mass flow rate for even smaller hard metal granular systems through orifices. Can the obtained values for the k and C parameters in the Beverloo law be used to find optimized granule properties for the application in an industrial environment?

11 References

[1] P.W. Anderson, More Is Different, Sci. 177. (1972) 393–396. https://doi.org/10.1126/science.177.4047.393.

[2] CERATIZIT Luxembourg S.à r.l., Powder Metallurgy Process Route, (2023).

[3] G.F. Bocchini, Influence of small die width on filling and compacting densities, Powder Metall. 30 (1987) 261–266. https://doi.org/10.1179/pom.1987.30.4.261.

[4] C.-Y. Wu, L. Dihoru, A.C.F. Cocks, The flow of powder into simple and stepped dies, Powder Technol. 134 (2003) 24–39. https://doi.org/10.1016/S0032-5910(03)00130-X.

[5] V.I. Faikin, V.P. Levin, Y.N. Gribenyuk, Influence of the rate of die filling on the density of the powder, Sov. Powder Metall. Met. Ceram. 15 (1976) 590–592. https://doi.org/10.1007/BF01159442.

[6] M. Just, A. Peschiutta Medina, J. Baller, R. Useldinger, Understanding the flow of hard metal powders and pastes, (2022). https://doi.org/10.13140/RG.2.2.27687.93608.

[7] W.A. Beverloo, H.A. Leniger, J. van de Velde, The flow of granular solids through orifices, Chem. Eng. Sci. 15 (1961) 260–269. https://doi.org/10.1016/0009-2509(61)85030-6.

[8] B.J. Crewdson, A.L. Ormond, R.M. Nedderman, Air-Impeded Discharge of Fine Particles from a Hopper, Powder Technol. 16 (1977) 197–207. https://doi.org/10.1016/0032-5910(77)87007-1.

[9] H. Lu, J. Zhong, G.-P. Cao, H.-F. Liu, Gravitational Discharge of Fine Dry Powders with Asperities from a Conical Hopper, Part. Technol. Fluid. 64 (2018) 427–436. https://doi.org/10.1002/aic.15954.

[10] J. Garcia, W. Strelsky, Process development and scale up of cemented carbide production, in: M. Lackner (Ed.), Scale-up Metall., Verlag ProcessEng Engineering GmbH, 2010: pp. 235–266.

[11] E.S. Oran, J.P. Boris, Fluid dynamics, in: R.A. Meyers (Ed.), Encycl. Phys. Sci. Technol., 3rd ed., Academic Press, 2002: pp. 31–43. https://doi.org/10.1016/B0-12-227410-5/00248-9.

[12] M.D. Tousey, The Granulation Process 101 - Basic Technologies for Tablet Making, Pharm. Technol. 26 (2002) 8–13.

[13] J.P. Mallory, D.Q. Adams, The Oxford Introduction to Proto-Indo-European and the Proto-Indo-European World, Oxford University Press, New York, 2006.

[14] C.T. Lewis, C. Short, Harpers Latin Dictionary - A new Latin dictionary founded on the translation of Freund's Latin-German lexicon, Clarendon Press, Oxford, 1891.

[15] H. Douglas, Online Etymology Dictionary, (n.d.). https://www.etymonline.com/word/granular (accessed September 16, 2022).

[16] H. Stahl, Comparing Granulation Methods, 2010. https://www.gea.com/en/binaries/GEA_Pharma_-_Granulation-Methods_-_ART_-_GBpdf_tcm11-16923.pdf.

[17] P. Guigon, O. Simon, K. Saleh, G. Bindhumadhavan, M. J. Adams, J.P.K. Seville, Roll pressing, in: A.D. Salman, M.J. Hounslow, J.P.K. Seville (Eds.), Handb. Powder Technol., Elsevier Science B.V., 2007: pp. 255–288. https://doi.org/10.1016/S0167-3785(07)80040-6.

[18] M. Eslamian, N. Ashgriz, Effect of atomization method on the morphology of spray-generated

particles, J. Eng. Mater. Technol. 129 (2007) 130–142. https://doi.org/10.1115/1.2400270.

[19] R.P. Patel, M.P. Patel, A.M. Suthar, Spray drying technology: an overview, Indian J. Sci. Technol. 2 (2009) 44–47. https://doi.org/10.17485/ijst/2009/v2i10.3.

[20] K.E. Mis Solval, Developing Co-current and Counter-current Spray Drying Computational Fluid Dynamics (CFD) Simulation Studies to Predict the Quality of Microencapsulated Fish Oil with Egg White Hydrolysates Powders, Louisiana State University and Agricultural and Mechanical College, 2015. https://digitalcommons.lsu.edu/gradschool_dissertations/295.

[21] G.M. Walker, Drum Granulation Processes, in: A.D. Salman, M.J. Hounslow, J.P.K. Seville (Eds.), Handb. Powder Technol., 1st ed., Elsevier, Amsterdam, 2007. https://doi.org/10.1016/S0167-3785(07)80039-X.

[22] J.A. Drahun, J. Bridgwater, The mechanisms of free surface segregation, Powder Technol. 36 (1983) 39–53. https://doi.org/10.1016/0032-5910(83)80007-2.

[23] P. Bhatt, A. Kumar, Handbook of pharmaceutical Technology Practical, LAP LAMBERT Academic, 2019.

[24] S. Shanmugam, Granulation techniques and technologies: Recent progresses, BioImpacts. 5 (2015) 55–63. https://doi.org/10.15171/bi.2015.04.

[25] W. Zhai, W. Zhou, S.M.L. Nai, J. Wei, Characterization of nanoparticle mixed 316 L powder for additive manufacturing, J. Mater. Sci. Technol. 47 (2020) 162–168. https://doi.org/10.1016/j.jmst.2020.02.019.

[26] I. Baesso, D. Karl, A. Spitzer, A. Gurlo, J. Günster, A. Zocca, Characterization of powder flow behavior for additive manufacturing, Addit. Manuf. 47 (2021) 102250. https://doi.org/10.1016/j.addma.2021.102250.

[27] M. Cyr, A. Tagnit-Hamou, Particle size distribution of fine powders by LASER diffraction spectrometry. Case of cementitious materials, Mater. Struct. Constr. 34 (2001) 342–350. https://doi.org/10.1007/bf02486485.

[28] M. Kempkes, T. Vetter, M. Mazzotti, Measurement of 3D particle size distributions by stereoscopic imaging, Chem. Eng. Sci. 65 (2010) 1362–1373. https://doi.org/10.1016/j.ces.2009.10.008.

[29] G.A. Loomis, Grain size of whiteware clays as determined by the andreasen pipette, J. Am. Ceram. Soc. 21 (1938) 393–399. https://doi.org/10.1111/j.1151-2916.1938.tb15740.x.

[30] K.L. Dishman, Sieving in Particle Size Analysis, in: R.A. Meyers, R.B. Flippen (Eds.), Encycl. Anal. Chem., 2006. https://doi.org/10.1002/9780470027318.a1514.

[31] M. Li, D. Wilkinson, K. Patchigolla, Comparison of particle size distributions measured using different techniques, Part. Sci. Technol. 23 (2005) 265–284. https://doi.org/10.1080/02726350590955912.

[32] D.J. Muñoz Sierra, C. Lafita, C. Gabaldón, H. Spanjers, J.B. Van Lier, Trace metals supplementation in Anaerobic membrane bioreactors treating highly saline phenolic wastewater Bioresource Technology Trace metals supplementation in anaerobic membrane bioreactors treating highly saline phenolic wastewater, Bioresour. Technol. 234 (2017) 106–114. https://doi.org/10.1016/j.biortech.2017.03.032.

[33] P.B. Kowalczuk, J. Drzymala, Physical meaning of the Sauter mean diameter of spherical particulate matter, Part. Sci. Technol. 34 (2016) 645–647. https://doi.org/10.1080/02726351.2015.1099582.

[34] A. Linke, J. Weiss, R. Kohlus, Factors determining the surface oil concentration of encapsulated lipid particles: impact of the emulsion oil droplet size, Eur. Food Res. Technol. 246 (2020) 1933–1943. https://doi.org/10.1007/s00217-020-03545-5.

[35] E. Piacentini, Droplet Size, in: E. Drioli, L. Giorno (Eds.), Encycl. Membr., Springer Berlin Heidelberg, 2016: pp. 591–592. https://doi.org/10.1007/978-3-662-44324-8_1789.

[36] L. Wang, N.F. Fang, Z.J. Yue, Z.H. Shi, L. Hua, Raindrop Size and Flow Depth Control Sediment Sorting in Shallow Flows on Steep Slopes, Water Resour. Res. 54 (2018) 9978–9995. https://doi.org/10.1029/2018WR022786.

[37] M.P. Hofmann, Physikalische Charakterisierung von Calciumphosphat-Pulvern zur Einstellung von Prozessparametern für die Herstellung von Knochenzement, Julius-Maximilian-Universität würzburg, 2003. https://opus.bibliothek.uni-wuerzburg.de/opus4-wuerzburg/frontdoor/deliver/index/docId/638/file/Druckversion_einseitig.pdf.

[38] Malvern, Basic principles of particle size analysis, 2014. https://www.atascientific.com.au/wp-content/uploads/2017/02/AN020710-Basic-Principles-Particle-Size-Analysis.pdf (accessed January 23, 2022).

[39] R.A. Mugele, H.D. Evans, Droplet Size Distribution in Sprays, Ind. Eng. Chem. 43 (1951) 1317–1324. https://doi.org/10.1021/ie50498a023.

[40] A.H. Lefebvre, V.G. Mcdonell, Atomization and Sprays, CRC Press, London, 2017. https://doi.org/10.1201/9781315120911.

[41] Y.N. Mishra, Droplet size, concentration, and temperature mapping in sprays using SLIPI-based techniques, Lund University, 2018. https://lucris.lub.lu.se/ws/portalfiles/portal/37305834/Thesis_Yogeshwar_without_articles.pdf.

[42] Y.S. Cho, J.S. Laskowski, Effect of flotation frothers on bubble size and foam stability, Int. J. Miner. Process. 64 (2002) 69–80. https://doi.org/10.1016/S0301-7516(01)00064-3.

[43] G.L. Martinez, F. Poursadegh, G.M. Magnotti, K.E. Matusik, D.J. Duke, B.W. Knox, A.L. Kastengren, C.F. Powell, C.L. Genzale, Measurement of sauter mean diameter in diesel sprays using a scattering–absorption measurement ratio technique, Int. J. Engine Res. 20 (2019) 6–17. https://doi.org/10.1177/1468087418819912.

[44] S. Humby, U. Tüzün, A.B. Yu, Prediction of hopper discharge rates of binary granular mixtures, Chem. Eng. Sci. 53 (1998) 483–494. https://doi.org/10.1016/S0009-2509(97)00326-6.

[45] R.A. Werby, A. Mousa, Some Physical and Mechanical Properties of Jatropha Fruits, Misr J. Agric. Eng. 33 (2016) 475–490. https://doi.org/10.21608/mjae.2016.97971.

[46] H.M.B. Al-Hashemi, O.S.B. Al-Amoudi, A review on the angle of repose of granular materials, Powder Technol. 330 (2018) 397–417. https://doi.org/10.1016/j.powtec.2018.02.003.

[47] N.-S. Cheng, K. Zhao, Difference between static and dynamic angle of repose of uniform sediment grains, Int. J. Sediment Res. 32 (2017) 149–154. https://doi.org/10.1016/j.ijsrc.2016.09.001.

[48] L.J. Johnston, J. Goihl, G.C. Shurson, Selected Addtives did not improve flowabilty of DDGS in Commercial Systems, Appl. Eng. Agric. 25 (2009) 75–82. https://doi.org/10.13031/2013.25422.

[49] A. Sangamithra, S.G. John, R. Sorna Prema, K. Nandini, K. Kannan, S. Sasikala, P. Suganya, Moisture dependent physical properties of maize kernels, Int. Food Res. J. 23 (2016) 109–115.

[50] F. Elekes, E.J.R. Parteli, An expression for the angle of repose of dry cohesive granular materials on

Earth and in planetary environments, Proc. Natl. Acad. Sci. 118 (2021). https://doi.org/10.1073/pnas.2107965118.

[51] A.K. Zaalouk, F.I. Zabady, Effect of moisture content on angle of repose and friction coefficient of wheat grain, Misr J. Agric. Eng. 26 (2009) 418–427. https://doi.org/10.21608/mjae.2020.110159.

[52] P. Dunst, P. Bornmann, T. Hemsel, W. Sextro, Vibration-assisted handling of dry fine powders, Actuators. 7 (2018) 1–11. https://doi.org/10.3390/act7020018.

[53] ASTM International, ASTM D6393-21 Standard Test Method for Bulk Solids Characterization by Carr Indices, (2021). https://doi.org/10.1520/D6393-14.

[54] E. Lajeunesse, A. Mangeney-Castelnau, J.P. Vilotte, Spreading of a granular mass on a horizontal plane, Phys. Fluid. 16 (2004) 2371–2381. https://doi.org/10.1063/1.1736611.

[55] H.N. Pitanga, J.P. Gourc, O.M. Vilar, Interface shear strength of geosynthetics: Evaluation and analysis of inclined plane tests, Geotext. Geomembranes. 27 (2009) 435–446. https://doi.org/10.1016/j.geotexmem.2009.05.003.

[56] I.D. Akcali, A. Ince, E. Guzel, Selected Physical Properties of Peanuts, Int. J. Food Prop. 9 (2006) 25–37. https://doi.org/10.1080/10942910500471636.

[57] A. Wójcik, P. Klapa, B. Mitka, J. Sładek, The use of the photogrammetric method for measurement of the repose angle of granular materials, Measurement. 115 (2018) 19–26. https://doi.org/10.1016/j.measurement.2017.10.005.

[58] G. Lumay, F. Boschini, K. Traina, S. Bontempi, J. Remy, R. Cloots, N. Vandewalle, Measuring the flowing properties of powders and grains, Powder Technol. 224 (2012) 19–27. https://doi.org/10.1016/j.powtec.2012.02.015.

[59] C. Willibald, H. Löwe, T. Theile, J. Dual, M. Schneebeli, Angle of repose experiments with snow: Role of grain shape and cohesion, J. Glaciol. 66 (2020) 658–666. https://doi.org/10.1017/jog.2020.36.

[60] P. Li, M. Ucgul, S.-H. Lee, C. Saunders, A new approach for the automatic measurement of the angle of repose of granular materials with maximal least square using digital image processing, Comput. Electron. Agric. 172 (2020) 105356. https://doi.org/10.1016/j.compag.2020.105356.

[61] D. Müller, E. Fimbinger, C. Brand, Algorithm for the determination of the angle of repose in bulk material analysis, Powder Technol. 383 (2021) 598–605. https://doi.org/10.1016/J.POWTEC.2021.01.010.

[62] H. Chen, S. Zhao, X. Zhou, DEM investigation of angle of repose for super-ellipsoidal particles, Particuology. 50 (2020) 53–66. https://doi.org/10.1016/j.partic.2019.05.005.

[63] W.J. Staple, The Influence of Size Distribution on the Bulk Density of Uniformly Packed Glass Particles, Soil Sci. Soc. Am. J. 39 (1975) 404–408. https://doi.org/10.2136/sssaj1975.03615995003900030017x.

[64] H. Chen, Y.L. Liu, X.Q. Zhao, Y.G. Xiao, Y. Liu, Numerical investigation on angle of repose and force network from granular pile in variable gravitational environments, Powder Technol. 283 (2015) 607–617. https://doi.org/10.1016/j.powtec.2015.05.017.

[65] J. Blum, Astrophysical microgravity experiments with dust particles, Microgravity Sci. Technol. 22 (2010) 517–527. https://doi.org/10.1007/s12217-010-9236-3.

[66] K. Miura, K. Maeda, S. Toki, Method of measurement for the angle of repose of sands, Japanese

Geotech. Soc. 37 (1997) 89–96. https://doi.org/10.3208/sandf.37.2_89.

[67] M.A. Madrid, J.M. Fuentes, F. Ayuga, E. Gallego, Determination of the Angle of Repose and Coefficient of Rolling Friction for Wood Pellets, Agronomy. 12 (2022) 424. https://doi.org/10.3390/agronomy12020424.

[68] H. Lu, X. Guo, Y. Liu, X. Gong, Effect of Particle Size on Flow Mode and Flow Characteristics of Pulverized Coal, KONA Powder Part. J. 32 (2015) 143–153. https://doi.org/10.14356/kona.2015002.

[69] Y.C. Zhou, B.H. Xu, A.B. Yu, P. Zulli, An experimental and numerical study of the angle of repose of coarse spheres, Powder Technol. 125 (2002) 45–54. https://doi.org/10.1016/S0032-5910(01)00520-4.

[70] Z.Y. Zhou, R.P. Zou, D. Pinson, A.B. Yu, Angle of repose and stress distribution of sandpiles formed with ellipsoidal particles, Granul. Matter. 16 (2014) 695–709. https://doi.org/10.1007/s10035-014-0522-4.

[71] M. Alizadeh, A. Hassanpour, M. Pasha, M. Ghadiri, A. Bayly, The effect of particle shape on predicted segregation in binary powder mixtures, Powder Technol. 319 (2017) 313–322. https://doi.org/10.1016/j.powtec.2017.06.059.

[72] M. Khanal, M. Elmouttie, D. Adhikary, Effects of particle shapes to achieve angle of repose and force displacement behaviour on granular assembly, Adv. Powder Technol. 28 (2017) 1972–1976. https://doi.org/10.1016/j.apt.2017.04.016.

[73] J.-J. Fu, C. Chen, J.-F. Ferellec, J. Yang, Effect of Particle Shape on Repose Angle Based on Hopper Flow Test and Discrete Element Method, Adv. Civ. Eng. 2020 (2020) 10. https://doi.org/10.1155/2020/8811063.

[74] S. Bhople, A. Kumar, P. Haldkar, Effect of moisture content on angle of repose for different cereals and pulses, Int. J. Chem. Stud. 5 (2017) 2283–2286.

[75] H.M. Jaeger, S.R. Nagel, R.P. Behringer, The physics of granular materials, Am. Inst. Phys. 4 (1996). https://pdodds.w3.uvm.edu/files/papers/others/1996/jaeger1996a.pdf.

[76] G.H.L. Hagen, Über den Druck und Bewegung des trockenen Sandes, Bericht Über Die Zur Bekanntmachung Geeigneten Verhandlungen Der Königlich Preuss. Akad. Der Wissenschaften Zu Berlin. (1852) 35–42.

[77] B.P. Tighe, M. Sperl, G. Heinrich, L. Hagen, Pressure and motion of dry sand : translation of Hagen ' s paper from 1852, Granul. Matter. (2007) 141–144. https://doi.org/10.1007/s10035-006-0027-x.

[78] F.C. Franklin, L.N. Johanson, Flow of granular material through a circular orifice, Chem. Eng. Sci. 4 (1953) 119–129. https://doi.org/10.1016/0009-2509(55)80003-6.

[79] R.T. Fowler, J.R. Glastonrury, The flow of granular solids through orifices, Chem. Eng. Sci. 10 (1958) 150–156. https://doi.org/10.1016/0009-2509(59)80042-7.

[80] S. Sadighpour, P. Mort, R.P. Behringer, Jamming and Flow in 2-D Hopper, (2015). https://www.slideshare.net/sepehr125/jamming-in-hopper.

[81] C. Mankoc, A. Janda, R. Arévalo, J.M. Pastor, I. Zuriguel, A. Garcimartín, D. Maza, The flow rate of granular materials through an orifice, Granul. Matter. 9 (2007) 407–414. https://doi.org/10.1007/s10035-007-0062-2.

[82] P. Lin, S. Zhang, J. Qi, Y.M. Xing, L. Yang, Numerical study of free-fall arches in hopper flows, 417 (2015) 29–40. https://doi.org/10.1016/j.physa.2014.09.032.

[83] A. Guarin, R. Roque, S. Kim, O. Sirin, Disruption factor of asphalt mixtures, Int. J. Pavement Eng. 14 (2015) 472–485. https://doi.org/10.1080/10298436.2012.727992.

[84] D.A. Serrano, G. Ruiz-Chavarría, M. Pliego, C.A. Vargas, A. Medina, On the validity of the Hagen and Beverloo formulas for grains discharge through thin sidewalls of bins, Rev. Mex. Física. 65 (2019) 139–147. https://doi.org/10.31349/revmexfis.65.139.

[85] D.A. Serrano, F. Sanchéz-Silva, J. Klapp, A. Medina, The Hagen-Beverloo law for outflow of granular solids from holes on side walls, Rev. Mex. Física. 61 (2015) 207–210.

[86] R.O. Uñac, A.M. Vidales, O.A. Benegas, I. Ippolito, Experimental study of discharge rate fluctuations in a silo with different hopper geometries, Powder Technol. 225 (2012) 214–220. https://doi.org/10.1016/j.powtec.2012.04.013.

[87] T. Li, H. Zhang, M. Liu, Z. Huang, H. Bo, Y. Dong, DEM study of granular discharge rate through a vertical pipe with a bend outlet in small absorber sphere system, Nucl. Eng. Des. 314 (2017) 1–10. https://doi.org/10.1016/j.nucengdes.2017.01.008.

[88] A. Anand, J.S. Curtis, C.R. Wassgren, B.C. Hancock, W.R. Ketterhagen, Predicting discharge dynamics of wet cohesive particles from a rectangular hopper using the discrete element method (DEM), Chem. Eng. Sci. 64 (2009) 5268–5275. https://doi.org/10.1016/j.ces.2009.09.001.

[89] J. Tierrie, H. Baaj, P. Darmedru, Modeling the relationship between the shape and flowing characteristics of processed sands, Constr. Build. Mater. 104 (2016) 235–246. https://doi.org/10.1016/j.conbuildmat.2015.11.046.

[90] S.D. Liu, Z.Y. Zhou, R.P. Zou, D. Pinson, A.B. Yu, Flow characteristics and discharge rate of ellipsoidal particles in a flat bottom hopper, Powder Technol. 253 (2014) 70–79. https://doi.org/10.1016/j.powtec.2013.11.001.

[91] H.A. Janssen, Versuche über Getreidedruck in Silozellen, Zeitung Verein Dtsch. Ingenieure. 39 (1895) 1045–1049.

[92] B. Saint-Michel, M. Georgelin, S. Deville, A. Pocheau, Wall friction and Janssen effect in the solidification of suspensions, Soft Matter, R. Soc. Chem. 14 (2018) 9498–9510. https://doi.org/10.1039/C8SM01572D.

[93] Y. Bertho, T. Brunet, F. Giorgiutti-Dauphiné, J.P. Hulin, Influence of humidity on granular packings with moving walls, Europhys. Lett. 67 (2004) 955–961. https://doi.org/10.1209/epl/i2004-10157-x.

[94] J.W. Landry, G.S. Grest, S.J. Plimpton, Discrete element simulations of stress distributions in silos: Crossover from two to three dimensions, Powder Technol. 139 (2004) 233–239. https://doi.org/10.1016/j.powtec.2003.10.016.

[95] P.G. De Gennes, T. Boutreux, E. Raphae, Propagation of a pressure step in a granular material: The role of wall friction, Phys. Rev. E. 55 (1997) 5759–5773. https://doi.org/10.1103/PhysRevE.55.5759.

[96] D. Schulze, Powders and Bulk Solids - Behavior, Characterization, Storage and Flow, 1., Springer Berlin, Heidelberg, 2008. https://doi.org/10.1007/978-3-540-73768-1.

[97] K. Saleh, S. Golshan, R. Zarghami, A review on gravity flow of free-flowing granular solids in silos –

Basics and practical aspects, Chem. Eng. Sci. 192 (2018) 1011–1035. https://doi.org/10.1016/j.ces.2018.08.028.

[98] R.L. Brown, J.C. Richards, Kinematics of the Flow of Dry Powders and Bulk Solids, Rheol. Acta. 4 (1965) 153–165. https://doi.org/10.1007/BF01969251.

[99] F. Vivanco, S. Rica, F. Melo, Dynamical arching in a two dimensional granular flow, Granul. Matter. 14 (2012) 563–576. https://doi.org/10.1007/s10035-012-0359-7.

[100] J. Wan, F. Wang, G. Yang, S. Zhang, M. Wang, P. Lin, L. Yang, The influence of orifice shape on the flow rate: A DEM and experimental research in 3D hopper granular flows, Powder Technol. 335 (2018) 147–155. https://doi.org/10.1016/j.powtec.2018.03.041.

[101] S. Dorbolo, L. Maquet, M. Brandenbourger, F. Ludewig, G. Lumay, H. Caps, N. Vandewalle, S. Rondia, M. Mélard, S. Vincent-bonnieu, J. Van Loon, A. Dowson, Influence of the gravity on the discharge of a silo, Granul. Matter. 15 (2013) 263–273. https://doi.org/10.1007/s10035-013-0403-2.

[102] M. Gentzler, G.I. Tardos, Measurement of velocity and density profiles in discharging conical hoppers by NMR imaging, Chem. Eng. Sci. 64 (2009) 4463–4469. https://doi.org/10.1016/j.ces.2009.08.010.

[103] A. Janda, I. Zuriguel, D. Maza, Flow Rate of Particles through Apertures Obtained from Self-Similar Density and Velocity Profiles, Phys. Rev. Lett. 108 (2012) 248001. https://doi.org/10.1103/PhysRevLett.108.248001.

[104] H. Péter, A. Libál, C. Reichhardt, C.J.O. Reichhardt, Crossover from Jamming to Clogging Behaviours in Heterogeneous Environments, Sci. Rep. 8 (2018) 2–10. https://doi.org/10.1038/s41598-018-28256-6.

[105] A. Janda, I. Zuriguel, A. Garcimart, L.A. Pugnaloni, D. Maza, Jamming and critical outlet size in the discharge of a two-dimensional silo, A Lett. J. Explor. Forntiers Phys. 84 (2008) 44002. https://doi.org/10.1209/0295-5075/84/44002.

[106] J.W. Landry, G.S. Grest, Jamming in granular hopper flow, (2005). http://arxiv.org/abs/cond-mat/0506110.

[107] H. Liu, Y. Han, F. Jia, Y. Xiao, H. Chen, S. Bai, H. Zhao, An experimental investigation on jamming and critical orifice size in the discharge of a two-dimensional silo with curved hopper, Adv. Powder Technol. 32 (2021) 88–98. https://doi.org/10.1016/j.apt.2020.11.020.

[108] M.A. Aguirre, J.G. Grande, A. Calvo, L.A. Pugnaloni, J.C. Géminard, Pressure independence of granular flow through an aperture, Phys. Rev. Lett. 104 (2010) 10–13. https://doi.org/10.1103/PhysRevLett.104.238002.

[109] S.S. Park, E.S. Kim, Jamming probability of granular flow in 3D hopper with shallow columns: DEM simulations, Granul. Matter. 22 (2020) 1–13. https://doi.org/10.1007/s10035-020-01050-w.

[110] M.Y. Gundogdu, Discharge Characteristics of Polydisperse Powders through Conical Hoppers . Part 2 : Predictions for Coarse , Granular , Free Flowing Powders, Part. Sci. Technol. 24 (2007) 23–37. https://doi.org/10.1080/02726350500212863.

[111] W. Huang, X. Gong, X. Guo, Z. Dai, H. Liu, L. Zheng, J. Zhao, Y. Xiong, Discharge characteristics of cohesive fine coal from aerated hopper, Powder Technol. 194 (2009) 126–131. https://doi.org/10.1016/j.powtec.2009.03.037.

[112] D. Sun, H. Lu, J. Cao, Y. Wu, X. Guo, X. Gong, Flow mechanisms and solid flow rate prediction of powders discharged from hoppers with an insert, Powder Technol. 367 (2020) 277–284. https://doi.org/10.1016/j.powtec.2020.03.053.

[113] F. Boschini, V. Delaval, K. Traina, N. Vandewalle, G. Lumay, Linking flowability and granulometry of lactose powders, Int. J. Pharm. 494 (2015) 312–320. https://doi.org/10.1016/j.ijpharm.2015.08.030.

[114] H. Tangri, Y. Guo, J.S. Curtis, Hopper discharge of elongated particles of varying aspect ratio: Experiments and DEM simulations, Chem. Eng. Sci. X. 4 (2019) 100040. https://doi.org/10.1016/j.cesx.2019.100040.

[115] A. Medina, D.A. Serrano, G.J. Gutiérrez, K. Kesava Rao, C.A. Vargas, On the mass flow rate of granular material in silos with lateral exit holes, Rev. Mex. Fis. 59 (2013) 261–266. https://doi.org/10.1007/978-3-642-27723-8_21.

[116] ASTM International, ASTM B213-13: Standard Test Methods for Flow Rate of Metal Powders using the Hall Flowmeter Funnel, ASTM Int. (2013). https://doi.org/10.1520/B0213-13.

[117] J.C. Mathews, W. Wu, Model tests of silo discharge in a geotechnical centrifuge, Powder Technol. 293 (2016) 3–14. https://doi.org/10.1016/j.powtec.2015.11.025.

[118] E. Hjortsberg, B. Bergquist, Filling induced density variations in metal powder, Powder Metall. 45 (2002) 146–153.

[119] E.R. Rice, J. Tengzelius, Die Filling Characteristics of Metal Powders, Powder Metall. 29 (1986) 183–194. https://doi.org/10.1179/pom.1986.29.3.183.

[120] R. Kumar, A.K. Jana, S.R. Gopireddy, C.M. Patel, Effect of horizontal vibrations on mass flow rate and segregation during hopper discharge: discrete element method approach, Sādhanā. 45 (2020) 1–13. https://doi.org/10.1007/s12046-020-1300-0.

[121] L. Cai, C. Xiaoping, X. Pan, L. Bo, Z. Changsui, X. Chuanlong, Effect of moisture content on conveying characteristics of pulverized coal for pressurized entrained flow gasification, Exp. Therm. Fluid Sci. 35 (2011) 1143–1150. https://doi.org/10.1016/j.expthermflusci.2011.03.009.

[122] D.F. Heaney, Powders for metal injection molding (MIM), in: D.F. Heaney (Ed.), Handb. Met. Inject. Molding, Woodhead Publishing, 2012: pp. 50–63. https://doi.org/10.1533/9780857096234.1.50.

[123] S. Columbu, M. Mulas, F. Mundula, R. Cioni, Strategies for helium pycnometry density measurements of welded ignimbritic rocks, Meas. J. Int. Meas. Confed. 173 (2021) 108640. https://doi.org/10.1016/j.measurement.2020.108640.

[124] L. Lanzl, K. Wudy, D. Drummer, The effect of short glass fibers on the process behavior of polyamide 12 during selective laser beam melting, Polym. Test. 83 (2020) 106313. https://doi.org/10.1016/j.polymertesting.2019.106313.

[125] D. Huang, G. Sun, K. Lu, Relationship between the flow rate and the packing fraction in the choke area of the two-dimensional granular flow, Phys. Rev. E - Stat. Nonlinear, Soft Matter Phys. 74 (2006). https://doi.org/10.1103/PhysRevE.74.061306.

[126] L. Meng, P. Lu, S. Li, Packing properties of binary mixtures in disordered sphere systems, Particuology. 16 (2014) 155–166. https://doi.org/10.1016/j.partic.2014.02.010.

[127] C.M. Kong, J.J. Lannutti, Effect of agglomerate size distribution on loose packing fraction, J. Am. Ceram. Soc. 83 (2000) 2183–2188. https://doi.org/10.1111/j.1151-2916.2000.tb01533.x.

[128] R.K. McGeary, Mechanical Packing of Spherical Particles, J. Am. Ceram. Soc. 44 (1961) 513–522. https://doi.org/10.1111/j.1151-2916.1961.tb13716.x.

[129] R.M. German, Particulate composites: Fundamentals and applications, Springer, 2016. https://doi.org/10.1007/978-3-319-29917-4.

[130] A.S. Tulina, V.M. Semenov, L.N. Rozanova, T. V. Kuznetsova, N.A. Semenova, Influence of Moisture on the Stability of Soil Organic Matter and Plant Residues, Eurasian Soil Sci. 42 (2009) 1241–1248. https://doi.org/10.1134/S1064229309110064.

[131] G. Lumay, K. Traina, F. Boschini, V. Delaval, A. Rescaglio, R. Cloots, N. Vandewalle, Effect of relative air humidity on the flowability of lactose powders, J. Drug Deliv. Sci. Technol. 35 (2016) 207–212. https://doi.org/10.1016/j.jddst.2016.04.007.

[132] T. Iqbal, J.J. Fitzpatrick, Effect of storage conditions on the wall friction characteristics of three food powders, J. Food Eng. 72 (2006) 273–280. https://doi.org/10.1016/j.jfoodeng.2004.12.007.

[133] L. Dai, Y. Zhulin, G. Lei, G. Conghui, Investigation of wet coal flow characteristics in silos by experiments and simulations, Asia-Pacific J. Chem. Eng. 16 (2021) 1–15. https://doi.org/10.1002/apj.2618.

[134] J. Khanam, A. Nanda, Flow of granules through cylindrical hopper, Powder Technol. 150 (2005) 30–35. https://doi.org/10.1016/j.powtec.2004.11.016.

[135] R. Kobyłka, J. Wiącek, P. Parafiniuk, J. Horabik, M. Bańda, M. Stasiak, M. Molenda, Discharge flow of spherical particles from a cylindrical bin: Experiment and DEM simulations, Processes. 9 (2021). https://doi.org/10.3390/pr9111860.

[136] F.L. Leite, C.C. Bueno, A.L. Da Róz, E.C. Ziemath, O.N. Oliveira, Theoretical models for surface forces and adhesion and their measurement using atomic force microscopy, 2012. https://doi.org/10.3390/ijms131012773.

[137] K. Terzaghi, Theoretical Soil Mechanics, John Wiley & Sons, Inc, 1943. https://doi.org/10.1002/9780470172766.

[138] A. Castellanos, The relationship between attractive interparticle forces and bulk behaviour in dry and uncharged fine powders, Adv. Phys. 54 (2005) 263–376. https://doi.org/10.1080/17461390500402657.

[139] D. McGlinchey, Characterisation of Bulk Solids, Blackwell;CRC Press, Oxford, 2005.

[140] H. Rumpf, Systematische Entwicklung von Verfahren zur Kornvergrößerung durch Agglomerieren, Chemie Ing. Tech. 48 (1974).

[141] H. Zhou, Y. Xiong, Y. Pei, Effect of moisture content on dense-phase pneumatic conveying of pulverized lignite under high pressure, Powder Technol. 287 (2016) 355–363. https://doi.org/10.1016/j.powtec.2015.10.026.

[142] C.D. Willett, S.A. Johnson, M.J. Adams, J.P.K. Seville, Pendular capillary bridges, in: A.D. Salman, M.J. Hounslow, J.P.K. Seville (Eds.), Handb. Powder Technol., Elsevier Science B.V., 2007: pp. 1317–1351. https://doi.org/10.1016/S0167-3785(07)80063-7.

[143] N. Vandewalle, G. Lumay, F. Ludewig, J.E. Fiscina, How relative humidity affects random packing experiments, Phys. Rev. E. 85 (2012) 1–5. https://doi.org/10.1103/PhysRevE.85.031309.

[144] N. Hesse, M.A. Dechet, J.S.G. Bonilla, C. Lübbert, S. Roth, A. Bück, J. Schmidt, W. Peukert, Analysis of tribo-charging during powder spreading in selective laser sintering: Assessment of polyamide 12

powder ageing effects on charging behavior, Polymers (Basel). 11 (2019). https://doi.org/10.3390/polym11040609.

[145] T.A.L. Burgo, C.A. Silva, L.B.S. Balestrin, F. Galembeck, Friction coefficient dependence on electrostatic tribocharging, Sci. Rep. 3 (2013) 1–8. https://doi.org/10.1038/srep02384.

[146] A. Rescaglio, J. Schockmel, F. Francqui, N. Vandewalle, G. Lumay, How tribo-electric charges modify powder flowability, Annu. Trans. Nord. Rheol. Soc. 25 (2017) 17–21. https://nrs.blob.core.windows.net/pdfs/nrspdf-0ff63bbe-bace-4967-bef9-291b63d5382b.pdf.

[147] J.N. Israelachvili, Intermolecular and Surface Forces, 3rd ed., Elsevier Inc., Amsterdam, 2011. https://doi.org/10.1016/C2009-0-21560-1.

[148] X. Wang, S. Ramírez-Hinestrosa, J. Dobnikar, D. Frenkel, The Lennard-Jones potential: When (not) to use it, Phys. Chem. Chem. Phys. 22 (2020) 10624–10633. https://doi.org/10.1039/c9cp05445f.

[149] D. Leckband, J. Israelachvili, Intermolecular forces in biology, Q. Rev. Biophys. 34 (2001) 105–267. https://doi.org/10.1017/s0033583501003687.

[150] H.C. Hamaker, The London-van der Waals attraction between spherical particles, Physica. 4 (1937) 1058–1072. https://doi.org/10.1016/S0031-8914(37)80203-7.

[151] J.M. Valverde, A. Castellanos, A. Ramos, P.K. Watson, Avalanches in fine, cohesive powders, Phys. Rev. E - Stat. Physics, Plasmas, Fluids, Relat. Interdiscip. Top. 62 (2000) 6851–6860. https://doi.org/10.1103/PhysRevE.62.6851.

[152] J.H. Adair, E. Suvaci, J. Sindel, Surface and Colloid Chemistry, in: K.H.J. Buschow, R.W. Cahn, M.C. Flemings, B. Ilschner, E.J. Kramer, S. Mahajan, P. Veyssière (Eds.), Encycl. Mater. Sci. Technol., Elsevier, 2001: pp. 1–10. https://doi.org/10.1016/B0-08-043152-6/01622-3.

[153] I. Dobryden, E. Mensi, A. Holmgren, N. Almqvist, Surface forces between nanomagnetite and silica in aqueous Ca2+ solutions studied with AFM colloidal probe method, Colloids Interfaces. 4 (2020). https://doi.org/10.3390/colloids4030041.

[154] M. Capece, R. Ho, J. Strong, P. Gao, Prediction of powder flow performance using a multi-component granular Bond number, Powder Technol. 286 (2015) 561–571. https://doi.org/10.1016/j.powtec.2015.08.031.

[155] K. Siliveru, C.G. Jange, J.W. Kwek, R.P.K. Ambrose, Granular bond number model to predict the flow of fine flour powders using particle properties, J. Food Eng. 208 (2017) 11–18. https://doi.org/10.1016/j.jfoodeng.2017.04.003.

[156] H.-Y. Xie, The role of interparticle forces in the fluidization of fine panicles, Powder Technol. 94 (1997) 99–108. https://doi.org/10.1016/S0032-5910(97)03270-1.

[157] H. Rumpf, Particle Technology, 1st ed., CHAPMAN AND HALL, London, 1990. https://doi.org/10.1007/978-94-011-7944-7.

[158] Y. Chen, J. Yang, R.N. Dave, R. Pfeffer, Fluidization of Coated Group C Powders, Am. Inst. Chem. Eng. J. 54 (2008) 215–228. https://doi.org/10.1002/aic.11368.

[159] Y.I. Rabinovich, J.J. Adler, A. Ata, R.K. Singh, B.M. Moudgil, Adhesion between nanoscale rough surfaces. I. Role of asperity geometry, J. Colloid Interface Sci. 232 (2000) 10–16. https://doi.org/10.1006/jcis.2000.7167.

[160] T. Young, An Essay on the cohesion of fluids, Phil. Trans. R. Soc. 95 (1805) 65–87. https://doi.org/10.1098/rstl.1805.0005.

[161] X. Yu, S.M. Hörst, C. He, P. McGuiggan, K. Kristiansen, X. Zhang, Surface Energy of the Titan Aerosol Analog "Tholin," Astrophys. J. 905 (2020) 88. https://doi.org/10.3847/1538-4357/abc55d.

[162] M.A. Dupré, Théorie mécanique de la chaleur, 1st ed., Gauthier-Villars, Paris, 1869. https://archive.org/details/thoriemcaniqued00duprgoog/page/n7/mode/2up.

[163] F.M. Fowkes, Attractive Forces at Interfaces, Ind. Eng. Chem. 56 (1964) 40–52. https://doi.org/10.1021/ie50660a008.

[164] D.K. Owens, R.C. Wendt, Estimation of the surface free energy of polymers, J. Appl. Polym. Sci. 13 (1969) 1741–1747. https://doi.org/10.1002/app.1969.070130815.

[165] D.H. Kaelble, K.C. Uy, A Reinterpretation of Organic Liquid - Polytetrafluoroethylene Surface Interactions, J. Adhes. 2 (1970) 50–60.

[166] G. Santner, B. Freytag, D. Ph, J. Juhart, D. Ph, E. Baumgartner, D. Ph, F. Schmied, D. Ph, C. Teichert, D. Ph, Adhesive Power of Ultra High Performance Concrete from a Thermodynamic Point of View, Am. Soc. Civ. Eng. 24 (2012) 1050–1058. https://doi.org/10.1061/(ASCE)MT.1943-5533.0000481.

[167] A.J. Forsyth, S. Hutton, M.J. Rhodes, Effect of cohesive interparticle force on the flow characteristics of granular material, Powder Technol. 126 (2002) 150–154. https://doi.org/10.1016/S0032-5910(02)00046-3.

[168] A.B. Yu, C.L. Feng, R.P. Zou, R.Y. Yang, On the relationship between porosity and interparticle forces, Powder Technol. 130 (2003) 70–76. https://doi.org/10.1016/S0032-5910(02)00228-0.

[169] L.J. Jallo, Y. Chen, J. Bowen, F. Etzler, R. Dave, Prediction of inter-particle adhesion force from surface energy and surface roughness, J. Adhes. Sci. Technol. 25 (2011) 367–384. https://doi.org/10.1163/016942410X525623.

[170] H. Shi, S. Roy, T. Weinhart, V. Magnanimo, S. Luding, Steady state rheology of homogeneous and inhomogeneous cohesive granular materials, Granul. Matter. 22 (2020) 1–20. https://doi.org/10.1007/s10035-019-0968-5.

[171] Y. He, A. Hassanpour, A.E. Bayly, Combined effect of particle size and surface cohesiveness on powder spreadability for additive manufacturing, Powder Technol. 392 (2021) 191–203. https://doi.org/10.1016/j.powtec.2021.06.046.

[172] P. Jop, Y. Forterre, O. Pouliquen, A constitutive law for dense granular flows, Nature. 441 (2006) 727–730. https://doi.org/10.1038/nature04801.

[173] F. Da Cruz, S. Emam, M. Prochnow, J.N. Roux, F. Chevoir, Rheophysics of dense granular materials: Discrete simulation of plane shear flows, Phys. Rev. E. 72 (2005) 021309. https://doi.org/10.1103/PhysRevE.72.021309.

[174] GDR MiDi, On dense granular flows, Eur. Phys. J. E. 14 (2004) 341–365. https://doi.org/10.1140/epje/i2003-10153-0.

[175] E. DeGiuli, M. Wyart, Friction law and hysteresis in granular materials, Proc. Natl. Acad. Sci. U. S. A. 114 (2017) 9284–9289. https://doi.org/10.1073/pnas.1706105114.

[176] J.A. Dijksman, G.H. Wortel, L.T.H. Van Dellen, O. Dauchot, M. Van Hecke, Jamming, yielding, and rheology of weakly vibrated granular media, Phys. Rev. Lett. 107 (2011) 1–4. https://doi.org/10.1103/PhysRevLett.107.108303.

[177] N.J. Van Der Elst, E.E. Brodsky, P.Y. Le Bas, P.A. Johnson, Auto-acoustic compaction in steady shear flows: Experimental evidence for suppression of shear dilatancy by internal acoustic vibration, J.

Geophys. Res. Solid Earth. 117 (2012) 1–18. https://doi.org/10.1029/2011JB008897.

[178] A.W. Jenike, Storage and Flow of solids, Utah Univ., Salt Lake City (USA), 1964. https://digital.library.unt.edu/ark:/67531/metadc1067072/.

[179] ASTM International, ASTM D6128-06 Standard Test Method for Shear Testing of Bulk Solids Using the Jenike Shear Cell, (2013). https://doi.org/10.1520/D6128-06.

[180] D. Schulze, Round robin test on ring shear testers, Adv. Powder Technol. 22 (2011) 197–202. https://doi.org/10.1016/j.apt.2010.10.015.

[181] H. Salehi, D. Barletta, M. Poletto, A comparison between powder flow property testers, Particuology. 32 (2017) 10–20. https://doi.org/10.1016/j.partic.2016.08.003.

[182] X. Zhang, Z. Chen, Y. Liu, Constitutive models, in: X. Zhang, Z. Chen, Y. Liu (Eds.), Mater. Point Method - A Contin. Part. Method Extrem. Load. Cases, Academic Press, 2017: pp. 175–219. https://doi.org/10.1016/B978-0-12-407716-4.00006-5.

[183] R. Lepakshi, B. V. Venkatarama Reddy, Shear strength parameters and Mohr-Coulomb failure envelopes for cement stabilised rammed earth, Constr. Build. Mater. 249 (2020) 118708. https://doi.org/10.1016/j.conbuildmat.2020.118708.

[184] J.W. Carson, H. Wilms, Development of an international standard for shear testing, Powder Technol. 167 (2006) 1–9. https://doi.org/10.1016/j.powtec.2006.04.005.

[185] H.A. Barnes, Q.D. Nguyen, Rotating vane rheometry-a review, J. Nonnewton. Fluid Mech. 98 (2001) 1–14. https://doi.org/10.1016/S0377-0257(01)00095-7.

[186] J.L. Briggs, J.F. Steffe, Z. Ustunol, Vane Method to Evaluate the Yield Stress of Frozen, J. Dairy Sci. 79 (1996) 527–531. https://doi.org/10.3168/jds.S0022-0302(96)76395-6.

[187] Y. Byoungseung, M.A. Rao, Yield Stress and Relative Viscosity of Tomato Concentrates : Effect of Total Solids and Finisher Screen Size, J. Food Sci. 60 (1995) 777–779.

[188] H.A. Barnes, J.O. Carnali, The vane-in-cup as a novel rheometer geometry for shear thinning and thixotropic materials, J. Rheol. (N. Y. N. Y). 34 (1990) 841–866. https://doi.org/10.1122/1.550103.

[189] Q.D. Nguyen, D. V. Boger, Yield Stress Measurement for Concentrated Suspensions, J. Rheol. (N. Y. N. Y). 27 (1983) 321–349. https://doi.org/10.1122/1.549709.

[190] M. Haist, J. Link, D. Nicia, S. Leinitz, C. Baumert, T. von Bronk, D. Cotardo, M. Eslami Pirharati, S. Fataei, H. Garrecht, C. Gehlen, I. Hauschildt, I. Ivanova, S. Jesinghausen, C. Klein, H.W. Krauss, L. Lohaus, D. Lowke, O. Mazanec, S. Pawelczyk, U. Pott, N.W. Radebe, J.J. Riedmiller, H.J. Schmid, W. Schmidt, E. Secrieru, D. Stephan, M. Thiedeitz, M. Wilhelm, V. Mechtcherine, Interlaboratory study on rheological properties of cement pastes and reference substances: comparability of measurements performed with different rheometers and measurement geometries, Mater. Struct. Constr. 53 (2020). https://doi.org/10.1617/s11527-020-01477-w.

[191] C. Tao, E. Rosenbaum, B. Kutchko, M. Massoudi, The Importance of Vane Configuration on Yield Stress Measurements of Cement Slurry, Morgantown, 2020. https://doi.org/10.18141/1614691.

[192] A.S. Gylland, H.P. Jostad, S. Nordal, Failure geometry around a shear vane in sensitive clay, in: NGM 2012 Proc., 2012: pp. 103–110. https://www.researchgate.net/publication/263621089_Failure_geometry_around_a_shear_vane_in_sensitive_clay.

[193] J.J. Assaad, J. Harb, Y. Maalouf, Effect of vane configuration on yield stress measurements of

cement pastes, J. Nonnewton. Fluid Mech. 230 (2016) 31–42. https://doi.org/10.1016/j.jnnfm.2016.01.002.

[194] M. Keentok, J.F. Milthorpe, E. O'Donovan, On the shearing zone around rotating vanes in plastic liquids: theory and experiment, J. Nonnewton. Fluid Mech. 17 (1985) 23–35. https://doi.org/10.1016/0377-0257(85)80003-3.

[195] M. Keentok, The measurement of the yield stress of liquids, Rheol. Acta. 21 (1982) 325–332. https://doi.org/10.1007/BF01515720.

[196] R.C. Daniel, A.P. Poloski, A.E. Sáez, Vane rheology of cohesionless glass beads, Powder Technol. 181 (2008) 237–248. https://doi.org/10.1016/j.powtec.2007.05.003.

[197] D.C.H. Cheng, R. Farley, Comments on the Paper "Rheological Behaviour of Powder in a Rotational Visco-meter" by Hiroshi Kuno and Kozo Kurihara, Rheol. Acta. 5 (1966) 53–56. https://doi.org/10.1007/BF01973580.

[198] A.P. Poloski, P.R. Bredt, R.C. Daniel, A.E. Saez, The contribution of frictional contacts to the shear strength of coarse glass bead powders and slurries, Rheol. Acta. 46 (2006) 249–259. https://doi.org/10.1007/s00397-006-0105-3.

[199] K. Shinohara, Fundamental and Rheological Properties of Powders, in: M.E. Fayed, L. Otten (Eds.), Handb. Powder Sci. Technol., 2nd ed., Chapman & Hall, New York, 1984: pp. 96–145. https://doi.org/10.1007/978-1-4615-6373-0.

[200] K. Shinohara, T. Tanaka, Ultimate tensile strength of cohesive powders based on non-uniform packing model, J. Chem. Eng. Japan. 8 (1975) 50–56. https://doi.org/10.1252/jcej.8.50.

[201] R.P. Behringer, D. Howell, L. Kondic, S. Tennakoon, C. Veje, Predictability and granular materials, Phys. D. 133 (1999) 1–17. https://doi.org/10.1016/S0167-2789(99)00094-9.

[202] Granutools, Granutools, (n.d.). https://www.granutools.com/en/ (accessed May 1, 2022).

[203] Micromeritcs, Gas Displacement Pycnometry System, Brochure. (2019). https://www.micromeritics.com/Product-Showcase/AccuPyc-II-1340.aspx.

[204] B. Han, P. Wang, H. Jin, Z. Hou, X. Bai, Wettability and surface energy of parylene F deposited on PDMS, Phys. Lett. Sect. A Gen. At. Solid State Phys. 384 (2020) 126628. https://doi.org/10.1016/j.physleta.2020.126628.

[205] W.M. Haynes, Handbook of Chemistry and Physics, 97th ed., CRC Press, Boca Raton, 2016. https://doi.org/10.1201/9781315380476.

[206] M. Akram, S. Bhowmik, K.M.B. Jansen, L.J. Ernst, Surface modification of polyimide by atmospheric pressure plasma for adhesive bonding with titanium and its application to aviation and space, in: Int. SAMPE Symp. Exhib., 2010. https://doi.org/10.13140/2.1.3327.0408.

[207] B. Jańczuk, W. Wójcik, A. Zdziennicka, Determination of the components of the surface tension of some liquids from interfacial liquid-liquid tension measurements, J. Colloid Interface Sci. 157 (1993) 384–393. https://doi.org/10.1006/jcis.1993.1200.

[208] Y. Pan, S. Huang, F. Li, X. Zhao, W. Wang, Coexistence of superhydrophilicity and superoleophobicity: Theory, experiments and applications in oil/water separation, J. Mater. Chem. A. 6 (2018) 15057–15063. https://doi.org/10.1039/c8ta04725a.

[209] H. Xie, H. Zhang, J. Song, X. Meng, Y. Wen, L. Sun, High-Precision Automated Micromanipulation and Adhesive Microbonding with Cantilevered Micropipette Probes in the Dynamic Probing Mode,

IEEE/ASME Trans. Mechatronics. 23 (2018) 1425–1435. https://doi.org/10.1109/TMECH.2018.2816957.

[210] M. Just, A. Medina Peschiutta, F. Hippe, R. Useldinger, J. Baller, Determination of the angle of repose of hard metal granules, Powder Technol. 407 (2022) 117695. https://doi.org/10.1016/j.powtec.2022.117695.

[211] J.C. Calllahan, G.W. Cleary, M. Elefant, G. Kaplan, T. Kensler, R.A. Nahs, Equilibirum moisture content of pharmaceutical expicients, Drug Dev. Ind. Pharm. 8 (1982) 355–369. https://doi.org/10.3109/03639048209022105.

[212] Y.B. Guo, L. Yang, D.G. Wang, Preparation and hydrophobic behaviours of polystyrene composite coating, Surf. Eng. 32 (2016) 95–101. https://doi.org/10.1179/1743294415Y.0000000016.

[213] E.J.R. Parteli, J. Schmidt, C. Blümel, K.E. Wirth, W. Peukert, T. Pöschel, Attractive particle interaction forces and packing density of fine glass powders, Sci. Rep. 4 (2014) 1–7. https://doi.org/10.1038/srep06227.

[214] J. Schmidt, E.J.R. Parteli, N. Uhlmann, N. Wörlein, K.E. Wirth, T. Pöschel, W. Peukert, Packings of micron-sized spherical particles – Insights from bulk density determination, X-ray microtomography and discrete element simulations, Adv. Powder Technol. 31 (2020) 2293–2304. https://doi.org/10.1016/j.apt.2020.03.018.

[215] D.C.C. Lam, M. Nakagawa, Effect of Particle Size Distribution Shape in Bimodal Packing, Elsevier B.V., 1994. https://doi.org/10.1016/B978-0-444-81991-8.50032-7.

[216] H.H. Hausner, Friction conditions in a mass of metal powder, Int. J. Powder Metall. 3 (1967) 7–13. https://www.osti.gov/biblio/4566075.

[217] R.O. Grey, J.K. Beddow, On the Hausner Ratio and its Relationship to Some Properties of Metal Powders, Powder Technol. 2 (1969) 323–326. https://doi.org/10.1016/0032-5910(69)80024-0.

[218] P. Li, S.H. Lee, J.S. Park, Development of a global batch clustering with gradient descent and initial parameters in colour image classification, IET Image Process. 13 (2019) 161–174. https://doi.org/10.1049/iet-ipr.2018.5956.

[219] Y.L. Xiao, E. Specht, J. Mellmann, Experimental study of the lower and upper angles of repose of granular materials in rotating drums, Powder Technol. 154 (2005) 125–131. https://doi.org/10.1016/j.powtec.2005.04.040.

[220] G. Bradski, The OpenCV Library, Dr. Dobb's J. Softw. Tools. (2000).

[221] P. Virtanen, R. Gommers, T.E. Oliphant, M. Haberland, T. Reddy, D. Cournape, E. Burovski, P. Peterson, W. Weckesser, J. Bright, S.J. van der Walt, M. Brett, J. Wilson, K.J. Millman, N. Mayorov, A.R.J. Nelson, E. Jones, R. Kern, E. Larson, C.J. Carey, İ. Polat, Y. Feng, E.W. Moore, J. VanderPlas, D. Laxalde, J. Perktold, R. Cimrman, I. Henriksen, E.A. Quintero, C.R. Harris, A.M. Archibald, A.H. Ribeiro, F. Pedregosa, P. van Mulbregt, A. Vijaykumar, A. Pietro Bardelli, A. Rothberg, A. Hilboll, A. Kloeckner, A. Scopatz, A. Lee, A. Rokem, C.N. Woods, C. Fulton, C. Masson, C. Häggström, C. Fitzgerald, D.A. Nicholson, D.R. Hagen, D. V. Pasechnik, E. Olivetti, E. Martin, E. Wieser, F. Silva, F. Lenders, F. Wilhelm, G. Young, G.A. Price, G. Ingold, G.E. Allen, G.R. Lee, H. Dren, I. Probst, J.P. Dietrich, J. Silterra, J.T. Webber, J. Slavič, J. Nothman, J. Buchner, J. Kulick, J.L. Schönberger, J.V. de Miranda Cardoso, J. Reimer, J. Harrington, J.L.C. Rodríguez, J. NunezIglesias, J. Kuczynski, K. Tritz, M. Thoma, M. Newville, M. Kümmerer, M. Bolingbroke, M. Tartre, M. Pak, N.J. Smith, N. Nowaczyk, N. Shebanov, O. Pavlyk, P.A. Brodtkorb, P. Lee, R.T. McGibbon, R. Feldber, S. Lewis, S. Tygier, S.

Sievert, S. Vigna, S. Peterson, S. More, T. Pudlik, T. Oshima, T.J. Pingel, T.P. Robitaille, T. Spura, T.R. Jones, T. Cera, T. Leslie, T. Zito, T. Krss, U. Upadhyay, Y.O. Halchenko, Y. VázquezBaeza, SciPy 1.0: Fundamental Algorithms for Scientific Computing in Python, Nat. Methods. 17 (2020) 261–272. https://doi.org/10.1038/s41592-019-0686-2.

[222] S. Walfish, A Review of Statistical Outlier Methods, Pharm. Technol. 30 (2006) 82–88.

[223] H.S. Kim, S. Park, J.S. Koo, S. Kim, J.Y. Kim, S. Nam, H.S. Park, S. Il Kim, B.W. Park, Risk factors associated with discordant Ki-67 levels between preoperative biopsy and postoperative surgical specimens in breast cancers, PLoS One. 11 (2016) 1–10. https://doi.org/10.1371/journal.pone.0151054.

[224] M. Pirson, M. Dramaix, P. Leclercq, T. Jackson, Analysis of cost outliers within APR-DRGs in a Belgian general hospital: Two complementary approaches, Health Policy (New. York). 76 (2006) 13–25. https://doi.org/10.1016/j.healthpol.2005.04.008.

[225] A. Wójcik, P. Klapa, B. Mitka, I. Piech, The use of TLS and UAV methods for measurement of the repose angle of granular materials in terrain conditions, Measurement. 146 (2019) 780–791. https://doi.org/10.1016/j.measurement.2019.07.015.

[226] O. Macho, K. Demková, L. Gabrišová, M. Cierny, J. Mužíková, P. Galbavá, Ž. Nižnanská, J. Blaško, P. Peciar, R. Fekete, M. Peciar, Analysis of static angle of repose with respect to powder material properties, 60 (2020) 73–80. https://doi.org/10.14311/AP.2020.60.0073.

[227] S. Pillitteri, E. Opsomer, G. Lumay, N. Vandewalle, How size ratio and segregation affect the packing of binary granular mixtures, Soft Matter. 16 (2020) 9094–9100. https://doi.org/10.1039/d0sm00939c.

[228] A. Santomaso, P. Lazzaro, P. Canu, Powder flowability and density ratios: the impact of granules packing, Chem. Eng. Sci. 58 (2003) 2857–2874. https://doi.org/10.1016/S0009-2509(03)00137-4.

[229] Y.M. Wang, Y. Li, J.B. Zheng, A camera calibration technique based on OpenCV, Proc. - 3rd Int. Conf. Inf. Sci. Interact. Sci. ICIS 2010. (2010) 403–406. https://doi.org/10.1109/ICICIS.2010.5534797.

[230] M. Just, A. Medina Peschiutta, F. Hippe, R. Useldinger, J. Baller, Gravitational mass flow measurements of various granular materials in relation to an extended Bond number, Int. J. Refract. Met. Hard Mater. 112 (2023) 106142. https://doi.org/10.1016/j.ijrmhm.2023.106142.

[231] A.G. Cunha, A. Gandini, Turning polysaccharides into hydrophobic materials: A critical review. Part 1. Cellulose, Cellulose. 17 (2010) 875–889. https://doi.org/10.1007/s10570-010-9434-6.

[232] K. Kyziol, J. Oczkowska, D. Kottfer, M. Klich, L. Kaczmarek, A. Kyziol, Z. Grzesik, Physicochemical and biological activity analysis of low-density polyethylene substrate modified by multi-layer coatings based on DLC structures, obtained using RF CVD method, Coatings. 8 (2018). https://doi.org/10.3390/coatings8040135.

[233] D. Budelmann, C. Schmidt, D. Meiners, Adhesion-cohesion balance of prepreg tack in thermoset automated fiber placement. Part 1: Adhesion and surface wetting, Compos. Part C Open Access. 6 (2021) 100204. https://doi.org/10.1016/j.jcomc.2021.100204.

[234] M.N. Abd Rahman, M.F. Dimin, M.Z. Izani, M. Mazliah, Influence of Surface Treatment on the Surface Energy of Tungsten Carbide Inserts, Appl. Mech. Mater. 699 (2014) 38–43. https://doi.org/10.4028/www.scientific.net/amm.699.38.

[235] F. Piscitelli, G. Saccone, A. Gianvito, G. Cosentino, L. Mazzola, Characterization and manufacturing of a paraffin wax as fuel for hybrid rockets, Propuls. Power Res. 7 (2018) 218–230.

https://doi.org/10.1016/j.jppr.2018.07.007.

[236] D.E. Packham, Surface energy, surface topography and adhesion, Int. J. Adhes. Adhes. 23 (2003) 437–448. https://doi.org/10.1016/S0143-7496(03)00068-X.

[237] M. Capece, K.R. Silva, D. Sunkara, J. Strong, P. Gao, On the Relationship of Inter-particle Cohesiveness and Bulk Powder Behavior : Flowability of Pharmaceutical Powders, Int. J. Pharm. 511 (2016) 178–189. https://doi.org/10.1016/j.ijpharm.2016.06.059.

[238] E. Chibowski, R. Perea-Carpio, Problems of contact angle and solid surface free energy determination, Adv. Colloid Interface Sci. 98 (2002) 245–264. https://doi.org/10.1016/S0001-8686(01)00097-5.

[239] C.E. Owens, A.J. Hart, G.H. Mckinley, Improved rheometry of yield stress fluids using bespoke fractal 3D printed vanes, J. Rheol. (N. Y. N. Y). 64 (2020) 643. https://doi.org/10.1122/1.5132340.

[240] T.G. Mezger, The Rheology Handbook, 4th ed., Vincentz Network, Hanover, 2021. https://doi.org/10.1108/ijppm.2010.07959dab.003.

[241] X. Wang, W.W. Carr, D.G. Bucknall, J.F. Morris, High-shear-rate capillary viscometer for inkjet inks, Rev. Sci. Instrum. 81 (2010). https://doi.org/10.1063/1.3449478.

[242] P. V. Liddell, D. V. Boger, Yield stress measurements with the vane, J. Nonnewton. Fluid Mech. 63 (1996) 235–261. https://doi.org/10.1016/0377-0257(95)01421-7.

[243] Y.R. Li, A. Aydin, Behavior of rounded granular materials in direct shear: Mechanisms and quantification of fluctuations, Eng. Geol. 115 (2010) 96–104. https://doi.org/10.1016/j.enggeo.2010.06.008.

[244] A. Fall, G. Ovarlez, D. Hautemayou, C. Mézière, J. Roux, F. Chevoir, Dry granular flows: Rheological measurements of the μ (I) -rheology, J. Rheol. (N. Y. N. Y). 59 (2015) 1065–1080. https://doi.org/10.1122/1.4922653.

[245] H. Dogan, J.L. Kokini, Rheological properties of foods, in: D.R. Heldman, D.B. Lund, C. Sabliov (Eds.), Handb. Food Eng., 2nd ed., CRC Press, Boca Raton, 2006: pp. 1–124. https://doi.org/10.1201/9781420014372.

[246] K. Lu, E. Brodsky, H. Kavehpour, Shear-weakening of the transitional regime for granular flow, J. Fluid Mech. 587 (2007) 347–372. https://doi.org/10.1017/S0022112007007331.

[247] S. Wegner, R. Stannarius, A. Boese, G. Rose, B. Szabó, E. Somfai, T. Börzsönyi, Effects of grain shape on packing and dilatancy of sheared granular materials, Soft Matter. 10 (2014) 5157–5167. https://doi.org/10.1039/c4sm00838c.

[248] K.-L. Lee, F.-L. Yang, Relaxation-type nonlocal inertial-number rheology for dry granular flows, Phys. Rev. E. 96 (2018) 062909. https://doi.org/10.1103/PhysRevE.96.062909.

[249] G. Koval, J.-N. Roux, A. Corfdir, F. Chevoir, Annular shear of cohesionless granular materials: From the inertial to quasistatic regime, Phys. Rev. E. 79 (2009) 021306. https://doi.org/10.1103/PhysRevE.79.021306.

[250] P.E. Peyneau, J.N. Roux, Frictionless bead packs have macroscopic friction, but no dilatancy, Phys. Rev. E - Stat. Nonlinear, Soft Matter Phys. 78 (2008) 011307. https://doi.org/10.1103/PhysRevE.78.011307.

[251] S.B. Savage, M. Sayed, Stresses developed by dry cohesionless granular materials sheared in an annular shear cell, J. Fluid Mech. 142 (1984) 391–430.

https://doi.org/10.1017/S0022112084001166.

[252] R.A. Bagnold, Experiments on a Gravity-Free Dispersion of Large Solid Spheres in a Newtonian Fluid under Shear Article cited in :, Proc. R. Soc. Lond. A. 225 (1954) 49–63. https://doi.org/10.1098/rspa.1954.0186.

[253] M. Just, A. Medina Peschiutta, R. Useldinger, J. Baller, Maximum in Mass Flow Rates of Hard Metal Granules through Circular Orifices in Relation to the Angle of Repose, in: Eur. 2023 Congr. Exhib., European Powder Metallurgy Association (EPMA), Lissabon, 2023. https://doi.org/10.59499/EP235765170.

[254] Z. Zatloukal, Z. Šklubalová, Drained angle of free-flowable powders, Part. Sci. Technol. 26 (2008) 595–607. https://doi.org/10.1080/02726350802501369.

[255] T.M. Verghese, R.M. Nedderman, The discharge of fine sands from conical hoppers, Chem. Eng. Sci. 50 (1995) 3143–3153. https://doi.org/10.1016/0009-2509(95)00165-2.

[256] G. Fasano, R. Vio, Fitting a Straight Line with Errors on both Coordinates, Bull. d'Information Du Cent. Donnees Stellaires. 35 (1988) 191–196. https://ui.adsabs.harvard.edu/abs/1988BICDS..35..191F/abstract.

12 Acknowledgements

This research was funded in whole, or in part, by the Luxembourg National Research Fund (FNR), grant reference [13320318]. I want to thank the Luxembourg National Research Fund (FNR) for their support in starting the PhD in the field of physics within the framework of the Industrial Fellowships.

Gratitude goes to CERATIZIT Luxembourg S.à r.l. and the University of Luxembourg for the collaboration and for their support during this thesis. Furthermore, I would like to thank Dr. Ralph Useldinger, Dr. Roland Sanctuary and Dr. Jörg Baller for their supervision. Additionally, I would like to thank once more Dr Jörg Baller and Dr Ralph Useldinger for sharing exciting moments over the last few years. Your input and unlimited support helped me to progress in the scientific field and develop new skills for my career.

I want to thank the jury members of the defence for their time to evaluate my thesis.

Also, gratitude goes to Dr. Frankie Hippe for his support. I would like to thank Alexander Medina Peschiutta for a great time, creativity and exciting discussions about science and economy.

I want to thank Ricardo Jorge Goncalinho Poeira for their support in measuring granular materials' surface roughness. Additionally, Evandro Martin Lanzoni for the support of the preparation and helping in the atomic force microscopy measurements. Furthermore, I would like to thank Victor da Silva of the Physics of Living Matter Group (University of Luxembourg) for supporting me with the contact angle measurements.

I want to strongly thank the support by the Physics of Advanced Materials group, represented by Olga Astasheva, Sergey Ershov, Ulrich Siegel and Patricia Ramoa.

I want to thank Eric Lemans, Daniel Goddard and Jörg Louis from CERATIZIT Luxembourg S.à r.l. for their creative ideas and support in constructing the angle of repose measurement device.

I am thankful to my parents and brother. Furthermore, I am very grateful to my wife, who endlessly supported me during the thesis. Thanks to you, I am who I am.

13 Publications

Journal Paper

M. Just, A. Medina Peschiutta, F. Hippe, R. Useldinger, J. Baller, Determination of the angle of repose of hard metal granules, Powder Technol. 407 (2022) 117695. https://doi.org/10.1016/j.powtec.2022.117695.

M. Just, A. Medina Peschiutta, F. Hippe, R. Useldinger, J. Baller, Gravitational mass flow measurements of various granular materials in relation to an extended Bond number, Int. J. Refract. Met. Hard Mater. 112 (2023) 106142. https://doi.org/10.1016/j.ijrmhm.2023.106142.

Conference Paper

M. Just, A. Peschiutta Medina, F. Hippe, R. Useldinger, J. Baller, Gravitational mass flow measurements of various granular materials in relation to an extended Bond number, 20th Plansee Semin., 2022.

M. Just, A. Medina Peschiutta, R. Useldinger, J. Baller, Maximum in Mass Flow Rates of Hard Metal Granules through Circular Orifices in Relation to the Angle of Repose, in: Eur. 2023 Congr. Exhib., European Powder Metallurgy Association (EPMA), Lissabon, 2023. https://doi.org/10.59499/EP235765170.

A. Medina Peschiutta, M. Just, R. Useldinger, J. Baller, Comparative Analysis of Methods for Determining the Critical Binder Volume Concentration in Hard Metal Pastes, in: Eur. 2023 Congr. Exhib., European Powder Metallurgy Association (EPMA), Lissabon, 2023. https://doi.org/10.59499/EP235764669.

Poster

M. Just, A. Peschiutta Medina, J. Baller, R. Useldinger, Understanding the flow of hard metal powders and pastes, MRT/DPhyMS PhD day and DPPM General Assembly 2022

M. Just, A. Peschiutta Medina, J. Baller, R. Useldinger, Maximum in Mass Flow Rates of Hard Metal Granules through Circular Orifices in Relation to the Angle of Repose, EuroPM 2023, 2023

14 Appendix

14.1 Granule size distribution

Information can be found in the corresponding chapters.

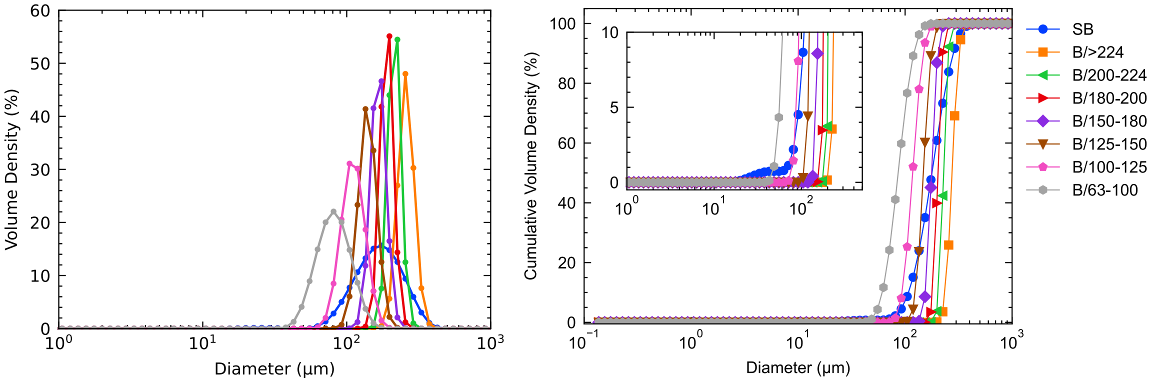

Figure 110: Granule size distribution (left) and cumulated granule size distribution of type B. Both figures share the same legend.

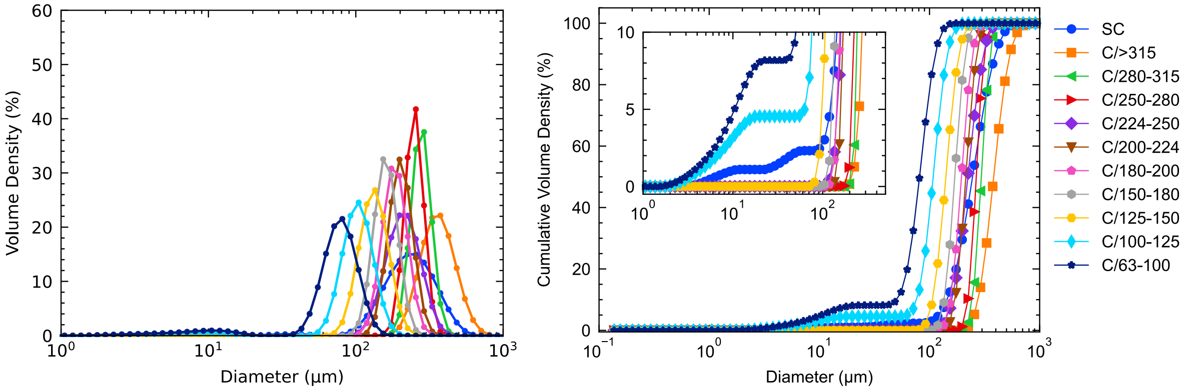

Figure 111: Granule size distribution (left) and cumulated granule size distribution of type C. Both figures share the same legend.

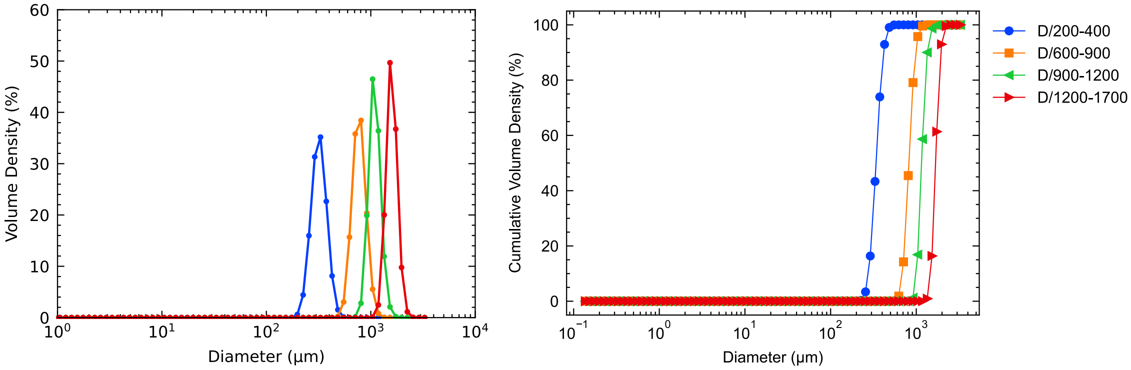

Figure 112: Granule size distribution (left) and cumulated granule size distribution of type D. Both figures share the same legend.

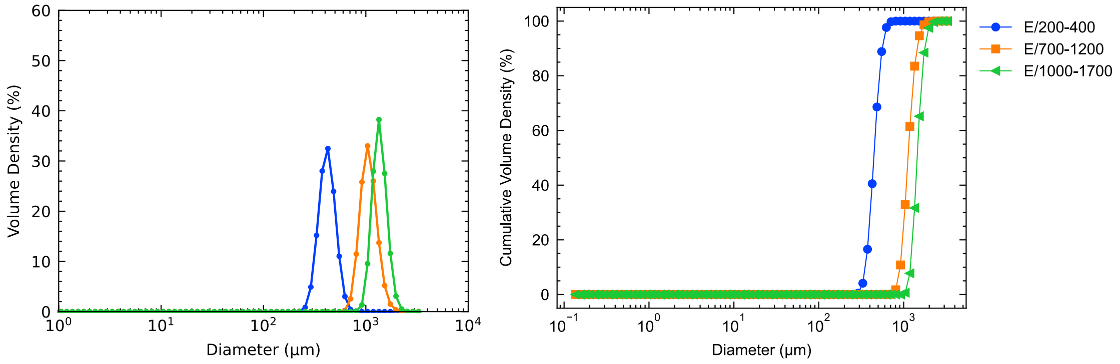

Figure 113: Granule size distribution (left) and cumulated granule size distribution of type E. Both figures share the same legend.

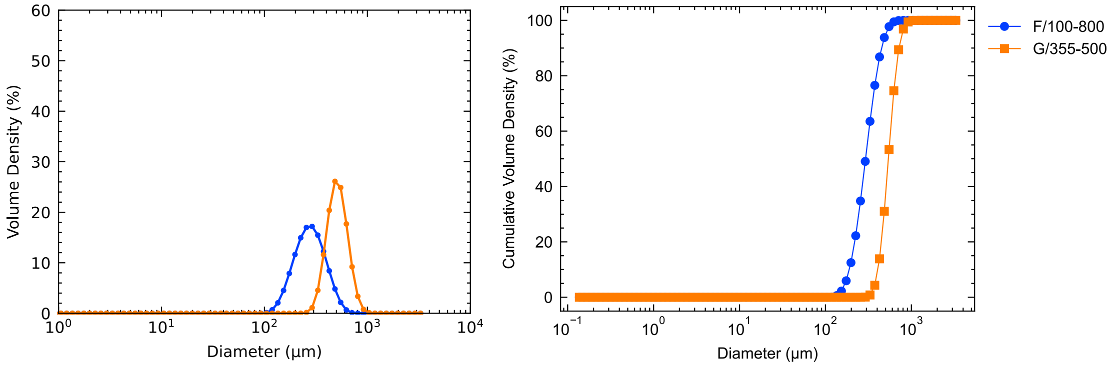

Figure 114: Granule size distribution (left) and cumulated granule size distribution of type F and G. Both figures share the same legend.

14.2 Densification of granular samples

Information can be found in the corresponding chapters.

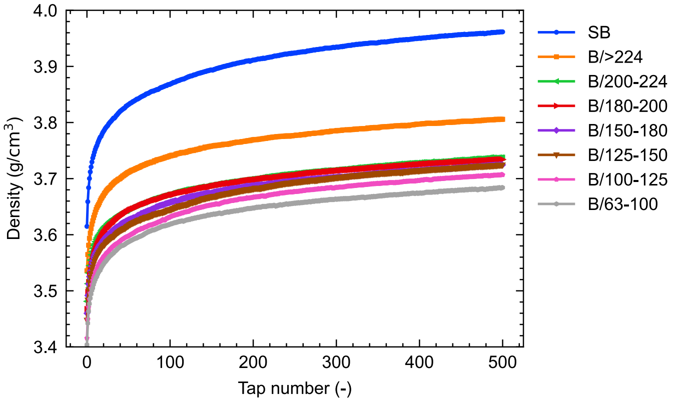

Figure 115: Densification of granular material of type B in the function of the tap number. The graph shows a single measurement for each sample.

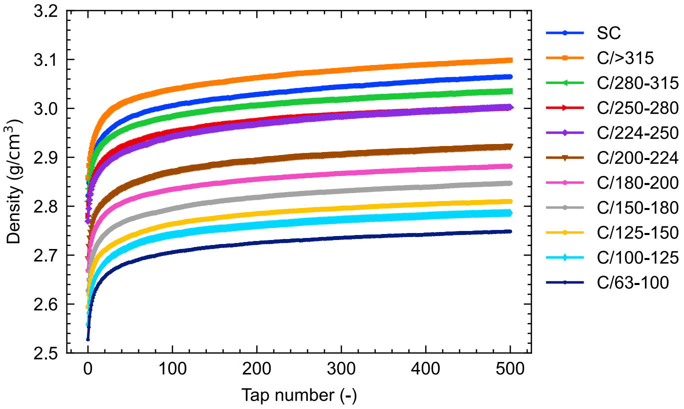

Figure 116: Densification of granular material of type C in the function of the tap number. The graph shows a single measurement for each sample

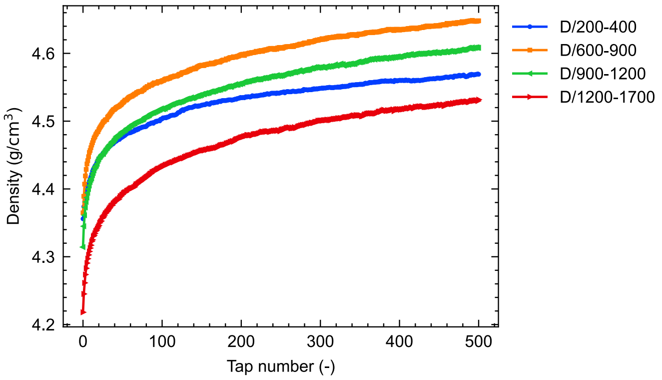

Figure 117: Densification of granular material of type D in the function of the tap number. The graph shows a single measurement for each sample.

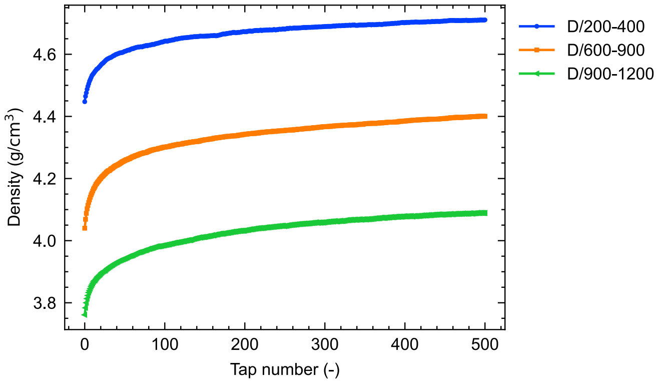

Figure 118: Densification of granular material of type E in the function of the tap number. The graph shows a single measurement for each sample.

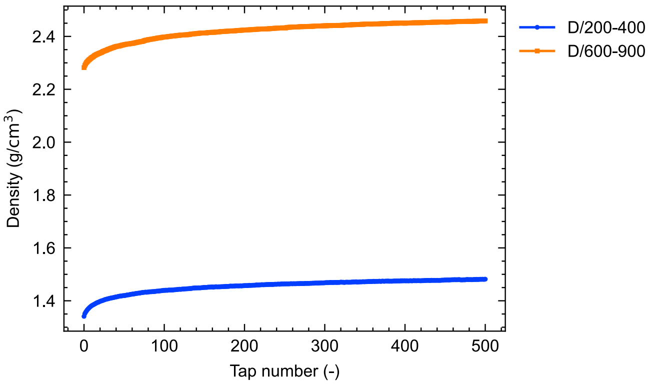

Figure 119: Densification of granular material of type F and G in the function of the tap number. The graph shows a single measurement for each sample.

14.3 Morphology of granular materials

Information can be found in the corresponding chapters.

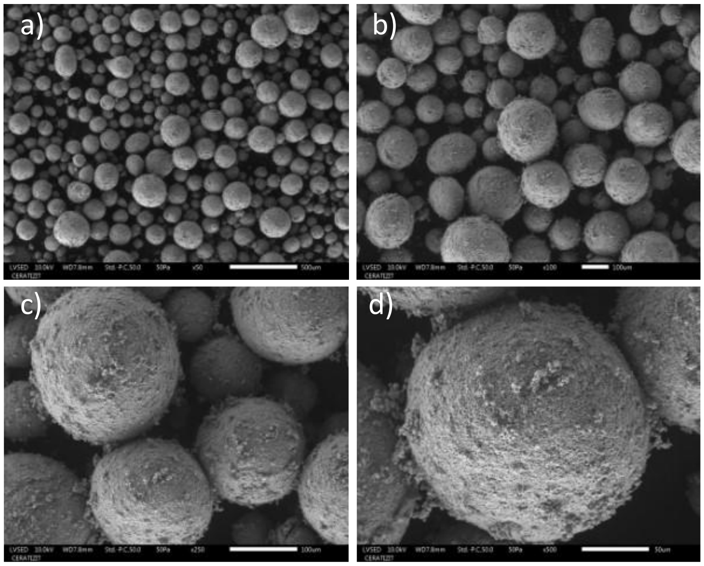

Figure 120: Sample SB at various magnifications: a) 50x, b) 100x, c) 250x, d) 500x. All sieved samples stem from this sample.

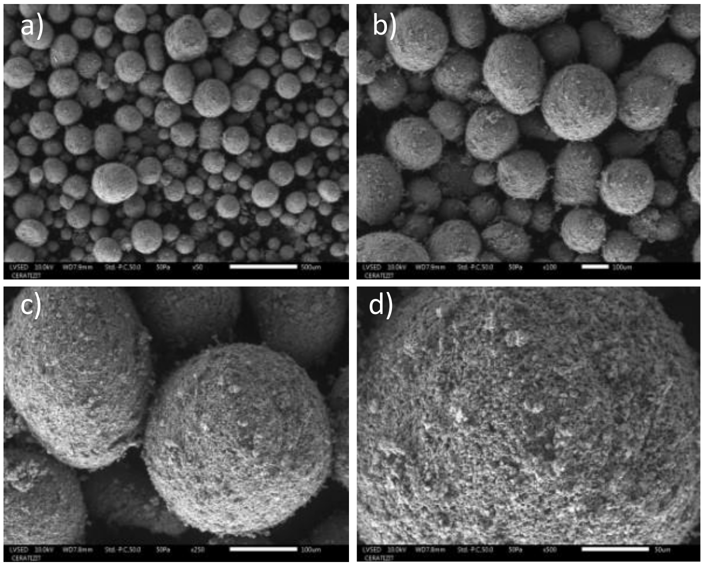

Figure 121: Sample SC at various magnifications: a) 50x, b) 100x, c) 250x, d) 500x. All sieved samples stem from this sample.

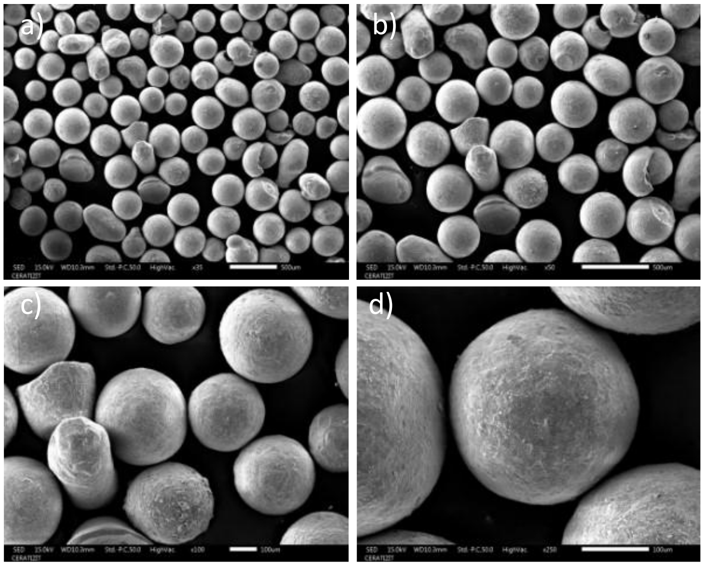

Figure 122: Sample D/200-400 at various magnifications: a) 35x, b) 50x, c) 100x, d) 250x

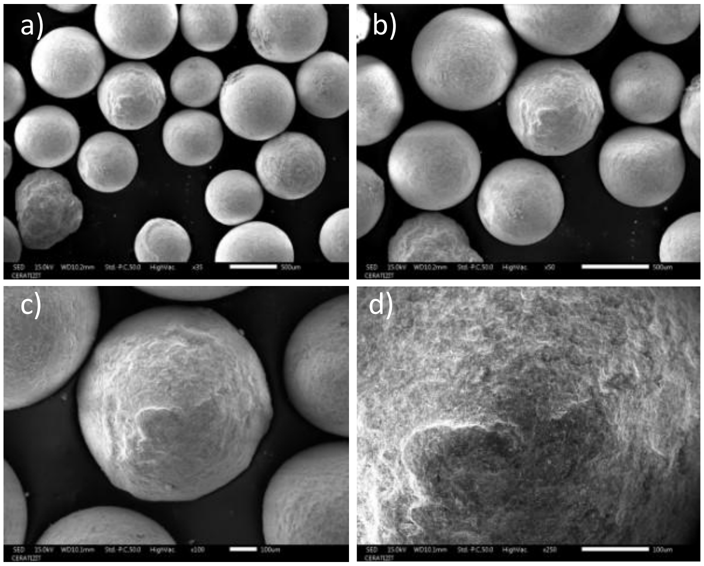

Figure 123: Sample D/600-900 at various magnifications: a) 35x, b) 50x, c) 100x, d) 250x

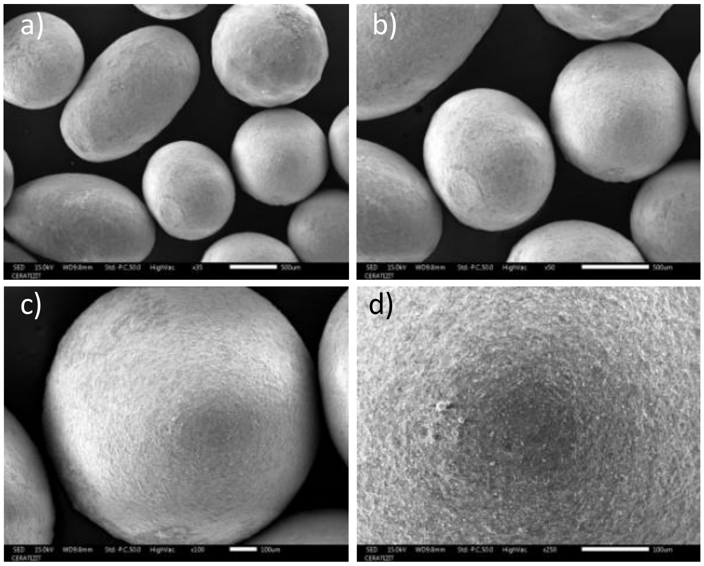

Figure 124: Sample D/900-1200 at various magnifications: a) 35x, b) 50x, c) 100x, d) 250x

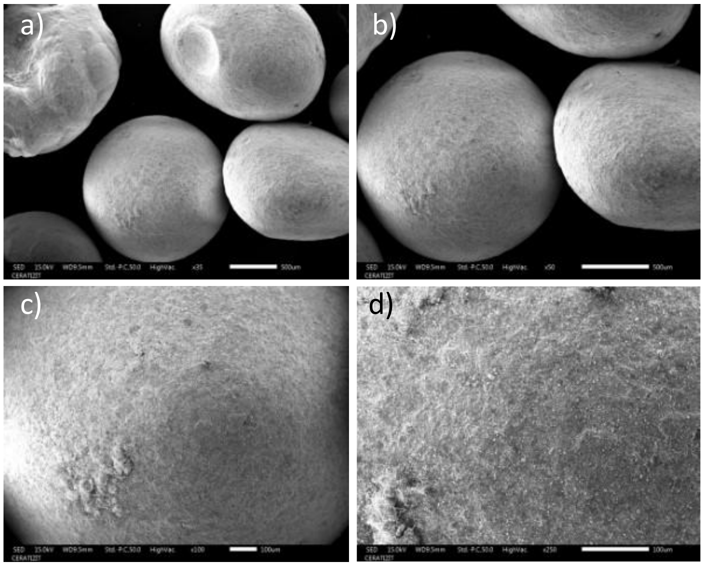

Figure 125: Sample D/1200-1700 at various magnifications: a) 35x, b) 50x, c) 100x, d) 250x

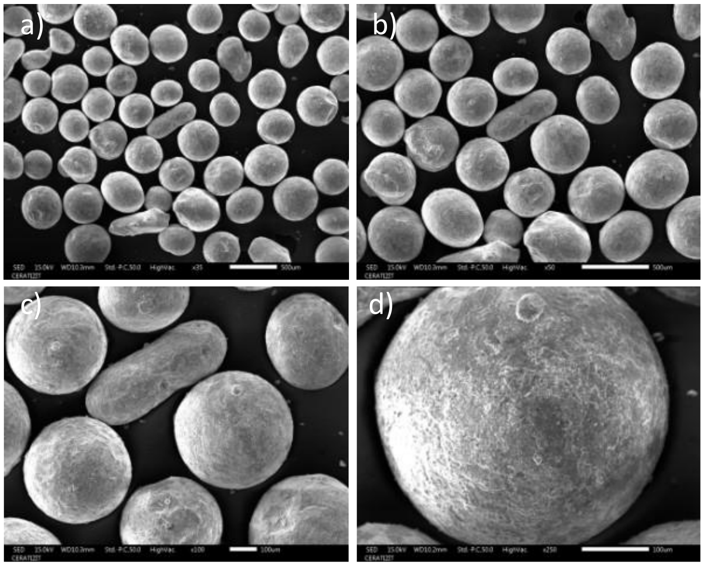

Figure 126: Sample E/200-400 at various magnifications: a) 35x, b) 50x, c) 100x, d) 250x

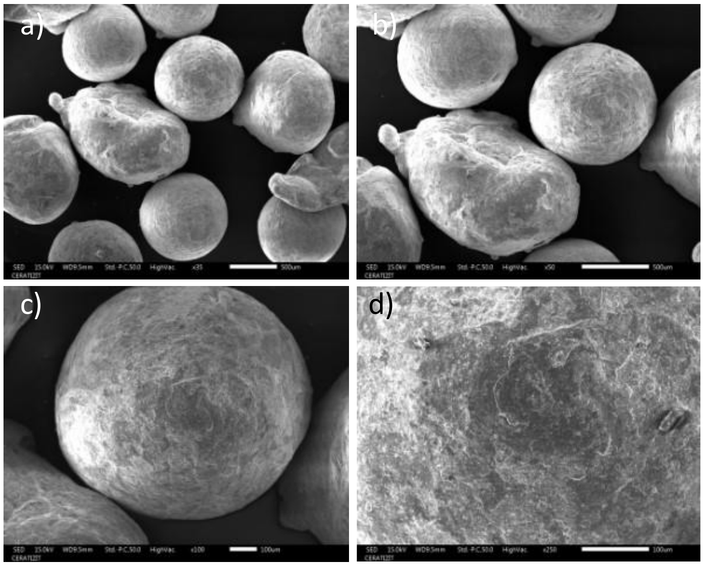

Figure 127: Sample E/700-1200 at various magnifications: a) 35x, b) 50x, c) 100x, d) 250x

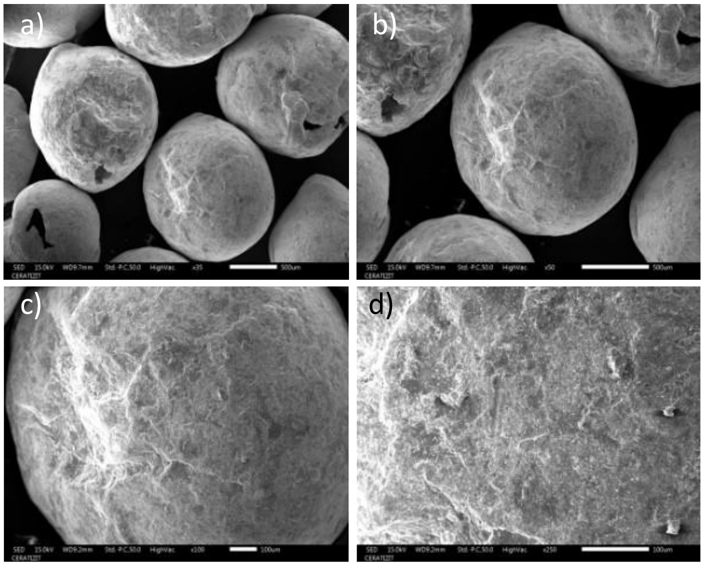

Figure 128: Sample E/1000-1700 at various magnifications: a) 35x, b) 50x, c) 100x, d) 250x

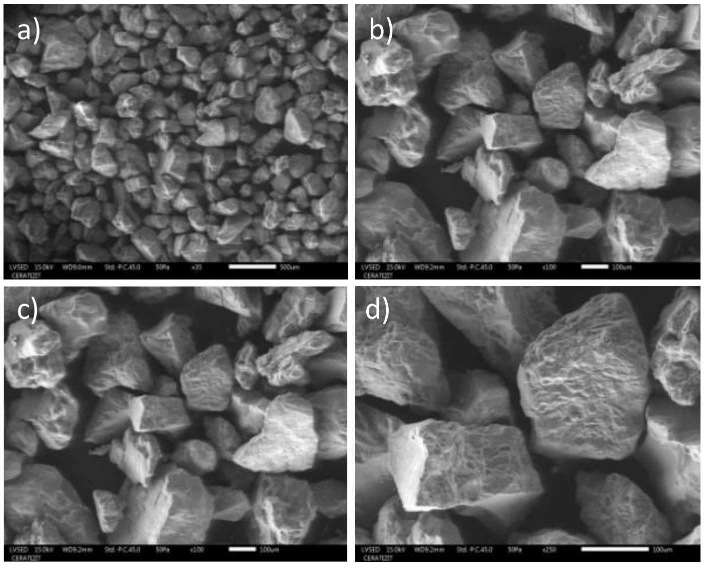

Figure 129: Sample F/100-800 at various magnifications: a) 35x, b) 50x, c) 100x, d) 250x

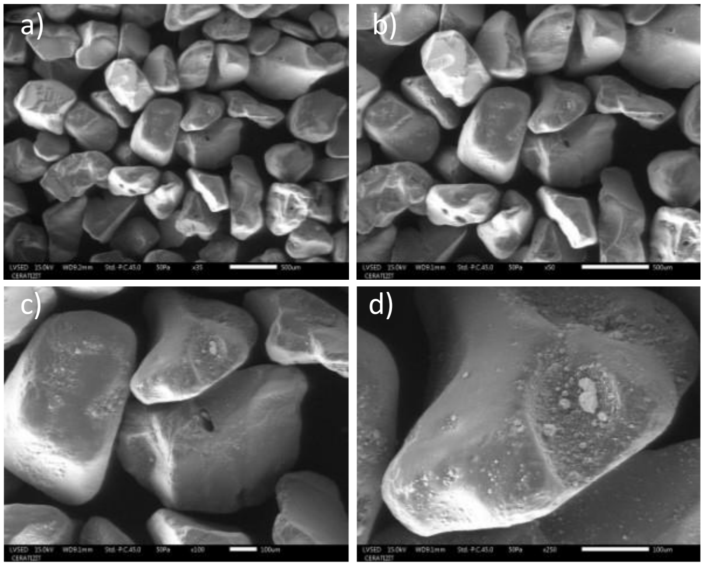

Figure 130: Sample G/355-500 at various magnifications: a) 35x, b) 50x, c) 100x, d) 250x

14.4 Mass flow rates in the function of the granular Bond number

Information can be found in the corresponding chapters.

<u>Sieved and unsieved granular system of type A.</u>

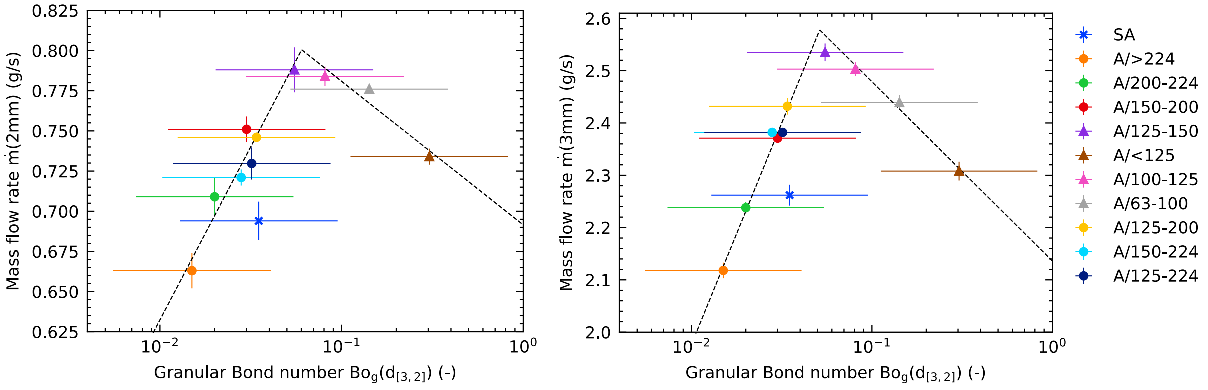

Figure 131: Mass flow rate for two different orifice sizes 2mm (left) and 3mm (right) in the function of the granular Bond number. Both graphs share the same legend. Sample SA.

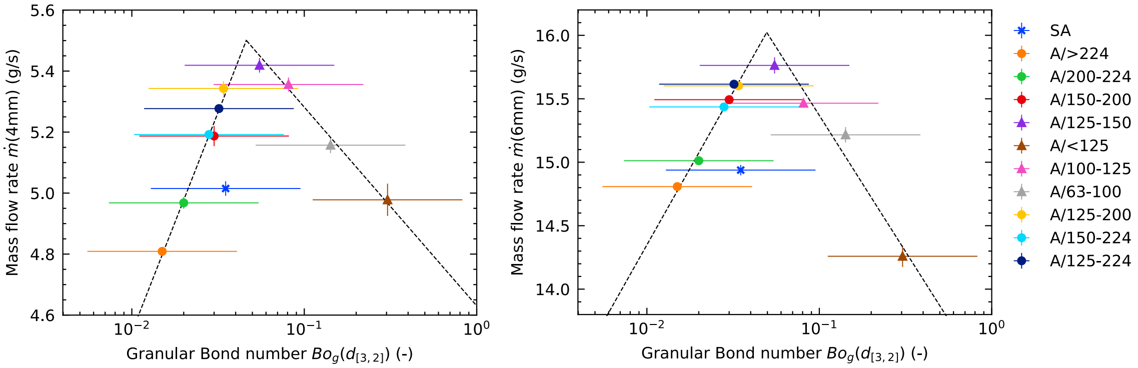

Figure 132: Mass flow rate for two different orifice sizes 4mm (left) and 5mm (right) in the function of the granular Bond number. Both graphs share the same legend. Sample SA.

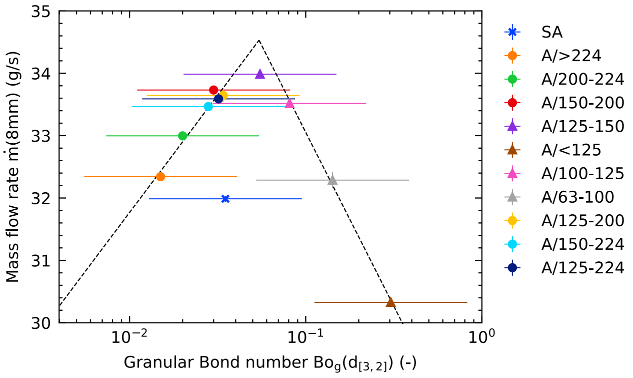

Figure 133: Mass flow rate for an orifice size of 8 mm in the function of the granular Bond number. Both graphs share the same legend. Sample SA.

Sieved and unsieved granular system of type C.

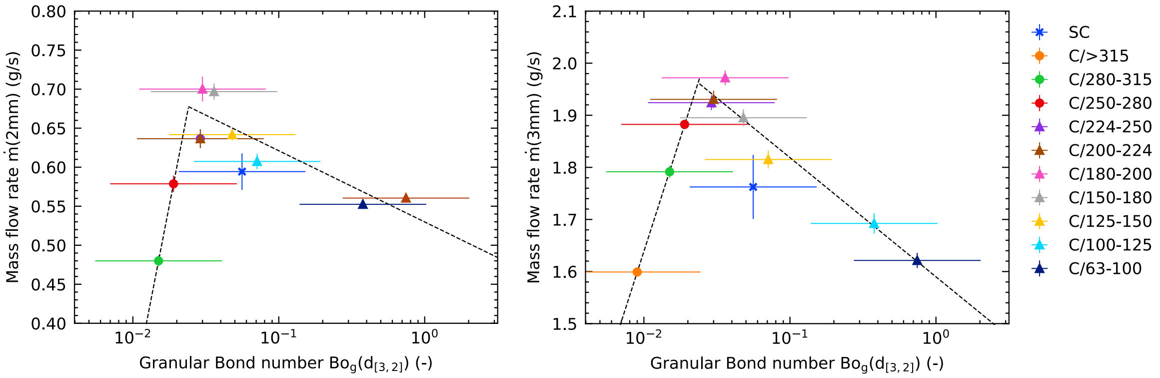

Figure 134: Mass flow rate for two different orifice sizes 2 mm (left) and 3 mm (right) in the function of the granular Bond number. Both graphs share the same legend. Samples are of type C. Jamming was observed for sample C1.1 with an orifice diameter of 2 mm.

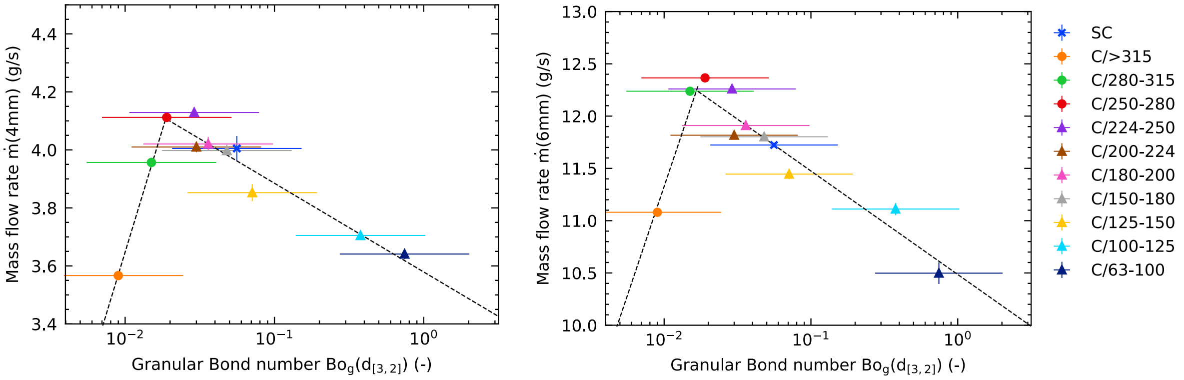

Figure 135: Mass flow rate for two different orifice sizes 4 mm (left) and 6 mm (right) in the function of the granular Bond number. Both graphs share the same legend. Samples are of type C.

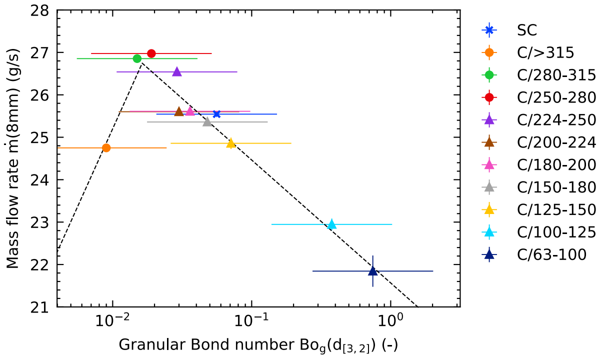

Figure 136: Mass flow rate for two different orifice sizes 8 mm in the function of the granular Bond number. Both graphs share the same legend. Samples are of type C.

14.5 Angle of repose of hard metal granular systems

Information can be found in the corresponding chapters.

Table 18: Angle of repose of hard metal granules

Sample	**AOR (°)**	**Friction coefficient μ (-)**
H-HM4	34.4 ± 0.1	0.685 ± 0.002
I-HM5	36.6 ± 0.1	0.742 ± 0.004
J-HM6	38.5 ± 0.1	0.796 ± 0.004
K-HM7	35.3 ± 0.1	0.708 ± 0.002
L-HM8	33.0 ± 0.1	0.649 ± 0.002
M-HM9	33.7 ± 0.1	0.667 ± 0.002
N-HM10	32.7 ± 0.1	0.642 ± 0.002
O-HM11	35.5 ± 0.1	0.712 ± 0.002
P-HM12	31.8 ± 0.1	0.621 ± 0.002
Q-HM13	36.7 ± 0.1	0.745 ± 0.002
R-HM14	35.9 ± 0.1	0.725 ± 0.002